UNIVERSITY OF STRATHCLYDE
Department of Physics

High performance microstructured light emitting diodes - mechanisms and processes

by

Enyuan Xie

A thesis presented in fulfilment of the
requirements for the degree of
Doctor of Philosophy

May 2013

Declaration of Authorship

This thesis is the result of the author's original research. It has been composed by the author and has not been previously submitted for examination which has led to the award of a degree.

Signed: ________________________________

Date: ________________________________

Frontispiece

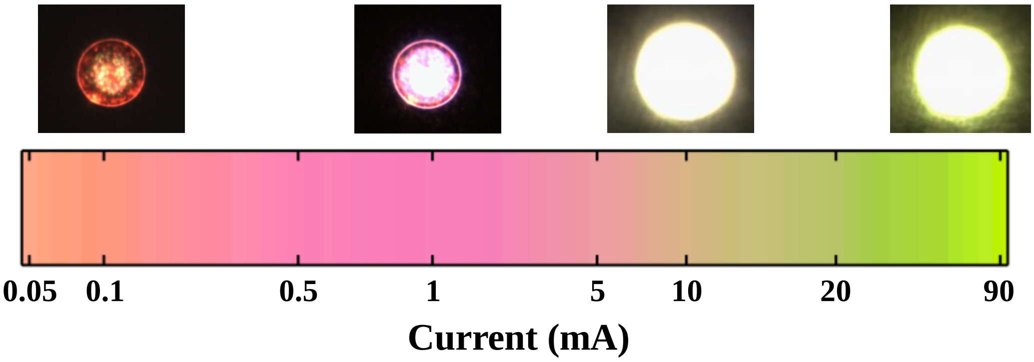

A single III-nitride colour-tunable micro-light emitting diode. The bottom bar is the calculated (see later) emission colour at different operating currents. Representative optical images of the device operated at 0.1, 1, 10, 90 mA (from left to right), respectively, are displayed.

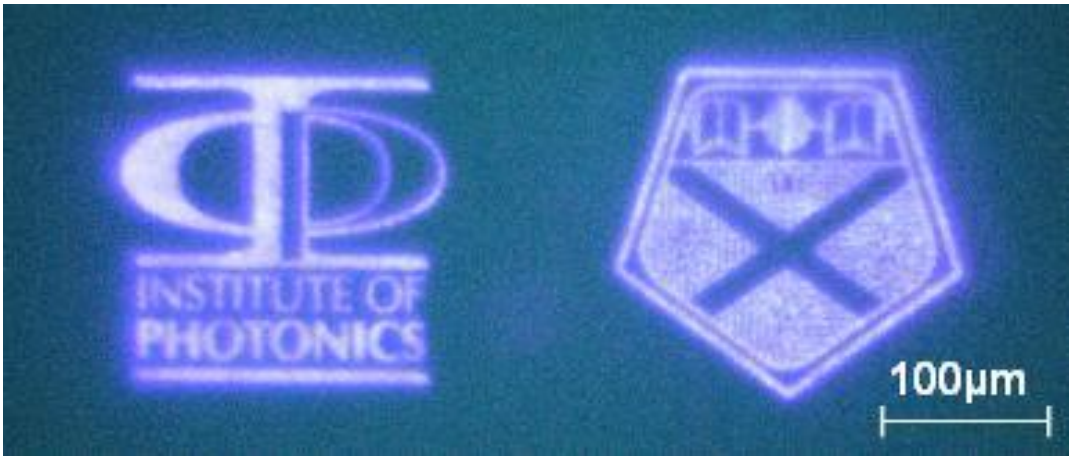

III-nitride 405 nm microstructured-image light emitting diode displaying the logos of Institute of Photonics (left) and University of Strathclyde (right).

Abstract

The research work presented in this thesis focuses on the mechanisms and development of novel III-nitride microstructured light emitting diodes (LEDs). In particular, we focus on micro-sized LEDs (‘μ-LEDs’) and LEDs containing micro-scale emission images i.e. ‘microstructured-image LEDs’.

III-nitride μ-LEDs, which are devices with dimensions less than 100 μm, show improved device performance and novel potential applications compared with broad-area LEDs. The internal electric field in III-nitride materials, which is mainly caused by the strain due to lattice mismatch with the substrate, is a serious issue for III-nitride LEDs. As the strain can be relaxed in micro-scale structures, the performance of μ-LEDs can be improved. In this work, we have investigated the strain relaxation process in III-nitride micro-pillars as a function of pillar diameter by high-spatial-resolution cathodoluminescence. The results of this study give a guideline for further design of μ-LEDs with high efficiency. The internal electric field can also be screened by injection of carriers, leading to a blue-shift of the emission wavelength for III-nitride LEDs. Due to the high operating current density that μ-LEDs can sustain, the magnitude of this blue-shift is remarkably increased for μ-LEDs. Based on this characteristic, colour-tunable μ-LEDs have been demonstrated in this work, which offers a simple way to achieve multi-colour displays. In order to further improve the performance of μ-LEDs, we have also developed Pd-based contacts to p-type GaN and investigated the current-density dependent specific contact resistivity. At high current densities, the μ-LEDs with optimized Pd-based contacts have better electrical performance compared with devices using oxidized Ni/Au contacts. The optimized Pd-based contact also leads to improved optical power for blue LEDs in flip-chip configurations.

III-nitride microstructured-image LEDs are devices in which micro-scale emission patterns are created in single LEDs. These devices offer a simple approach to the display of high-resolution images. CHF_3 plasma treatment is a novel technique used for the fabrication of these devices. This plasma treatment can locally modify the electrical properties of p-type GaN and define the emission image. An application of these devices for maskless image writing is demonstrated.

Acknowledgements

First of all I'd like to thank my supervisor, Dr. Erdan Gu, for giving me this opportunity and for his guidance, inspiration, patience and support, particularly in helping me to overcome all the difficulties during my PhD studies. I am also thankful to Prof. Martin Dawson and Dr. Ian Watson for their guidance and encouragement throughout my studies.

Many thanks must be given to Dr. Zheng Gong, Dr. David Massoubre and Dr. Benoit Guilhabert for teaching me patiently the LED fabrication and image writing processes. They also provide invaluable advice and discussions during my studies. I am grateful to Dr. Paul Edwards and Prof. Robert Martin for their support on cathodoluminescence and temperature-dependent photoluminescence measurements.

I also want to thank all my colleagues, past and present, for making IoP such a good place to work. I am lucky to have made some good friends during my time at the IoP.

Finally, I wish to express my sincere appreciation to my family for their unconditional love, support and encouragement all the time. Special thanks to my wife Sarah for all she has done for me.

Contents

List of Figures

List of Tables

Dedicated to my family

Chapter 1

Introduction

This thesis focuses on the mechanism and development of novel III-nitride microstructured light emitting diodes (LEDs). As such, the first chapter presented here functions as a general introduction to LEDs especially for those fabricated from III-nitride materials. The motivations of the work presented in the thesis are also introduced in this chapter. In section 1.1, the historical development and further prospects of LEDs are summarized. The basic working principles of LEDs are described in section 1.2. Section 1.3 focuses on the III-nitride materials and related growth processes, which provides the basic background for III-nitride LEDs. The III-nitride LEDs are introduced in section 1.4. Besides the general properties of III-nitride LEDs, two formats of devices, micro-LEDs and novel microstructured-image LEDs, are specifically introduced in subsections 1.4.1 and 1.4.2, respectively. Finally, an outline of this thesis is given in section 1.5.

1.1 Development of light emitting diodes

The light emitting diode (LED) is a semiconductor electroluminescent light source. It is considered that the first LED was invented by the British experimenter H. J. Round in 1907 using a crystal-metal-point-contact structure fabricated from SiC [1]. A yellow light was thus produced when a SiC crystal was touched by a metal electrode. In 1928, a detailed investigation of the luminescence phenomenon of the first LED was reported [2]. It was proven that the light emitted from the device is not generated by the black-body light emission resulting from heat glow (incandescence) but in response to the passage of an electric current or to an electric field. The phenomenon where a material emits light when electricity is passed through it is called electroluminescence.

The SiC and II-VI semiconductors were well-known materials for LED fabrication until the 1950's, when the III-V compound semiconductors were postulated and demonstrated [3, 4]. These novel man-made III-V compounds attracted great attention from the mid 1950's and accelerated the development of LEDs with different emission wavelengths. The first infrared (IR) (~870 nm) LED based on GaAs was reported in 1962 [5]. In the same year, the first commercial red LED based on $GaAs_{1-x}P_x$ was offered by General Electric Corporation [6]. The subscript notations (x, $1-x$) of the material here describe the relative composition of an alloy, which are adjustable depending on the target emission wavelength. Then the emission spectra of LEDs were extended from the red to green region by N-doped GaAsP LEDs [7]. Green LEDs were also achieved by using N-doped GaP [8].

Along with the development of high-performance red-to-green LEDs, a lot of work was concentrated on extending the emission spectra of LEDs to blue and ultraviolet (UV) wavelength regions. III-nitride materials were considered as possible candidates for UV and blue emission. However, due to the low crystal quality and the inability to produce p-type doping in GaN [9], the development of III-nitride materials was not successful until the late 1980's. Thus, prior to the 1990's, the commercial blue LEDs on the market were based on SiC. However, the best electrical-to-optical power-conversion efficiency of blue SiC LEDs was only 0.03 % [10]. This value is very low and, hence, limited the application of blue SiC LEDs. The breakthroughs in III-nitride materials began from 1986, when the crystal quality of a GaN film was significantly improved by the incorporation of an AlN nucleation layer at a low growth temperature before the deposition of the main GaN film [11]. The incorporation of an AlN or GaN nucleation layer at a low growth temperature is now a standard process to grow high-quality III-nitride films with a low density of defects. In addition, Mg acceptors in GaN were activated by electron-beam irradiation [12] and post-growth annealing [13], which resulted in p-type GaN being achieved. These breakthroughs opened the door to the development of high-performance III-nitride LEDs [14] and laser diodes (LDs) [15]. The main work reported in this thesis concerns microstructured LEDs fabricated from III-nitride materials. Thus, a detailed introduction of the III-nitride materials and related LEDs will be given in sections 1.3 and 1.4, respectively.

In the past twenty years, great effort has been made to improve the performance of LEDs with different emission wavelengths. Two important parameters are used to evaluate the performance of LEDs: internal quantum efficiency (IQE, or η_{int}) and external quantum efficiency (EQE, or η_{ext}). The IQE is defined as the ratio of the number of photons emitted by the LED active region to the number of injected charge carriers. As we will discuss in subsection 1.2.1, the injected charge carriers recombine either radiatively to emit photons or nonradiatively to release in form of heat in semiconductors. Thus, the IOE of LEDs can be determined by the radiative recombination lifetime (τ_r) and noradiative recombination lifetime (τ_{nr}) as [16]:

$$\eta_{int} = \frac{\tau_r^{-1}}{\tau_r^{-1} + \tau_{nr}^{-1}} \tag{1.1}$$

The EQE refers to the ratio of the number of photons emitted by the LED into free space to the number of injection charge carriers. So the EQE of LEDs can be expressed as:

$$\eta_{ext} = \eta_{int} \times \eta_{extraction} \tag{1.2}$$

where the $\eta_{extraction}$ is light extraction efficiency (LEE). The LEE is thus the ratio of the number of photons emitted into free space to the number of photons generated in the LED active region. Nowadays, high-performance LEDs with emission wavelengths covering the entire visible spectrum have been commercialized. Invisible UV and IR LEDs are also available on the market. Figure 1.1 shows the EQE versus emission wavelength for high-performance LEDs based on two III-V material systems, along with the human-eye response [$V(\lambda)$]. As shown, in the green-to-yellow emission region, the achieved EQE is relatively low, where the human eye is the most sensitive. This low EQE in the green-to-yellow emission region is referred as the ‘green gap’ or ‘green-yellow gap’.

As the high-performance LEDs have become available, different applications of these devices continued to emerge. Thanks to their low energy consumption, long lifetime and mechanical robustness, LEDs are attractive in different application fields. Figure 1.2 shows some examples of various LED applications in our daily life. Of these applications, the white-light LED lamps used in home and office lighting are arguably the most important. Compared with conventional lighting using incandescent and fluorescent lamps, the LED lighting technology is able to generate white light more efficiently. It is anticipated that the efficiency of LED-based white-light sources will eventually be, respectively, up to 63 % and 90 % more than that of fluorescent and incandescent sources [18]. Figure 1.3

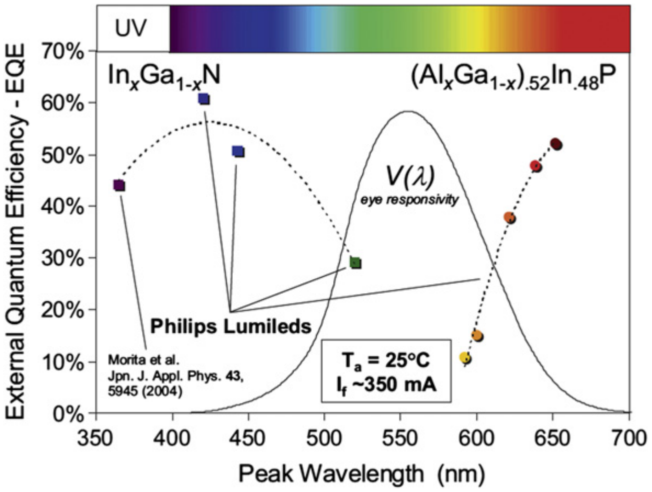

Figure 1.1: EQE versus emission wavelength for high-performance LEDs based on III-nitride and III-phosphide materials. After [17].

shows a comparison of the luminous efficacy of conventional light sources with that expected for LED lighting technology in the near future. Here, the luminous efficacy is the conversion efficiency from optical power to luminous flux, which is measured in the unit of lm/W. The lumen (lm) is the unit of luminous flux which represents the power as perceived by the human eye. Furthermore, the low energy consumption and long lifetime are additional advantages for the LED lighting technology. All of these advantages will lead to huge economic and environmental benefits when the white-light LED lamps replace the fluorescent and incandescent ones in coming years.

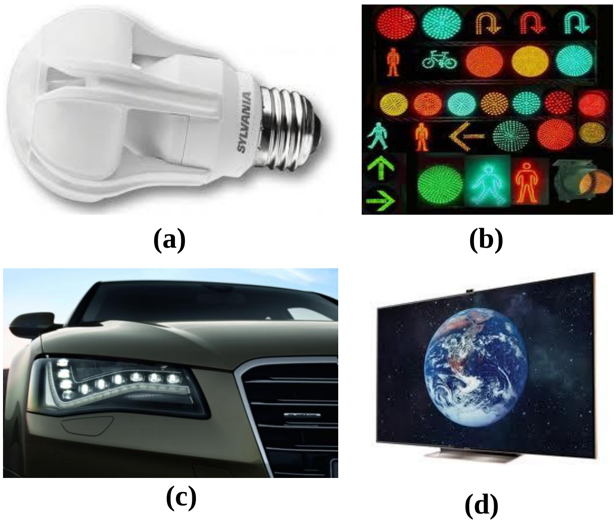

Figure 1.2: Typical applications of LEDs in our daily life: (a) Osram 100 W white-light LED lamp; (b) LED-based traffic light; (c) LED headlights in the Audi A8; (d) Samsung ES9000 LED back-lit television.

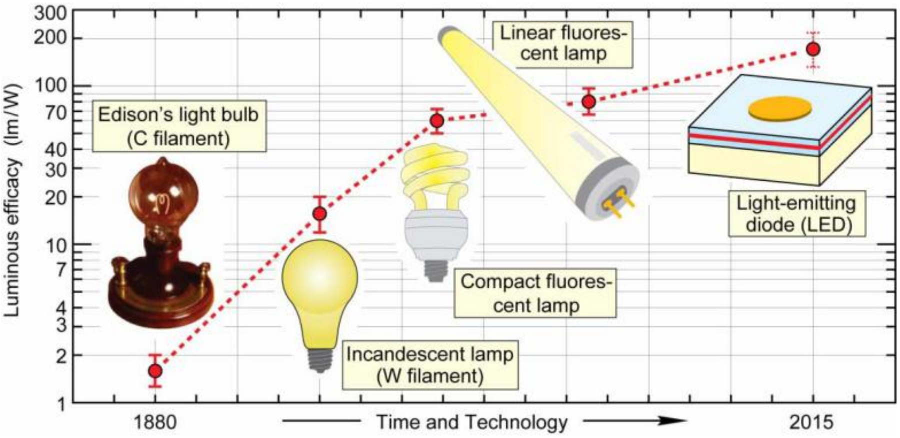

FIGURE 1.3: Comparison of the luminous efficacy of conventional lighting technologies with the potential of LED lighting technology. After [18].

Figure 1.4(a) schematically shows the typical package of a low-power LED. Such an LED is usually a single chip of area around 300 × 300 μm^2. It is bonded to a metal frame with leads for the anode and cathode via thin gold wires. The epoxy dome is used to protect the LED and is shaped as a lens to direct the output light. The refractive index of this epoxy (∼1.5) also improves the LEE of the LEDs. These low-power LEDs are normally used as indicator lights for consumer electronics. On the other hand, a high-power packaged LED, as shown in Figure 1.4(b), consists of multiple LEDs to increase the total output power. In order to prevent the LEDs being damaged due to excess heat generated during operation, an additional thermal heat sink is required. These high-power LEDs are intended for general illumination used such as in home and office lighting.

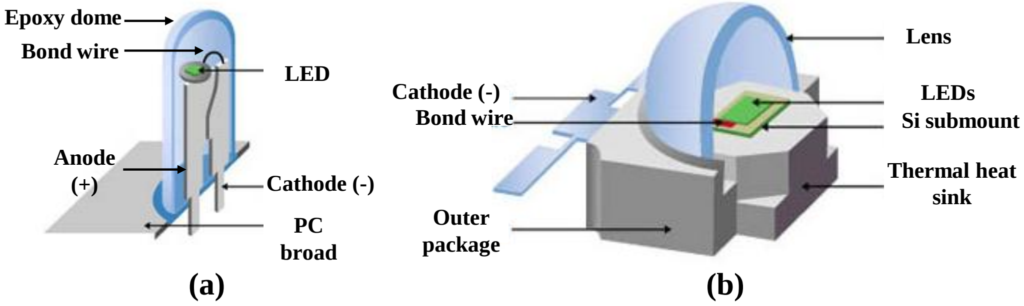

FIGURE 1.4: Schematic packages of (a) low-power and (b) high-power LEDs.

1.2 Operating principles of light emitting diodes

As mentioned in the last section, LEDs are fabricated from different semiconductors. Based on solid-state energy band theory, the periodic atomic arrangement in a semiconductor crystal leads to the energy band structure of a semiconductor which can be visualized as having a valence band and a conduction band separated by a bandgap. The bandgap represents the forbidden energy region between the valence and conduction bands. A semiconductor has two types of free carriers, namely electrons and holes. Free electrons are located close to the minimum of the conduction band while the holes are close to the maximum of the valence band. The recombination of electrons and holes leads to the possible emission of photons. The value of the bandgap, E_g, determines the energy and, hence, the wavelength (λ) of photons emitted from the semiconductor. This relationship can be expressed as:

$$E_g = E_C - E_V \approx \frac{hc}{\lambda} \tag{1.3}$$

where E_C is the energy of the conduction band minimum, E_V is the energy of the valence band maximum, h is Planck's constant and c is the speed of light in a vacuum. When the electrons recombine with holes, the excess energy ($\sim E_g$) can be released either by the emission of photons or as heat for increasing lattice-atom vibrations. These two processes correspond to the radiative and nonradiative recombinations in a semiconductor, which will be discussed in subsection 1.2.1 in detail.

Intrinsic semiconductors are pure semiconductors without impurity atoms and no lattice defects in the crystal [19]. For the intrinsic semiconductors, under external excitation, the number of generated free electrons in the conduction band is equal to the one of free holes in the valence band. So the intrinsic semiconductors are neutrally charged and their conductivity is relatively low. In order to modify the conductivity of semiconductors, some impurities (dopants) can be intentionally induced into semiconductors. This process is known as doping. In general, the dopants can be classified as donors and acceptors. A donor can generate a free electron in the conduction band without generating a hole in the valence band. Inversely, an acceptor can produce a hole to the valence band without creating an electron in the conduction band. The semiconductors doped with donors are so-called n-type semiconductors, in which the electrons are majority carriers while the holes are minority carriers. On the other hand, the semiconductors doped with acceptors are so-called p-type semiconductors. For p-type semiconductors, the majority carriers are holes and the minority carriers are electrons. The basic form of an LED is a p-n junction, which is formed at the interface of p-type and n-type semiconductors. The detailed introduction of the p-n junction will be given in subsection 1.2.2.

There are two general categories of semiconductors, namely, direct and indirect bandgap semiconductors. Figure 1.5 shows the simplified band structures of direct and indirect bandgap semiconductors and related band-to-band electron transition processes. The band-to-band electron transition process may result in the photon emission via electron-hole recombination. The horizontal axis in this figure is the crystal momentum, which is directly proportional to the electron wavenumber k. The crystal momentum represents the allowed momentum of electrons within the crystal structure. For direct bandgap semiconductors, as shown in Figure 1.5(a), the bottom of the conduction band and the top of the valence band coincide in k-space. Thus, the electron transition may occur directly without a change of momentum. For indirect bandgap semiconductors, the bottom of the conduction band does not coincide with the top of the valence band in k-space [Figure 1.5(b)], which leads to an indirect electron transition. This indirect electron transition occurs with a change of momentum and, thus, requires the assistance of a lattice vibration (phonon) to conserve momentum. Consequently, the probability of direct electron transitions is much higher than that of indirect electron transitions. Thus, the efficiency of LEDs fabricated from direct bangap semiconductors is much higher than that of devices fabricated from indirect bandgap materials. Thus the indirect bandgap of SiC results in the low efficiency of blue SiC LEDs as mentioned previously. Besides the material selection, subsection 1.2.3 will discuss the other concepts and designs to achieve high-efficiency LEDs .

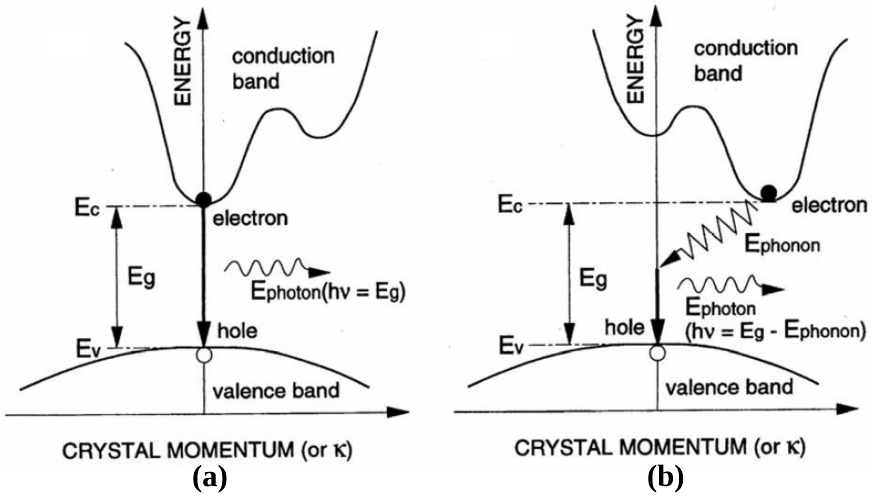

FIGURE 1.5: Band structures of (a) direct and (b) indirect bandgap semiconductors and related band-to-band electron transition processes. After [20].

1.2.1 Radiative and nonradiative recombination processes

As mentioned above, electrons and holes recombine either radiatively or nonradiatively in a semiconductor. The radiative recombination process of electrons and holes results in the emission of photons. On the other hand, during the nonradiative recombination process, the excess energy of electrons is released in the form of heat and, thus, is converted to the vibrational energy of lattice atoms. For LEDs, the radiative recombination process is clearly the preferred one. However, the nonradiative recombination process cannot be totally eliminated. Figure 1.6 shows the band diagram illustrating the radiative recombination process and two dominant nonradiative recombination processes with different physical mechanisms. The E_{Fi} in the figure represents the intrinsic Fermi level for the semiconductor.

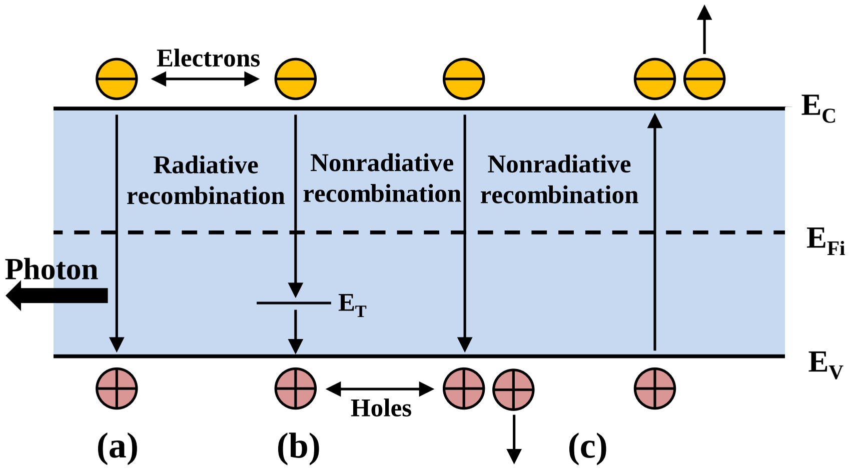

FIGURE 1.6: Band diagram illustrating electron and hole recombination processes: (a) radiative recombination; (b) nonradiative recombination via defect level; (c) nonradiative recombination via Auger recombination. The vertical axis represents energy and the horizontal axis is space (for illustrative purposes).

Process (a) in Figure 1.6 illustrates the radiative recombination in a semiconductor. Clearly, the radiative recombination process depends on the density of available electrons and holes. Thus, the radiative recombination rate (R_{rad}) is expected to be proportional to the product of electron and hole densities (n and p), that is $R_{rad} \propto np$. By using a proportional factor, the R_{rad} can be expressed as [16]:

$$R_{rad} = Bnp \tag{1.4}$$

Equation 1.4 is the bimolecular rate equation. The proportionality factor B is the bimolecular (radiative) recombination coefficient and has the unit of $\mathrm{cm^3 s^{-1}}$.

For nonradiative recombination, there are several different physical mechanisms. Processes (b) and (c) in Figure 1.6 represent two dominant nonradiative recombinations in semiconductors, which are caused by crystal defects and Auger recombination respectively. The crystal defects are unavoidable in real semiconductors and include unwanted foreign atoms, native defects and dislocations. All of these defects may lead to different energy levels within the bandgap of semiconductors, represented by the trap level E_T denoted in the process (b) of Figure 1.6. These energy levels are efficient recombination centres which may result in nonradiative recombination. Furthermore, these trap-level-assisted recombination centres are more effective when they are close to the middle of the bandgap [16]. It has been found that the recombination rate of trap-level-assisted nonradiative recombination processes ($R_{trap,nr}$) is strongly dependent on the capture rate of the minority carriers and minority carrier density in the semiconductor. So $R_{trap,nr}$ can be expressed similarly to Equation 1.4 but dependent on the doping type of the semiconductor. For n-type semiconductors ($n \gg p$), the equation can be written as:

$$R_{trap,nr} = A_p p \tag{1.5}$$

And for p-type semiconductors ($p \gg n$), it is:

$$R_{trap,nr} = A_n n \tag{1.6}$$

In both equations, the proportionality constant A is the trap-level-assisted nonradiative recombination coefficient and has the unit of s^{-1}. Another important nonradiative recombination mechanism is Auger recombination. The Auger recombination process involves three carries. In this process, the resultant energy ($\sim E_g$) generated via the electron-hole recombination is transferred to another electron or hole. This resultant energy is dissipated by the excitation of electrons high into the conduction band or the excitation of holes deep into the valence band. It can be found that the Auger nonradiative recombination rate ($R_{Auger,nr}$) is proportional to the square of the carrier density, since two carriers of the same type are required. So the $R_{Auger,nr}$ corresponding to the two Auger processes shown as process (c) in Figure 1.6 are given as [16]:

$$R_{Auger,nr} = C_n n^2 p \tag{1.7}$$

and

$$R_{Auger,nr} = C_p n p^2 \tag{1.8}$$

where the proportional constant C is the Auger recombination coefficient and has the unit of cm^{-6}s^{-1}. The process described by Equation 1.7 is more likely to happen in n-type semiconductors, while the process described by Equation 1.8 is dominant in p-type semiconductors.

Based on above introduction to the radiative and nonradiative recombination processes in semiconductors, the following subsection will describe how an LED is designed to realize radiative recombination by the injection of carriers.

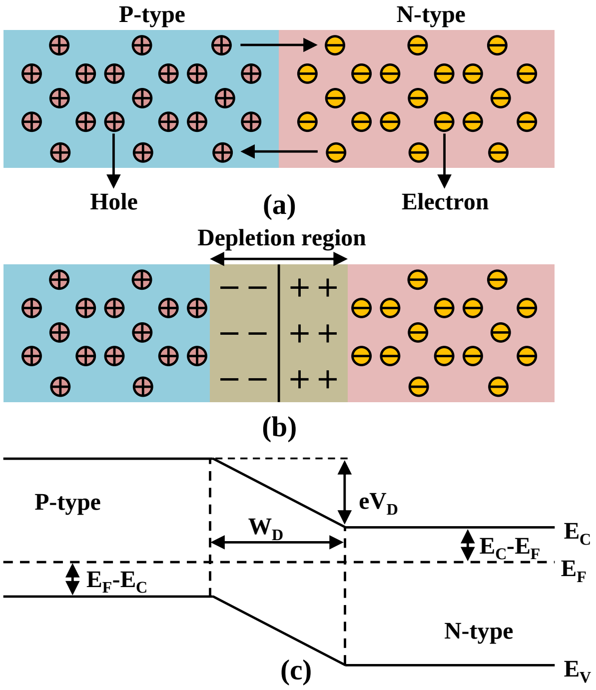

FIGURE 1.7: (a) Simplified geometry of a p-n junction; (b) p-n junction under zero bias, showing the depletion region; (c) band diagram of a p-n junction under zero bias.

1.2.2 P-n junction

The basic structure of an LED is the p-n junction, as shown in Figure 1.7(a). The entire p-n junction is a single-crystal material in which one region is of heavily doped p-type semiconductor and the adjacent region is of heavily doped n-type semiconductor. If a p-n junction consists of a single material, it is known as a p-n homojunction. The so-called heterojunction employs two semiconductor materials with different bandgap energy. In this subsection, the general introduction of a p-n junction is given based on the p-n homojunction. A discussion of the heterojunction will be given in the next subsection.

For an unbiased p-n junction, there is a large density gradient for both electrons and holes. Therefore, the majority carriers (electrons) in the n-type region diffuse to the p-type region and the majority carriers (holes) in the p-type region diffuse to the n-type region. This diffusion results in a region which is depleted of any free carriers around the interface between p-type and n-type semiconductors. This region is known as the depletion region, as denoted in Figure 1.7(b). In the depletion region, the free carries are absent and the only charges are from ionized

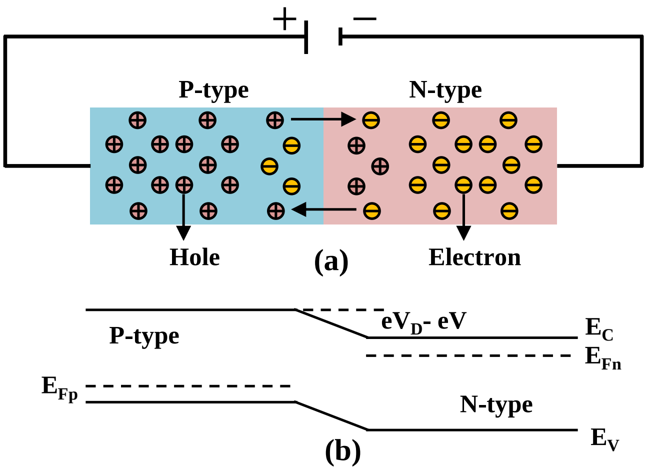

FIGURE 1.8: (a) P-n junction under forward-bias conditions; (b) band diagram of a p-n junction under forward-bias conditions.

dopants, such as positively charged donors in the n-type region and negatively charged acceptors in the p-type region. These charges produce a potential across the depletion region, which is known as the diffusion voltage (V_D). The direction of V_D is opposite to that of electron and hole diffusion. In a thermal equilibrium state therefore, the diffusion of carriers is balanced by V_D. From Figure 1.7(c), it can be found the eV_D actually represents the barrier that the free carriers must overcome to reach the regions with the opposite conductivity type, where e is the elementary charge.

When an external bias voltage is applied to the p-n junction, the external potential is mainly dropped across the depletion region. This is because of the high resistance of this depletion region. So the external bias voltage can be used to intentionally change the potential across the depletion region. Under reverse-bias conditions, the potential will be increased and will further impede the diffusion of carries. Oppositely, under forward-bias conditions, as shown in Figure 1.8, the potential across the depletion region will be decreased and, thus, the carriers will be injected into regions with the opposite conductivity type and the current will increase. This will lead to the recombination of electrons and holes generating photons. Clearly, in order to produce light emitted from the p-n junction, a forward-bias voltage needs to be applied.

1.2.3 Double heterostructure and quantum well structure

Figure 1.9(a) shows the carrier distribution in a p-n homojunction under forward-bias conditions. The L_n and L_p in this figure respectively represent the diffusion length of minority carriers. With the value of several micrometres, the diffusion length is the average distance over which a minority carrier diffuses before recombination. From this figure, it can be seen that the minority carriers distribute over a long distance (diffusion length) in the adjacent region before recombination and, thus, the density of minority carriers is relatively low in that region. As discussed in subsection 1.2.1, the R_{rad} is proportional to the carrier density (Equation 1.4). So, the R_{rad} in the p-n homojunction is relatively low, which is the main disadvantage of LEDs based on p-n homojunctions.

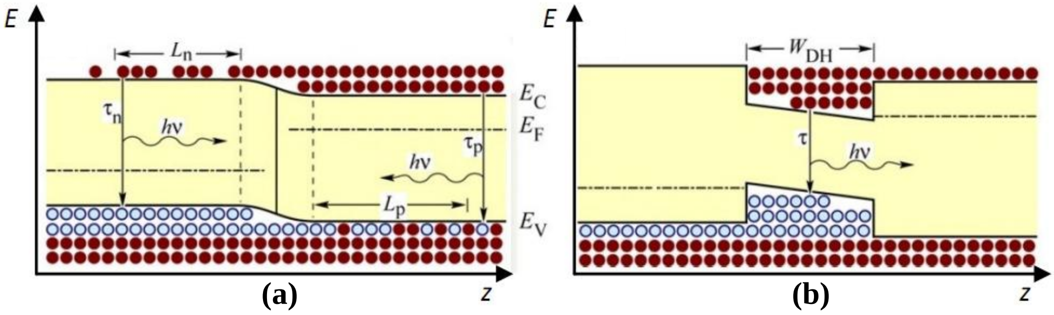

(a) **(b)**

FIGURE 1.9: Band diagrams of (a) a p-n homojunction and (b) a p-n heterojunction under forward-bias conditions. After [16].

In order to achieve the high R_{rad}, currently all high-performance LEDs employ p-n heterojunctions. A p-n heterojunction normally has two semiconductor materials with unequal bandgap energy. The small-bandgap semiconductor is used for the active region and the larger-bandgap one is used for the barrier region. If the structure consists of two barrier regions, this structure is known as a double heterostructure. In the double heterostructure, as shown in Figure 1.9(b), the small-bandgap active region is sandwiched between two heavily doped p-type and n-type barrier regions with the larger bandgap. This leads to the result that injected carriers are confined in the active region by means of the barriers. So the thickness of the active region (W_{DH}) is the region in which the carriers recombine. The thickness W_{DH} can be much smaller than the diffusion length of the carriers. This results in a much higher carrier density in the double heterostructure compared with that in a homojunction. Consequently, the R_{rad} in the double heterostructure is significantly increased compared with that in the homojunction.

When W_{DH} is sufficiently small and comparable to the de Broglie wavelength of the carriers, quantum confinement of carriers takes place. The active region of the double heterostructure then becomes a quantum well (QW). In the QW, the carriers are confined in one crystal direction. In this direction, the permitted energy levels no longer form a continuous energy band, and the carriers can only occupy quantized energy levels with discrete energy values. The quantized energy values of carriers can be simply calculated (for appropriate situations) by the one-dimensional infinite-well-approximation method. In this method, a potential well is viewed as being sandwiched between two potential barriers with infinite height. The carriers are confined in the well by these two potential barriers. The quantized energy values calculated by this method are given by:

$$E_n = \frac{h^2}{8m^*}\left[\frac{(n+1)}{L_{QW}}\right]^2, n = 0, 1, 2, 3\cdots \tag{1.9}$$

where m^* is the effective mass of the carriers and L_{QW} is the width of the QW. Figure 1.10 shows the typical 'band edge' band diagram of a QW. The $E_{0,e}$ and $E_{0,h}$ in the figure are the ground-state energy (lowest-state energy, when $n = 0$) of electrons and holes, respectively. From this figure, it can be found the emission energy of the QW ($E_{g,QW}$) is different from either bandgap energy of two semiconductors used for the barrier and well. Furthermore, as illustrated in Equation 1.9, $E_{g,QW}$ can also be intentionally changed by the careful alteration of L_{QW}. Moreover, because L_{QW} is smaller than W_{DH}, R_{rad} further increases in the QW compared with that in the double heterostructure. The active region of most LEDs consists of several closely-spaced QWs, which is referred to as a multi-quantum well (MQW) region.

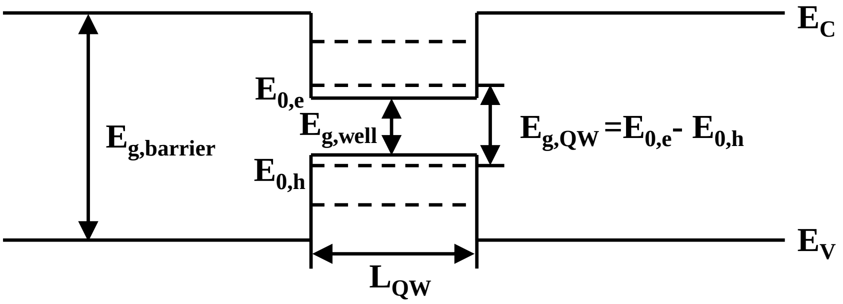

FIGURE 1.10: Band diagram of a QW. The vertical axis is energy and the horizontal axis represents distance perpendicular to the layers.

1.3 III-nitride materials

The microstructured LEDs investigated and developed in this thesis are all fabricated from LED wafers based on III-nitride materials. In order to provide a basic background of III-nitride LEDs, this section will give a general introduction to the III-nitride materials.

III-nitride materials have three basic binary alloys: AlN, GaN and InN. Under normal ambient conditions, the stable crystal of these materials has a hexagonal wurtzite structure [21]. Some other crystal structures for these materials can be achieved under special conditions [22]. The LED materials used in this work are all III-nitride materials with the wurtzite structure. Table 1.1 summarizes the important properties of these binary alloys with the wurtzite structure at room temperature (RT).

Parameter	Unit	AlN	GaN	InN
Lattice constant a_0	Å	3.112	3.189	3.545
Lattice constant c_0	Å	4.982	5.185	5.703
Bandgap energy E_g	eV	6.28	3.425	0.77
Electron mobility μ_n	cm^2/Vs	300	1500	3200
Hole mobility μ_p	cm^2/Vs	14	30	N/A

TABLE 1.1: Important properties of binary alloys from III-nitride materials at RT. The lattice constants are cited from Ref. [21] and the other parameters are cited from Ref. [16].

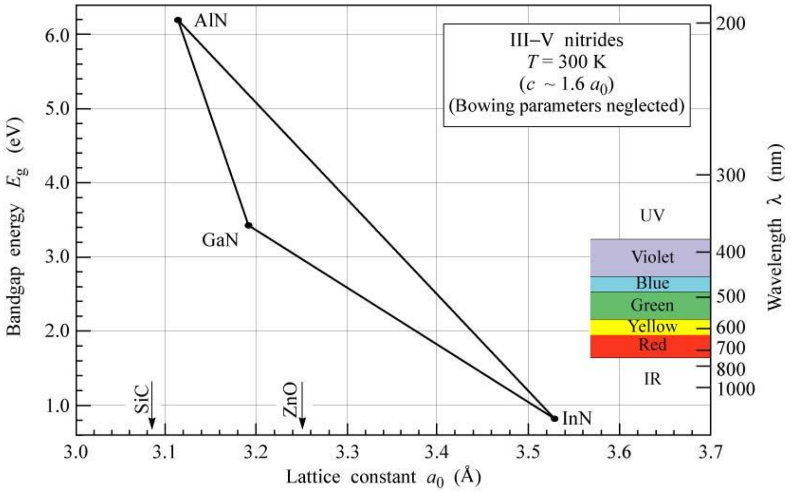

Figure 1.11: Bandgap energy versus lattice constant a_0 of III-nitride materials at RT. After [16].

The isomorphous nature of III-nitride materials results in the formation of ternary and quaternary alloys maintaining a wurtzite structure. The bandgap energy of these ternary and quaternary alloys can be tuned by altering the relative amount of the individual materials making up the alloys. Figure 1.11 shows bandgap energy versus lattice constant a_0 of III-nitride materials at RT. From this figure, it can be seen that the bandgap energy of III-nitride materials spans a wide range, i.e. from deep-UV to near-IR. Furthermore, the $In_xGa_{1-x}N$ ternary alloys, which are represented as the lower side of the triangle in Figure 1.11, have direct bandgaps covering the whole visible spectrum. This makes $In_xGa_{1-x}N$ ternary alloys exciting and attractive materials for the development of visible-light LEDs. Nowadays, high-performance blue and green LEDs are all based on these $In_xGa_{1-x}N$ ternary alloys. However, it is difficult to achieve a high-indium-content $In_xGa_{1-x}N$ ternary alloy with high radiative efficiency. The possible reason of this difficulty will be discussed later.

The majority of commercial III-nitride LED wafers are grown epitaxially by metal-organic chemical vapour deposition (MOCVD). In MOCVD, the crystal growth is by chemical reactions, rather than by the physical deposition of materials. During the MOCVD growth process, the substrate is exposed to one or more volatile metal-organic precursors. These precursors react and/or decompose on the substrate surface to deposit the desired materials and, in turn, form epitaxial films. However, the chemical bond energy of III-nitride materials is relatively strong compared with other III-V materials [23]. This leads to the requirement of high growth temperatures (~1000 °C) for III-nitride materials. Thus, the choice of substrates is limited to those that are stable at these high temperatures. The most commonly used substrate is sapphire. Some other substrates, such as SiC and Si [24, 25], have also been demonstrated for the growth of III-nitride materials. Since the LEDs presented in this thesis are all fabricated from III-nitride LED wafers grown on sapphire substrates, we will focus on III-nitride materials grown on sapphire substrate in this section.

Figure 1.12(a) shows the crystal orientation of sapphire. The III-nitride materials are normally grown on a c-plane (0001) sapphire substrate in the c-axis crystal direction ([0001] orientation). In order to align with the sapphire unit cell, the unit cells of III-nitride materials need to be rotated by 30 ° with respect to the c-axis of sapphire. This rotation leads to a large lattice mismatch between the sapphire substrate and III-nitride materials. Figure 1.12(b) shows an example of the atomic arrangement of an AlN film grown on a c-plane (0001) sapphire substrate. The lattice mismatch between AlN and sapphire is also emphasized in this figure; the lattice mismatch between these two materials is around 15 %. Such a large lattice mismatch results in a low-quality III-nitride film with a high density of dislocations for growth on the c-plane (0001) sapphire substrate. The early III-nitride films were therefore typically rough and fractured, with many hillocks observed on their surface. Fortunately, it was demonstrated that the quality of III-nitride films grown on the c-plane (0001) sapphire substrate can be improved if the growth is performed in two steps [11, 26]. In the first step, a thin GaN or AlN nucleation layer (~20 nm) is deposited on the sapphire substrate at a low temperature (~500 °C) and then followed by a thermal annealing process [27]. In the second step, the main III-nitride film is grown at higher temperatures (~1000 °C). The initial buffer layer is believed to promote the lateral growth of the main film and relax the strain caused by the lattice mismatch between the III-nitride film and the sapphire substrate. This two-step growth process leads to a smooth III-nitride film with a lower density of dislocations when grown on the c-plane (0001) sapphire substrate.

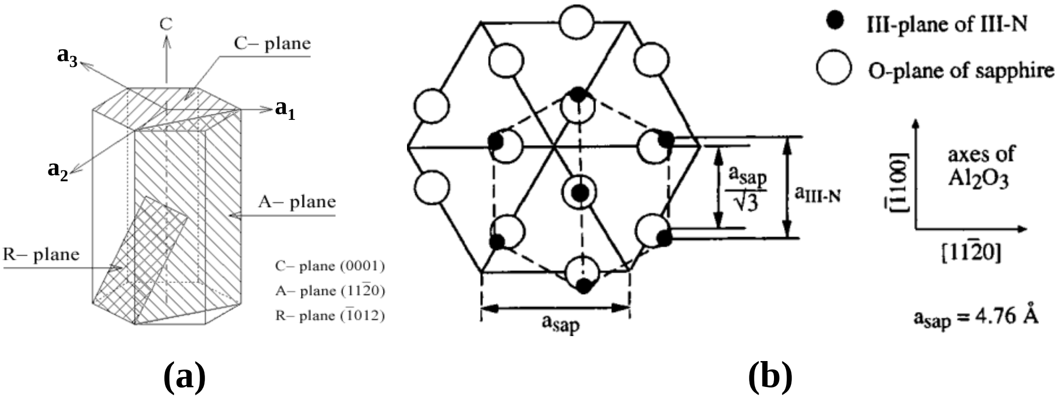

Figure 1.12: (a) Crystal orientation of sapphire; (b) atomic arrangement of an AlN film grown on a c-plane (0001) sapphire substrate. After [27].

As was mentioned in subsection 1.2.1, dislocations are nonradiative recombination centres which greatly reduce the radiative efficiency of semiconductors. In order to achieve a III-nitride material with high radiative efficiency, the density of dislocations needs to be low. The deposition of a buffer layer has proven to be an effective process to reduce the density of dislocations and the mechanism for the dislocation reduction is explained as shown in Figure 1.13. It was found that the initial layers grown on the c-plane (0001) sapphire substrate, including the buffer layer and faulted zone, are highly dislocated. As previously mentioned, these layers are grown at a low temperature and subsequently annealed. During the thermal annealing process, the dislocations undergo a self-annihilation process, which leads to the lower densities of dislocations in the layers subsequently deposited (the semi-sound and sound zones, as denoted in Figure 1.13). Although the deposition of a buffer layer greatly reduces the density of dislocations, the typical value of the dislocation density in III-nitride materials grown on the c-plane (0001) sapphire is still on the order of 10^8 to 10^9 cm^{-2}. This value is much higher than that typical in other materials. It has been proven that the radiative efficiency of GaAs will be limited if the density of dislocations is on the order of 10^4 cm^{-2}. Surprisingly, III-nitride materials grown on the c-plane (0001) sapphire substrate show high radiative efficiency despite such a high density of dislocations. This phenomenon indicates the radiative efficiency of III-nitride materials is not sensitive to dislocations. Some research results have been proposed to explain this phenomenon, although none of them is generally accepted. One possible explanation is that the energy levels generated by dislocations are outside the bandgap of III-nitride materials, as shown in Figure 1.14(a). This leads to the fact that these energy levels are not effective nonradiative recombination centres. Another possible reason for the high radiative efficiency of III-nitride materials are compositional fluctuations, as shown in Figure 1.14(b). The compositional fluctuations result in localized potential minima and, thus, an inhomogeneous bandgap of the III-nitride materials. The carriers are confined in these localized potential minima and prevented from diffusion to dislocations. This explanation is especially plausible for III-nitride ternary and quaternary alloys. Furthermore, when a III-nitride LED is operated at different currents, the inhomogeneous bandgap of QWs also leads to a band-filling effect in which the emission wavelength keeps blue-shifting accompanied by a broadening of the full width at half maximum (FWHM) of its emission spectrum. This is because the injection carriers fill the localized potential minima of the QWs first, which results in a longer emission wavelength and a narrow FWHM. When these localized potential minima are fully filled by injected carriers, further injected carriers will be distributed in higher energy states and, thus, the emission wavelength becomes shorter. In turn, the FHWM of emission spectrum becomes broader. This phenomenon is considered to be the one of possible reasons for the tuning of colour-tunable micro-LEDs (μ-LEDs) developed in this work. The detailed discussion of these colour-tunable μ-LEDs can be found in chapter 4.

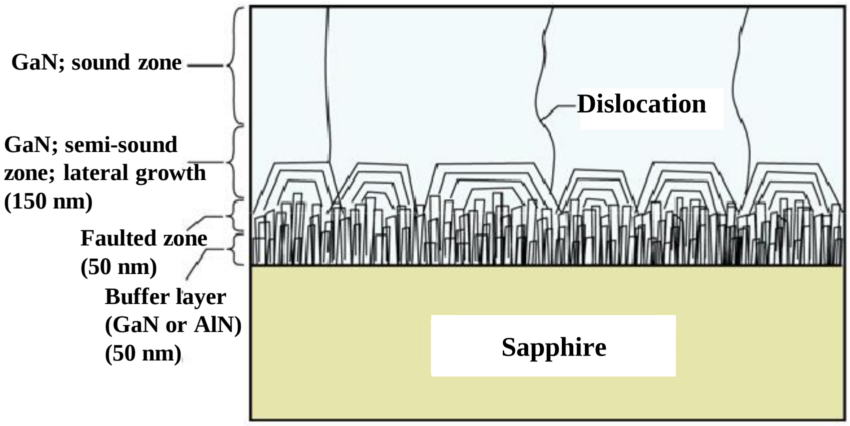

Figure 1.13: Dislocation structures of a GaN film grown on a c-plane (0001) sapphire substrate. After [16].

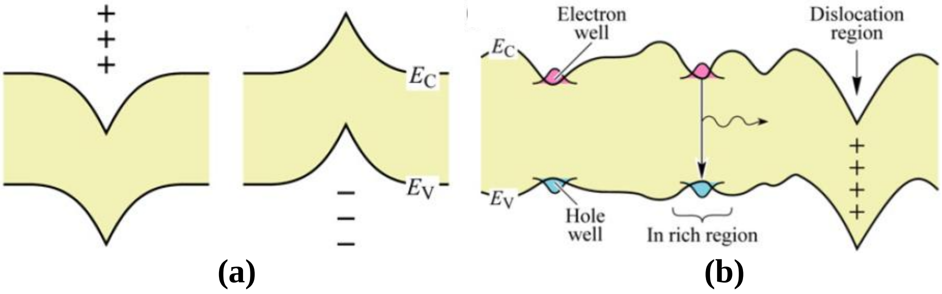

FIGURE 1.14: Band diagrams illustrating two possible explanations as to why III-nitride materials are not sensitive to dislocations: (a) energy levels generated by dislocations are outside the bandgap; (b) carrier confinement resulting from compositional fluctuations. After [16].

In addition to the high-quality III-nitride crystal films, the n-type and p-type doping in III-nitride materials is also important for developing III-nitride devices. As-grown GaN layers are always n-type with an electron concentration of $\sim 10^{16}$ cm^{-3}. This is mainly attributed to the high density of N vacancies in the GaN layer. These N vacancies are believed to act as shallow donors and, hence, result in the n-type doped GaN layer [27]. The intentional and controllable n-type doping in the GaN layer can easily be achieved by introducing Si dopants [28]. The achievable electron concentration of intentionally doped n-type material is on the order of 10^{19} cm^{-3}. However, p-type III-nitride material with a high hole concentration has barely been achieved. Mg is a good p-type acceptor for III-nitride materials. However, the holes cannot be effectively produced by Mg acceptors in these materials. This is probably due to the Mg being compensated by n-type defects (N vacancies) or passivated with H atoms. The H atoms are normally induced during the MOCVD growth process and they can chemically deactivate the p-type doping by forming a Mg-H complex. Thus, the acceptors in the as-grown Mg-doped GaN layer are not electrically active. The most common method for the activation of acceptors in the Mg-doped GaN layer is high-temperature post-growth thermal annealing [13]. This thermal annealing process normally takes place in a N_2 ambient at temperatures above 600 °C. During the thermal annealing process, the chemical bonds of Mg-H complexes are broken. Furthermore, the small H atoms can be driven out of GaN since they can easily escape through the interstitial sites of the crystal structure. Although a p-type GaN layer can thus be achieved, its hole concentration is relatively low, on the order of 10^{17} cm^{-3}. This is attributed to the high activation energy of Mg acceptors. The activation energy of Mg acceptors in GaN was found to be 170 meV [29], which is much larger than the thermal energy at RT. Therefore, only a small percentage of the acceptors are ionized.

1.4 III-nitride light emitting diodes

Following the achievement of high-quality III-nitride materials with appropriate n-type and p-type conductivities, various devices based on these materials have been developed. Due to the highest radiative efficiency of $In_xGa_{1-x}N$ ternary alloys being in the near-UV, blue and green regions, III-nitride materials are especially important for optoelectronic devices such as LEDs and LDs in these regions. Figure 1.15 shows the typical layer structure of a commercial $In_xGa_{1-x}N$/GaN-based LED wafer grown on a c-plane (0001) sapphire substrate. As shown, the MQW region comprising $In_xGa_{1-x}N$ wells and GaN barriers is used as an active region for high radiative efficiency light emission. In a commercial LED wafer, the MQW region is normally capped with an electron blocking layer (EBL). The EBL is a region with the higher bandgap energy to prevent the electrons overflowing or escaping the MQW region [16]. A p-type wider-bandgap $Al_xGa_{1-x}N$ ternary alloy is normally used as the EBL in the $In_xGa_{1-x}N$/GaN-based LED wafer.

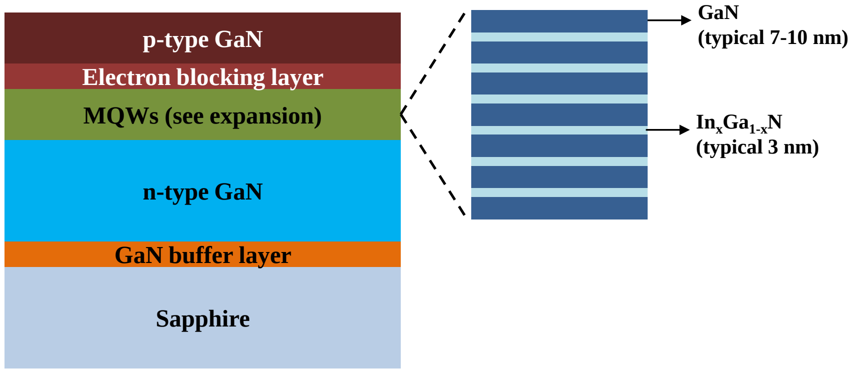

FIGURE 1.15: Typical structure of a commercial $In_xGa_{1-x}N$/GaN-based LED wafer grown on a c-plane (0001) sapphire substrate.

As shown in Figure 1.15 and mentioned in the last section, sapphire is commonly used as the substrate for III-nitride LED wafer growth. Due to the electrically insulating nature of the sapphire substrate, the n-type and p-type ohmic contacts of the LED are normally made on the same side of the device. Thus, part of the

LED wafer needs to be etched away to expose the n-type material. The etching process of III-nitride materials is relatively complicated and a related introduction can be found in chapter 6 of this thesis. The most common configuration of III-nitride LEDs is shown in Figure 1.16(a). This is the most straightforward LED configuration in which the light is directly extracted through the top p-type material; this is the so-called top-emission configuration. However, in order to achieve uniform current injection and a low contact resistance, a p-type ohmic contact serving as a current spreading layer needs to be deposited on the p-type nitride semiconductor surface. Furthermore, a thick metal pad for wire bonding is also necessary. Both of them absorb the light and, thus, reduce the optical power of LEDs with top-emission configurations. In order to overcome this problem, devices with a flip-chip configuration have been developed as shown in Figure 1.16(b). In this configuration, although the n-type and p-type ohmic contacts are still made on the same side of the device, the device is inverted and the light is extracted through the transparent sapphire substrate rather than through the p-type material. Thus, the thickness of p-type ohmic contact and bonding pad can be increased – a thicker p-type ohmic contact reducing the contact resistance and a thicker bonding pad acting as a reflective mirror. Furthermore, the optical power of LEDs with flip-chip configurations can be further improved by using a p-type ohmic contact with a high reflectivity. Figure 1.16(c) and (d) show the other two LED configurations, i.e. vertical-injection thin film [30] and thin film [31]. For these two configurations, the sapphire substrate of the III-nitride LEDs needs to be removed by advanced technologies such as laser lift-off [32]. The III-nitride LEDs presented in this thesis are all with either top-emission or flip-chip configurations. The fabrication process of III-nitride LEDs and related techniques will be introduced in detail in chapter 2.

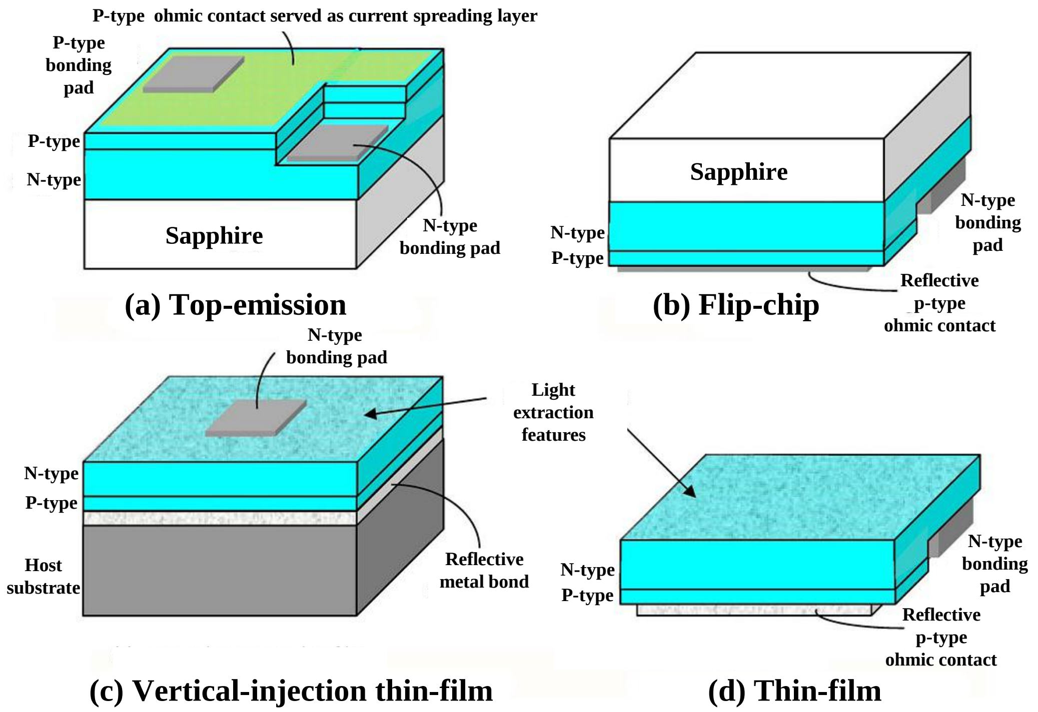

FIGURE 1.16: Four configurations of III-nitride LEDs: (a) top-emission; (b) flip-chip; (c) vertical-injection thin-film; (d) thin-film. All III-nitride LEDs presented in this thesis are based on first two configurations. After [33].

In the past twenty years, extensive scientific and technological efforts has been devoted to III-nitride LEDs. At present, the commercial blue and green LEDs on the market are all based on III-nitride materials. Dazzling blue $\mathrm{In}_x\mathrm{Ga}_{1-x}\mathrm{N}$ LEDs with a record EQE of 75.5 % have been reported [34]. Furthermore, these high-performance blue LEDs also promote the development of white-light LEDs. A common white-light LED combines a phosphor wavelength converter and a blue $\mathrm{In}_x\mathrm{Ga}_{1-x}\mathrm{N}$ LED. The phosphor commonly used for the wavelength conversion is Ce-doped YAG [35]. Figure 1.17(a) shows the typical structure of a white-light LED lamp. As shown, a blue LED is surrounded by the YAG phosphor. Thus, a fraction of the blue light generated by the LED will be absorbed by the phosphor and, in turn, re-emitted as secondary (longer-wavelength) emission light. The typical emission spectrum of the white-light LED lamp is shown in Figure 1.17(b). This spectrum consists of the blue emission from the LED and the secondary (longer-wavelength) phosphorescence. Both emissions are mixed to generate white light.

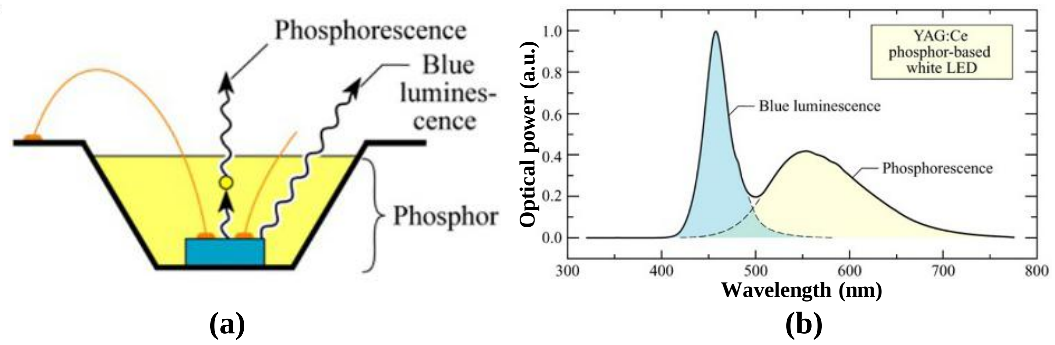

FIGURE 1.17: (a) Schematic structure and (b) emission spectrum of a typical white-light LED lamp. After [16].

Although great success has been achieved for III-nitride LEDs, there are still some problems limiting their performance and applications. In the following parts, three main problems will be briefly introduced.

Polarization effect

As was introduced in section 1.3, the III-nitride materials are commonly grown on a c-plane (0001) sapphire substrate along the [0001] direction. Due to the non-centrosymmetric nature of the wurtzite structure for III-nitride materials, a polarization effect exists in the III-nitride materials grown on the c-plane (0001) sapphire substrate. The polarization effect can be further classified into two types as an intrinsic spontaneous polarization effect and a strain-induced piezoelectric polarization effect. Both polarization effects result in the separate distribution of the positive and negative polarization charges at two different surfaces of the III-nitride materials and, thus, lead to an internal electric field. However, for the spontaneous and piezoelectric polarization effects, the directions of resultant internal electric fields depend on different conditions.

The spontaneous polarization effect is an intrinsic property of the material, and results from the asymmetry of the atomic bonding in the equilibrium wurtzite crystal structure. Thus, the direction of the resultant internal electric field (E_{sp}) is only dependent on the growth orientation. To give an example, for a GaN film grown on the c-plane (0001) sapphire substrate along the [0001] direction, the distribution of spontaneous polarization charges and the direction of the resultant E_{sp} in the GaN film are shown in Figure 1.18(a). On the other hand, the piezoelectric polarization effect is induced by the strain applied to the material. So, the distribution of piezoelectric polarization charges and the direction of the resultant

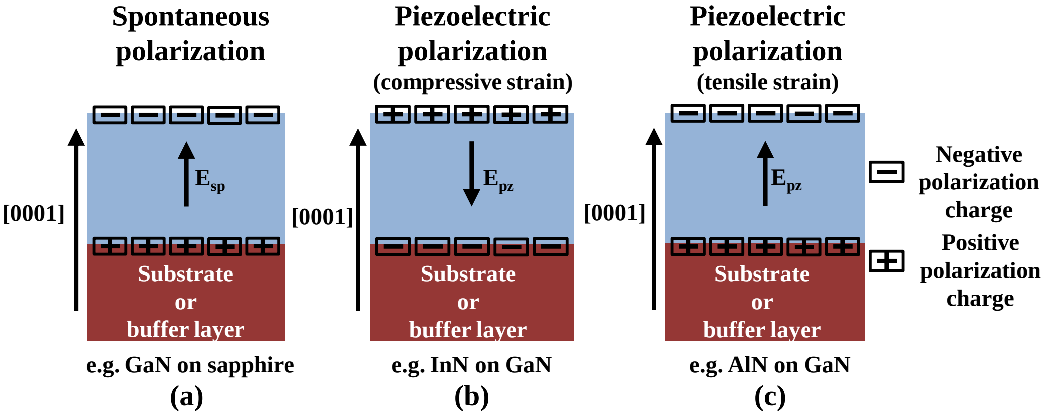

FIGURE 1.18: Distribution of polarization charges and the direction of the resultant internal electric field for (a) the spontaneous polarization effect, (b) the piezoelectric polarization effect under compressive strain and (c) the piezoelectric polarization effect under tensile strain in III-nitride materials.

internal electric field (E_{pz}) are dependent on not only the growth orientation but also the strain type. The strain in the material can be compressive or tensile. In the case of compressive strain, the material is laterally compressed. For example, for InN grown on a relaxed GaN buffer layer along the [0001] direction, the larger lattice constant a_0 of InN as shown in Table 1.1 makes the InN layer compressively strained. The resultant piezoelectric polarization effect is shown in Figure 1.18(b). In the case of tensile strain, the material is expanded along the lateral direction. For example, when growing AlN on a relaxed GaN buffer layer along the [0001] direction, the smaller lattice constant a_0 of AlN leads to a tensile-strained AlN layer. The resultant piezoelectric polarization effect for this case is shown in Figure 1.18(c).

The spontaneous polarization effect in III-nitride materials is relatively weak. However, the ternary alloy materials such as $In_xGa_{1-x}N$ and $Al_xGa_{1-x}N$ have a large lattice mismatch (the difference of the lattice constant a_0 as mentioned) to GaN. Therefore, the strain-induced piezoelectric polarization effect always needs to be considered for III-nitride LEDs. The MQW region in an LED wafer consists of at least two different III-nitride materials. The lattice mismatch between these two materials leads to the pronounced piezoelectric polarization effect and thus to a larger E_{pz} in the MQW region. One consequence of this E_{pz} for a QW structure is shown in Figure 1.19. As shown, the E_{pz} tilts the energy bands, resulting in a triangular-shaped QW, which reduces the effective bandgap energy by the amount of $eE_{pz}L_{QW}$ [36]. It also leads to a spatial separation of the electrons and holes

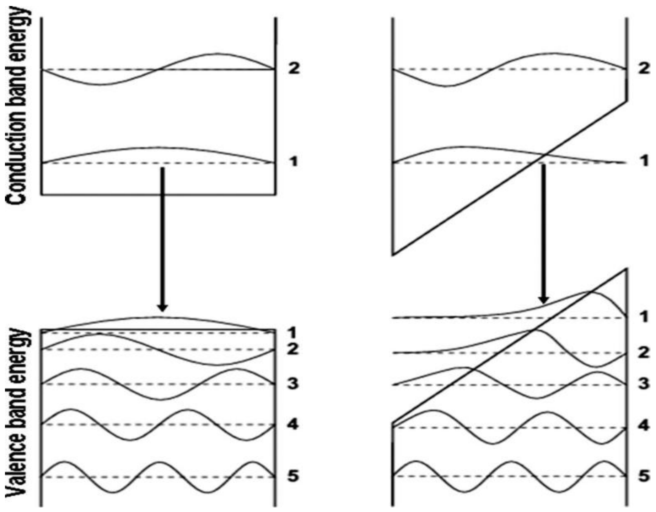

Figure 1.19: Band diagram illustrating the effect of an internal electric field for a QW structure. After [37].

towards opposite sides of a QW. This separation not only prevents the efficient radiative recombination but also leads to a broadening of the FWHM of the emission spectrum. These effects for the QW caused by an electric field are the so-called quantum-confined Stark effect (QCSE) [37].

The lattice mismatch between $In_xGa_{1-x}N$ and GaN becomes larger as the indium content increases. This results in the increase of the E_{pz} in the $In_xGa_{1-x}N$ QW emitting longer-wavelength light. This is one of possible reasons for the low efficiency of yellow-to-red $In_xGa_{1-x}N$ LEDs. Meanwhile, this E_{pz} is also considered as an explanation for the efficiency droop observed for III-nitride LEDs, which will be introduced later. Furthermore, when III-nitride LEDs are under electrical operation, the polarization charges can be compensated by the injected carriers and, thus, the E_{pz} is screened. This effect flattens the energy band and, in turn, leads to a blue-shift of the emission wavelength and a narrowing of the FWHM for the emission spectrum. This blue-shift of the emission wavelength is generally undesirable for applications where a constant emission wavelength is required.

Many methodologies have been proposed to suppress or eliminate the influence of the polarization effect in III-nitride materials. The most common way is to make the QW very thin [16]. In this way, the separation of electrons and holes caused by the polarization effect in the QW can be minimized. It has also been reported that the heavily n-type doped quantum barriers for III-nitride QWs can minimize the influence of the polarization effect [38]. When III-nitride LEDs are under electrical operation, the free electrons in the quantum barrier can also be injected into the QW. These carries can improve the screening effect of the internal electric field caused by the polarization effect. In order to completely remove the polarization effect in III-nitride materials, the growth of nonpolar III-nitride LED structures was also proposed [39].

Since the strain caused by the lattice mismatch between different III-nitride materials is directly responsible for the piezoelectric polarization effect, some studies have been carried out to investigate the strain relaxation process in different-sized structures of III-nitride materials. It has been proven that the strain caused by lattice mismatch can be partly or fully relaxed in micro-/nano-scale structures [40, 41]. In order to understand the strain relaxation process in such smaller structures, a characterization technique with high spatial resolution is essential. Photoluminescence (PL) is the most commonly used technique to characterize the strain relaxation process in micro-/nano-scale structures. However, the spatial resolution of this technique is relatively low, the best being, to our best knowledge, around 500 nm at RT. The localized strain relaxation processes in micro-/nano-structures can barely be observed at such resolution. Thus, in our work, a high-spatial-resolution cathodoluminescence (CL) technique was employed to investigate the strain relaxation process in III-nitride micro-pillars with different diameters. These micro-pillars were fabricated from a yellow-green $In_{0.25}Ga_{0.75}N/GaN$-based LED wafer. By the detailed CL measurements with a high spatial resolution (∼100 nm), different localized strain relaxation processes were observed at the pillar edge and centre, respectively. We also optimized a simulation model for the strain relaxation process by considering the strain in the QWs and the whole-wafer bending. These experimental and simulation results on different-sized micro-pillars were then used to explore the size effect on strain relaxation. This size effect study provides a useful guideline for the design of high-performance μ-LEDs. The detailed description of this size-dependent strain relaxation for III-nitride micro-pillars can be found in chapter 3.

The other work relevant to the polarization effect in this thesis is the colour-tunable μ-LEDs presented in chapter 4. As previously introduced, the emission wavelength of III-nitride LEDs is blue-shifted at different operating currents due to the screening effect of the internal electric field. This blue-shift becomes larger in III-nitride LEDs with longer-wavelength emissions due to the larger internal electric field in these devices. The large blue-shift can be used to change the emission colour of the LEDs. Thus, colour-tunable LEDs are developed from an amber $In_{0.40}Ga_{0.60}N$/GaN-based LED wafer. Our study demonstrates that this colour tunability can be enhanced by the μ-LEDs, which show an emission colour from amber to green at different operating currents. This enhanced colour tunability is due to the much higher operating current density that the μ-LEDs can sustain, which is a special property of these micro-scale LEDs and will be discussed in subsection 1.4.1. In contrast to other techniques for colour tunability, such as mechanical packaging of different colour components [42], colour conversion by different materials [43–45] and alternative growth methodologies for III-nitride materials [46, 47], the colour tunability of these μ-LEDs is dependent on the intrinsic propertise of III-nitride materials and μ-LEDs. So, it offers a much simpler method to achieve the colour-tunable device and an LED multi-colour display.

Ohmic contact to p-type GaN

An ohmic contact is a metal-semiconductor contact in which a potential barrier at the interface does not manifest itself [48]. In other words, the ohmic contact is a non-rectifying junction without additional resistance. So the current-voltage (I-V) characteristic of an ohmic contact should be linear and symmetric under reverse-bias and forward-bias conditions. In principle, under electrical operation, the voltage drop across an ideal ohmic contact should be much smaller than the one dropped across the semiconductor layer. This means the contact resistance of an ohmic contact should be much lower than that of the semiconductor layer. Producing ohmic contacts with a low specific contact resistivity (ρ_c, in the unit of Ωcm^2) to both n-type and p-type GaN is essential for III-nitride optoelectronic devices such as LEDs and LDs. A large voltage drop at a metal/GaN interface limits the electrical and optical performance of devices. So the high-quality ohmic contact is extremely important especially for high-power III-nitride LEDs.

It has been demonstrated that the creation of ideal ohmic contacts to n-type GaN is straightforward [48]. However, achieving an ideal ohmic contact with a low ρ_c to p-type GaN is challenging. Generally, in order to form an ohmic contact to p-type GaN, there are two basic strategies. The first one is to eliminate the potential barrier between the metal and the p-type GaN layer by an appropriate metal selection. Figure 1.20(a) shows the band diagram of the ohmic contact to p-type GaN formed by this strategy. In this figure, the Φ_m is the work function of metals and χ_s is the electron affinity of the semiconductors. Both parameters are measured in unit of eV. As shown, if the Φ_m of metal is larger than the sum of χ_s and E_g of p-type GaN [48], there is no potential barrier for holes flowing from the p-type GaN layer to the metal and, thus, an ohmic contact to p-type GaN is formed. The values of E_g and χ_s of p-type GaN is 3.4 eV and 4.1 eV, respectively. So, a metal with a Φ_m larger than 7.5 eV can form the ohmic contact to p-type GaN by this strategy. However, the application of this strategy is limited by the absence of appropriate metals having such a large Φ_m. The other strategy is narrowing the potential barrier region to be tunnelling-enabled. It can be attained by a heavily doped p-type GaN layer. The related band diagram of this strategy is shown in Figure 1.20(b). As shown, because the Φ_m of the metal is smaller than 7.5 eV, a potential barrier exists at the interface between the metal and the p-type GaN layer preventing the flowing of holes. Fortunately, the holes still can pass through this barrier by quantum mechanical tunnelling and the tunnelling probability increases as the width of the potential barrier region (W_d) decreases [49]. Furthermore, it has been found that W_d can be reduced as the doping concentration in the p-type GaN layer is increased [49]. Thus, with increasing doping concentration in the p-type GaN layer, the tunnelling probability of holes through the barrier increases as well. This leads to the result that, in principle, an ohmic contact can be formed to the heavily doped p-type GaN layer. However, as described previously, heavy doping in p-type GaN with a hole concentration exceeding 10^{18} cm^{-3} is very difficult. This is mainly due to the high activation energy of deep Mg acceptors and the formation of Mg-H complexes in the p-type GaN layer, as was described in section 1.3. Thus, the applicability of this strategy is also limited.

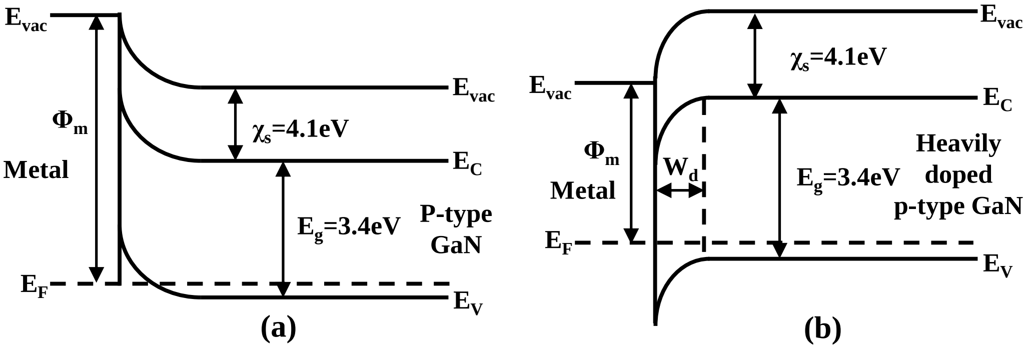

FIGURE 1.20: Band diagrams illustrating two strategies to achieve an ohmic contact to p-type GaN: (a) metal with a larger Φ_m; (b) heavily doped p-type GaN layer. The E_{vac} is the vacuum energy level.

Due to the fundamental problems of p-type GaN as mentioned, it is difficult to form an ideal ohmic contact with a low ρ_c to p-type GaN. So it is not surprising that nonlinear I-V characteristics are obtained for the metal contacts to p-type GaN. The high ρ_c of contact to p-type GaN limits the electrical performance of III-nitride LEDs, especially for the devices with a smaller contact area on the p-type GaN layer, i.e. μ-LEDs. Additionally, the nonlinear I-V characteristics show that the ρ_c of the contact to p-type GaN is dependent on the injection current density. Although there are quite a lot of studies on the development of ohmic contacts to p-type GaN and the related mechanisms, less work has been done to compare the ρ_c of different contacts to p-type GaN as a function of injection current density. For the μ-LEDs which will be introduced in subsection 1.4.1, their smaller contact area on the p-type GaN layer leads to a lower junction temperature and, thus, a wider operation current-density region. However, this smaller contact area also increases the total resistance contributed from the ρ_c of the metal contact to p-type GaN. Thus, a proper selection of the metal contacts to p-type GaN for these devices, with a consideration of the current-density dependent ρ_c, is important. This has motivated our work concentrating on Pd-based contacts to p-type GaN. Besides the optimization of the fabrication process of Pd-based contacts to p-type GaN, a methodology has been introduced to compare the ρ_c of different contacts to p-type GaN as a function of injection current density. The device performance of μ-LEDs with different contacts to p-type GaN are also compared. The details on this work can be found in chapter 5 of this thesis.

Efficiency droop

It has been found that the efficiency of III-nitride LEDs is generally highest at a low operating current density (around 10 A/cm^2). As the current density further increases, the efficiency gradually decreases. This phenomenon is known as efficiency droop and has been observed in both visible-light In$_x$Ga$_{1-x}$N LEDs [50] and deep-UV Al$_x$Ga$_{1-x}$N LEDs [51]. Furthermore, the efficiency droop occurs even without the self-heating effect during LED operation. Figure 1.21 shows the typical characteristic of efficiency droop for a blue In$_x$Ga$_{1-x}$N LED grown on a c-plane (0001) sapphire substrate. In order to exclude the influence of the self-heating effect, the data plotted in the figure are all measured under pulsed driving conditions with a repetition rate of 1 kHz and a duty cycle of 0.1 % [52]. As shown, the EQE of this device peaks at an operating current density of around 10 A/cm^2 and then falls by half at 100 A/cm^2. III-nitride LEDs are intended for high-power applications such as for lighting in home and office. This leads to the fact that these devices

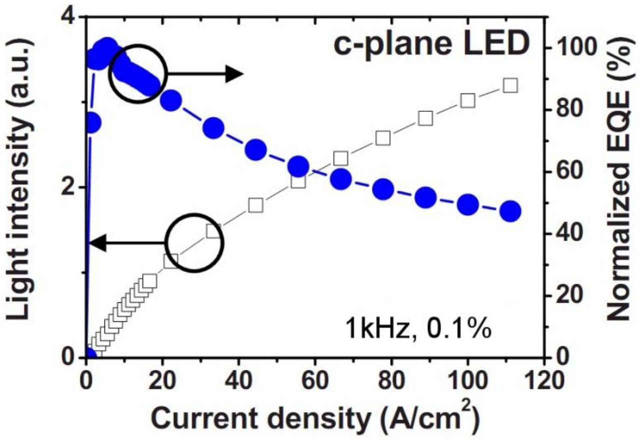

FIGURE 1.21: Light intensity and related EQE of a blue In$_x$Ga$_{1-x}$N LED, showing the efficiency droop phenomenon. The EQE in the figure is normalized to the peak value. After [52].

need to be operated in a current-density region of 100-1000 A/cm^2. Clearly, the efficiency droop limits the performance of III-nitride LEDs at these high operating current densities. So, understanding the mechanism of efficiency droop and mitigating its effects are especially important for III-nitride LEDs. Many different mechanisms have been proposed to explain this phenomenon. However, different experimental conditions and applied models result in the fact that none of them has been generally accepted. Here, the two dominant explanations postulated for efficiency droop are summarized.

The first explanation for efficiency droop is the nonradiative Auger recombination process, which was introduced in subsection 1.2.1. This hypothesis was first proposed by Shen et al. [53]. In their work, through lifetime studies on the quasi-bulk In$_x$Ga$_{1-x}$N layers, they concluded that the Auger recombination coefficient (C) in the In$_x$Ga$_{1-x}$N layer is on the order of 10^{-30} cm^{6}s^{-1}. As shown in Figure 1.22, the simulated IQE of III-nitride LEDs with different Auger recombination coefficients [54], this value is high enough to dominate the LED performance at high operating current densities and to result in the observed efficiency droop. However, this value is not consistent with the one obtained from a theoretical calculation for the direct band-to-band Auger losses in blue In$_x$Ga$_{1-x}$N/GaN QWs which is on the order of 10^{-34} cm^{6}s^{-1} [55]. It has motived several works concentrating on the theoretical investigation of other relevant Auger processes such as phonon-assisted Auger recombination [56] and indirect Auger recombination [57]. Most recently, the Auger electrons emitted from a $In_{0.18}Ga_{0.82}N$/GaN LEDs under electrical injection were directly measured by electron emission spectroscopy [58]. This seems to confirm the hypothesis that nonradiative Auger recombination is the dominant mechanism of efficiency droop. Another possible explanation for efficiency droop is carrier leakage, in which the carriers cannot be confined in the MQW region for radiative recombination. There are many forms of carrier leakage such as carrier tunnelling through defect levels [59] and carriers not being captured by the QW [60]. The most common form is considered to be the overflow and escape of electrons in the MQW region. As described earlier, the EBL is normally introduced into the commercial III-nitride LED wafers to prevent the overflow and escape of electrons. However, due to the polarization effect in III-nitride materials, the EBL is often unable to perform its function efficiently. Figure 1.23 shows the simulated band diagrams of a blue $In_xGa_{1-x}N$ LED with (blue) and without (red) the polarization effect. It can be seen that the polarization effect reduces the conduction band difference between the EBL and the last GaN barrier. This leads to the fact that the EBL cannot efficiently block the electrons. Meanwhile, this figure also shows that the quantum barriers on the n-side of each QW are higher than those on the p-side which further promotes the escape of electrons [61]. It has been proven that efficiency droop can be reduced by decreasing the polarization effect in III-nitride materials [62].

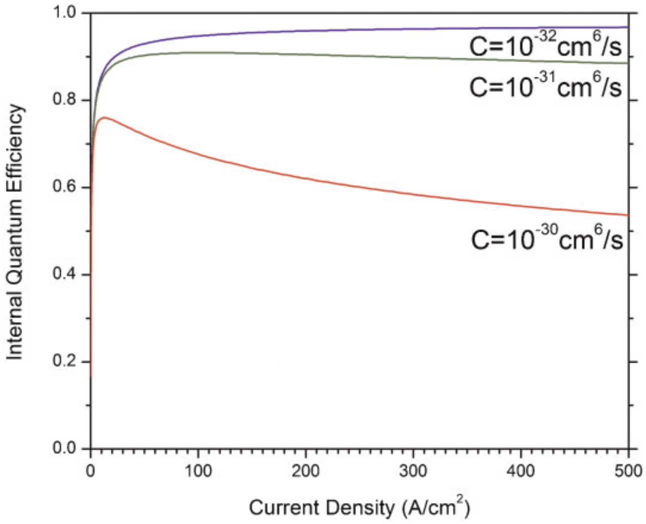

Figure 1.22: IQE plots with different Auger nonradiative recombination coefficients C. After [54].

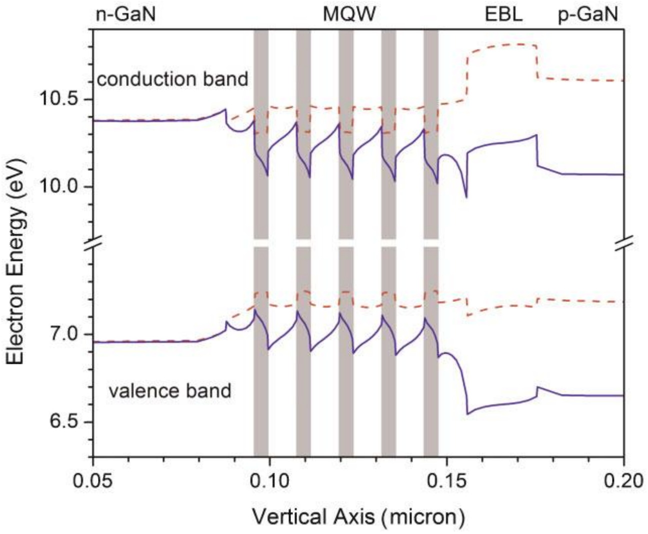

FIGURE 1.23: Simulated band diagrams of a blue $In_xGa_{1-x}N$ LED with (blue) and without (red) the polarization effect. After [54].

1.4.1 III-nitride micro-light emitting diodes

In this subsection, we focus on introducing III-nitride μ-LEDs. The conventional broad-area LEDs have dimensions over a few hundred micrometres. The μ-LEDs are devices with an emission area of less than 100 μm in each dimension. Thus, a μ-LED has a much smaller emission area compared with a broad-area LED. A few hundred, or even thousand, individual μ-LEDs can be produced in the same area as a single broad-area LED. The first III-nitride μ-LED was demonstrated in 2000 by Jin et al. [63]. In their work, disc-shaped μ-LEDs with a diameter of 12 μm were fabricated as shown in Figure 1.24. This device was fabricated from an $In_xGa_{1-x}N$/GaN-based LED wafer with the emission wavelength of 408 nm. Since there were no electrical bonding pads for this first μ-LED, the device was only operated by a probe station. In order to overcome this limitation, an insulating layer was deposited between each μ-LED and electrical bonding pads were further made on this insulating layer. In 2001, a 10×10 blue $In_xGa_{1-x}N$ μ-LED array was developed in this way [64]. As show in Figure 1.25(a), each disc-shaped (12 μm in diameter) μ-LED element in this array has its own p-contact pad and, thus, can be individually addressed. This μ-LED array could be used to demonstrate a simple semiconductor display as shown in Figure 1.25(b). However, the addressing scheme used in this μ-LED array (two contacts per pixel) is impractical for a larger number of elements. The matrix-addressing scheme provides a simple way to control each element in a large μ-LED array. In the matrix-addressing scheme, row and column electrodes are used to operate μ-LEDs in the array. This means that if there are $m \times n$ elements in an array, only $m + n$ electrodes are required to control each element. Our group subsequently demonstrated a high-performance 64×64 matrix-addressable μ-LED array [65]. Figure 1.26(a) shows an optical image of this μ-LED array. Each μ-LED element in this array has a diameter of 16 μm and the pitch between two adjacent μ-LED elements is 50 μm. This matrix-addressable μ-LED array can also be controlled via a computer interface and a driver board for image display, which was developed by our group as well. The user-friendly graphic user interface (GUI) allows the users to easily operate this μ-LED array for different image outputs. The GUI and an optical image of corresponding output of this μ-LED array are shown in Figure 1.26(b) and (c), respectively.

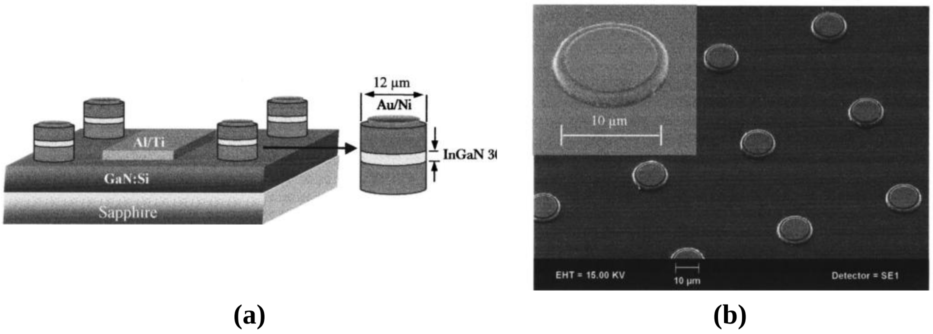

FIGURE 1.24: (a) Schematic diagram and (b) SEM image of the first III-nitride μ-LED. After [63].

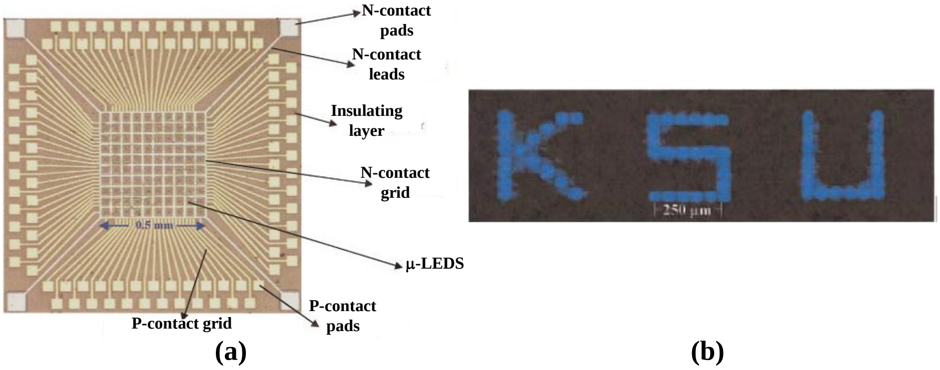

FIGURE 1.25: Optical images of (a) an individually-addressable μ-LED array and (b) its output image. After [64].

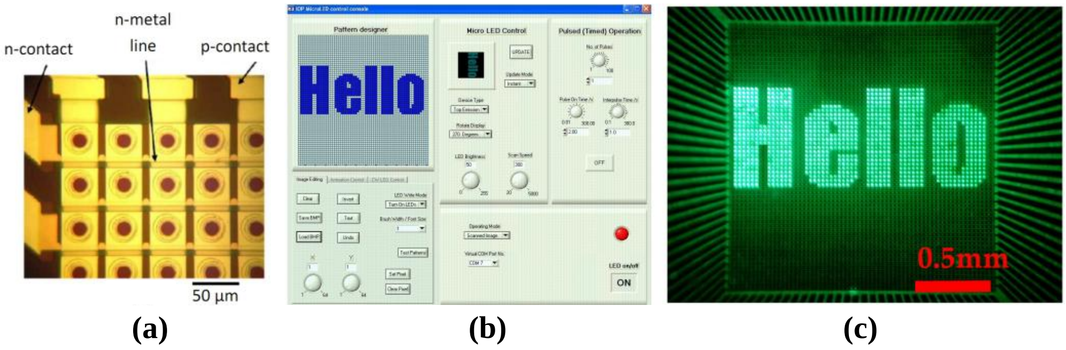

FIGURE 1.26: (a) Optical image of a 64 × 64 matrix-addressable μ-LED array; (b) developed GUI for this μ-LED array; (c) optical image of the output from this μ-LED array. After [65].

The μ-LEDs are an attractive format of III-nitride LEDs. In contrast to broad-area LEDs, the μ-LEDs employ micro-scale III-nitride structures, which have a smaller top-surface p-type GaN area but higher surface-to-volume ratio (the ratio of the sidewall-surface area over the micro-pillar volume). These III-nitride μ-LEDs show performance enhancements compared with the broad-area LEDs. These enhancements mainly comprise three aspects. Firstly, the IQE of III-nitride μ-LEDs is improved compared with the broad-area LEDs. This is mainly due to the partial strain relaxation in micro-scale structures, which can relieve the piezoelectric polarization effect in III-nitride materials as introduced above. Secondly, the LEE of III-nitride μ-LEDs is higher than that of broad-area devices. Due to the higher surface-to-volume ratio of μ-LEDs, more scattered light can emit from the sidewall of μ-LEDs [66]. Furthermore, as predicted by the simulation, with the decreasing of the structure size of III-nitride materials, the waveguiding effect of III-nitride materials is more pronounced [67]. At the same operating current density, it has been found that, due to these two effects, III-nitride μ-LEDs produce a higher optical power density compared with the broad-area LEDs. Thirdly, the operating current density of III-nitride μ-LEDs can be significant higher than broad-area devices. The smaller top-surface area of the p-type GaN layer of μ-LEDs is able to improve the uniformity of the injection current [68]. Meanwhile, the higher surface-to-volume ratio can also enhance the thermal dissipation of μ-LEDs during the electrical operation [69]. Both effects lead to a low junction temperature for μ-LEDs compared with broad-area LEDs at the same operating current density. Thus, the III-nitride μ-LEDs can be operated at a current density of several kA/cm^2, which is much higher than the operating current density of broad-area LEDs. The higher operating current density of III-nitride μ-LEDs enhances the colour tunability of the LEDs presented in chapter 4 of this thesis. It also motivates the research work presented in chapter 5, which concerns the Pd-based contacts to p-type GaN and consideration of the current-density dependent ρ_c.

Due to the advantages of III-nitride μ-LEDs, these devices have been widely used for different novel applications. As introduced, μ-LEDs can produce the micro-scale light patterns with a high optical power density. Thus, these devices are suitable to act as the light sources for photosensitive samples of interest. One example of this application is the μ-LED maskless photolithography developed by our group [70]. In the maskless photolithography, a μ-LED is used as a light source to expose the photoresist and generate micro-scale patterns. Complex patterns can be achieved by well-controlled μ-LED exposure and sample movement. Furthermore, since the optical turn-on/off times of μ-LEDs are shorter than those of broad-area devices [71], μ-LEDs are particularly useful for applications which require short optical pulses or high modulation bandwidths such as visible light communications [72]. In addition, the compact μ-LED array is also a good candidate for micro-displays. The μ-LED array has high efficiency, high contrast and increased brightness. Thus, micro-displays based on μ-LED arrays show obvious advantages over those based on the other technologies such as liquid-crystals.

1.4.2 III-nitride microstructured-image light emitting diodes

As introduced in subsection 1.4.1, one of the important applications of μ-LED arrays is as a high-performance micro-display. However, for the display application in which only fixed patterns are required, the micro-display based on the μ-LED array has its own limitations. Firstly, as shown in Figure 1.26(c), the output images of a micro-display normally consist of hundreds of turned-on μ-LED elements. Thus, in order to achieve a high-quality output image, all the μ-LED elements need to work well and the output power from them should be uniform. This leads to a relatively challenging fabrication process for the μ-LED array with a large number of elements. Meanwhile, although the matrix-addressing scheme simplifies the structure of a μ-LED array, a complicated driver board is required to control each μ-LED element to form the desired output images. Furthermore, the resolution of micro-displays based on the μ-LED array is limited by the pitch between each μ-LED element. In addition, the non-planar surface of μ-LEDs left by the mesa etching may also lead to a complicated process for further integration of additional elements to make microsystems. To overcome these limitations, a single III-nitride LED containing a complex microstructured image is required. Some previous studies have demonstrated that the plasma technology modifies the electrical properties of III-nitride materials, which can be used to defined the emission images of III-nitride LEDs [73, 74]. Thus, by introducing the plasma treatment as an additional step in the conventional III-nitride LED fabrication process, novel microstructured-image LEDs, which contains complex emission images on single devices, were developed in our work.

Figure 1.27 shows examples of these novel microstructured-image LEDs emitting at 405 nm. As shown, high-quality complex emission images are achieved by this novel microstructured-image LED. Here, it is necessary to indicate some important properties of this device. Firstly, these two emission images are generated by a single III-nitride LED, thus only one n-type and one p-type contact electrode are needed to operate this device. So, the driver board for this device is much simpler compared with the μ-LED array. Secondly, the micro-scale emission image can be achieved by this device and the spacing between any two features on the image is no longer limited by the device pitch as in the case of the μ-LED array. Thus, the image resolution on this device can be even higher than that of micro-displays based on the μ-LED array. Thirdly, the flat surface of these microstructured emission images leads to a simple process for the further integration of micro-elements. These microstructured-image LEDs are fabricated by combining a CHF_3 plasma treatment and photoresist patterning. The detailed physical mechanism, process development, characterization and maskless writing application of these novel LEDs will be given in chapter 6.

Figure 1.27: Novel III-nitride microstructured-image LED with an emission wavelength of 405 nm. The left image is the logo of Institute of Photonics and the right one is the logo of University of Strathclyde.

1.5 Outline of this thesis

In this chapter, a general introduction of LEDs particularly for the devices based on III-nitride materials was given. The motivations of the research work presented in this thesis were also presented in this chapter. Chapter 2 will describe the experimental techniques used in the work to develop the novel microstructured LEDs. From chapter 3 to chapter 6, the results achieved in the work will be presented. The investigation of the strain relaxation process in $In_{0.25}Ga_{0.75}N/GaN$-based micro-pillars as a function of pillar diameter will be presented in chapter 3. Chapter 4 will demonstrate the colour-tunable μ-LEDs fabricated from an amber $In_{0.40}Ga_{0.60}N/GaN$-based LED wafer. Chapter 5 will describe the development of Pd-based metal contacts to p-type GaN with a consideration of the current-density dependent ρ_c. The performance of μ-LEDs with different contacts to p-type GaN will also be compared in this chapter. Chapter 6 will present the development of novel III-nitride microstructured-image LEDs and their applications. Finally, the conclusions of this thesis, along with some future work plans, are given in chapter 7.

References

[1] H.J. Round. A note on carborundum. *Electrical World*, 49(9):309, 1907.

[2] O.V. Lossev. CII. Luminous carborundum detector and detection effect and oscillations with crystals. *The London, Edinburgh, and Dublin Philosophical Magazine and Journal of Science*, 6(39):1024–1044, 1928.

[3] H. Welker. On new semiconducting compounds. *Zeitschrift fur Naturforschung A (Astrophys., Phys. Physikal. Chem.)*, 7a(39):774–749, 1952.

[4] H. Welker. On new semiconducting compounds,II. *Zeitschrift fur Naturforschung A (Astrophys., Phys. Physikal. Chem.)*, 8a(39):248–251, 1953.

[5] R.N. Hall, G.E. Fenner, J.D. Kingsley, T.J. Soltys, and R.O. Carlson. Coherent light emission from GaAs junctions. *Physical Review Letters*, 9(9):366–368, 1962.

[6] N. Holonyak and S.F. Bevacqua. Coherent (visible) light emission from Ga ($\mathrm{As}_{1-x}\mathrm{P}_x$) junctions. *Applied Physics Letters*, 1(4):82–83, 1962.

[7] C.B. Duke and N. Holonyak. Advances in light-emitting diodes. *Physics Today*, 26:23, 1973.

[8] R.A. Logan, H.G. White, and W. Wiegmann. Efficient green electroluminescence in nitrogen-doped GaP p-n junctions. *Applied Physics Letters*, 13(4):139–141, 1968.

[9] R.B. Jain and H.P. Maruska. How it really happened: The history of p-type doping of gallium nitride. *Physica Status Solidi (a)*, 204(6):1970–1976, 2007.

[10] J.A. Edmond, H.S. Kong, and C.H. Carter. Blue LEDs, UV photodiodes and high-temperature rectifiers in 6H-SiC. *Physica B: Condensed Matter*, 185(1):453–460, 1993.

[11] H. Amano, N. Sawaki, I. Akasaki, and Y. Toyoda. Metalorganic vapor phase epitaxial growth of a high quality GaN film using an AlN buffer layer. *Applied Physics Letters*, 48 (5):353–355, 1986.

[12] H. Amano, M. Kito, K. Hiramatsu, and I. Akasaki. P-type conduction in Mg-doped GaN treated with low-energy electron beam irradiation (LEEBI). *Japanese Journal of Applied Physics*, 28(12):L2112–L2114, 1989.

[13] S. Nakamura, N. Iwasa, and M. Senoh. Method of manufacturing p-type compound semiconductor, April 26 1994. US Patent 5,306,662.

[14] S. Nakamura, T. Mukai, and M. Senoh. Candela-class high-brightness InGaN/AlGaN double-heterostructure blue-light-emitting diodes. *Applied Physics Letters*, 64(13):1687–1689, 1994.

[15] S. Nakamura, M. Senoh, S. Nagahama, N. Iwasa, T. Yamada, T. Matsushita, H. Kiyoku, and Y. Sugimoto. InGaN-based multi-quantum-well-structure laser diodes. *Japanese Journal of Applied Physics Part 2 Letters*, 35:74–76, 1996.

[16] E.F. Schubert. *Light emitting diodes.* Cambridge University Press, 2^{nd} edition, 2006.

[17] U. Lafont, H. van Zeijl, and S. van der Zwaag. Increasing the reliability of solid state lighting systems via self-healing approaches: A review. *Microelectronics Reliability*, 52(1): 71–89, 2012.

[18] J.K. Kim and E.F. Schubert. Transcending the replacement paradigm of solid-state lighting. *Optics Express*, 16(26):21835–21842, 2008.

[19] J.P. Colinge and C.A. Colinge. *Physics of semiconductor devices.* Springer, 2002.

[20] M. Fukuda. *Optical semiconductor devices*, volume 46. Wiley-interscience, 1998.

[21] I. Vurgaftman and J.R. Meyer. Band parameters for nitrogen-containing semiconductors. *Journal of Applied Physics*, 94(6):3675–3696, 2003.

[22] J. Schormann, S. Potthast, D.J. As, and K. Lischka. In situ growth regime characterization of cubic GaN using reflection high energy electron diffraction. *Applied Physics Letters*, 90 (4):041918, 2007.

[23] W.A. Harrison. *Elementary electronic structure.* World Scientific Publishing Company Incorporated, 1999.

[24] F. Hamdani, A. Botchkarev, W. Kim, H. Morkoç, M. Yeadon, J.M. Gibson, S.C.Y. Tsen, D.J. Smith, D.C. Reynolds, D.C. Look, K. Evans, C.W. Litton, W.C. Mitchel, and P. Hemenger. Optical properties of GaN grown on ZnO by reactive molecular beam epitaxy. *Applied Physics Letters*, 70(4):467–469, 1997.

[25] D.G. Zhao, S.J. Xu, M.H. Xie, S.Y. Tong, and H. Yang. Stress and its effect on optical properties of GaN epilayers grown on Si (111), 6H-SiC (0001), and c-plane sapphire. *Applied Physics Letters*, 83(4):677–679, 2003.

[26] S. Nakamura. GaN growth using GaN buffer layer. *Japanese Journal of Applied Physics*, 30(10A):L1705–L1707, 1991.

[27] S.C. Jain, M. Willander, J. Narayan, and R.V. Overstraeten. III–nitrides: Growth, characterization, and properties. *Journal of Applied Physics*, 87(3):965–1006, 2000.

[28] S. Nakamura, T. Mukai, and M. Senoh. In situ monitoring and Hall measurements of GaN grown with GaN buffer layers. *Journal of Applied Physics*, 71(11):5543–5549, 1992.

[29] W. Gotz, N.M. Johnson, J. Walker, D.P. Bour, and R.A. Street. Activation of acceptors in Mg-doped GaN grown by metalorganic chemical vapor deposition. *Applied Physics Letters*, 68(5):667–669, 1996.

[30] L. Zhou, J.E. Epler, M.R. Krames, W. Goetz, M. Gherasimova, Z. Ren, J. Han, M. Kneissl, and N.M. Johnson. Vertical injection thin-film AlGaN/AlGaN multiple-quantum-well deep ultraviolet light-emitting diodes. *Applied Physics Letters*, 89:241113, 2006.

[31] O.B. Shchekin, J.E. Epler, T.A. Trottier, T. Margalith, D.A. Steigerwald, M.O. Holcomb, P.S. Martin, and M.R. Krames. High performance thin-film flip-chip InGaN–GaN light-emitting diodes. *Applied Physics Letters*, 89(7):071109, 2006.

[32] M.K. Kelly, O. Ambacher, R. Dimitrov, R. Handschuh, and M. Stutzmann. Optical Process for Liftoff of Group III-Nitride Films. *Physica Status Solidi (a)*, 159(1):R3–R4, 1997.

[33] M.R. Krames, O.B. Shchekin, R. Mueller-Mach, G.O. Mueller, L. Zhou, G. Harbers, and M.G. Craford. Status and future of high-power light-emitting diodes for solid-state lighting. *Display Technology, Journal of*, 3(2):160–175, 2007.

[34] Y. Narukawa, M. Sano, M. Ichikawa, S. Minato, T. Sakamoto, T. Yamada, and T. Mukai. Improvement of luminous efficiency in white light emitting diodes by reducing a forward-bias voltage. *Japanese Journal of Applied Physics*, 46:L963–L965, 2007.

[35] S. Nakamura and G. Fasol. The blue laser diode-gallium-nitride based light emitters and laser. *Springrt, Berlin*, 1997.

[36] P. Perlin, C. Kisielowski, V. Iota, B.A. Weinstein, L. Mattos, N.A. Shapiro, J. Kruger, E.R. Weber, and J. Yang. InGaN/GaN quantum wells studied by high pressure, variable temperature, and excitation power spectroscopy. *Applied Physics Letters*, 73(19):2778–2780, 1998.

[37] J.H. Ryou, P.D. Yoder, J. Liu, Z. Lochner, H. Kim, S. Choi, H.J. Kim, and R.D. Dupuis. Control of quantum-confined stark effect in InGaN-based quantum wells. *Selected Topics in Quantum Electronics, IEEE Journal of*, 15(4):1080–1091, 2009.

[38] T. Deguchi, A. Shikanai, K. Torii, T. Sota, S. Chichibu, and S. Nakamura. Luminescence spectra from InGaN multiquantum wells heavily doped with Si. *Applied Physics Letters*, 72(25):3329–3331, 1998.

[39] A. Chakraborty, B.A. Haskell, S. Keller, J.S. Speck, S.P. DenBaars, S. Nakamura, and U.K. Mishra. Nonpolar InGaN/GaN emitters on reduced-defect lateral epitaxially overgrown a-plane GaN with drive-current-independent electroluminescence emission peak. *Applied Physics Letters*, 85:5143, 2004.

[40] H.S. Chen, D.M. Yeh, Y.C. Lu, C.Y. Chen, C.F. Huang, T.Y. Tang, C.C. Yang, C.S. Wu, and C.D. Chen. Strain relaxation and quantum confinement in InGaN/GaN nanoposts. *Nanotechnology*, 17(5):1454, 2006.

[41] Y. Kawakami, A. Kaneta, L. Su, Y. Zhu, K. Okamoto, M. Funato, A. Kikuchi, and K. Kishino. Optical properties of InGaN/GaN nanopillars fabricated by postgrowth chemically assisted ion beam etching. *Journal of Applied Physics*, 107(2):023522, 2010.

[42] M. Koike, N. Shibata, H. Kato, and Y. Takahashi. Development of high efficiency GaN-based multiquantum-well light-emitting diodes and their applications. *Selected Topics in Quantum Electronics, IEEE Journal of*, 8(2):271–277, 2002.

[43] J.K. Sheu, S.J. Chang, C.H. Kuo, Y.K. Su, L.W. Wu, Y.C. Lin, W.C. Lai, J.M. Tsai, G.C. Chi, and R.K. Wu. White-light emission from near UV InGaN-GaN LED chip precoated with blue/green/red phosphors. *Photonics Technology Letters, IEEE*, 15(1):18–20, 2003.

[44] G. Heliotis, P.N. Stavrinou, D.D.C. Bradley, E. Gu, C. Griffin, CW Jeon, and M.D. Dawson. Spectral conversion of InGaN ultraviolet microarray light-emitting diodes using fluorene-based red-, green-, blue-, and white-light-emitting polymer overlayer films. *Applied Physics Letters*, 87(10):103505, 2005.

[45] M. Wu, Z. Gong, A.J. Kuehne, A.L. Kanibolotsky, Y.J. Chen, I.F. Perepichka, A.R. Mackintosh, E. Gu, P.J. Skabara, R.A. Pethrick, and M.D. Dawson. Hybrid GaN/organic microstructured light-emitting devices via ink-jet printing. *Optics Express*, 17(19):16436–16443, 2009.

[46] C.B. Soh, W. Liu, S.J. Chua, S.S. Ang, R.J.N. Tan, and S.Y. Chow. Generation of amber III-nitride based light emitting diodes by indium rich InGaN quantum dots with InGaN wetting layer and AlN encapsulation layer. *Journal of Applied Physics*, 108(9):093501, 2010.

[47] L. Zhang, K. Cheng, M. Leys, P. Favia, H. Bender, and G. Borghs. Two-color InGaN/GaN microfacet multiple-quantum well structures grown on Si substrate. *Journal of Applied Physics*, 110(8):083518, 2011.

[48] T.V. Blank and Y.A. GolDberg. Mechanisms of current flow in metal-semiconductor ohmic contacts. *Semiconductors*, 41(11):1263–1292, 2007.

[49] D.A. Neamen and B. Pevzner. *Semiconductor physics and devices: basic principles.* Irwin, 1992.

[50] Y. Yang, X.A. Cao, and C. Yan. Investigation of the nonthermal mechanism of efficiency rolloff in InGaN light-emitting diodes. *Electron Devices, IEEE Transactions on*, 55(7): 1771–1775, 2008.

[51] H. Hirayama, S. Fujikawa, N. Noguchi, J. Norimatsu, T. Takano, K. Tsubaki, and N. Kamata. 222–282 nm AlGaN and InAlGaN-based deep-UV LEDs fabricated on high-quality AlN on sapphire. *Physica Status Solidi (a)*, 206(6):1176–1182, 2009.

[52] S.C. Ling, T.C. Lu, S.P. Chang, J.R. Chen, H.C. Kuo, and S.C. Wang. Low efficiency droop in blue-green m-plane InGaN/GaN light emitting diodes. *Applied Physics Letters*, 96(23): 231101, 2010.

[53] Y.C. Shen, G.O. Mueller, S. Watanabe, N.F. Gardner, A. Munkholm, and M.R. Krames. Auger recombination in InGaN measured by photoluminescence. *Applied Physics Letters*, 91(14):141101, 2007.

[54] J. Piprek. Efficiency droop in nitride-based light-emitting diodes. *Physica Status Solidi (a)*, 207(10):2217–2225, 2010.

[55] J. Hader, J.V. Moloney, B. Pasenow, S.W. Koch, M. Sabathil, N. Linder, and S. Lutgen. On the importance of radiative and Auger losses in GaN-based quantum wells. *Applied Physics Letters*, 92(26):261103, 2008.

[56] B. Pasenow, S.W. Koch, J. Hader, J.V. Moloney, M. Sabathil, N. Linder, and S. Lutgen. Auger losses in GaN-based quantum wells: Microscopic theory. *Physica Status Solidi (c)*, 6(S2):S864–S868, 2009.

[57] E. Kioupakis, P. Rinke, K.T. Delaney, and C.G. Van de Walle. Indirect auger recombination as a cause of efficiency droop in nitride light-emitting diodes. *Applied Physics Letters*, 98 (16):161107, 2011.

[58] J. Iveland, L. Martinelli, J. Peretti, J.S. Speck, and C. Weisbuch. Direct Measurement of Auger Electrons Emitted from a Semiconductor Light-Emitting Diode under Electrical Injection: Identification of the Dominant Mechanism for Efficiency Droop. *Physical Review Letters*, 110(17):177406, 2013.

[59] N.I. Bochkareva, V.V. Voronenkov, R.I. Gorbunov, A.S. Zubrilov, Y.S. Lelikov, P.E. Latyshev, Y.T. Rebane, A.I. Tsyuk, and Y.G. Shreter. Defect-related tunneling mechanism of efficiency droop in III-nitride light-emitting diodes. *Applied Physics Letters*, 96(13):133502, 2010.

[60] X. Ni, X. Li, J. Lee, S. Liu, V. Avrutin, U. Ozgur, H. Morkoç, A. Matulionis, T. Paskova, G. Mulholland, et al. InGaN staircase electron injector for reduction of electron overflow in InGaN light emitting diodes. *Applied Physics Letters*, 97(3):031110, 2010.

[61] M.H. Kim, M.F. Schubert, Q. Dai, J.K. Kim, E.F. Schubert, J. Piprek, and Y. Park. Origin of efficiency droop in GaN-based light-emitting diodes. *Applied Physics Letters*, 91(18): 183507, 2007.

[62] M.F. Schubert, J. Xu, J.K. Kim, E.F. Schubert, M.H. Kim, S. Yoon, S.M. Lee, C. Sone, T. Sakong, and Y. Park. Polarization-matched GaInN/AlGaInN multi-quantum-well light-emitting diodes with reduced efficiency droop. *Applied Physics Letters*, 93:041102, 2008.

[63] S.X. Jin, J. Li, J.Z. Li, J.Y. Lin, and H.X. Jiang. GaN microdisk light emitting diodes. *Applied Physics Letters*, 76(5):631–633, 2000.

[64] H.X. Jiang, S.X. Jin, J. Li, J. Shakya, and J.Y. Lin. III-nitride blue microdisplays. *Applied Physics Letters*, 78(9):1303–1305, 2001.

[65] Z. Gong, H.X. Zhang, E. Gu, C. Griffin, M.D. Dawson, V. Poher, G. Kennedy, P.M.W. French, and M.A.A. Neil. Matrix-addressable micropixellated InGaN light-emitting diodes with uniform emission and increased light output. *Electron Devices, IEEE Transactions on*, 54(10):2650–2658, 2007.

[66] H.W. Choi, C.W. Jeon, M.D. Dawson, P.R. Edwards, R.W. Martin, and S. Tripathy. Mechanism of enhanced light output efficiency in InGaN-based microlight emitting diodes. *Journal of Applied Physics*, 93(10):5978–5982, 2003.

[67] V. Zabelin, D.A. Zakheim, and S.A. Gurevich. Efficiency improvement of AlGaInN LEDs advanced by ray-tracing analysis. *Quantum Electronics, IEEE Journal of*, 40(12):1675–1686, 2004.

[68] X. Guo and E.F. Schubert. Current crowding and optical saturation effects in GaInN/GaN light-emitting diodes grown on insulating substrates. *Applied Physics Letters*, 78(21):3337–3339, 2001.

[69] Z. Gong, S. Jin, Y. Chen, J. McKendry, D. Massoubre, I. Watson, E. Gu, and M.D. Dawson. Size-dependent light output, spectral shift, and self-heating of 400 nm InGaN light-emitting diodes. *Journal of Applied Physics*, 107(1):013103, 2010.

[70] D. Elfström, B. Guilhabert, J. McKendry, S. Poland, Z. Gong, D. Massoubre, E. Richardson, B.R. Rae, G. Valentine, G. Blanco-Gomez, E. Gu, J.M. Cooper, R.K. Henderson, and M.D. Dawson. Mask-less ultraviolet photolithography based on CMOS-driven micro-pixel light emitting diodes. *Optics Express*, 17(26):23522–23529, 2009.

[71] S.X. Jin, J. Shakya, J.Y. Lin, and H.X. Jiang. Size dependence of III-nitride microdisk light-emitting diode characteristics. *Applied Physics Letters*, 78(22):3532–3534, 2001.

[72] J.J.D. McKendry, R.P. Green, AE Kelly, Z. Gong, B. Guilhabert, D. Massoubre, E. Gu, and M.D. Dawson. High-speed visible light communications using individual pixels in a micro light-emitting diode array. *Photonics Technology Letters, IEEE*, 22(18):1346–1348, 2010.

[73] T.W. Kuo, S.X. Lin, P.K. Hung, K.K. Chong, C.I. Hung, and M.P. Houng. Formation of Selective High Barrier Region by Inductively Coupled Plasma Treatment on GaN-Based Light-Emitting Diodes. *Japanese Journal of Applied Physics*, 49(11):6504, 2010.

[74] R. Chu, C.S. Suh, M.H. Wong, N. Fichtenbaum, D. Brown, L. McCarthy, S. Keller, F. Wu, J.S. Speck, and U.K. Mishra. Impact of CF_4 Plasma Treatment on GaN. *Electron Device Letters, IEEE*, 28(9):781–783, 2007.

Chapter 2

Experimental techniques for fabrication and characterization of microstructured light emitting diodes

The purpose of the research to be described was to investigate and develop novel III-nitride microstructured light emitting diodes (LEDs). In this chapter, the main techniques used for microstructured LED fabrication and characterization are reviewed and discussed. There are two sections in this chapter. Firstly, the main steps in the microstructured LED fabrication process are described, including pattern definition, pattern transfer and formation of metal contacts. The techniques used in each step are also briefly introduced. In section 2.2, two main characterization techniques used in the work, namely cathodoluminescence and temperature-dependent photoluminescence, are presented. These two techniques play an important role characterizing both the III-nitride materials and microstructured LEDs.

2.1 Fabrication of microstructured light emitting diodes

The typical fabrication process of III-nitride light emitting diodes (LEDs) is schematically shown in Figure 2.1. The basic fabrication process of microstructured LEDs

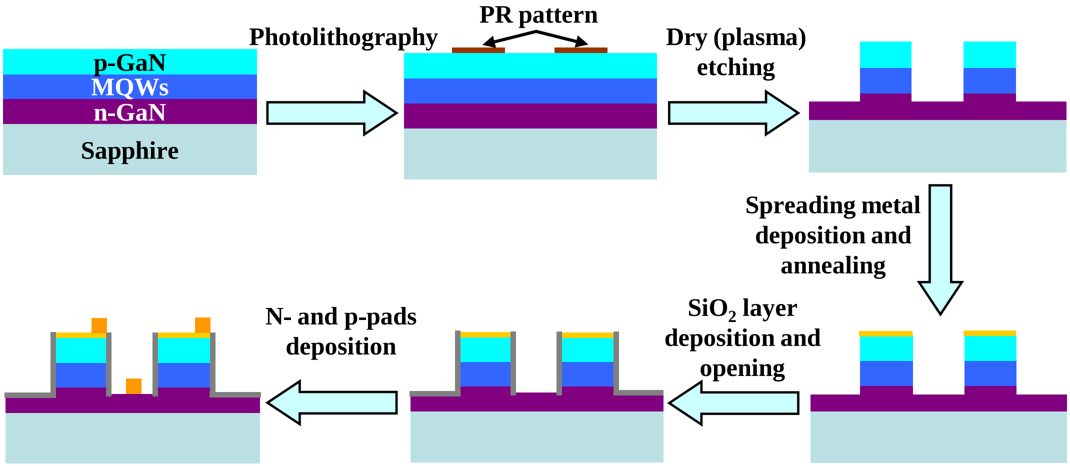

FIGURE 2.1: Typical process flow for the fabrication of III-nitride LEDs.

is almost the same as this. However, due to the smaller feature size and novel characteristics of microstructured LEDs, the fabrication process is more challenging, and some additional steps are introduced. The main steps in the fabrication process of III-nitride LEDs include pattern definition, pattern transfer and formation of metal contacts. A brief introduction to these steps and related techniques used in each step will be given in the following subsections. The challenges and additional steps for the fabrication of microstructured LEDs will be discussed as well.

2.1.1 Pattern definition

Pattern definition is the most crucial step in the fabrication process of LEDs, since the design of a device is transferred to the sample through the defined pattern. In the following parts, the techniques used for pattern definition in our work will be introduced including conventional photolithography and home-built maskless image writing based on III-nitride LEDs.

Photolithography

Photolithography is a common technique used for pattern definition in the modern semiconductor industry. It is a patterning process which transfers the designed patterns from a photomask to photosensitive materials, i.e. photoresist (PR), by light exposure. The basic process of photolithography is shown in Figure 2.2. The sample is first coated with a PR layer. This PR layer is then exposed by the light

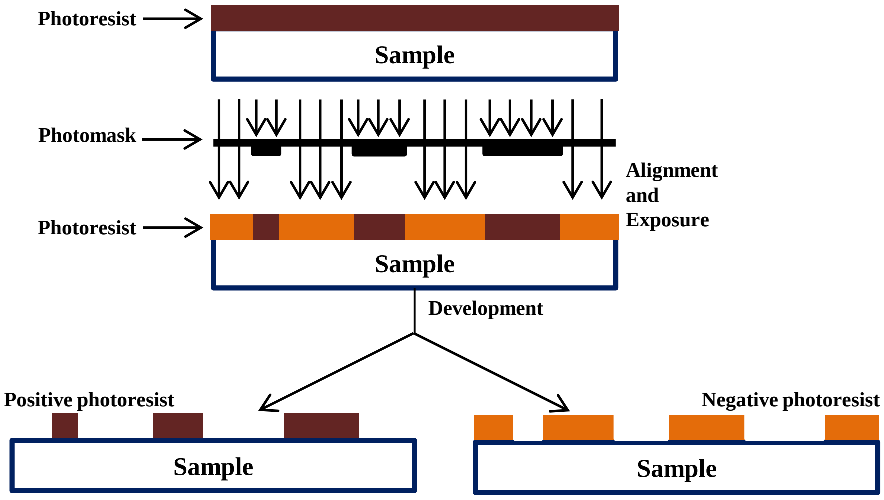

Figure 2.2: Basic photolithography process for both positive and negative PRs.

(usually ultraviolet) through the photomask. Based on the design of a device, the photomask contains different patterns consisting of clear and opaque regions. The exposure light can pass through the clear regions but is blocked at the opaque regions. The properties of the exposed PR layer under the clear regions will be changed due to a photochemical reaction. In the subsequent development process, the sample is dipped into a suitable developer to remove unwanted PR and to form a desired PR pattern. Depending on the properties of PRs, the final PR patterns formed on the sample surface will be either the same as that on the photomask (positive PR) or a reversed pattern (negative PR). The photolithography process can be further divided into three main steps, namely PR coating, alignment and exposure, and PR development.

In these steps, the operation of alignment and exposure plays a critical role in the photolithography process and also in the whole fabrication process of the LEDs. This operation determines the success of transferring the designed patterns on the photomask to the PR layer. Furthermore, for pattern exposure, the wavelength of the exposure light source is an important parameter to decide the minimum feature size and quality of final PR patterns. It is well known that the ideal resolution (R) of an optical system is determined by the wavelength (λ) of the light source and the numerical aperture (NA) of the system, which can be expressed as:

$$R = k_1 \frac{\lambda}{NA} \tag{2.1}$$

where k_1 is a system constant. From Equation 2.1, it can be seen that R is improved by reducing the wavelength and increasing the NA. However, the enhancement of R results in a reduction of depth of focus (DOF) for the system. DOF is the distance around focus in which a good R for projected patterns can be obtained. This is another important property of an optical system and is expressed as:

$$DOF = k_2 \frac{\lambda}{(NA)^2} \tag{2.2}$$

where k_2 is a system constant. As expressed above, DOF and R always work against each other. Consequently, in photolithography, it will be more difficult to achieve high-quality PR patterns with small feature size. This difficulty leads to a more challenging photolithography process in the fabrication process of micro-LEDs (μ-LEDs) which have dimensions of less than 100 μm.

In our work, the alignment and exposure were performed with a Karl Suss MA6 Mask Aligner (Figure 2.3) in our lab. This mask aligner consists of three main parts as lamp housing, microscope and alignment stage. The lamp housing accommodates the exposure light source, and in this MA6 mask aligner, the lamp housing model is UV400. The lamp housing consists of a high pressure mercury short-arc lamp and a corresponding electrical circuit. The emission wavelengths of this lamp mainly concentrate between 350 and 450 nm. Figure 2.4 shows the emission spectrum of a typical high pressure mercury short-arc lamp. With this multi-wavelength mercury lamp for exposure, the minimum feature size which can be achieved in this mask aligner is 2 μm. The microscope indicated in Figure 2.3 is used for observing the patterns on both photomask and sample during the alignment process. The alignment stage of the mask aligner allows the x-y and angle adjustments of the sample. To achieve a precise alignment for the patterns on both photomask and sample, the sample position is adjusted carefully by controlling this alignment stage. During the operation of alignment, there is a certain gap between the photomask and the sample so that the sample can be moved freely.

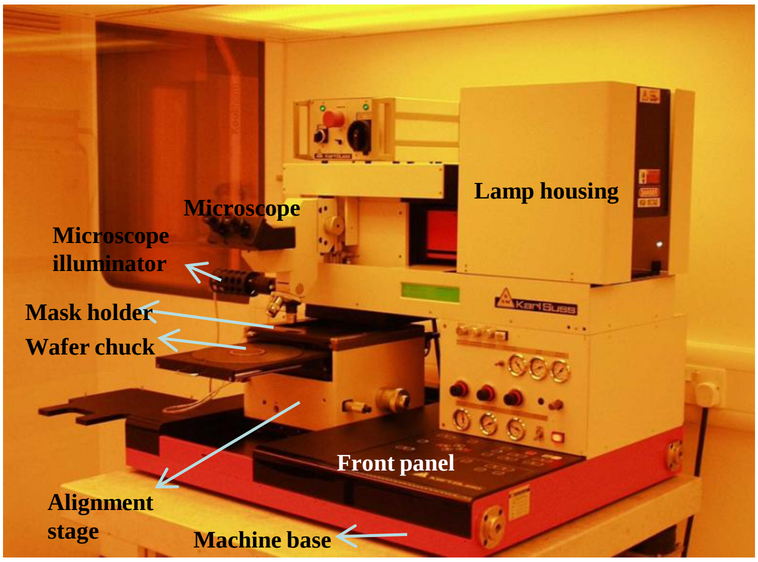

FIGURE 2.3: Image of a Karl Suss MA6 Mask Aligner used for the operation of alignment and exposure in the photolithography process.

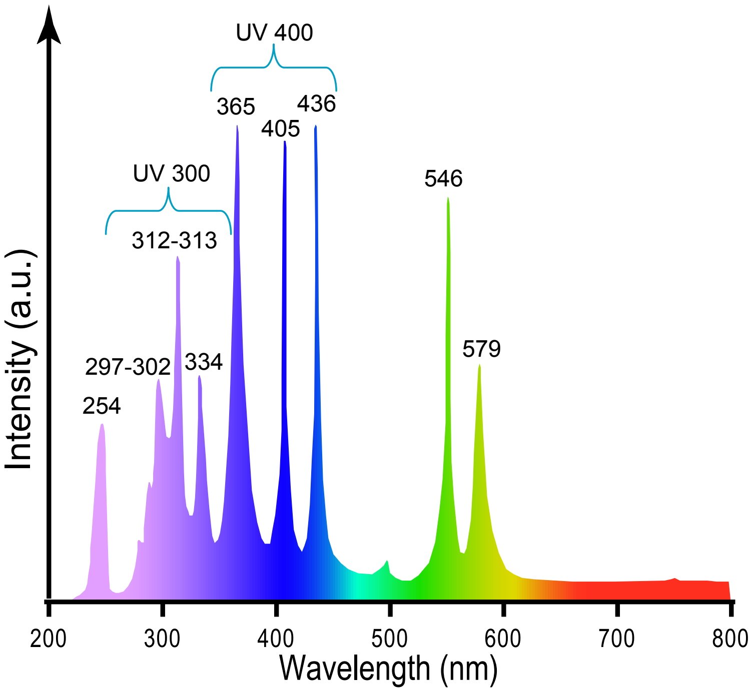

FIGURE 2.4: Emission spectrum of a typical high pressure mercury short-arc lamp.

Maskless image writing

Another technique used for pattern definition in my work is home-built maskless image writing based on III-nitride LEDs. As introduced in the previous part, a mask aligner and photomasks are normally required for photolithography. However, the photomask is expensive, especially when high-resolution pattern features are required. Furthermore, the photomask method is not flexible for trying different pattern designs. Thus, maskless image writing has its own advantages.

The idea of LED maskless image writing is based on the laser direct writing technique [1] which has been widely used to fabricate waveguides and other optical components in polymers and SiO_2 [2, 3]. By using LEDs to replace a laser, the cost of the writing setup can be greatly reduced and a multi-beam writing can be achieved. In our work, LED maskless image writing was used to directly transfer the complex emission patterns generated from a novel microstructured-image LEDs to the PR layer.

Figure 2.5 shows the home-built maskless image writing setup. Normally, a complementary metal-oxide-semiconductor driven μ-LED array was used as the light source for writing tests [4]. In our work, a particular microstructured-image LED was utilized for pattern writing. In this setup, a 4× microscope objective is used to collect the light emitted from the LED. Another microscope objective is used for image projection and this objective can be changed so as to get the required demagnifications for different writing processes. There is a beam splitter used to image the pattern on the sample surface, which is helpful to adjust the focus of the projected pattern and the written position on the sample before image writing. A time-controllable shutter is placed between the LED and the collection objective to accurately control the exposure time. A minimum exposure time as short as 100 ms can be achieved by this setup. The application of this setup for image writing with different demagnification factors can be found in section 6.3 of this thesis and Ref. [5].

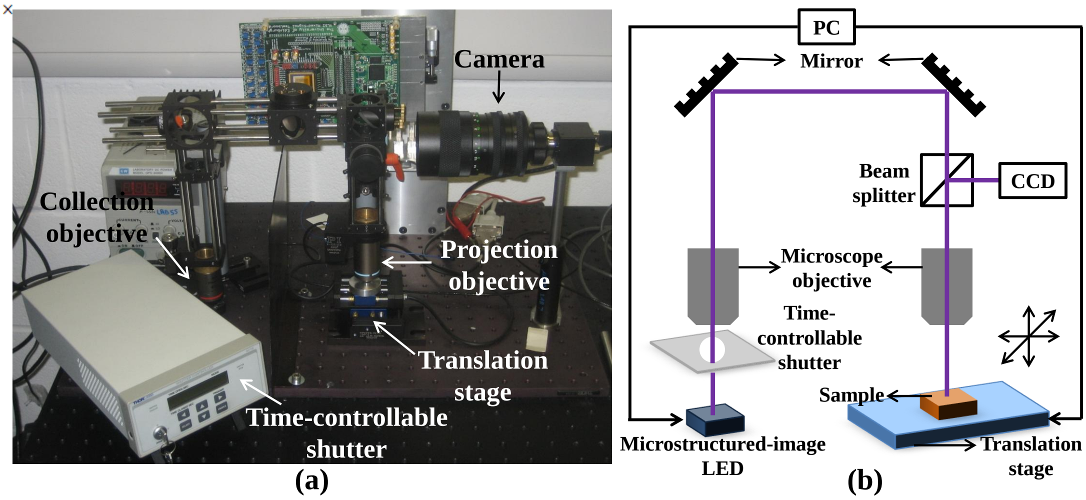

FIGURE 2.5: (a) Image and (b) schematic diagram of a home-built maskless image writing setup.

2.1.2 Pattern transfer

In the LED fabrication process, the patterns defined in the PR layer need to be further transferred to the sample. To achieve this pattern transfer, an etching process is necessary. Generally, the etching can be classified into two types, namely wet etching and dry (plasma) etching. Both types of etching and related facilities will be introduced in this subsection. Some typical etching recipes used in my work will be given as well.

Wet etching

Wet etching refers to a process which dissolves the material on the wafer surface by a chemical solution. Normally, a suitable selectivity between an etch mask and the etched materials can be achieved in wet etching, which is determined by the temperature and concentration of the chemical solution. However, wet etching normally produces an isotropic etching profile and its etching rate strongly dependents on the crystallographic plane of materials. Thus, it is hard to achieve high-quality etching results with small feature size by wet etching.

The common wet etching used in my work is to etch SiO_2 deposited by plasma-enhanced chemical vapour deposition (PECVD). The SiO_2 is normally used as an isolation layer for LEDs or as a hard etching mask on the GaN layer for further dry (plasma) etching to achieve a better etching selectivity. Almost all the wet etching of SiO_2 is done by a hydrofluoric (HF) acid solution. The chemical reaction of this process is given by:

$$SiO_2 + 6HF = H_2SiF_6 + 2H_2O \tag{2.3}$$

Because the high-concentrated HF (typically 49 % HF in water) etches SiO_2 too fast at room temperature and also peels off the PR layer used for pattern definition, buffered oxide etch (BOE) is normally used in our laboratory to achieve a more controllable SiO_2 etching process. BOE is a mixture solution which commonly comprises a 6:1 volume ratio of 40 % NH_4F in water to 49 % HF in water. It gives an etching rate of 100 nm/min for the SiO_2 deposited by PECVD.

Dry (plasma) etching

In dry etching, the material is exposed to gaseous etchants which dislodge part of the material from the exposed surface. There are mainly two kinds of reactions in dry etching, namely, physical ion bombardment and pure chemical etching. Both reactions are schematically shown in Figure 2.6. Figure 2.6(a) shows the reaction of physical ion bombardment in which the material is physically dislodged from the material surface by energetic ions. The etching rate of physical ion bombardment is relatively low and is mainly dependent on the flux and energy of the ions. The reaction of pure chemical etching is shown in Figure 2.6(b). In this case, the material is etched solely by the chemical reaction to form volatile byproducts. Here, it is necessary to indicate that the byproducts formed must be volatile, otherwise the non-volatile ones will cover on the etched surfaces which influences or even interrupts further chemical etching. The etching rate of pure chemical etching is strongly dependent on the particular chemical reaction of the gaseous etchants with the etched materials.

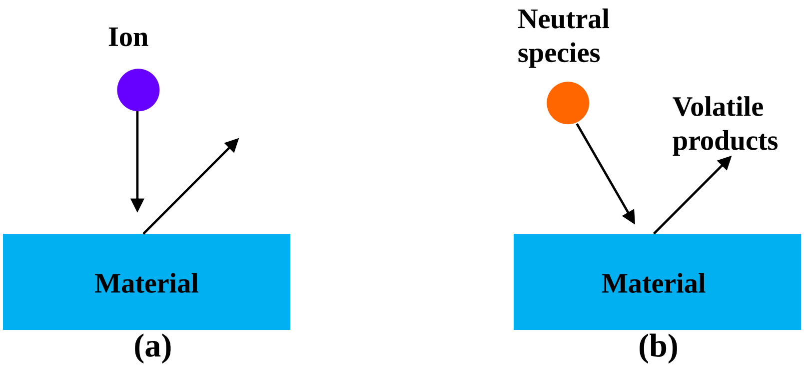

FIGURE 2.6: Schematics of two reactions in dry etching: (a) physical ion bombardment; (b) pure chemical etching.

In the modern semiconductor industry, the common dry etching is plasma etching. A plasma, which is an ionized gas with an equal number of negative and positive charges, generates free radicals with highly chemical activity. These radicals can significantly increase the chemical reaction rate and, hence, enhance pure chemical etching. The plasma etching can also include physical ion bombardment at the material surface. In plasma etching, physical ion bombardment may also alter the chemical properties of the material which accelerates pure chemical etching. In our work, plasma etching was used for etching SiO_2 and GaN-based materials in the fabrication process of III-nitride μ-LEDs. This was because of the inapplicability of wet etching to structures with such small feature size and because of its limited applicability to GaN-based materials. In addition, to develop the novel microstructured-image LEDs, we also utilized a plasma treatment as an additional step in the conventional LED fabrication process.

We have used two plasma etching tools in our work, namely the reactive ion etching (RIE) and inductively coupled plasma (ICP) systems. Figures 2.7(a) and (b) show, respectively, an image of the RIE system in our lab and a schematic diagram of its processing chamber. The RIE system possesses a capacitively coupled plasma source. The plasma in the chamber is initiated by applying a radio frequency (RF) electromagnetic field with a typical frequency of 13.56 MHz. The plasma density in the RIE chamber is around 1 to 5 $\times 10^9$ cm^{-3}, which is relatively low. The typical processing pressure in the RIE chamber is between 5 to 150 mTorr. The ion energy, which is directly related to the RF power and processing pressure, ranges from 30 to 1000 eV. In our work, the RIE system is mainly used for the plasma etching of SiO_2, especially when a small feature size is required. A typical etching recipe for the SiO_2 etching is given in Table 2.1, and by using this recipe, the etching rate of SiO_2 is 41 nm/min. Furthermore, the plasma treatment used to fabricate the microstructured-image LEDs was also performed in the RIE system. The detailed process of this plasma treatment will be presented in chapter 6.

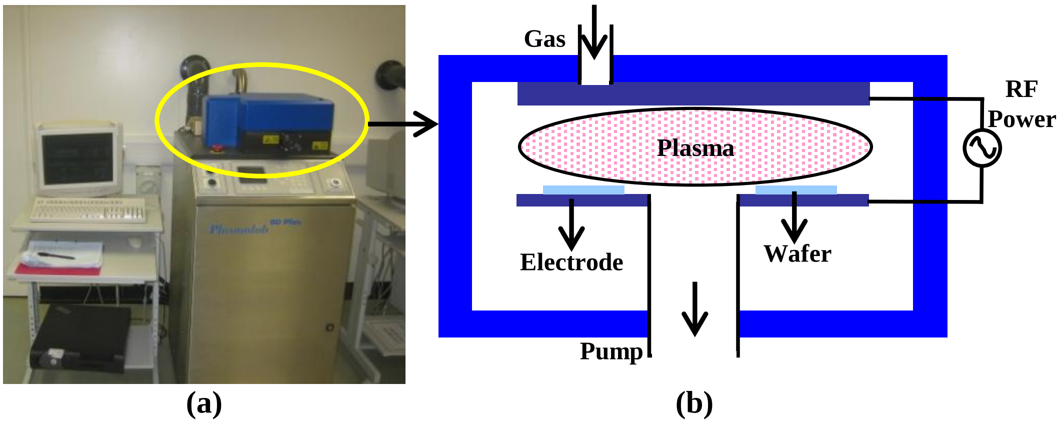

FIGURE 2.7: (a) Image and (b) schematic diagram of an RIE chamber. The processing chamber is highlighted by a yellow ellipse.

Pressure (mTorr)	Ar flow (sccm)	CHF_3 flow (sccm)	RF power (W)	Etching rate (nm/min)
66	15	5	200	41

TABLE 2.1: Etching recipe for SiO_2 in an RIE system.

The ICP is a modified RIE system with an inductively coupled plasma source which incorporates a radial inductive coil design. Compared with the plasma source in the RIE system, the radial inductive coil can generate high-density plasma and, hence, increase the etching rate. Figure 2.8(a) is an image of the ICP system used in our lab, and Figure 2.8(b) is a schematic diagram of the ICP processing chamber. The plasma density in this ICP system is mainly controlled by the coil power, and the energy of the ions for physical ion bombardment is strongly determined by the platen power. The typical processing pressure in the ICP chamber is between 1 to 100 mTorr, and plasma density is about 5×10^{11} cm^{-3}. In this work, the ICP system was used for the plasma etching of GaN-based materials. Two process recipes were used and they are given in Table 2.2. These two recipes were used with different purposes in the fabrication process of III-nitride μ-LEDs. The detailed investigations of these two recipes can be found in subsection 3.2.1.

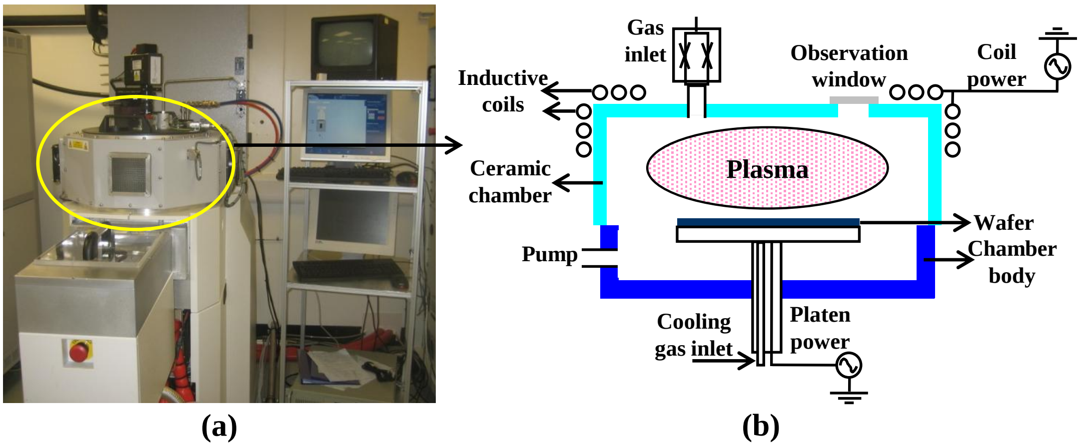

FIGURE 2.8: (a) Image and (b) schematic diagram of an ICP chamber. The processing chamber is highlighted by a yellow ellipse.

Process number	Pressure (mTorr)	Ar flow (sccm)	Cl_2 flow (sccm)	Coil power (W)	Platen power (W)	Etching rate (nm/min)
1	7	N/A	40	700	300	943
2	7	10	30	400	200	429

TABLE 2.2: Etching recipes for GaN-based materials in an ICP system.

2.1.3 Formation of metal contacts

In order to achieve fully functional LEDs, the formation of metal contacts to both p-type and n-type GaN is an important step in the fabrication process. In our work, different metals need to be deposited on the GaN surface to form metal-semiconductor contacts. A thermal annealing process is further applied for the metal contact to p-type GaN to achieve a low specific contact resistivity. A general introduction to the techniques used for metal deposition and thermal annealing will be given in the following parts.

Metal deposition

Deposited on the p-type GaN layer, a thin oxidized Ni/Au (10 nm/20 nm) bi-layer is normally used as the p-type metal contact in our work. A Pd-based metal contact to p-type GaN has also been developed in this work to enhance the performance of III-nitride μ-LEDs and the details will be presented in chapter 5 of this thesis. All of these metals are deposited by an electron-beam evaporator in our

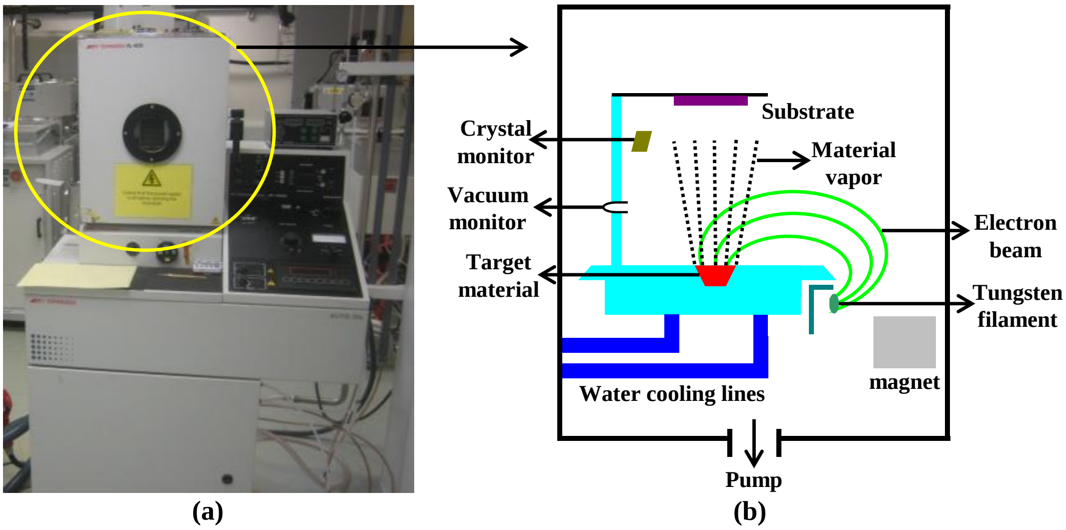

Figure 2.9: (a) Image and (b) schematic diagram of an electron-beam evaporator chamber. The processing chamber is highlighted by a yellow ellipse.

laboratory. Figures 2.9(a) and (b) show, respectively, an image of the electron-beam evaporator and a schematic diagram of its processing chamber. As shown in Figure 2.9(b), metal deposition in the electron-beam evaporator is performed in a vacuum chamber. The normal processing pressure of the electron-beam evaporator should be below 7.5×10^{-5} Torr, which is monitored by a vacuum gauge in the processing chamber. When the tungsten filament is heated by passing a high electric current through it, electrons are emitted from the filament. These electrons form a beam which is directed towards the target material by a magnetic field. When the electron beam impacts on the target material, the kinetic energy of the electrons is transferred into thermal energy to heat the target material. The target material is then melted and turned into vapour which travels to the substrate. On reaching the substrate, the vapour condenses and coats the substrate surface. Due to the high temperature generated by the electron beam, the holder of the target material must be cooled by water to prevent it from melting. The thickness of deposited materials can be measured using a crystal monitor in the processing chamber.

For n-type GaN, a thick Ti/Au (50 nm/200 nm) bilayer acts as the n-type metal contact in our work. This bilayer is also used as the additional reflector for LEDs with flip-chip configurations. These metals are deposited by a magnetron sputter as shown in Figure 2.10(a). The metal deposition in the magnetron sputter is also performed in a high-vacuum chamber with a processing pressure lower than

1×10^{-6} Torr. As shown in Figure 2.10(b), in the chamber, the target material is mounted on a plate which is always negatively biased. An insert gas, commonly Ar, is injected into the chamber and ionized to produce positively charged Ar ions. When a high direct-current voltage is applied, the Ar ions are accelerated towards the negatively biased target material. These energetic Ar ions bombard the target surface and result in the sputtering of atoms from the target material. These sputtered atoms deposit on the substrate surface forming a thin film.

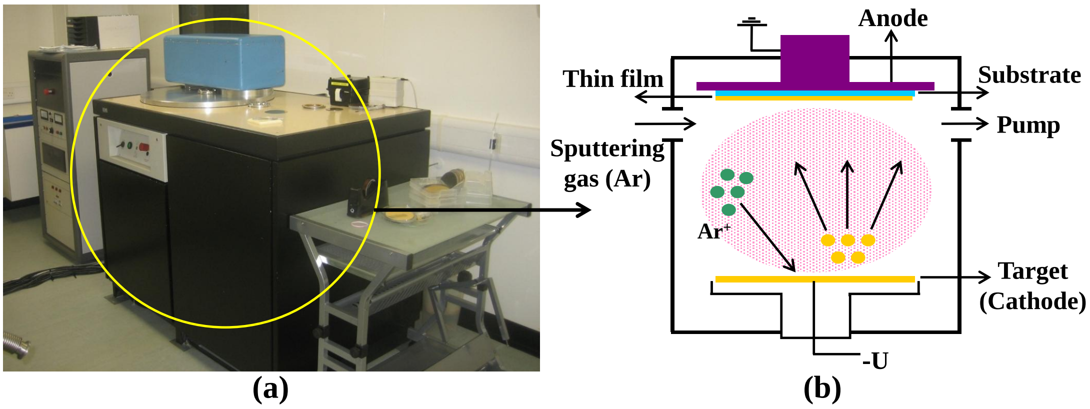

FIGURE 2.10: (a) Image and (b) schematic diagram of a magnetron sputter chamber. The processing chamber is highlighted by a yellow ellipse.

Thermal annealing

Thermal annealing is widely used in the semiconductor fabrication for different purposes such as doping activation [6], defect recovery [7] and contact formation [8]. In our work, thermal annealing is mainly used to form a metal contact to p-type GaN with a low specific contact resistivity. In our lab, the thermal annealing process is performed in the chamber of rapid thermal annealing (RTA) equipment as shown in Figure 2.11(a). Compared with a furnace, the RTA can ramp up the temperature at a higher rate of 75 to 200 °C/s. As shown in Figure 2.11(b), a tungsten-halogen lamp, which can generate intense heat in the form of infrared (IR) radiation, is used as a heating element. The vertical array of lamps allows a uniform heating on the wafer. The wafer temperature is monitored by an IR pyrometer and controlled by the lamp power. The steady peak temperature of the RTA in our lab is 1000 °C while the maximum peak temperature is 1300 °C. The gas inlet allows introduction of different gases such as N_2, air and Ar, so the wafer can be annealed in different ambients.

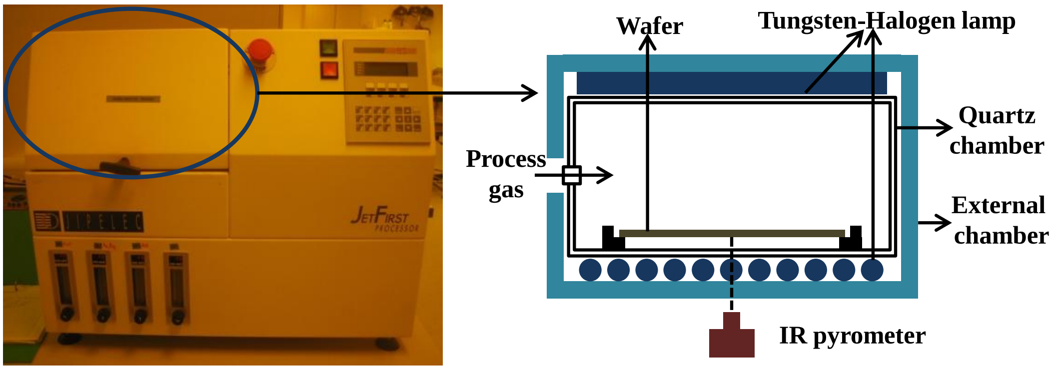

(a) **(b)**

Figure 2.11: (a) Image and (b) schematic diagram of a RTA chamber. The processing chamber is highlighted by a blue ellipse.

Thermal annealing is extremely important to achieve a high-quality metal contact to p-type GaN for III-nitride LEDs, especially for μ-LEDs due to their reduced contact area on the p-type GaN layer as introduced in subsection 1.4.1. Our commonly used annealing process is at an optimized temperature of 500 °C in an air ambient for the Ni/Au bilayer [9]. In this work, we also study the effect of thermal annealing on Pd-based metal contacts to p-type GaN. The detailed results of this investigation can be found in subsection 5.2.2.

2.2 Characterization of microstructured light emitting diodes

In order to characterize the microstructured LEDs and investigate the mechanisms of these devices, some advanced characterization techniques are used in this work. Among these techniques, cathodoluminescence (CL) and temperature-dependent photoluminescence (T-PL) play important roles in the III-nitride material and microstructured LED characterization. In the following subsections, both techniques and their related setups will be introduced.

2.2.1 Cathodoluminescence

CL is an optical and electrical phenomenon in which photons are emitted from a luminescent material impinged by an energetic electron beam. CL is one of many forms of luminescence and is well explained by solid-state energy band theory. The energy bands of a semiconductor consists of a valence band and a conduction band separated by a bandgap. When the high-energy electron beam bombards a semiconductor, the electrons in the valence band will be excited to the conduction band. These excited electrons return to the valence band accompanied by an energy loss leading to the possible emission of photons. The probability of photon emission and the energy of the photons are strongly dependent on the material properties such as bandgap energy, defects and purity. So the CL measurement can provide such information and is widely used for semiconductor characterization.

Compared with other luminescence techniques, the prime advantage of CL is its high spatial resolution. The spatial resolution of CL is strongly dependent on the measurement conditions such as the accelerating voltage and electron-beam current. When an electron beam interacts with a sample, the lateral spread of electrons in the sample (consequently the CL resolution) is determined by these beam conditions. The interaction of electrons with a sample can be investigated by Monte Carlo electron trajectory simulations [10, 11]. Figure 2.12 shows the typical simulated interaction volumes when 200 representative electrons are injected on a 1 nm spot of the GaN surface at 1, 3 and 10 kV accelerating voltages, respectively. As shown, the interaction volume is dependent nonlinearly on the accelerating voltage. Furthermore, it can also be found that, for each interaction volume, the lateral spreading distance and the penetration depth of the electrons are approximately equal to each other. This simulation confirms that a low acceleration voltage is required for CL measurements with high spatial resolution. Thus, for the CL measurements on the quantum wells (QWs) within a III-nitride LED structure, an appropriate sample preparation is necessary, especially when a high spatial resolution is required. The top p-type GaN layer must be thinned so as to reduce the accelerating voltage needed to excite QW emission and, in turn, improve the spatial resolution. An application of CL measurements for the QWs within an LED structure with high spatial resolution (∼100 nm) can be found in chapter 3. However, the CL technique also presents its own drawback. The damage caused by the electron-beam impingement is an unavoidable problem for CL measurements. The degradation of material quality is observed when $In_xGa_{1-x}N$ QWs are exposed to the electron beam [12]. This degradation has been attributed to increased dislocation mobility following the electron-beam impingement and is more pronounce when using a low accelerating voltage [12]. To minimize the effect of this damage, a high accelerating voltage and/or a short acquisition time needs

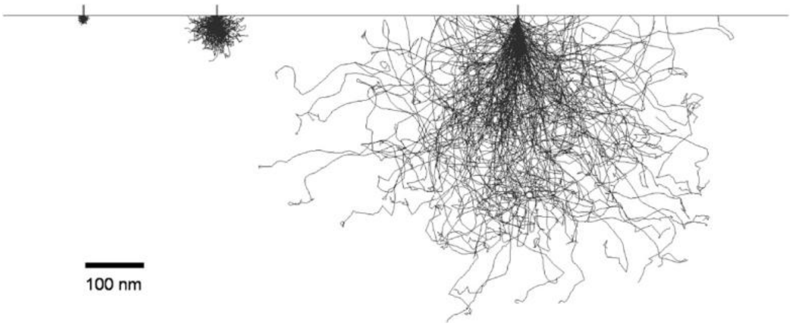

Figure 2.12: Monte Carlo electron trajectory simulations of interaction volumes for (left to right) 1, 3 and 10 kV beams impinging on a GaN layer. After [13].

to be used in CL measurements. The acquisition time is the period used to collect the CL signal at each point during a scan. Because the accelerating voltage used in CL measurements strongly affect the spatial resolution as discussed early, it is hard to use the high accelerating voltage to minimize the damage of the electron-beam impingement especially when a high-spatial resolution is required. Thus, a short acquisition time is necessary. In our work, this time is normally set at millisecond scale.

The facility for CL measurements used in this work is a home-built detection system installed on an FEI Sirion 200 ultrahigh-resolution Schottky field-emission scanning electron microscope (SEM), as shown in Figure 2.13(a). Figure 2.13(b) illustrates the schematic diagram of the CL setup. As shown, the electron beam is generated by the electron gun of the SEM and impinges on the sample. The sample is inclined at 45 °, and the luminescence is collected by a Schwarzschild-type reflecting objective at right angles to the electron beam. The light is then coupled directly to the entrance slit of a 1/8 m spectrograph using a paraboloidal mirror and detected using a cooled electron-multiplying charge coupled device (EMCCD) detector [13]. Compared with the conventional CL setup which takes the spectrum at a fixed point or scans the sample at a fixed wavelength, the EMCCD detector used in our setup enables recording of the full hyperspectral imaging with low noise at each point under the scanning beam. The hyperspectral imaging mode enhances the power of CL technique by recoding the full set of spectroscopic and microscopic information together [14]. By acquiring the whole spectrum at each scanning point, a large multidimensional dataset is assembled which can be further manipulated to yield different information as a function of position [15]. Furthermore, the optical design of our CL setup is also different from the conventional CL facility. In this setup, a low-NA reflecting objective takes the place of large solid angle conic mirrors. This change can enhance the spatial resolution of CL measurements without additional signal loss. The detailed discussion on the optical design of this CL setup can be found in Ref. [16].

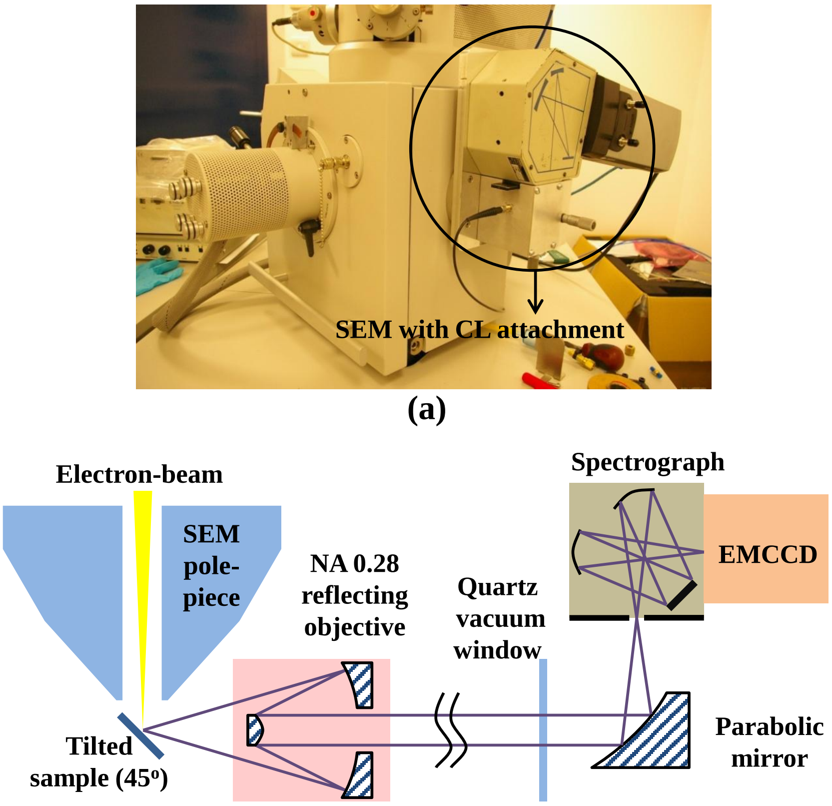

(a)

(b)

FIGURE 2.13: (a) Image and (b) schematic diagram of a home-built CL detection system installed on the SEM (Department of Physics).

2.2.2 Temperature-dependent photoluminescence

Photoluminescence (PL) is another form of luminescence in which photons are emitted from a luminescent material excited by an external light source. The PL process can also be explained by solid-state energy band theory as an excitation of electrons by photons to the conduction band and then return to the valence band accompanied by photon emission. PL is also a common technique used to measure the purity and crystal quality of semiconductors. Compared with CL, the excitation source in PL is replaced by a light beam and there is therefore almost no damage when the material is irradiated by the excitation light. However, the spatial resolution of conventional PL is relatively low. The interaction volume of

PL is mainly dependent on the beam spot size irradiated on the material surface and the material absorption at the wavelength of the excitation light. The spatial resolution of conventional PL systems is on a micron scale. Some advanced PL techniques, such as micro-PL [17] and PL confocal microscopy [18], can enhance the spatial resolution down to a few hundred nanometres or less at the specific wavelength.

There are several variations of the PL system to measure different properties of materials. Time-resolved PL is a direct method to measure the carrier lifetime of a semiconductor [19]. In this technique, a pulsed light source is used to excite a semiconductor sample and then the PL decay time, which corresponds to the carrier lifetime of the sample, is measured. Another common technique is T-PL which is used in my work. Since the nonradiative recombination processes are activated by thermal excitation [20], the luminescence efficiency of a semiconductor can be obtained by comparing the PL spectrum at low temperature and the one at room temperature [21]. In addition, the measured temperature-dependent variations of PL emission peak and spectral width can also provide more information about the energy band structure of QWs [22]. A detailed analysis of the T-PL spectra of $In_xGa_{1-x}N$ QWs can be found in section 4.2 of this thesis.

Figures 2.14(a) and (b) show, respectively, the image and schematic diagram of the home-built T-PL setup used in this work. As plotted in Figure 2.14(b), the excitation light in this setup is reflected by a dichroic beam splitter and focused on the sample surface through a reflecting objective. The dichroic beam splitter is a type of beam splitter with nearly 100 % reflectivity for a specific wavelength range. For excitation light sources with different wavelengths, different dichroic beam splitters are used to effectively reflect the excitation light from the light source to the sample. The luminescence emitted from the sample is collected by the same reflecting objective. Then the luminescence is coupled directly to the entrance slit of a 1/8 m spectrograph using a normal plate beam splitter and is detected by a CCD detector. Because both the excitation light and luminescence from sample are collected by the same reflecting objective, there is a longpass filter in front of spectrograph to prevent the excitation light being detected by the CCD. The longpass filter is an optical component with nearly 100 % transparency for a specific long-wavelength (compared with the emission wavelength of the excitation light) range. The luminescence emitted from the sample can also pass through the dichroic beam splitter and reach another CCD detector without a spectrograph. This detector is used to image the sample with the purpose of controlling the excitation position on the sample surface. The temperature of a sample can be controlled between 15 and 300 K using a closed cycle helium refrigerator in conjunction with a heater.

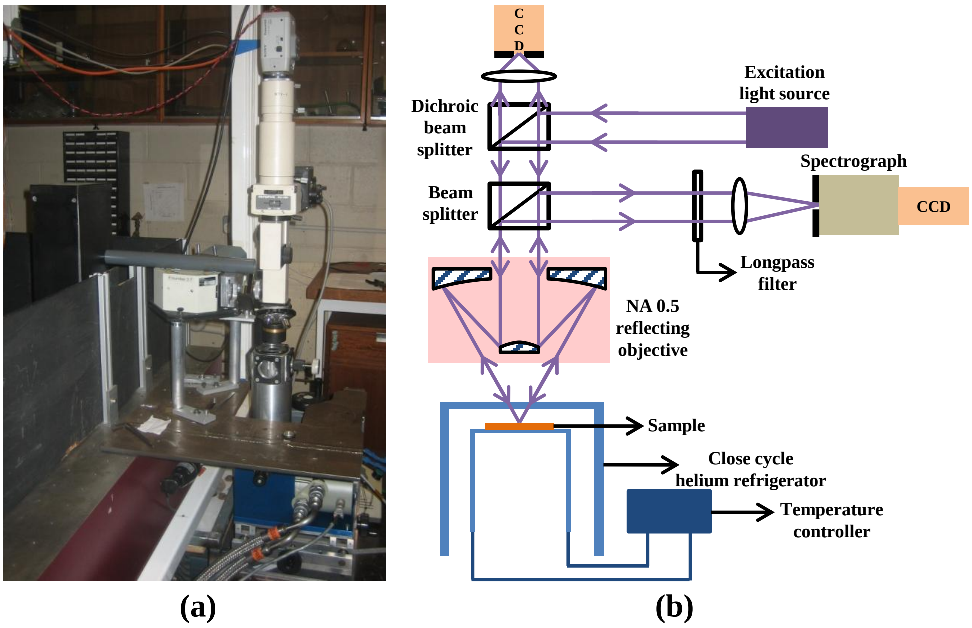

FIGURE 2.14: (a) Image and (b) schematic diagram of a home-built T-PL setup (Department of Physics).

2.3 Summary

In this chapter, the main steps in the fabrication process of III-nitride microstructured LEDs have been introduced in section 2.1 including pattern definition, pattern transfer and formation of metal contacts. The general working principles and typical processes of the techniques used in each step were presented and commented on. In order to fabricate fully operational microstructured LEDs, these techniques play important roles. In section 2.2, a brief introduction to two techniques used for microstructured LED characterization, namely CL and T-PL, was given. In addition to the general working principles, the primary advantages of both techniques were illustrated and discussed. Because both techniques are performed using home-built facilities, detailed illustrations of their designs were given as well. These techniques will be used in later chapters for mechanism investigations of microstructured LEDs.

References

[1] M. Häfner, C. Pruss, and W. Osten. Laser direct writing. *Optik & Photonik*, 6(4):40–43, 2011.

[2] M. Svalgaard. Direct writing of planar waveguide power splitters and directional couplers using a focused ultraviolet laser beam. *Electronics Letters*, 33(20):1694–1695, 1997.

[3] A.J.C. Kuehne, D. Elfström, A.R. Mackintosh, A.L. Kanibolotsky, B. Guilhabert, E. Gu, I.F. Perepichka, P.J. Skabara, M.D. Dawson, and R.A. Pethrick. Direct Laser Writing of Nanosized Oligofluorene Truxenes in UV-Transparent Photoresist Microstructures. *Advanced Materials*, 21(7):781–785, 2008.

[4] D. Elfström, B. Guilhabert, J. McKendry, S. Poland, Z. Gong, D. Massoubre, E. Richardson, B.R. Rae, G. Valentine, G. Blanco-Gomez, E. Gu, J.M. Cooper, R.K. Henderson, and D.W. Dawson. Mask-less ultraviolet photolithography based on CMOS-driven micro-pixel light emitting diodes. *Optics Express*, 17(26):23522–23529, 2009.

[5] B. Guilhabert, D. Massoubre, E. Richardson, J.J.D. McKendry, G. Valentine, R.K. Henderson, I.M. Watson, E. Gu, and M.D. Dawson. Sub-micron lithography using ingan micro-leds: Mask-free fabrication of led arrays. *Photonics Technology Letters, IEEE*, 24(24):2221–2224, 2012.

[6] S.J. Pearton, J.C. Zolper, R.J. Shul, and F. Ren. GaN: Processing, defects, and devices. *Journal of Applied Physics*, 86(1):1–78, 1999.

[7] X.A. Cao, H. Cho, S.J. Pearton, G.T. Dang, A.P. Zhang, F. Ren, R.J. Shul, L. Zhang, R. Hickman, and J.M. Van Hove. Depth and thermal stability of dry etch damage in GaN Schottky diodes. *Applied Physics Letters*, 75(2):232–234, 1999.

[8] J.K. Sheu, Y.K. Su, G.C. Chi, W.C. Chen, C.Y. Chen, C.N. Huang, J.M. Hong, Y.C. Yu, C.W. Wang, and E.K. Lin. The effect of thermal annealing on the Ni/Au contact of p-type GaN. *Journal of Applied Physics*, 83(6):3172–3175, 1998.

[9] J.K. Ho, C.S. Jong, C.C. Chiu, C.N. Huang, K.K. Shih, L.C. Chen, F.R. Chen, and J.J. Kai. Low-resistance ohmic contacts to p-type GaN achieved by the oxidation of Ni/Au films. *Journal of Applied Physics*, 86(8):4491–4497, 1999.

[10] J. Goldstein, D.E. Newbury, D.C. Joy, C.E. Lyman, P. Echlin, E. Lifshin, L. Sawyer, and J.R. Michael. *Scanning electron microscopy and X-ray microanalysis.* Springer, 2003.

[11] D. Drouin, A.R. Couture, D. Joly, X. Tastet, V. Aimez, and R. Gauvin. CASINO V2. 42A Fast and Easy-to-use Modeling Tool for Scanning Electron Microscopy and Microanalysis Users. *Scanning*, 29(3):92–101, 2007.

[12] H. Nykänen, P. Mattila, S. Suihkonen, J. Riikonen, E. Quillet, E. Homeyer, J. Bellessa, and M. Sopanen. Low energy electron beam induced damage on InGaN/GaN quantum well structure. *Journal of Applied Physics*, 109:083105, 2011.

[13] P.R. Edwards and R.W. Martin. Cathodoluminescence nano-characterization of semiconductors. *Semiconductor Science and Technology*, 26(6):064005, 2011.

[14] J. Christen, M. Grundmann, and D. Bimberg. Scanning cathodoluminescence microscopy: A unique approach to atomic-scale characterization of heterointerfaces and imaging of semiconductor inhomogeneities. *Journal of Vacuum Science & Technology B: Microelectronics and Nanometer Structures*, 9(4):2358–2368, 1991.

[15] P.R. Edwards, R.W. Martin, I.M. Watson, C. Liu, R.A. Taylor, J.H. Rice, J.H. Na, J.W. Robinson, and J.D. Smith. Quantum dot emission from site-controlled InGaN/GaN micropyramid arrays. *Applied Physics Letters*, 85:4281, 2004.

[16] P.R. Edwards, L.K. Jagadamma, R.W. Martin, and A. Wark. Cathodoluminescence hyperspectral imaging on the nanometre scale. *HSI 2011*, pages 87–89, 2011.

[17] K. Tachibana, T. Someya, S. Ishida, and Y. Arakawa. Selective growth of InGaN quantum dot structures and their microphotoluminescence at room temperature. *Applied Physics Letters*, 76(22):3212–3214, 2000.

[18] C. Griffin, E. Gu, H.W. Choi, C.W. Jeon, J.M. Girkin, M.D. Dawson, and G. McConnell. Beam divergence measurements of InGaN/GaN micro-array light-emitting diodes using confocal microscopy. *Applied Physics Letters*, 86:041111, 2005.

[19] K. Okamoto, I. Niki, A. Scherer, Y. Narukawa, T. Mukai, and Y. Kawakami. Surface plasmon enhanced spontaneous emission rate of InGaN/GaN quantum wells probed by time-resolved photoluminescence spectroscopy. *Applied Physics Letters*, 87:071102, 2005.

[20] R.C. Miller, D.A. Kleinman, W.A. Nordland, and A.C. Gossard. Luminescence studies of optically pumped quantum wells in GaAs-$\mathrm{Al}_x\mathrm{Ga}_{1-x}\mathrm{As}$ multilayer structures. *Physical Review B*, 22:863–871, Jul 1980.

[21] M. Leroux, N. Grandjean, B. Beaumont, G. Nataf, F. Semond, J. Massies, and P. Gibart. Temperature quenching of photoluminescence intensities in undoped and doped GaN. *Journal of Applied Physics*, 86(7):3721–3728, 1999.

[22] R. Pecharroman-Gallego, R.W. Martin, and I.M. Watson. Investigation of the unusual temperature dependence of InGaN/GaN quantum well photoluminescence over a range of emission energies. *Journal of Physics D: Applied Physics*, 37(21):2954, 2004.

Chapter 3

Size-dependent strain relaxation in $\mathrm{In}_{0.25}\mathrm{Ga}_{0.75}\mathrm{N}$/GaN-based micro-pillars

In this chapter, size-dependent strain relaxation and its effects on the optical properties of $\mathrm{In}_x\mathrm{Ga}_{1-x}\mathrm{N}$ quantum wells in micro-pillars (μ-pillars) is investigated through a combination of cathodoluminescence (CL) hyperspectral imaging and numerical modelling. These results provide significant insights into the mechanism of strain relaxation in $\mathrm{In}_x\mathrm{Ga}_{1-x}\mathrm{N}$/GaN-based μ-pillars and also give practical guidance for design and development of novel III-nitride micro-/nano-LEDs. The first section of this chapter summarizes the previous studies on strain relaxation in $\mathrm{In}_x\mathrm{Ga}_{1-x}\mathrm{N}$/GaN-based micro-/nano-pillars. Based on these previous results, we have used the high-spatial-resolution CL hyperspectral technique and a new simulation model to further investigate the strain relaxation in $\mathrm{In}_x\mathrm{Ga}_{1-x}\mathrm{N}$/GaN-based μ-pillars and have obtained some new results. Sections 3.2 and 3.3 describe the experimental and simulation results of a single-sized μ-pillar in detail including the sample preparation, data analysis and model setting up. Finally, the size effect on the strain relaxation in μ-pillars is investigated and is discussed in section 3.4.

3.1 Overview of previous research on strain relaxation in $\mathbf{In_xGa_{1-x}N}$/GaN-based micro-/nano-pillars

As described in section 1.4, the compressive strain due to the lattice mismatch between InN and GaN in quantum wells (QWs) is directly responsible for the piezoelectric polarization effect. The induced polarization effect generates a larger internal electric field and, thus, quantum-confined Stark effect (QCSE) as the indium content in the QWs increases. Consequently, for III-nitride light emitting diodes (LEDs) emitting in the green-to-red region, there is a progressive tendency for quantum efficiency to decrease as the emission wavelength increases, which is the so-called ‘green-yellow gap’. Since the strain can be partly or fully relaxed in $In_xGa_{1-x}N$/GaN-based micro-/nano-pillars because of the pillars’ free sidewalls, the investigation of this strain relaxation in micro-/nano-pillars has attracted great attention.

The fabrication method of $In_xGa_{1-x}N$/GaN-based micro-/nano-pillars has typically involved top-down patterning by etching an initially planar epitaxial structure containing $In_xGa_{1-x}N$ QWs, although the techniques of directly grown nano-columnar structures have also been reported [1]. There were a number of previous studies focusing on strain relaxation in $In_xGa_{1-x}N$/GaN-based micro-/nano-pillars [1–10]. The investigations on strain relaxation in $In_xGa_{1-x}N$/GaN-based pillars usually focused on photoluminescence (PL) characterization including micro-PL (μ-PL) [8] and confocal laser scanning microscopy [9]. The spatial resolution of the PL measurements used so far was limited by the size of the excitation beam spot. To the best of our knowledge, the highest spatial resolution achieved for PL measurement of the strain relaxation in $In_xGa_{1-x}N$/GaN-based micro-/nano-pillars has been 500 nm at room temperature (RT) by employing confocal laser scanning microscopy [9]. Due to the low spatial resolution, the PL emission spectrum of micro-/nano-pillars was normally obtained by fitting. In Ref. [8], a nano-pillar with a diameter of 300 nm and a height of 2 μm was fabricated from an $In_{0.2}Ga_{0.8}N$/GaN LED wafer by using Pt as an etching mask. The nano-pillar was then characterized by μ-PL. However, being limited by the resolution of μ-PL, it was hard to directly measure the emission spectrum of this nano-pillar. Thus, the emission spectrum of the nano-pillar was achieved by comparing the overall μ-PL spectrum before and after removing the Pt mask as shown in Figure 3.1(a) and

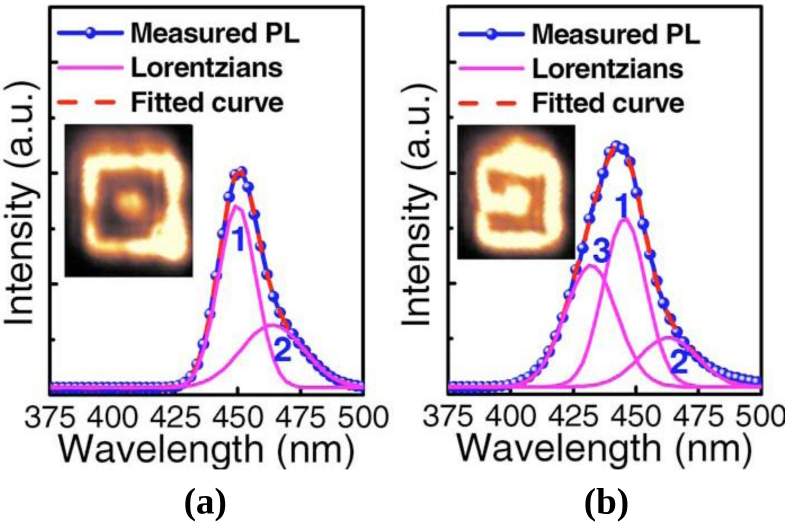

FIGURE 3.1: Emission spectrum of a nano-pillar (a) with and (b) without the Pt etching mask measured by μ-PL. After [8].

(b) [8], respectively. The emission spectrum of the nano-pillar, which is denoted as spectrum 3 in Figure 3.1(b), was then obtained through a Lorentzian fitting process. Figures 3.2(a) and (b) show the maps of emission intensity and wavelength for a 2 μm-diameter $In_{0.25}Ga_{0.75}N/GaN$-based micro-pillar (μ-pillar) with the highest spatial resolution at RT [9]. As shown in these figures, the μ-pillar presented a doughnut-shaped emission pattern due to the partial strain relaxation at free sidewalls. However, this spatial resolution is still not high enough to investigate the detailed strain relaxation process at a sub-micron scale.

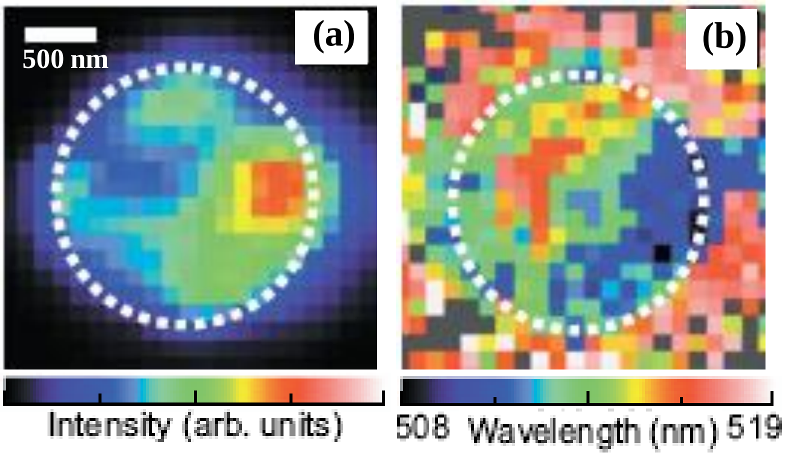

FIGURE 3.2: (a) Emission intensity map and (b) emission wavelength map of a 2 μm-diameter μ-pillar taken at RT by confocal laser scanning microscopy. After [9].

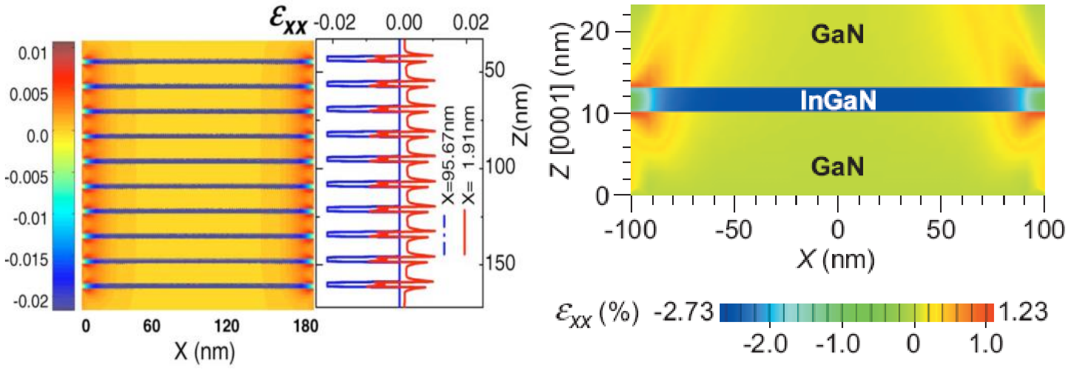

(a) **(b)**

FIGURE 3.3: (a) In-plane strain distribution in an In$_{0.2}$Ga$_{0.8}$N/GaN nano-pillar with a diameter of 200 nm simulated by VFF method; (b) in-plane strain distribution in an In$_{0.25}$Ga$_{0.75}$N/GaN nano-pillar with a diameter of 200 nm simulated by FEM. After [8, 9].

Numerical simulations of strain relaxation in the QWs of In$_x$Ga$_{1-x}$N/GaN-based micro-/nano-pillars have also been carried out [8, 9]. Yu et al. employed an atomistic valence force field (VFF) method for strain calculations [8]. VFF is a microscopic model which determines the positions of each individual atom in the material by minimizing the elastic energy of the entire structure. In Ref. [9], the finite element method (FEM), embodying macroscopic elastic theory, was also used. Analogous FEM calculations have proven to be effective in simulating semiconductor nanostructures including InAs quantum dots [11] and nanocolumnar GaN/Al$_x$Ga$_{1-x}$N-based disks [12]. As shown in Figure 3.3(a) [8] and (b) [9], the simulated strain relaxation in In$_x$Ga$_{1-x}$N/GaN-based nano-pillars by the VFF and FEM methods is generally the same. The ϵ_{xx} in the figure represents the in-plane strain of different layers. As shown, clear strain relaxation at the pillar edge can be observed. However, from these figures, it can also be found only the local environment of the QWs was considered while neglecting the influence from other layers in both models of VFF and FEM simulations. This assumption becomes increasingly inaccurate when the fill factor of etched pillar mesas (the ratio of mesa area to total sample area) is very small and the height of the mesa is relatively large. Limited by the spatial resolution and simulation accuracy, the detailed correlations between spectroscopic results and numerical simulations of strain relaxation in the QWs of In$_x$Ga$_{1-x}$N/GaN-based micro-/nano-pillars are hard to achieve.

3.2 Strain relaxation in $\mathbf{In_{0.25}Ga_{0.75}N}$/GaN-based micro-pillars characterized by a high-spatial-resolution cathodoluminescence technique

As summarized in the last section, further improvement of the spatial resolution of characterization techniques can enable a better understanding of the mechanism of strain relaxation in $In_xGa_{1-x}N$/GaN-based micro-/nano-pillars, which is critically important to the design and development of novel III-nitride micro-/nano-LEDs for a wide range of applications [3, 13–15]. To overcome the limitation of PL measurements, cathodoluminescence (CL) hyperspectral imaging was employed in our work to record spectrally resolved emission and its distribution on $In_{0.25}Ga_{0.75}N$/GaN-based μ-pillars with spatial resolution of approximately 100 nm. By this method, clear strain relaxation processes were observed and analyzed. The experimental processes and results are shown below.

3.2.1 Fabrication and characterization of $\mathbf{In_{0.25}Ga_{0.75}N}$/GaN-based micro-pillars

A yellow-green $In_{0.25}Ga_{0.75}N$/GaN-based LED wafer (supplied by Peking University, China) was used for μ-pillar fabrication in this experiment. This wafer was grown on a c-plane (0001) sapphire substrate by metal-organic chemical vapour deposition. The epitaxial structure comprised the following functional layers: a 2 μm-thick undoped GaN buffer layer; a 2 μm-thick n-type GaN layer; two $In_{0.10}Ga_{0.90}N$ QWs of 3 nm thickness with 10 nm GaN barrier layers; six $In_{0.25}Ga_{0.75}N$ QWs again of 3 nm thickness and separated by 10 nm GaN barriers; and finally a 240 nm p-type GaN layer. The first two QWs function as an electron reservoir layer (ERL) for improving the carrier capture rate [16] and mitigating the efficiency droop by reducing the overflow of hot electrons [17]. In the context of this study, their presence also gave an opportunity to compare the effect of strain relaxation in QWs with different indium contents. As schematically shown in Figure 3.4, the μ-pillars with diameters ranging from 2 to 150 μm were fabricated as followed: the top p-type GaN layer was firstly thinned down to 40 nm by inductively coupled plasma (ICP) etching using Cl_2 plasma. This step facilitated

CL measurements with high spatial resolution by reducing the accelerating voltage needed to excite the emission of QWs. A 300 nm-thick SiO_2 layer was then deposited on the residual p-type GaN layer by plasma-enhanced chemical vapour deposition. The SiO_2 layer was then patterned into an array of micro-disks using photolithography followed by reactive ion etching. Defined by the SiO_2 hard mask, plasma with a combination of Cl_2 and Ar was used to etch $In_{0.25}Ga_{0.75}N$/GaN-based μ-pillars with a height of 1.1 μm which is a typical height for LED structures. Prior to the CL measurements, the SiO_2 mask was removed by buffered oxide etch. The cross-sectional structure of an $In_{0.25}Ga_{0.75}N$/GaN-based μ-pillar is shown in Figure 3.5.

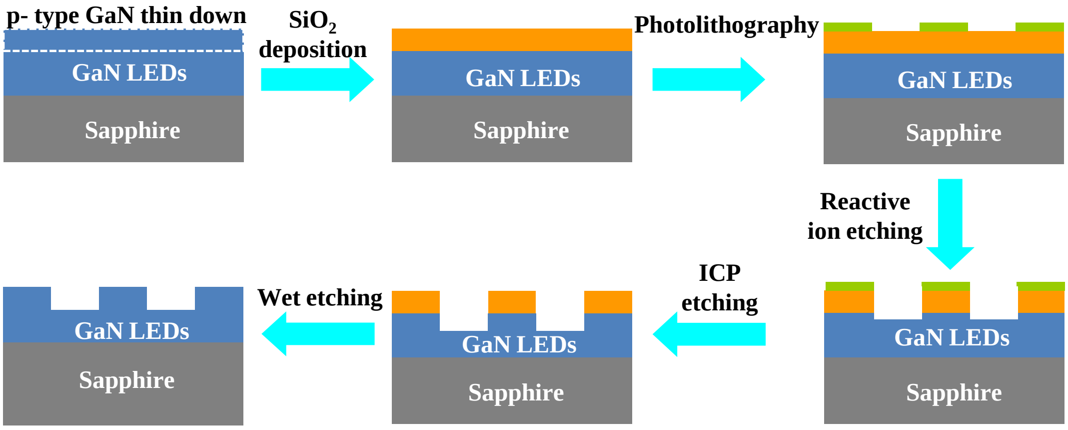

FIGURE 3.4: Process flow for the fabrication of $In_{0.25}Ga_{0.75}N$/GaN-based μ-pillars.

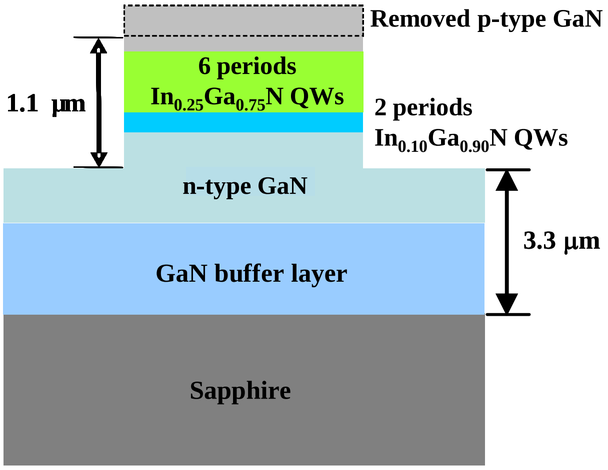

FIGURE 3.5: Cross-sectional structure of an $In_{0.25}Ga_{0.75}N$/GaN-based μ-pillar.

As mentioned above and in subsection 2.1.2, two plasma etching recipes, i.e. Cl_2 plasma and Cl_2/Ar plasma, were used to fabricate the $In_{0.25}Ga_{0.75}N$/GaN-based μ-pillars in the ICP system. By using Cl_2 plasma, pure chemical etching, which gives the lowest etching damage [18], dominates the plasma etching. This recipe was employed to thin down the top p-type GaN layer in order to minimize the influence of etching damage on the CL measurements. However, when Cl_2 plasma is used for pillar etching, the residual byproducts coming from the chemical reaction between Cl and GaN adhere on the pillar sidewalls which leads to a rough surface. The scanning electron microscope (SEM) image of a 16 μm-diameter μ-pillar etched by the Cl_2 plasma is shown in Figure 3.6(a). The rough and irregular sidewalls can be observed for this pillar. Thus, to improve the quality of sidewalls, Ar gas was introduced in the optimized recipe for pillar etching. The energetic Ar ions can sputter away the deposited etching byproducts on the pillar sidewalls and increase the anisotropy of the etching. Moreover, due to the low etching selectivity between photoresist and GaN (around 1:1) and the diffraction effect in optical exposure, there is always a hole formed in the pillar centre when the pillar diameter is below 5 μm as shown in Figure 3.6(c). Due to the high etching selectivity between SiO_2 and GaN (around 1:4), a SiO_2 hard mask was used to prevent the formation of the hole during plasma etching. With the optimized etching recipe and SiO_2 hard mask, high-quality μ-pillars with different diameters were fabricated and typical SEM images of pillars with diameters of 16 μm and 2 μm are shown in Figure 3.6(b) and (d), respectively. It can be seen that the top surface of the pillar is smooth and the etch pits, which may result from preferential etching around structural defects, are much less. The smooth sidewall is almost perpendicular, with an inclination angle of about 85 °. The hole is eliminated in the smallest 2 μm-diameter μ-pillar as well.

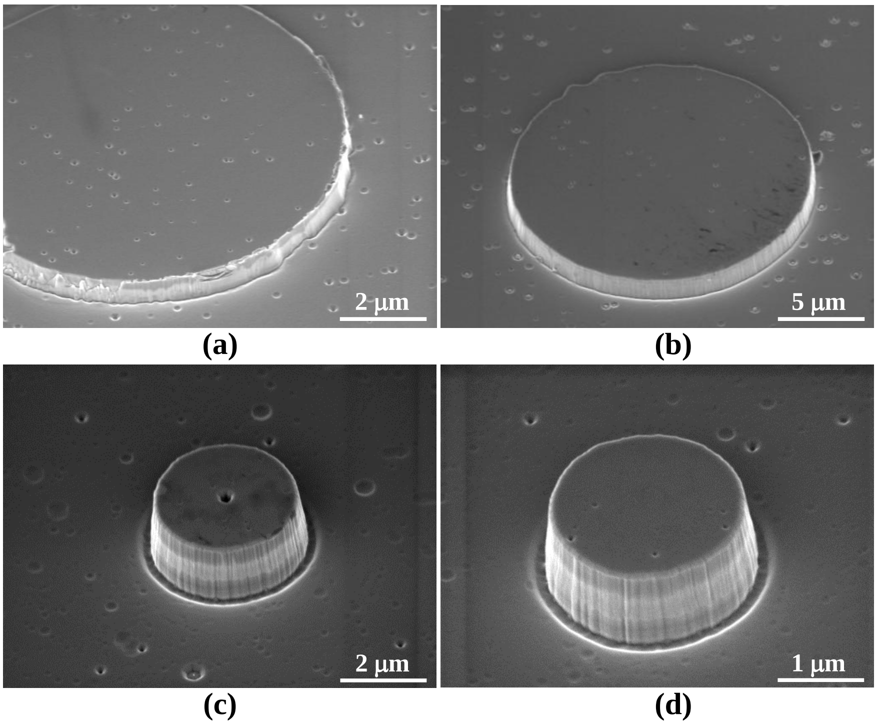

FIGURE 3.6: SEM images of μ-pillars with a diameter of 16 μm etched by (a) pure Cl_2 plasma and (b) an optimized recipe with additional Ar plasma; SEM images of 2 μm-diameter μ-pillars (c) with and (d) without a central hole.

The CL technique used here has been introduced in subsection 2.2.1 in detail. For the CL measurements on μ-pillars with different diameters, a low accelerating voltage of 5 kV and an electron-beam current of 1.5 nA were used to limit the beam interaction volume down to 100 nm and, hence, improve the spatial resolution of CL measurements. To avoid the damage of electron-beam impingement, a short acquisition time of 40 ms is used in these measurements.

3.2.2 Results of cathodoluminescence hyperspectral imaging

Figure 3.7 shows typical CL spectra extracted from the centre and edge of a μ-pillar with a diameter of 16 μm. There are two emission peaks from different-indium-content $In_xGa_{1-x}N$ QWs visible in the CL spectra, centered at 560 nm (yellow-green) and at 425 nm (blue). The strong yellow-green emission originates from the $In_{0.25}Ga_{0.75}N$ QWs, which is also the dominant emission in the electroluminescence (EL) spectrum of a 16 μm-diameter micro-LED (μ-LED) fabricated from the same wafer (without thinning down the top p-type GaN layer so as to achieve a good metal contact to p-type GaN) shown inset. The blue luminescence in both CL and EL spectra is emitted from the $In_{0.10}Ga_{0.90}N$ QWs. Compared with the CL spectra, the EL spectrum at a low operating current of 1 mA (to exclude the self-heating effect during the LED operation) is similar to that from CL measurements. The main difference is the relatively weaker blue emission observed in the EL spectrum. This is due to the heavy effective mass and low mobility of holes in GaN which limit their migration distance. In contrast, the penetration depth in CL measurements depends mainly on the accelerating voltage supplied rather than the diffusion/drift length of carriers, which results in a much pronounced CL signal emitted from blue QWs. Unlike the area-integrated spectra of EL, CL is highly spatially-resolved which enables a direct spatial comparison. As plotted, the yellow-green emission from the edge (the black curve) shows a 7 nm blue-shift in the emission wavelength and 1.1 times intensity enhancement compared with that from the centre (the red curve). There is no comparable spectral shift or intensity enhancement for the blue emission. The spectral shift and enhanced emission can be largely attributed to the reduction of QCSE by partial strain relaxation resulting in a flat energy band and an enhancement on the overlap of electron and hole wavefunctions.

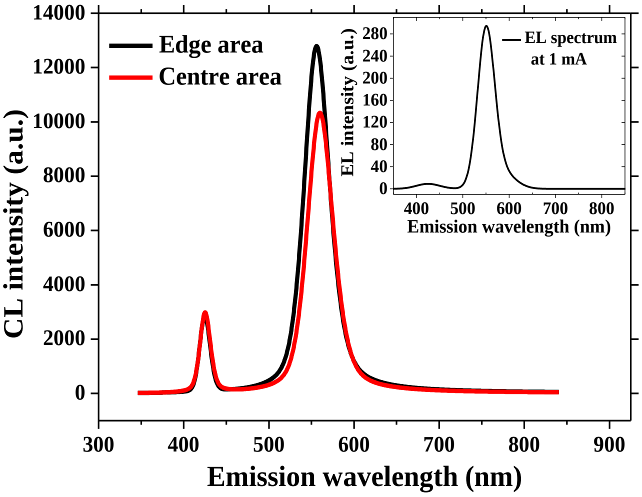

FIGURE 3.7: Typical CL spectra recorded from the edge and centre of a μ-pillar with a diameter of 16 μm, the insert is the EL spectrum of a same-sized μ-LED measured at an operating current of 1 mA.

The CL maps of emission wavelength and intensity corresponding to the yellow-green and blue QWs of a 16 μm-diameter μ-pillar are shown in Figure 3.8. These maps were extracted from CL hyperspectral imaging using nonlinear least-squares peak fitting. The step size of CL scans for these maps is 200 nm. For the yellow-green QWs, Figure 3.8(a) shows a clear blue-shift ring around the pillar perimeter with a maximum shift value of 7 nm relative to the centre. Such a ring region is dominated by higher emission intensities in Figure 3.8(c). Some imperfect areas may be caused by damage during sample preparation processes. However, Figure 3.8(b) and (d) show no corresponding blue-shift ring and enhanced emission at the edge of the pillar for the blue emission.

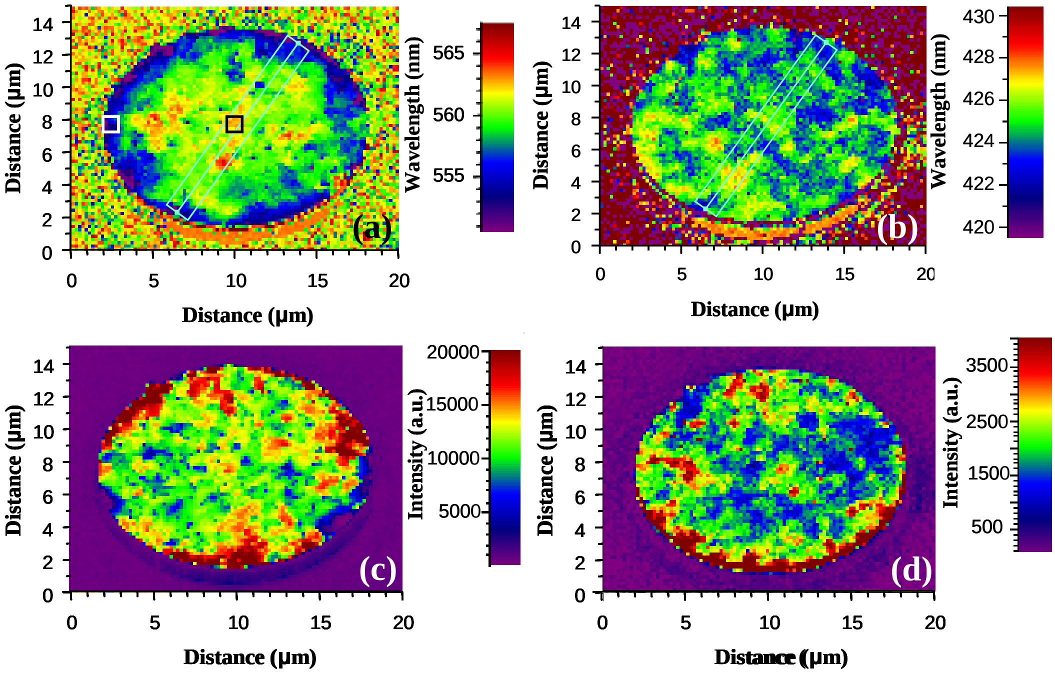

FIGURE 3.8: Spatially resolved CL maps of a 16 μm-diameter μ-pillar: wavelength distribution in the (a) yellow-green and (b) blue spectral region; corresponded emission intensity maps for (c) yellow-green and (d) blue QWs.

To further illustrate the variation of emission wavelength, line-scans of the emission wavelength in the two spectral regions are plotted along a typical diameter of the pillar as shown in Figure 3.9. The longer wavelength data highlight the blue-shifts reaching 7 nm within a 2 μm region around the pillar edge. Wavelength fluctuations from the mean value of 3 nm peak-to-peak are seen in the centre area of the pillar, and their non-systematic distribution suggests that such fluctuations are from variations in indium content and/or other inhomogeneities in the yellow-green QWs. This degree of intrinsic variation is considered in choosing a threshold shift of 3 nm to define the blue-shifted zone whose spatial extent is analyzed in later discussion on simulation results and size effect. The line-scan data for the blue QW emission confirm that any systematic blue-shift towards the pillar edge is indistinguishable from the fluctuation and thus constrains any such shift to below 1-2 nm in magnitude. Such a small blue-shift is due to the lower lattice mismatch between the active layers and barriers, which is consistent with our previous research [3].

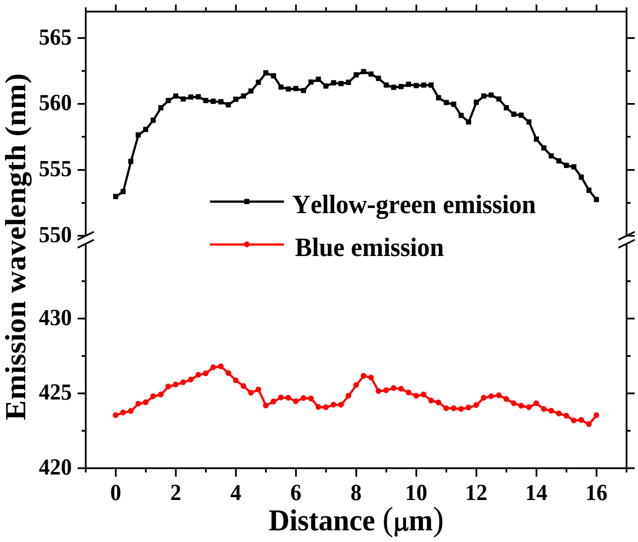

Figure 3.9: Variations of emission wavelengths along the representative pillar diameters as shown in Figure 3.8(a) and (b).

The higher-magnification (20 nm scanning step size) CL scans were performed at the edge and centre regions as labelled in Figure 3.8(a) with a $1 \times 1\ \mu m^2$ scanning area in order to have a further understanding of the strain relaxation process. The fitted wavelength maps of yellow-green QWs are shown in Figure 3.10(a) and (b) for edge and centre regions, respectively. The emission wavelengths of both maps are plotted along a typical diagonal as shown in Figure 3.10(c). It can be seen that the emission wavelength in the edge area shows a much sharper blue-shift compared with the one in the centre region. A nearly 7 nm shift occurs in the edge area. However, the blue-shift of the emission wavelength is less than 2 nm in the centre area which is barely distinguished from the intrinsic wavelength fluctuation as mentioned above. This indicates that strain relaxation is mainly occurring at the pillar edge due to the free constraints of the sidewalls. In the centre region of the pillar, the QWs are still constrained laterally and, thus, the strain relaxation magnitude is much less.

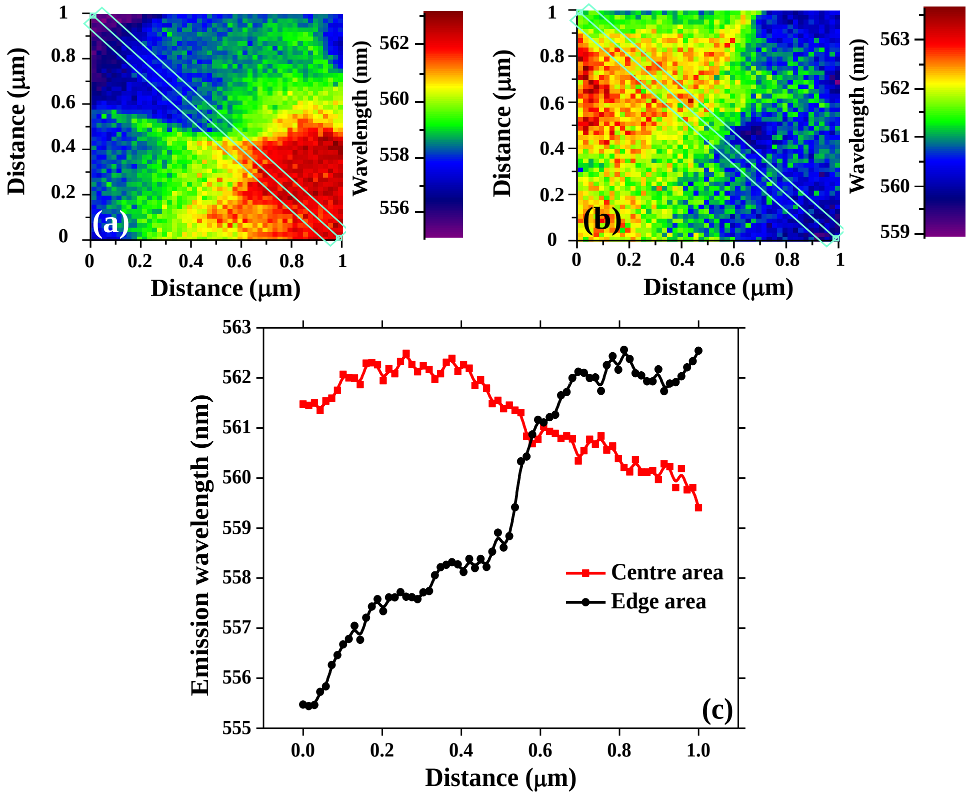

FIGURE 3.10: High-magnification wavelength maps for yellow-green QWs at (a) edge and (b) centre regions as labelled in Figure 3.8(a); (c) variations of emission wavelengths along the typical diagonals as shown in (a) and (b).

3.3 Finite element method simulation of strain relaxation in $In_{0.25}Ga_{0.75}N$/GaN-based micro-pillars

Based on the results of CL measurements shown in the last section, FEM simulation on strain relaxation in $In_{0.25}Ga_{0.75}N$/GaN-based μ-pillars is presented in this section. To increase the accuracy of the strain simulation, the GaN buffer layer and sapphire substrate below the emissive QWs which are normally neglected in previous research are included in our FEM model. Meanwhile, residual strain in the GaN buffer layer is considered in the simulation as well. The simulation results show a pronounced strain relaxation around the pillar edge. The calculated blue-shift wavelength and relaxation region agree well with the experimental results.

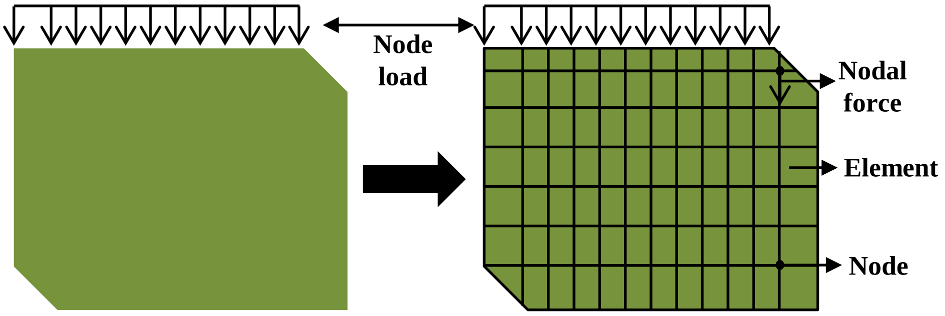

FIGURE 3.11: Schematic diagram of the basic idea of strain simulation by FEM.

3.3.1 Brief introduction of ANSYS

The strain relaxation in μ-pillars is simulated using the ANSYS 11.0 commercial finite element software package. As shown in Figure 3.11, the basic idea of FEM is discretization which transfers a complex object into finite elements with a simple shape. These finite elements are used to replace the original object and each element is connected by nodes which are considered as hinge joints. For strain calculation, the reaction between the elements is transferred by nodes, known as the nodal force which is an internal force. The external force applied on the node is called a node load. After discretization, a mechanical analysis process is first carried out on each element to find the relationship between the node force and the node displacement through Equation 3.1:

$$\{F\}^e = [K]^e \{\delta\}^e \tag{3.1}$$

where $\{F\}^e$ is the matrix of nodal force vectors, $[K]^e$ is the stiffness matrix and $\{\delta\}^e$ is the matrix of nodal displacement vectors. The superscript e of each matrix in the equation represents the components of each parameter along different vectors. Since the selected shape of the elements is normally as simple as a rectangle and/or a triangle, the mechanical analysis process on each element is feasible. After this simple process on each element, the mechanical analysis is extended to the whole structure to form a system of linear equations combining the relationships between the node loads and the displacements for all nodes. After introducing proper boundary and initial conditions, the system of linear equations becomes self-consistent and solvable. From the solutions, the strain and stress of every element are obtained.

Based on FEM, the simulation process carried by the ANSYS software could be generally divided into six parts as follows:

(1) Parameter Definition

In this part, the units of physical dimension, element type, real constants of the element and material parameters are defined.

(2) Geometric Model Establishment

The establishment of a finite element model can be achieved by using either the direct or indirect methods. The direct method, which is only applicable to simple structures, directly defines nodes and elements according to the geometrical shape of the structures. The indirect method is preferred for complex systems by means of point, line, surface and volume to create a real structure. The finite element model is established after element meshing.

(3) Element Meshing

Element meshing is a process to generate nodes and elements. It mainly includes the following three steps: element attribute definition, mesh control and mesh. The element attribute definition and mesh control are important steps because they not only affect the mesh results but also have a great influence on the solution accuracy.

(4) Load Definition

The loads include the boundary conditions (constraint, support or parameters of the boundary field) and other external or internal loads. Most of these loads are applied on the solid model (point, line and surface) or the element model (nodes and elements).

(5) Solution

There are two types of FEM solutions, namely fundamental and element solutions. The fundamental solutions are the value of freedom degrees for the nodes. The element solutions are primarily the centroidal solution values for each element.

(6) Post-processor

The calculated results could be illustrated through the post processing module of ANSYS. The illustrated results mainly include a strain or stress distribution and a deformation diagram.

3.3.2 Simulation process of strain relaxation and related wavelength shift

The simulation process, results and discussion here mainly focus on the μ-pillars with a diameter of 16 μm. For other pillars with different diameters, the simulation and calculation processes are almost the same. The detailed structure and material parameters used in my ANSYS model will be given first. In order to include the influence of neighboring pillars, simulation was performed on a 5 × 1 array consisting of identical 16 μm-diameter μ-pillars. This array had a pitch chosen to give a fill factor of 26 %, corresponding to the average value for the fabricated pillar array. The strain distribution calculated for the middle pillar was used to estimate the spectral shift. The in-plane strain isotropy (ϵ_{xx}=ϵ_{yy}) for the (0001) growth orientation allowed the simulation to be simplified to a two-dimensional (2D) case. The FEM simulation structure of the 16 μm-diameter μ-pillar array is illustrated in Figure 3.12. All the III-nitride layers shown in Figure 3.5 were included, although the FEM model did not extend through the full thickness of the sapphire substrate. Detailed analysis of the wafer bowing predicts that a bending-free plane in the sapphire substrate is at a depth of around 70 μm from the interface between the GaN layer and the sapphire substrate [19]. Therefore, a 80 μm sapphire thickness was adopted in the model in order to define a practical boundary condition. Pillar sidewalls were left free from constraints. The interface between different materials was 'glued' by Boolean operation to coincide with the real state. The plane 182 elements, which are defined by four nodes and used for a 2D modelling of solid structures, were employed in all models. The size-control-function was performed during the meshing process. The geometry was meshed with four-node rectangular elements which have a length of 100 nm in the QW region so as to get an accurate simulation result. For calculation, a strain variation with the thickness of the GaN layers as shown in Ref. [20] was used for estimating the residual strain in the GaN buffer layer below the first blue QW, which has a great influence on simulation results and will be discussed later in detail, while pseudomorphic growth was assumed for all QWs. Based on the data from Ref.

[21] and Vegards law (linear interpolation), elastic constants (C_{ij}) and unstrained lattice parameters (a_0) were calculated for the two relevant In$_x$Ga$_{1-x}$N ternary alloys through Equation 3.2:

$$Y(In_xGa_{1-x}N) = xY(InN) + (1-x)Y(GaN) \tag{3.2}$$

These calculated values are summarized in Table 3.1. Actual strain simulations for the In$_x$Ga$_{1-x}$N were performed by a thermoelastic method accommodated within ANSYS [11]. The piezoelectric polarization field was then calculated through Equation 3.3:

$$P_c^{PZ} = 2(e_{31} - e_{33}\frac{C_{13}}{C_{33}})\varepsilon_{xx} \tag{3.3}$$

where e_{ij} are the PZ constant and ϵ_{xx} is in-plane strain value calculated from FEM simulations. The electrostatic field induced by the polarization is

$$E = -\frac{1}{\varepsilon_r\varepsilon_0}P_c^{PZ} \tag{3.4}$$

where ε_r is the dielectric constant. The PZ constant e_{ij} was calculated by the E-first route preferred by Christmas et al. [22] through Equation 3.5:

$$e_{ij} = d_{ik}C_{kj} \tag{3.5}$$

The E-first method here means calculating e_{ij} of pure GaN and InN by Equation 3.5, and then using Equation 3.2 to get the e_{ij} values of different-indium-content materials. Finally, by introducing the piezoelectric potential into the one-dimensional Schrdinger equation [22] the optical transition energy of the QW was calculated. In this process, the inbuilt p-n junction field and carrier screening effect were neglected. In later discussion, the calculated emission shifts are compared with the measured QW emission shift directly, i.e. the Stokes shift is assumed to be constant. Furthermore, as the pillar sizes are in the micro-scale region, the alteration of QW transition energies due to lateral quantum confinement, which is considered in certain nano-pillars [6, 8], can be neglected.

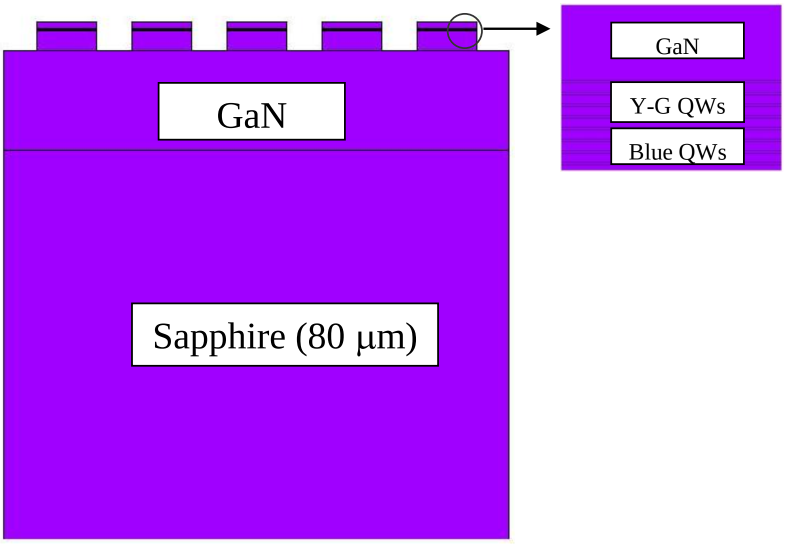

FIGURE 3.12: Illustration of the structure used in the FEM simulation for μ-pillars with a diameter of 16 μm.

Material	C_{11} (GPa)	C_{12} (GPa)	C_{13} (GPa)	C_{33} (GPa)	C_{44} (GPa)	a_0 (Å)	e_{31} (Cm^{-2})	e_{33} (Cm^{-2})
GaN	390	145	106	398	105	3.189	-0.53	0.89
Sapphire	490	165.4	113	490	145.4	4.758	N/A	N/A
$In_{0.10}Ga_{0.90}N$	373.3	142	104.6	380.6	99.3	3.225	-0.525	0.907
$In_{0.25}Ga_{0.75}N$	348.3	137.5	102.5	354.5	90.75	3.278	-0.5175	0.9325

TABLE 3.1: RT parameters used for different materials in FEM simulations and emission energy calculation. The C_{ij}, a_0 and e_{ij} for GaN and InN are cited from Ref. [21].

3.3.3 Results and discussion

Firstly, the distribution of simulated in-plane strain in the sapphire substrate ($\epsilon_{xx,sap}$, a component of the strain tensor) is shown in Figure 3.13. The lateral distance in the figure is measured from the pillar centre. As plotted, due to the residual strain in the GaN buffer layer, tensile strain exists in the sapphire substrate [20]. This strain keeps decreasing along the vertical direction from the interface between the GaN layer and the sapphire substrate. When the thickness is above 60 μm, the strain is close to zero. This result not only agrees well with the experimental results reported in Ref. [19], but also indicates the adopted sapphire thickness of 80 μm for this simulation is thick enough to achieve accurate results.

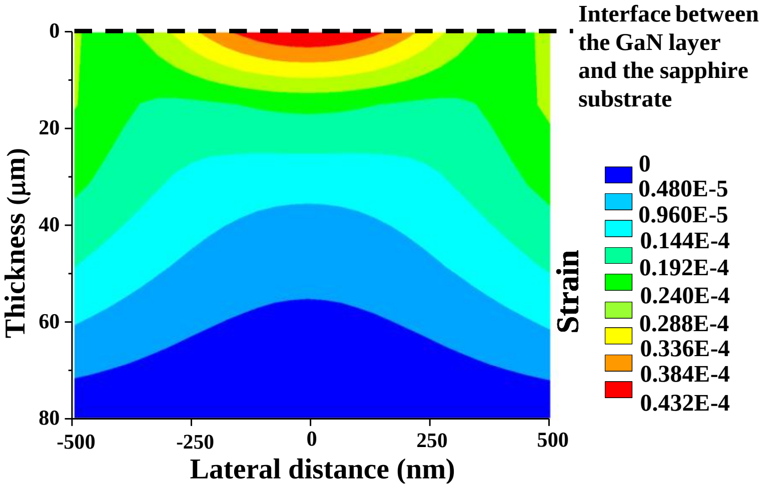

FIGURE 3.13: Simulated in-plane strain ($\epsilon_{xx,sap}$) distribution in the sapphire substrate.

Figure 3.14 illustrates the simulated in-plane compressive strain ($\epsilon_{xx,QW}$) distribution of (a) yellow-green and (b) blue QWs at the edge of a 16 μm-diameter pillar. The colour-coded range of the in-plane strain as per the key in the figure has been set to highlight the strain variations in different-indium-content QWs. The surrounding materials are shown in gray, as the strain in these regions is outside the colour-coded range. As plotted in Figure 3.14(a), the simulation reveals that $\epsilon_{xx,QW}$ is reduced up to 12.5 %, i.e. from -2.70×10^{-2} at the centre to -2.37×10^{-2} at the pillar edge for yellow-green QWs. This change in strain corresponds to an average blue-shift in the transition wavelength of 7.4 nm, which agrees well with the experimental result as shown in Figure 3.9. The simulation also confirms that the strain remains almost unchanged in the central 75 % area of the pillar. Compared with the initial strain in the as-grown yellow-green QWs (-2.72×10^{-2}), which is caused by the lattice mismatch and calculated from strain-free lattice constants, the maximum compressive strain in the pillar centre is also reduced. Thus, a blue-shift of the emission wavelength at the pillar centre relative to the as-grown wafer can be calculated as 1.3 nm. This blue-shift is defined as global blue-shift in later discussion. The calculated width of the blue-shifted ($\Delta\lambda \geq 3$ nm) region at the pillar edge is around 1 μm, which is slightly smaller than the average result observed in the CL maps. This may be due to the uncertain residual strain introduced in the GaN buffer layer. The in-plane compressive strain used in the simulation was -1.34×10^{-3} in the GaN buffer layer, which was interpolated from the experimental value reported in Ref. [20].

Although this strain is one order smaller than that in the QWs, it significantly influences the strain transfer and distribution in the whole pillar. Such influences have been confirmed by repeating the simulation with a series of different assumed strain values in the GaN buffer layer. While not increasing the magnitude of the blue-shift at the edge of the pillar, the lower the strain in the GaN buffer layer, the wider the blue-shift area. Furthermore, by reducing the strain in the GaN buffer layer, the global blue-shift of the pillar increases, giving better agreement with the experimental CL results. For the two lower $In_{0.10}Ga_{0.90}N$ QWs [Figure 3.14(b)], similar phenomena are observed. The $\epsilon_{xx,QW}$ is reduced up to 16.5 % at the pillar edge and the maximum strain at the pillar center is also slightly relaxed after the pillar formation. However, the corresponding blue-shift of the blue QWs emission is less than 2 nm on average, which is barely resolvable against the background fluctuation in CL maps. Therefore, the size effects of strain relaxation will mainly focus on the high-indium-content yellow-green QWs, which will be discussed in the next section.

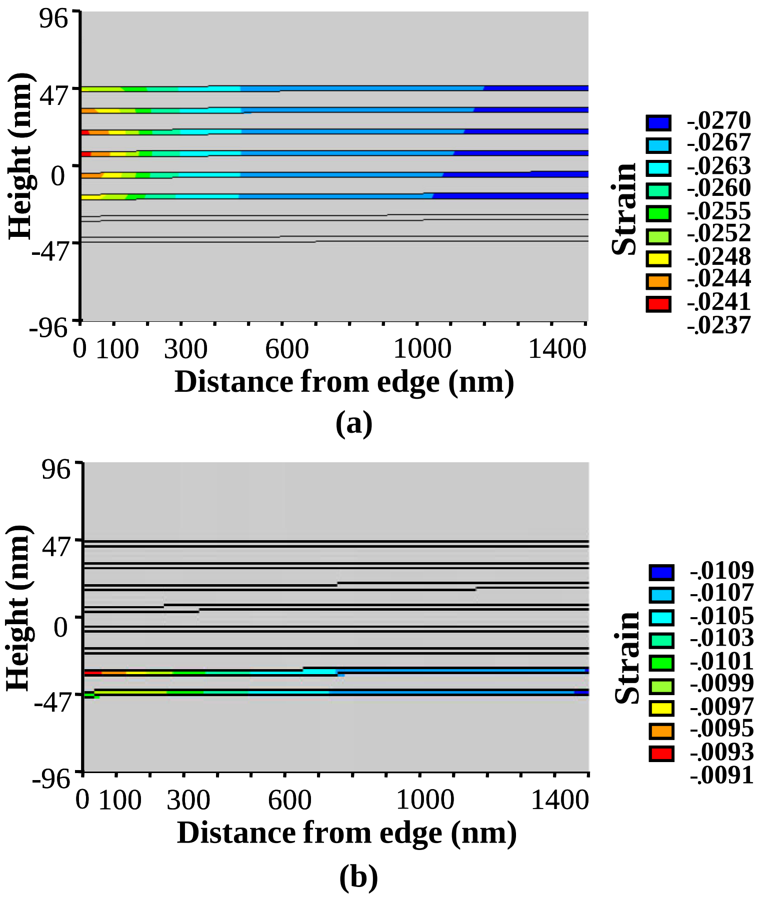

FIGURE 3.14: Simulated in-plane strain ($\epsilon_{xx,QW}$) distribution at the edge of (a) yellow-green and (b) blue QWs.

3.4 Size effect of strain relaxation in micro-pillars

As shown in section 3.2, high-spatial-resolution CL is a powerful technique for investigating the strain relaxation process in $\mathrm{In}_x\mathrm{Ga}_{1-x}\mathrm{N}$/GaN-based μ-pillars. Meanwhile, the strain simulation by FEM has also been carried out based on experimental results. To get further understanding of size effect of strain relaxation, such CL measurements and simulations were extended to a series of μ-pillars with diameters ranging from 2 to 150 μm.

Figure 3.15 summarizes the main information obtained through systematic experimental and simulation results on size effect of strain relaxation in high-indium-content yellow-green QWs. The black data points in Figure 3.15(a)-(d) show the measured maximum blue-shift at the pillar edge relative to the pillar centre [Figure 3.15(a)], the width of the blue-shift ring region (defined by $\Delta\lambda \geq 3$ nm, as above) [Figure 3.15(b)], the ratio of this blue-shift ring region to the whole pillar area [Figure 3.15(c)] and the global blue-shift observed at the pillar centre relative to a non-patterned wafer [Figure 3.15(d)] as a function of pillar diameter for the yellow-green QWs. The red data points in these figures are the corresponding simulation results. All measured data points plotted in Figure 3.15 were derived by averaging 10 line-scans across different pillar diameters, as previously illustrated in Figure 3.9. As plotted in Figure 3.15(a), the magnitude of the measured maximum shift decreases from 9.3 to 5.6 nm as the pillar diameter increases from 2 to 150 μm and becomes almost constant (around 6 nm) for pillar diameters in excess of 30 μm. In Figure 3.15(b), the width of the blue-shift ring region at the pillar edge is observed to reach a maximum value of 2.2 μm for a 20 μm-diameter μ-pillar. However, as shown in Figure 3.15(c), the proportion of this area decreases continuously as the pillar diameter increases, from 86 % at 2 μm to only 3 % at 150 μm. These results confirmed that for the smaller μ-pillars studied, the majority of the volume is significantly strain relaxed, and there is a strong gradient in the strain relaxation towards the edge. Figure 3.15(d) shows that the global blue-shift of the emission wavelength decreases with increasing pillar diameter, starting from a value of 8.2 nm for the μ-pillar with a diameter of 2 μm. It can be seen that over 30 μm, the decrease of this global blue-shift of the emission wavelength becomes slow and a zero global blue-shift is observed for the largest pillar. Clearly, these CL measurements confirm that the strain relaxation becomes dominant when the pillar size is less than 30 μm. It is also notable that by using high-spatial-resolution CL technique, a blue-shift ring region of the yellow-green

QW emission at the edge of the pillar was observed even for the μ-pillars with a diameter larger than 10 μm. Such a blue-shift ring region has not been observed and reported before for such large $In_xGa_{1-x}N/GaN$-based pillars.

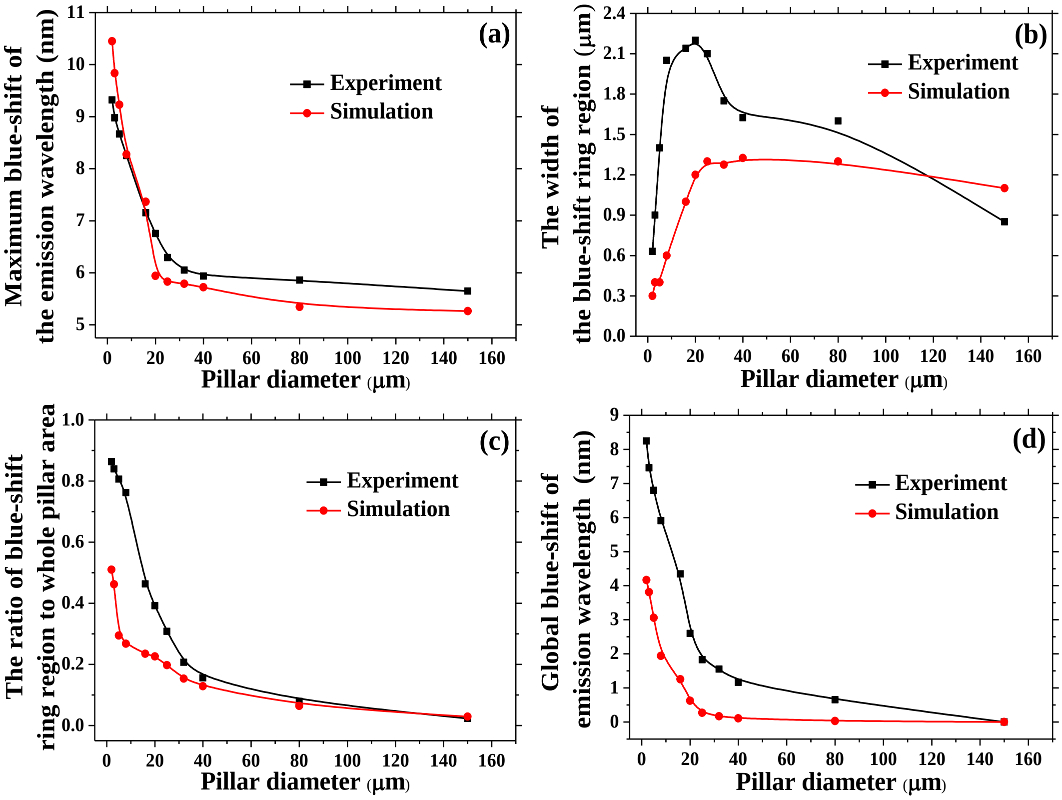

FIGURE 3.15: Experimental and simulated values for spectral shift parameters as a function of pillar diameter: (a) the maximum blue-shift of the emission wavelength at the pillar edge relative to pillar centre; (b) the width of the blue-shift ring region; (c) the ratio of the blue-shift ring region to whole pillar area; (d) the global blue-shift of the emission wavelength at the pillar centre.

The red points in Figure 3.15 group show the simulated values for the various parameters discussed above. For these simulations, the small contribution of strain-dependent changes in Stokes shift is not considered [5, 23]. Clearly, the variation trends of the experimental and simulated results are almost the same. The maximum blue-shift values measured agree very well with the simulation results for the smaller pillars, while only a slight difference is observed when the pillar diameter is larger than 16 μm [Figure 3.15(a)]. This suggests that the data collection and processing methods aimed at achieving high spatial resolution have successfully met the challenges of wavelength shift measurements on the smaller pillars imposed by intrinsic QW inhomogeneities and the strain gradients close to the pillar sidewalls. Nevertheless, some differences between the measured and simulated values are observed. A possible explanation for these differences is that the fill factors are slightly different for the fabricated μ-pillars arrays and for the simulation model. The fit for the smaller μ-pillars would be improved by performing the simulations with smaller fill factors, which would give larger global strain relaxation and wider blue-shifted regions. Another relevant factor which influences the simulation results is the strain value assumed in the GaN buffer layer immediately below the first blue QW, as pointed out in the last section.

3.5 Summary

The strain relaxation processes in μ-pillars with diameters ranging from 2 to 150 μm have been investigated by a combination of CL measurements and FEM simulations aimed to provide practical guidance for design of III-nitride micro-/nano-LEDs. The previous research on the strain effect of micro- and nanostructures was reviewed first. Two main obstacles in previous experimental and simulation processes have been identified and pointed out, i.e. the low spatial resolution of PL measurements could not provide the detail observation on the strain relaxation process especially in small In$_x$Ga$_{1-x}$N/GaN-based micro-/nano-pillars and the accuracy of strain simulation is limited by the model structure used before.

In our work, in order to overcome the limitations of PL, the CL techniques was used to record the spatial distribution of the emission wavelength in μ-pillars with two kinds of different-indium-content In$_x$Ga$_{1-x}$N QWs so as to investigate the strain relaxation process. The results demonstrate that the strain relaxation in these μ-pillars is strongly spatial localized and indium content dependent. The strain relaxation at the pillar centre and edge is dramatically different, resulting in two blue-shifts. CL maps also show there is a broad ring-shaped strain relaxation region at the pillar edge of all the investigated pillars. The systematic blue-shift in low-indium-content QWs is indistinguishable from the wavelength fluctuation caused by the indium content variation. On the simulation, the models used took account not only of the strain induced from the lattice mismatch in the QWs but also the residual strain in the GaN buffer layer. Thus, in our model, both compressive strain in QWs and whole wafer bending are considered at the same time. By these improvements, the calculated blue-shifts agree well with the values obtained by CL measurements. The size effect of strain relaxation in In$_x$Ga$_{1-x}$N/GaN-based μ-pillars has also been investigated in detail. The maximum blue-shift, the global blue-shift and the ratio of the blue-shift ring region to whole pillar area show dramatic increase when the pillar size is below 30 μm. These results give an insight into the strain relaxation mechanism in these μ-pillars and also provide important guidelines for designing high-efficiency μ-LEDs.

References

[1] Y. Kawakami, S. Suzuki, A. Kaneta, M. Funato, A. Kikuchi, and K. Kishino. Origin of high oscillator strength in green-emitting InGaN/ GaN nanocolumns. *Applied Physics Letters*, 89:163124, 2006.

[2] L. Dai, B. Zhang, J.Y. Lin, and H.X. Jiang. Comparison of optical transitions in InGaN quantum well structures and microdisks. *Journal of Applied Physics*, 89:4951, 2001.

[3] H.W. Choi, C.W. Jeon, M.D. Dawson, P.R. Edwards, R.W. Martin, and S. Tripathy. Mechanism of enhanced light output efficiency in InGaN-based microlight emitting diodes. *Journal of Applied Physics*, 93:5978, 2003.

[4] T.H. Hsueh, H.W. Huang, C.C. Kao, Y.H. Chang, M.C. Ou-Yang, H.C. Kuo, and S.C. Wang. Characterization of InGaN/GaN multiple quantum well nanorods fabricated by plasma etching with self-assembled nickel metal nanomasks. *Japanese Journal of Applied Physics*, 44(4B):2661–2663, 2005.

[5] S. Keller, C. Schaake, N.A. Fichtenbaum, C.J. Neufeld, Y. Wu, K. McGroddy, A. David, S.P. DenBaars, C. Weisbuch, J.S. Speck, and U.K. Mishra. Optical and structural properties of GaN nanopillar and nanostripe arrays with embedded InGaN/ GaN multi-quantum wells. *Journal of Applied Physics*, 100:054314, 2006.

[6] H.S. Chen, D.M. Yeh, Y.C. Lu, C.Y. Chen, C.F. Huang, T.Y. Tang, C.C. Yang, C.S. Wu, and C.D. Chen. Strain relaxation and quantum confinement in InGaN/GaN nanoposts. *Nanotechnology*, 17:1454, 2006.

[7] H.J. Chang, Y.P. Hsieh, T.T. Chen, Y.F. Chen, C.T. Liang, T.Y. Lin, S.C. Tseng, and L.C. Chen. Strong luminescence from strain relaxed InGaN/GaN nanotips for highly efficient light emitters. *Optics Express*, 15(15):9357–9365, 2007.

[8] P. Yu, C.H. Chiu, Y.R. Wu, H.H. Yen, J.R. Chen, C.C. Kao, H.W. Yang, H.C. Kuo, T.C. Lu, W.Y. Yeh, and S.C. Wang. Strain relaxation induced microphotoluminescence characteristics of a single InGaN-based nanopillar fabricated by focused ion beam milling. *Applied Physics Letters*, 93:081110, 2008.

[9] Y. Kawakami, A. Kaneta, L. Su, Y. Zhu, K. Okamoto, M. Funato, A. Kikuchi, and K. Kishino. Optical properties of InGaN/GaN nanopillars fabricated by postgrowth chemically assisted ion beam etching. *Journal of Applied Physics*, 107(2):023522, 2010.

[10] V. Ramesh, A. Kikuchi, K. Kishino, M. Funato, and Y. Kawakami. Strain relaxation effect by nanotexturing InGaN/GaN multiple quantum well. *Journal of Applied Physics*, 107(11): 114303, 2010.

[11] T. Benabbas, P. Francois, Y. Androussi, and A. Lefebvre. Stress relaxation in highly strained InAs/GaAs structures as studied by finite element analysis and transmission electron microscopy. *Journal of Applied Physics*, 80(5):2763–2767, 1996.

[12] J. Ristić, C. Rivera, E. Calleja, S. Fernández-Garrido, M. Povoloskyi, and A. Di Carlo. Carrier-confinement effects in nanocolumnar GaN/$Al_xGa_{1-x}N$ quantum disks grown by molecular-beam epitaxy. *Physical Review B*, 72(8):085330, 2005.

[13] H.X. Jiang, S.X. Jin, J. Li, J. Shakya, and J.Y. Lin. III-nitride blue microdisplays. *Applied Physics Letters*, 78:1303, 2001.

[14] H.W. Choi, C.W. Jeon, and M.D. Dawson. High-resolution 128 × 96 nitride microdisplay. *Electron Device Letters, IEEE*, 25(5):277–279, 2004.

[15] Z. Gong, H.X. Zhang, E. Gu, C. Griffin, M.D. Dawson, V. Poher, G. Kennedy, P.M.W. French, and M.A.A. Neil. Matrix-addressable micropixellated InGaN light-emitting diodes with uniform emission and increased light output. *Electron Devices, IEEE Transactions on*, 54(10):2650–2658, 2007.

[16] N. Otsuji, K. Fujiwara, and J.K. Sheu. Electroluminescence efficiency of blue InGaN/GaN quantum-well diodes with and without an n-InGaN electron reservoir layer. *Journal of Applied Physics*, 100:113105, 2006.

[17] X. Ni, X. Li, J. Lee, S. Liu, V. Avrutin, Ü. Özgür, H. Morkoç, A. Matulionis, T. Paskova, G. Mulholland, and K.R. Evans. InGaN staircase electron injector for reduction of electron overflow in InGaN light emitting diodes. *Applied Physics Letters*, 97:031110, 2010.

[18] R. Qiu, H. Lu, D. Chen, R. Zhang, and Y. Zheng. Optimization of inductively coupled plasma deep etching of GaN and etching damage analysis. *Applied Surface Science*, 257(7): 2700–2706, 2011.

[19] Y. Jang, W.R. Kim, D.H. Jang, J.I. Shim, and D.S. Shin. Analysis of the stress distribution in the nonuniformly bent GaN thin film grown on a sapphire substrate. *Journal of Applied Physics*, 107(11):113537, 2010.

[20] D.C. Reynolds, D.C. Look, B. Jogai, J.E. Hoelscher, R.E. Sherriff, and R.J. Molnar. Strain variation with sample thickness in GaN grown by hydride vapor phase epitaxy. *Journal of Applied Physics*, 88:1460, 2000.

[21] I. Vurgaftman and J.R. Meyer. Band parameters for nitrogen-containing semiconductors. *Journal of Applied Physics*, 94:3675, 2003.

[22] U.M.E. Christmas, A.D. Andreev, and D.A. Faux. Calculation of electric field and optical transitions in InGaN/GaN quantum wells. *Journal of Applied Physics*, 98(7):073522, 2005.

[23] R.W. Martin, P.G. Middleton, K.P. ODonnell, and W. Van der Stricht. Exciton localization and the Stokes shift in InGaN epilayers. *Applied Physics Letters*, 74:263, 1999.

Chapter 4

$In_{0.40}Ga_{0.60}N$/GaN-based colour-tunable micro-light emitting diodes

The work presented in this chapter focuses on III-nitride colour-tunable light emitting diodes (LEDs), especially on micro-LEDs (μ-LEDs). Previous research has demonstrated some different techniques to develop multi-colour displays utilizing III-nitride LEDs, as summarized in section 4.1. Compared with these techniques, the devices reported here, which show a colour-tunable emission, are simply fabricated from an amber $In_{0.40}Ga_{0.60}N$/GaN-based LED wafer grown by pre-strain technology. To deeply understand the optical properties of the LED wafer with high-indium-content quantum wells (QWs), the temperature-dependent photoluminescence and cathodoluminescence measurements were first carried out on this wafer as shown in section 4.2. The μ-LEDs were then fabricated from this wafer and are characterized in section 4.3. It is found the dominant emission peak of these devices shows a pronounced blue-shift with increasing current, which leads to a great change of the emission colour from amber to green. Thus, these colour-tunable μ-LEDs offer a range of potential applications such as multi-colour displays. Compared with broad-area LEDs, further experimental results also indicate the colour tunability is enhanced for μ-LEDs. Finally, the mechanisms of this colour tunability are investigated through pulsed electroluminescence measurements.

4.1 Colour displays based on III-nitride light emitting diodes

Great success has been achieved in inorganic light emitting diodes (LEDs) based on III-nitride materials in the past twenty years, especially in the blue and green emission regions [1]. Due to the unique properties of III-nitride materials such as mechanical robustness and long lifetime, III-nitride LEDs are considered ideal devices for different applications at extreme conditions such as high or low temperatures. Thus, III-nitride LEDs have been widely used as light sources for colour displays [2–4]. Compared with the liquid-crystal displays and organic LEDs, displays made by III-nitride LEDs provide superior performance such as higher brightness, space and power saving, and contrast ratio improvement.

However, conventional inorganic LEDs emit only a single colour that is determined by the thickness and composition of quantum wells (QWs) in the LED structure. With the purpose of achieving a multi-colour display, some different approaches have been demonstrated. The most direct method is to mechanically package together LEDs with different colours to form a multi-colour unit as reported in Ref. [5]. Normally, III-nitride LEDs are used as blue and green emitters in this method. Since the optical power of III-nitride red LEDs is relatively low, $(Al_xGa_{1-x})_{0.52}In_{0.48}P$ LEDs are commonly used as the source of red light. However, the different substrates of these LEDs lead to a complicated packaging process and a high cost. On the other hand, this method becomes increasingly difficult when reducing the size of LEDs and increasing unit density. Another common approach to achieve multi-colour displays is through luminescence down conversion, in which a III-nitride ultraviolet (UV) or blue LED pumps one or more colour converters, such as phosphor, to generate secondary (longer-wavelength) emissions [6]. In our previous work, some other colour converters, such as organic polymer and semiconductor nanocrystals, were also integrated with micro-LEDs (μ-LEDs) to achieve colour down conversion [7, 8]. Figure 4.1 shows a typical result of colour down conversion achieved in our group. As shown, a blue emission (right image) is achieved by the combination of a UV $Al_xGa_{1-x}N$ μ-LED (left image) and an organic semiconductor (truxene oligofluorene) through the inkjet printing technique [8]. However, issues of the converter degradation presently lead to a low reliability of these hybrid devices, which is the main limitation of this colour conversion methodology.

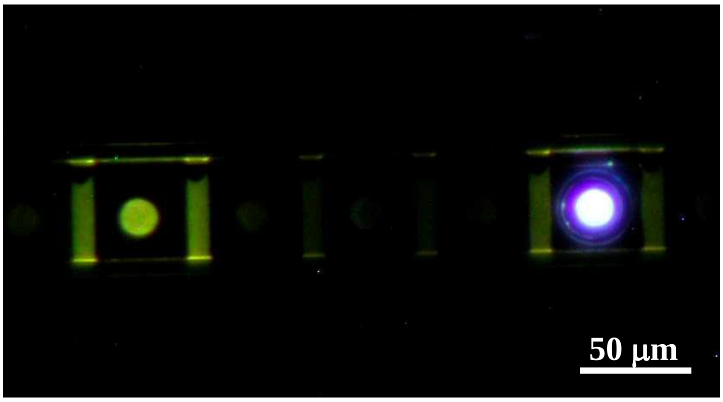

Figure 4.1: Optical images of two μ-LEDs: a bare UV μ-LED (left) and organic semiconductor integrated on the device (right). After [8].

Recently, the development of a single III-nitride LED with tunable colour emission has been explored and reported. By controlling the growth temperature and thickness of the QWs, indium-rich quantum dots or phase separation regions can be achieved in conventional (0001) blue $In_xGa_{1-x}N$ QWs [9, 10], leading to another longer-wavelength green or amber peak in these blue QWs. At different operating currents, the dominant emission is changed for the LEDs fabricated from these wafers, which leads to the tunable colour emission. However, due to the low repeatability of these growth processes, their application is restricted. Most recently, a micro-facet GaN LED structure has been obtained by selective growth through a patterned SiO_2 growth mask on different substrates [11, 12]. Using this growth methodology, wurtzite GaN nanorods with different facets can be obtained. It is also found, under the same growth conditions, that the indium contents of $In_xGa_{1-x}N$ QWs deposited on the different facets of this GaN nanorod are very different [12]. This leads to different emission peaks of these QWs. Figure 4.2(a) shows the transmission electron microscopy (TEM) image of a GaN nanorod with $In_xGa_{1-x}N$ QWs grown on two different facets as (0001) and $\{100\}$ planes [12]. The high-magnification TEM images of QWs grown on (0001) and $\{100\}$ planes of this GaN nanorod are shown in Figure 4.2(b) and (c), respectively. Figure 4.2(d) illustrates the energy dispersive X-ray (EDX) line profiles of indium content in these QWs. The indium contents are estimated to be 0.60 and 0.15 for the QWs deposited on (0001) and $\{100\}$ planes, which corresponds to the red and blue emission peaks respectively. At different operating currents, these spatially distributed QWs lead to a changed emission colour of LEDs fabricated from this wafer. However, this technique requires a complicated sample preparation process

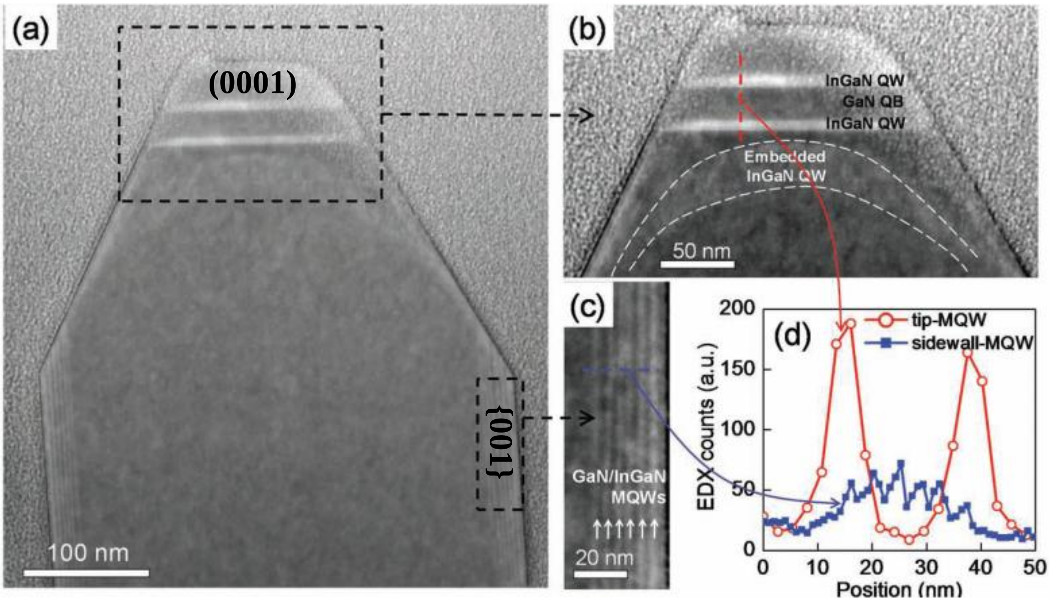

FIGURE 4.2: (a) Low-magnification scanning TEM image of $In_xGa_{1-x}N$/GaN nanorod QWs deposited on the (0001) and {100} planes of GaN; high-magnification scanning TEM images of QWs formed on (b) (0001) and (c) {100} planes of a GaN nanorod; (d) EDX lines profiles of the indium content of QWs on (0001) and {100} planes. After [12].

for the micro-facet structure growth which limits its further application.

In our work, we demonstrate a simpler way to obtain the colour-tunable LEDs from an amber $In_{0.40}Ga_{0.60}N$/GaN-based LED wafer. Firstly, the optical properties of this high-indium-content LED wafer are studied. Then, the μ-LEDs are fabricated and characterized. These devices show an obvious change of the emission colour from amber to green at different operating currents. It is also found that this colour tunability is enhanced for μ-LEDs compared with broad-area devices. The mechanisms of this colour tunability are further investigated.

4.2 Optical properties of amber $In_{0.40}Ga_{0.60}N$/GaN-based light emitting diode wafer

The amber $In_{0.40}Ga_{0.60}N$/GaN-based LED wafer used in this work (supplied by Peking University, China) was grown on a c-plane (0001) sapphire substrate by metal-organic chemical vapour deposition. The epitaxial structure of this amber LED wafer is shown in Figure 4.3. It consisted of a 1.5 μm-thick GaN buffer

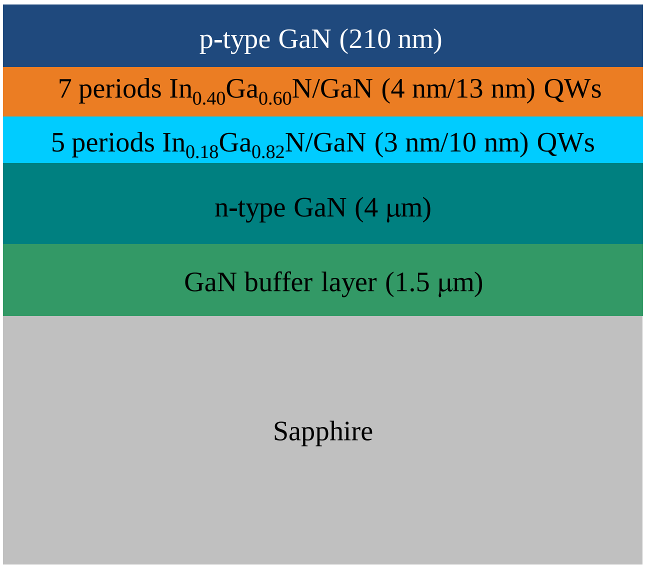

FIGURE 4.3: Epitaxial structure of an amber $In_{0.40}Ga_{0.60}N$/GaN-based LED wafer.

layer; a 4 μm-thick n-doped GaN layer; five periods $In_{0.18}Ga_{0.82}N$ (3 nm)/GaN (10 nm) QWs with an emission wavelength of 460 nm; seven periods $In_{0.40}Ga_{0.60}N$ (4 nm)/GaN (13 nm) QWs emitting at 620 nm and finally a 210 nm-thick p-type GaN layer. The first five low-indium-content QWs serve as an electron reservoir layer (ERL) [13]. The functions of the ERL have been described in subsection 3.2.1. Furthermore, these low-indium-content QWs can also enhance the indium incorporation into the upper QWs to achieve a longer wavelength by partial strain relaxation during growth [14]. This amber LED wafer was first studied by temperature-dependent photoluminescence (T-PL). The setup of the facility used has been introduced in detail in subsection 2.2.2. The amber LED wafer was excited by a continuous-wave 405 nm wavelength laser diode. The excitation power was around 40 mW at the top surface of the wafer, and the diameter of the excitation spot was about 5 μm. The wafer temperature was controlled from 18 to 300 K.

The temperature-dependent PL spectra for this amber LED wafer are plotted in Figure 4.4. Since upper high-indium-content amber QWs re-absorb the short-wavelength light and the experimental setup includes a longpass filter to block the light with the wavelength less than 470 nm, the blue emission from $In_{0.18}Ga_{0.82}N$ QWs is barely distinguished in these spectra. For amber QWs, the lowest temperature spectrum (T=18 K) presents a PL emission peaking at 618 nm with a full width at half maximum (FWHM) around 140 meV. Such a broad linewidth

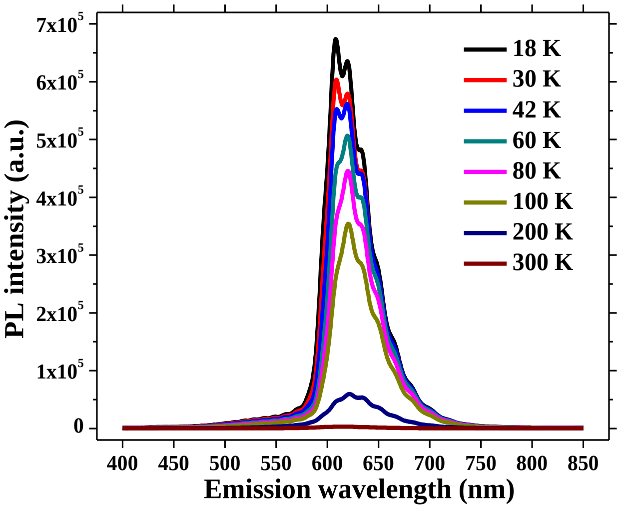

FIGURE 4.4: PL spectra at different temperatures for an amber $In_{0.40}Ga_{0.60}N$/GaN-based LED wafer.

makes it possible to observe the imposition of a Fabry-Perot interference pattern related to the GaN barrier thickness. With increasing temperature, the PL intensity decreases greatly due to thermalized nonradiative recombination processes [15].

The thermal evolution of these PL spectra was first characterized by the spectral shift and FWHM variation, as shown in Figure 4.5(a). Both peak position and FWHM plotted here were obtained through a closely Gaussian fitting process. As shown, when the temperature increases from 18 to 150 K, a red-shift of the PL peak for amber QWs is observed, followed by a blue-shift above 150 K. This S-shaped peak shift is normally observed for $In_xGa_{1-x}N$ QWs [16, 17]. This behaviour can be well explained by the inhomogeneous bandgap of amber QWs, which is caused by the nonuniform indium distribution in $In_xGa_{1-x}N$ as introduced in section 1.4. As demonstrated in Ref. [18], for these amber QWs, the photogenerated carriers are distributed randomly in QWs at the low temperature. These carriers do not have enough energy to move to the lowest energy state (high-indium-content regions). As temperature increases (18-150 K), the thermally activated carriers are able to occupy the lowest energy states, which results in a red-shift of emission peak and a narrowing of FWHM. Higher temperature (150-300 K) supplies enough energy for the carriers to overcome the energy difference between different indium-content regions and populate in higher energy states (low-indium-content regions), leading to a blue-shift of emission peak while the FWHM increases. In order to get direct evidence to support this explanation, typical PL spectra at different temperatures

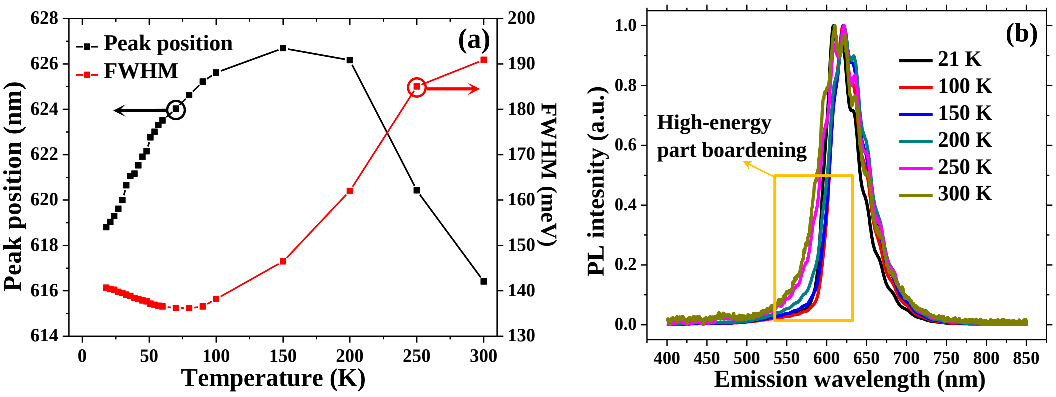

FIGURE 4.5: (a) Peak position and corresponded FWHM of amber QWs as a function of temperature; (b) normalized PL spectra at different temperatures to highlight a high-energy part broadening as labelled by a rectangle.

are normalized and plotted in Figure 4.5(b). It can be found that the great blueshift of the emission peak and increase of the FWHM are mainly caused by a high-energy (short-wavelength) part broadening of the PL spectra above 150 K, which is highlighted by a rectangle in the figure. This rapid growth on the high-energy side of the PL spectra with increasing temperature supports the above explanation and indicates that bandgap inhomogeneity does exist in these amber QWs.

The evolution of the integrated PL intensities as a function of temperature, normalized to the highest intensity at 18 K, is shown in Figure 4.6. By assuming no nonradiative recombination occurs at the lowest temperature, the luminescence efficiency at room temperature is estimated as around 1 % for amber QWs. Furthermore, since the emission peak of amber QWs presents an S-shaped characteristic as discussed, it is reasonable to consider the thermal quenching of the PL intensity, $I(T)$, is not only governed by the thermally activated nonradiative recombination process but also influenced by the carrier confinement in different indium-content regions. Thus, the data plotted in Figure 4.6 is then fitted by Equation 4.1 [19]:

$$I(T) = \frac{I(T=0\ K)}{(1+a_1 e^{-E_a/k_BT})(1+a_2 e^{-E_{con}/k_BT})}, \tag{4.1}$$

where E_a is the activation energy of the nonradiative recombination process, E_{con} is the average confinement energy between different indium-content regions, k_BT is the thermal energy, and a_1 and a_2 are fitting constants. The red curve in Figure

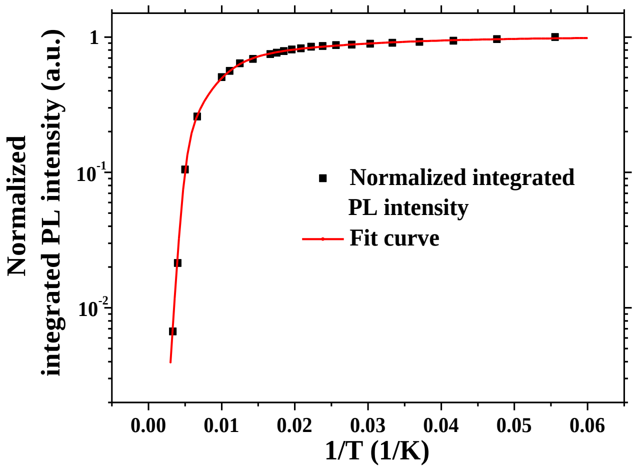

FIGURE 4.6: Thermal evolution of integrated PL intensities. Squares: experimental data; solid line: fitting result according to Equation 4.1.

4.6 shows the best fitting result with the values of E_a = 10 meV and E_{con} = 190 meV respectively. The fitting process also indicates that E_a (10 meV) plays an important role when the temperature is below 150 K. Above 150 K, E_{con} (190 meV) is dominant and its value is considered as the average energy required for carriers to be activated from high-indium-content regions to low-indium-content regions in amber QWs. Furthermore, the fitted value of E_{con} for these amber QWs is much higher than those reported for blue and green $In_xGa_{1-x}N$ QWs [16, 19]. This result indicates that the bandgap inhomogeneity is much pronounced in amber QWs.

In order to gain a direct insight into the indium distribution in amber QWs, a cathodoluminescence (CL) scan was performed on this wafer. The measurement conditions are the same as those we used in subsection 3.2.1, and the scanning step size is 50 nm in the x-axis and 70 nm in the y-axis. The mean spectrum of a CL scan over a 10 × 14 μm^2 area is shown in Figure 4.7. As plotted, two distinct emission peaks, the dominant amber one and an additional green emission, are observed in this CL spectrum. These two emission peaks are direct evidence for the bandgap inhomogeneity in amber QWs as concluded from the T-PL measurement. The observation of the green emission is mainly due to the low beam reaction volume (~100 nm) of CL compared with the excitation volume of PL which is mainly decided by the spot size of the incident light. By nonlinear least-squares peak fitting, the CL maps of emission intensity for amber and green peaks are extracted and shown in Figure 4.8(a) and (b). There is no clear correlation of intensity distribution between these two maps, which illustrates the random

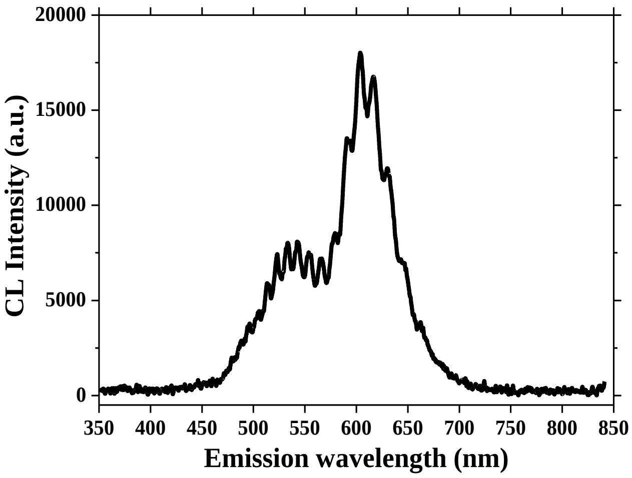

FIGURE 4.7: Mean spectrum of a CL scan on an amber $In_{0.40}Ga_{0.60}N$/GaN-based LED wafer over a 10 × 14 μm^2 area.

indium distribution in amber QWs. The blue emission from $In_{0.18}Ga_{0.82}N$ QWs is still absent in this CL spectrum similar with PL results. In section 3.2, a CL scan was shown as performed on the micro-pillars fabricated from a yellow-green $In_{0.25}Ga_{0.75}N$/GaN-based LED wafer with similar QWs structures as this amber one, and a blue emission from deeper low-indium-content QWs can be clearly observed for that wafer. This difference is probably caused by two reasons. Firstly, as shown in Figure 4.7, the additional green emission for this amber LED wafer is quite broad covering from 460 nm, which may lead to the blue emission being indistinguishable from it. Secondly, unlike the yellow-green wafer, the top p-type GaN layer of this amber LED wafer was not thinned down before the CL measurement in order to retain the same structure with PL measurements. At a low accelerating voltage (5 kV) which is same as the one used for previous CL measurements in section 3.2, the electron beam may not be able to be injected into the low-indium-content QWs below the amber ones in this measurement. This will result in an absence of blue emission from this amber LED wafer in CL results as well.

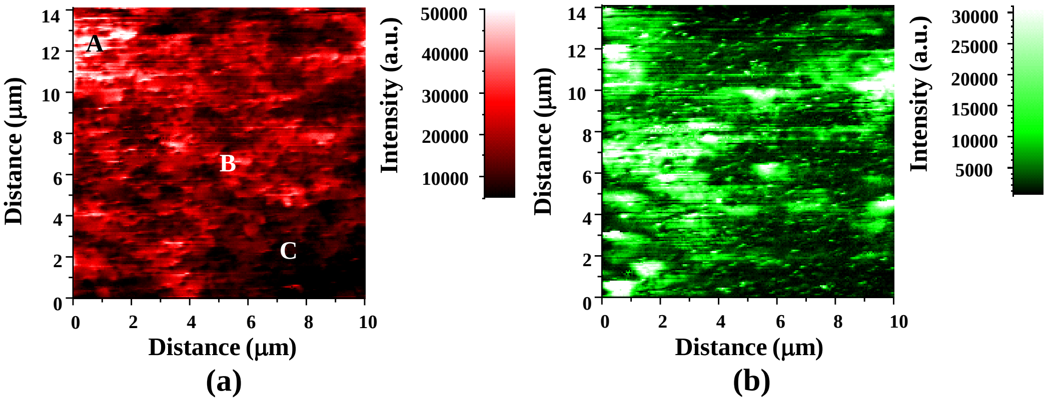

FIGURE 4.8: Spatially resolved CL maps of emission intensities for (a) amber and (b) green peaks.

Besides the overall bandgap inhomogeneity as discussed above, the influence of small indium fluctuations for each individual emission peak was also investigated based on CL results. As shown in Figure 4.8, the CL map for each peak shows the intensity inhomogeneity within the micron scale. Three typical CL spectra from different intensity regions as labelled in Figure 4.8(a) are plotted in Figure 4.9. As introduced in subsection 2.2.1, our CL measurement records the full emission spectrum at each scanning point, and the CL maps with different information are further manipulated from this dataset as a function of position. Thus, the spectra plotted in Figure 4.9 contain both amber and green emission peaks. As shown in this figure, this clearly demonstrates that the CL intensity is higher in the region with a shorter emission wavelength (low indium content) for both peaks. Further study also demonstrates that this correlation is more pronounced for the dominant amber peak. Previous researches on the UV-to-blue $In_xGa_{1-x}N$ QWs have indicated the high emission intensity is normally accompanied with a longer emission wavelength (high indium content) in PL and/or CL measurements, which is opposite to the results observed here. It appears that the indium-rich regions may no longer act as effective radiative recombination centres when the indium content is above a critical value. This phenomenon can be qualitatively explained by the contribution of a localized large internal electric field in these indium-rich regions. As introduced in section 1.4, since the internal electrical field resulting from the piezoelectric polarization effect directly depends on the lattice mismatch, it increases with increasing indium content. Although high indium content supplies an additional energy barrier preventing the transportation of carriers to nonradiative recombination centres, it also leads to a localized large internal electric field on the

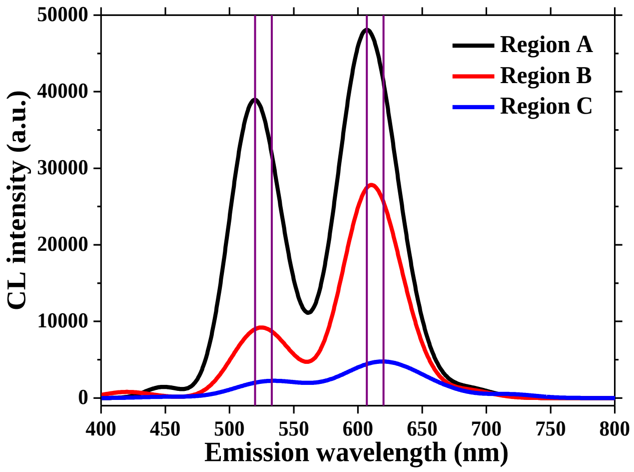

FIGURE 4.9: CL spectra extracted from regions with different emission intensities. These regions are labelled as A, B and C in Figure 4.8(a).

micron scale and, thus, a longer radiative recombination lifetime. When this effect is dominant, the emission intensity will be lower. This localized internal electric field may also increase the delocalization probability of carriers due to their fast diffusion [20], which leads to similar results as those observed. Another possible reason of this abnormal correlation between the intensity and the emission peak can be related to the additional defects generated in indium-rich regions to relax the large compressive strain between $In_xGa_{1-x}N$ and GaN.

4.3 Colour-tunable micro-light emitting diodes

4.3.1 Device fabrication and general performance

The μ-LEDs consisted of an array of 10 × 10 LED elements with flip-chip configurations were fabricated from this amber LED wafer. Each disk-shaped μ-LED mesa structure had a diameter of 40 μm on a 100 μm pitch. The mesa structure was first etched by Cl_2-based inductively coupled plasma down to the n-type GaN layer. After surface cleaning by a dilute HCl solution, a Ni/Au (10 nm/20 nm) metal bilayer was evaporated on the p-type GaN surface and thermally annealed in an air ambient at 500 °C to form a semi-transparent metal contact to p-type GaN. The metallization on the n-type GaN was formed by depositing a Ti/Au (50 nm/200 nm) metal bilayer, which filled the area between each LED element and enabled an improved current spreading. Then, a 300 nm-thick SiO_2 layer was

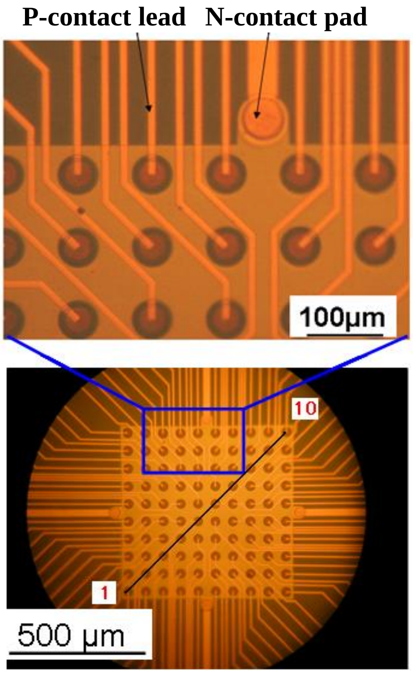

Figure 4.10: Top-view optical images of a 10 × 10 μ-LED array fabricated from an amber $In_{0.40}Ga_{0.60}N$/GaN-based LED wafer.

deposited by plasma-enhanced chemical vapour deposition to isolate each LED element. After selectively removing SiO_2 on top of each element, another Ti/Au metal bilayer was deposited on top of the oxidized Ni/Au bilayer as a reflector. This bilayer also connects each LED element so as to individually address them. The top-view optical images of this μ-LED array are shown in Figure 4.10. The electrical performance of the μ-LEDs was measured by a semiconductor analyzer (HP 4155). The optical power of the devices under direct-current (DC) conditions was measured using a Si detector placed at close proximity to the polished sapphire substrate. The electroluminescence (EL) spectra were collected with a spectrometer and charge coupled device (CCD) detection system. All the measurements were performed at room temperature.

Figure 4.11(a) shows the typical current-voltage (I-V) characteristic of a μ-LED fabricated from the amber LED wafer. For this device, the turn-on voltage at 5 mA is 6.2 V and the fitted series resistance is around 175 Ω. Both of these values are higher than those obtained from an equivalent LED fabricated from a commercial blue $In_xGa_{1-x}N$/GaN-based LED wafer, which may be due to the poorer crystalline quality of this high-indium-content material. The compressive strain coming from the lattice mismatch between $In_xGa_{1-x}N$ and GaN rises as the indium content increases. This strain induces more defects such as dislocations,

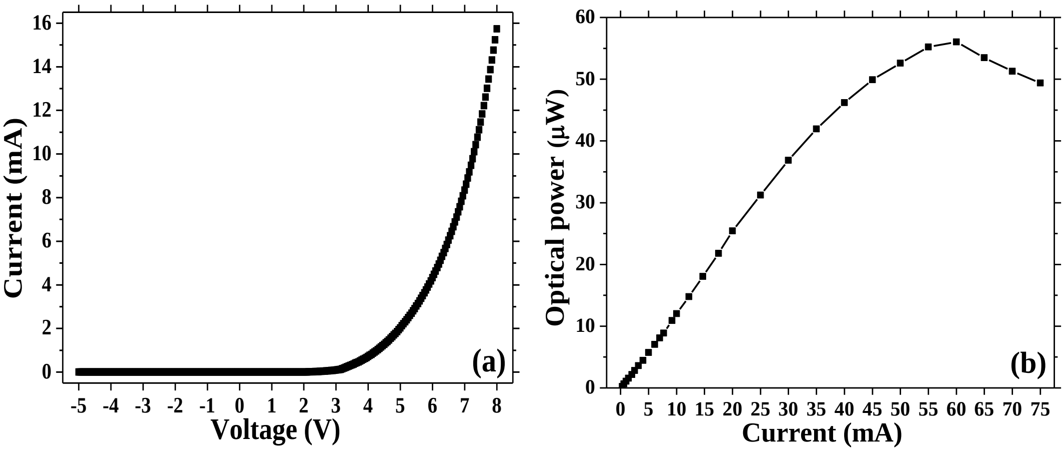

FIGURE 4.11: (a) I-V characteristic and (b) optical power of a μ-LED from a 10×10 μ-LED array fabricated from an amber $In_{0.40}Ga_{0.60}N$/GaN-based LED wafer. Note that the output spectrum of this device is shifting and broadening as current is increased in (b).

and results in the lower material quality. Furthermore, this compressive strain also generates a larger internal electric field which leads to pronounced quantum-confined Stark effect (QCSE) in QWs. As discussed in section 1.4, although longer emission wavelength can be achieved due to the bandgap narrowing caused by QCSE, the low internal quantum efficiency (around 1 % in this wafer as shown in the last section) results in the weak optical power as shown in Figure 4.11(b).

The normalized EL spectra of the μ-LED at different operating currents are plotted in Figure 4.12. At a low operating current, a dominant emission peak located at around 610 nm is observed, which is decorated with a low intensity shoulder in the green region. As previously discussed, this green shoulder comes from low-indium-content regions in the amber QWs. As operating current increases, this green shoulder is barely distinguished due to the increased FWHM and blue-shift of the dominant emission peak. As labelled by the gray points, the dominant emission peak shows a continuous blue-shift, even at higher operating currents when the self-heating effect is much pronounced. On the other hand, the blue emission, which is absent in both PL and CL measurements, shows a very pronounced intensity in these EL spectra, being maximized at a mid-range current. This blue emission is believed to come from the carrier recombination in $In_{0.18}Ga_{0.82}N$ QWs. Due to the small migration distance of holes in III-nitride materials, previous research has demonstrated that only the QW nearest the p-type GaN layer emits light in blue multiple QWs LEDs under electrical pumping [21, 22]. The observation

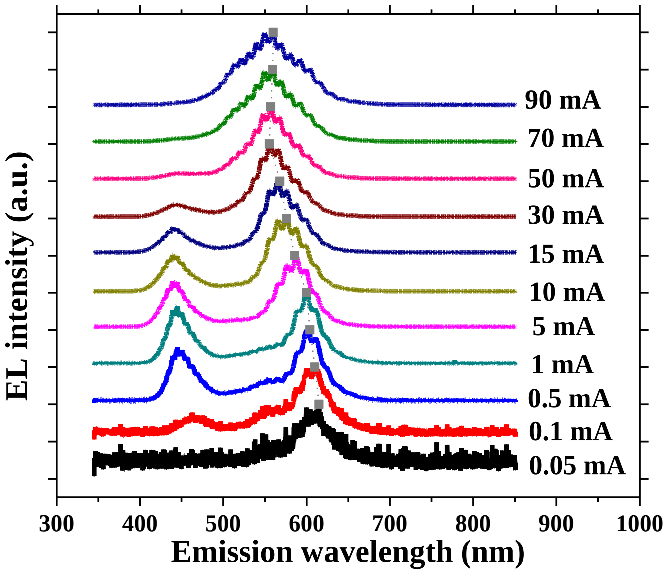

Figure 4.12: Normalized EL spectra of a μ-LED at different operating currents. The gray dots are guider to the eyes showing the peak-shift of the dominant emission peak.

of the blue emission in this device demonstrates that the carrier distribution in this long-wavelength LED is much different from a conventional blue LED. The mechanisms of the big blue-shift of the dominant emission peak and appearance of the blue emission will be discussed later in detail.

Due to the substantial blue-shift of the dominant emission peak, the emission colour of this μ-LED is tunable with operating currents. Based on the EL spectra of this device and sRGB colour space standard [23], the emission colours at different operating currents are calculated and shown in Figure 4.13. As shown, the emission colour of this device is gradually changed with increasing current, and nearly white light with a Commission Internationale de l'Eclairage (CIE) chromatic coordinate of (0.38, 0.38) is generated at a current of 10 mA. The representative optical images of the μ-LED operated at currents of, respectively, 0.1, 1, 10 and 90 mA are also shown in this figure. In addition, the CIE coordinate curve of this colour-tunable μ-LED is calculated according to the EL spectra, and is plotted as the red curve in Figure 4.14. In order to exclude the contribution of the blue emission to this colour tunability, the CIE coordinate curve of this device is re-calculated based on the EL spectra without blue emission (from 350 to 470 nm). The result is plotted as the blue curve in Figure 4.14. Four specific points, corresponding to the operating currents of representative images in Figure 4.13, are labelled on both curves. The chromatic coordinates at 90 mA are nearly

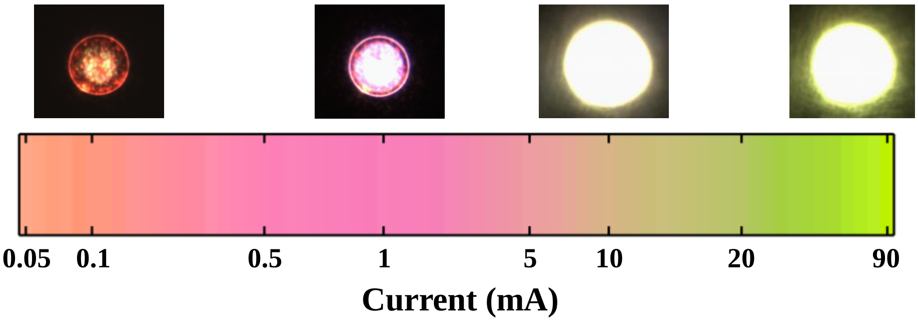

Figure 4.13: Calculated emission colours of a μ-LED at different operating currents. The representative optical images of this device operated at currents of 0.1, 1, 10 and 90 mA are inserted as well.

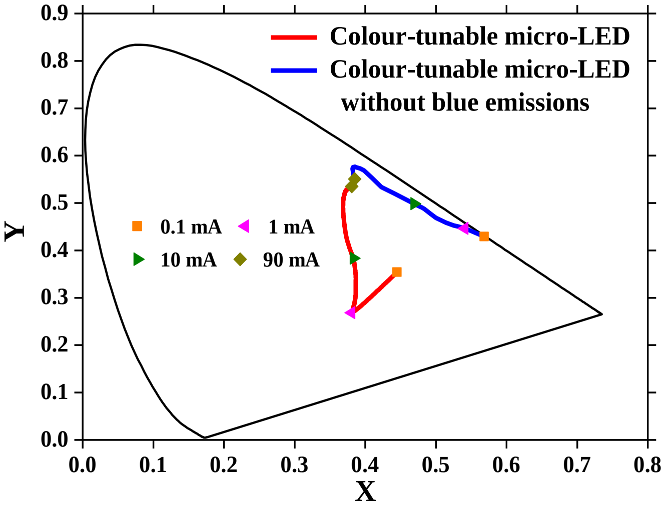

Figure 4.14: Calculated CIE coordinate curves according to the EL spectra of a colour-tunable μ-LED with and without blue emission. Four specific chromatic coordinates are labelled on both curves.

the same for both results due to an absence of the blue emission at this high current. From this figure, it can be concluded that the blue-shift of the dominant emission peak directly changes the emission colour of this device from amber to green, and the blue emission makes it possible to generate white light. For the white light, we comment that its generation is not directly dependent on the absolute intensity of the blue emission but is strongly determined by the intensity ratio of blue to dominant emissions.

The colour tunability of these μ-LEDs offers a range of applications. For instance, a multi-colour display can be achieved by these devices. As shown in Figure 4.15(a)-(c), the representative emission patterns at amber, green and yellow

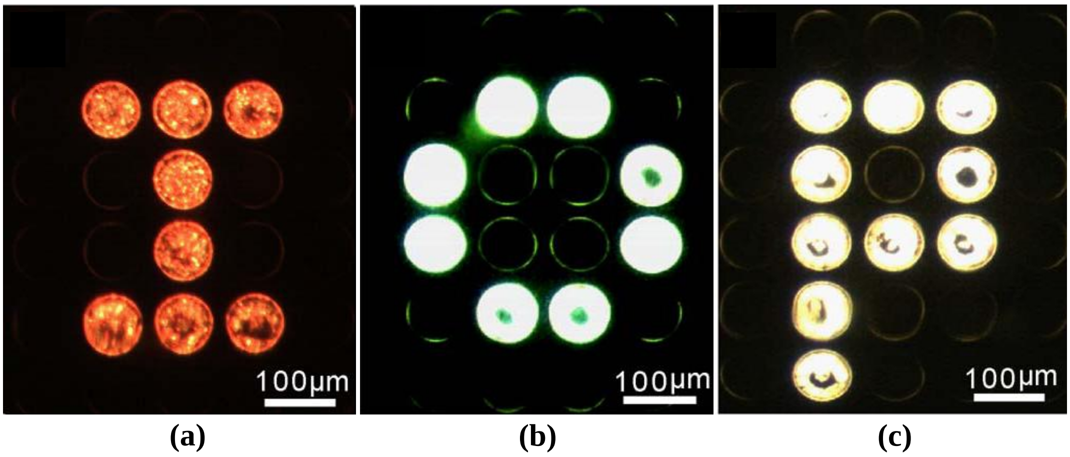

FIGURE 4.15: Emission pattern of 'IOP' generated by a COMS-controlled colour-tunable μ-LED array.

colours are generated by the colour-tunable μ-LED array which is controlled by a complementary metal-oxide-semiconductor (CMOS) driver [24]. Furthermore, this μ-LED array also has a potential for optical data transmission in visible light communications. The particulars of the CMOS driver and visible light communications are covered in detail elsewhere, and the interested reader can find related contents in Ref. [24] and Dr. Jonathan McKendry's PhD thesis [25].

Here, it is necessary to point out that this great colour tunability is a special property of μ-LEDs. In order to highlight this property quantitatively, broad-area LEDs with 300 × 300 μm^2 emission area were fabricated from the same amber LED wafer following a similar process. The colour tunability of broad-area and μ-LEDs were compared through the peak shift of the dominant emission peak and the intensity ratio of blue to dominant emissions. To extract the accurate peak shift of the dominant emission peak and the intensity ratio of blue to dominant emissions, the EL spectra of both broad-area and μ-LEDs were closely fitted by three Gaussian peaks corresponding to dominant, blue and green emissions, respectively. The fitted peak positions of the dominant emission peak for both broad-area and μ-LEDs are plotted in Figure 4.16(a) as a function of operating current. As shown, a blue-shift can be seen at first for both devices, followed by a slight red-shift caused by the self-heating effect when the current is higher than 40 mA. However, the μ-LED exhibits two special characteristics. Firstly, at low operating currents, for instance, 0.05 mA, the peak position of the μ-LED shows a 4 nm blue-shift compared with the one for the broad-area device. This shift can be attributed to the strain relaxation during the micro-pillar formation as discussed

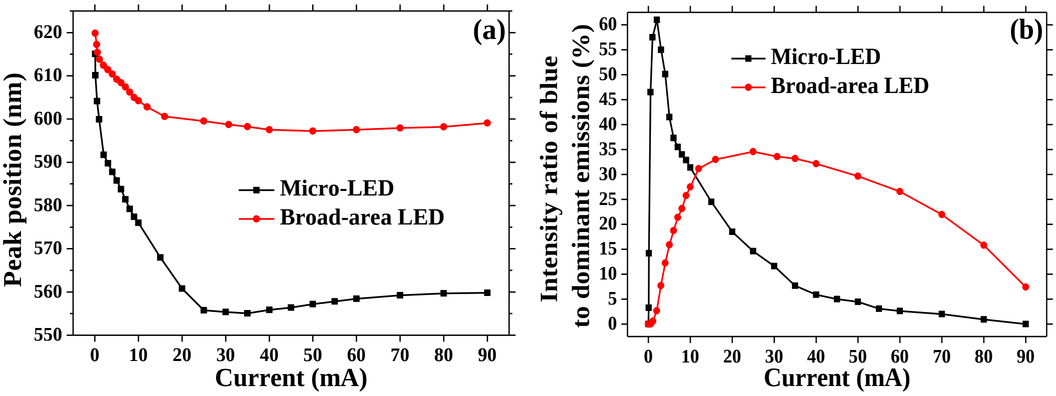

FIGURE 4.16: (a) Peak position of the dominant emission peak and (b) intensity ratio of blue to dominant emissions as a function of operating current for both broad-area and μ-LEDs.

in chapter 3. Considering the higher indium content of this amber wafer and the 40 μm diameter of micro-pillars, this blue-shift agrees well with the prediction. Secondly, the μ-LED demonstrates a much larger total blue-shift of the dominant emission peak of up to 60 nm at 35 mA, which is about 40 nm more than that found for the broad-area LED. This large peak shift enables the emission colour of the μ-LED to change in a wider range from amber to green. On the other hand, as shown in Figure 4.16(b), the μ-LED also shows a higher intensity ratio of blue to dominant emissions in the current range from 0 to 15 mA. The maximum intensity ratio is around 65 % at 2 mA for the μ-LED. This value is about 2 times higher than the maximum ratio observed for the broad-area device at 25 mA. Because of the enhanced blue-shift of the dominant emission peak and the higher intensity ratio of blue to dominant emissions, the μ-LED is preferred for the colour-tunable device compared with the broad-area device. This enhanced colour tunability is attributed to the higher operating current density of the μ-LED. As introduced in subsection 1.4.1, the μ-LEDs possess a small top-surface area of p-type GaN [26] and a high surface-to-volume ratio [27], which results in a low junction temperature under electrical operation. Thus the μ-LEDs can be operated at a much higher current density. In this comparison, at the same operating current, the corresponding current density of the fabricated μ-LED (40 μm in diameter) is about 70 times higher than that of the broad-area LED. Higher operating current density can adjust the emission colour more efficiently following different mechanisms of colour tunability. In the next subsection, the mechanisms of colour tunability in μ-LEDs will be discussed.

4.3.2 Mechanisms of colour tunability

As mentioned above, the blue-shift of the dominant emission peak is directly responsible for the colour tunability of the μ-LED. Furthermore, the appearance of the blue emission also influences the emission colour of this device. Thus, it is necessary to investigate the mechanisms of these two effects. This investigation is helpful to further optimize the wafer structure and improve the performance of this colour-tunable device.

Firstly, the blue-shift of the dominant emission peak was investigated. It is well known that an internal electric field, which is mainly caused by the piezoelectric nature of III-nitride materials and the lattice mismatch between the QWs and quantum barriers (QBs), exists in $\mathrm{In}_x\mathrm{Ga}_{1-x}\mathrm{N}$ QWs. Furthermore, the nonuniform indium distribution in $\mathrm{In}_x\mathrm{Ga}_{1-x}\mathrm{N}$ also leads to the band-filling effect resulted from an inhomogeneous bandgap. As introduced in sections 1.3 and 1.4, with current injection, the carriers attempt to fill the low-indium-content regions and/or screen the internal electric field. Thus, both effects result in a blue-shift of the emission wavelength. On the other hand, a red-shift of the emission wavelength also occurs due to bandgap-narrowing caused by the self-heating effect during LED operation. Thus, the net spectral-shift is a consequence of the competition between the above effects. With high indium contents, a large internal electric field and a pronounced bandgap inhomogeneity are expected in these amber QWs, which leads to a large blue-shift of the emission wavelength as observed.

Nevertheless, it is necessary to quantitatively evaluate the band-filling and screening effects on the blue-shift of the emission wavelength, and to understand how they depend on the operating current. As introduced in section 1.3, for the band-filling effect, a large FWHM broadening with increasing current is expected. In section 1.4, it was indicated that the screening effect will reduce the FWHM due to the flat energy band and enhanced overlap of electron and hole wavefunctions. Thus, the variation of the FWHM of the EL spectra is helpful to characterize the dependence of these two effects on the operating current. To exclude the influence of the self-heating effect on the spectral behaviours at different currents, the EL spectra of the colour-tunable μ-LED were also measured under 100 μs current pulses at 0.1 % duty cycle.

Figure 4.17 shows the spectral behaviour (peak position and FWHM) of the dominant emission peak at different currents. All the results plotted here are extracted

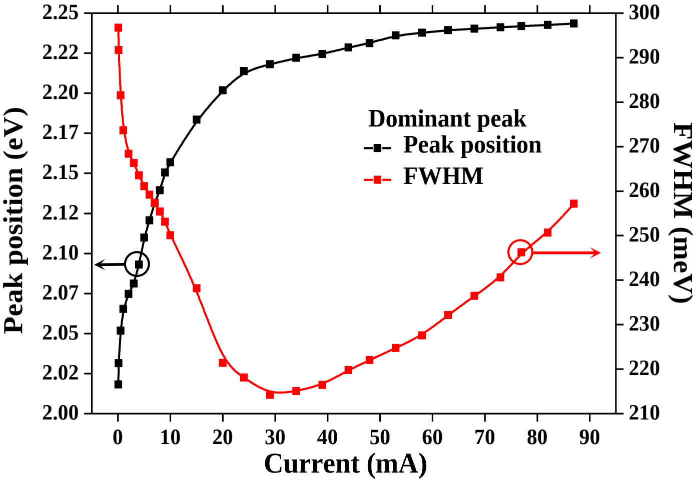

FIGURE 4.17: Peak position and corresponded FWHM of the dominant emission peak for a colour-tunable μ-LED as a function of pulsed operating current.

from fitted EL spectra measured under pulsed conditions. In order to have a clear observation, the peak positions are plotted in units of eV in this figure. It can be seen that, in the current range from 0.05 to 29 mA, there is a sharp blue-shift (about 55 nm) of the peak position accompanied by a narrowing of the FWHM. This result indicates that, in this current range, the blue-shift of the dominant emission peak is dominated by the screening effect of the internal electric field. The operating current of 29 mA corresponds to a high current density of 2309 A/cm^2 for this μ-LED. This value not only implies a large internal electric field exists in the amber QWs, but also highlights the enhanced colour tunability for the μ-LEDs which can sustain a high current density compared with the broad-area LEDs. Above 29 mA, the FWHM increases associated with a slight blue-shift of the peak position. Thus, the band-filling effect is considered to be the main reason for the blue-shift of the dominant emission peak when the operating current is higher than 29 mA.

On the other hand, the blue emission, which is attributed to the carrier recombination in In$_{0.18}$Ga$_{0.82}$N QWs, also makes contributions to the colour tunability of μ-LEDs. In III-nitride materials, holes have a high effective mass ($1.1m_0$) and a low mobility, which make it difficult for holes to be injected into QWs deeper within the structure. So it is generally agreed that a uniform distribution of holes is hard to achieve in III-nitride multiple QWs. This phenomenon leads to an accumulation of holes, and consequently most light emission only occurs in the QW near the p-type GaN layer in blue LEDs [21, 28]. Figure 4.18 shows the

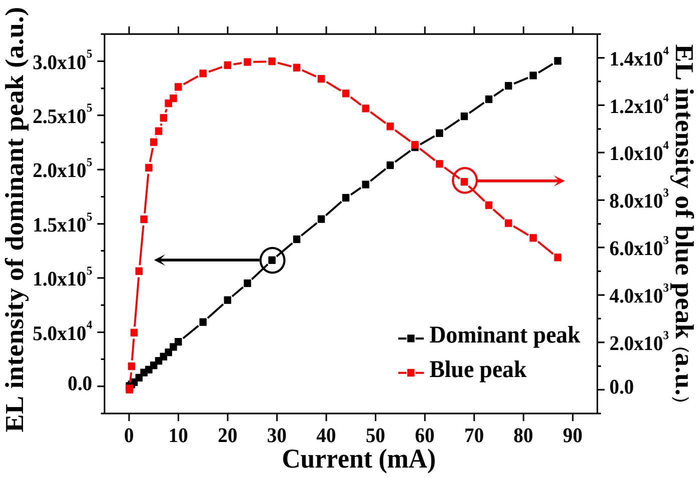

FIGURE 4.18: Integrated EL intensities of individual dominant and blue peaks for a colour-tunable μ-LED as a function of pulsed operating current.

integrated EL intensities of individual dominant and blue peaks for this colour-tunable μ-LED as a function of operating current extracted through the Gaussian fitting process. The observed blue emission in this device indicates that the holes can be injected into the deeper $\mathrm{In_{0.18}Ga_{0.82}N}$ QWs efficiently even at quite low operating currents. Compared with the nearly linear increase of the intensity for the dominant emission, the blue emission shows a decrease of the EL intensity at high currents. Because the $\mathrm{In_{0.18}Ga_{0.82}N}$ QWs are mostly adjacent to the n-type GaN layer, it is reasonable to assume that the decreased EL intensity of the blue emission is due to the lack of injected holes in the $\mathrm{In_{0.18}Ga_{0.82}N}$ QWs. This phenomenon demonstrates the hole distribution between different indium-content QWs in this colour-tunable μ-LED is strongly controlled by the operating current.

Although more work is still necessary to determine the exact physical mechanisms controlling the hole distribution between different indium-content QWs, the internal electric field in the QWs is considered a possible reason. Firstly, the large internal electric field in amber QWs leads to a longer radiative lifetime for carrier recombination. As a result, the holes may have more time to escape into deeper $\mathrm{In_{0.18}Ga_{0.82}N}$ QWs where they recombine radiatively with higher efficiency [29]. Meanwhile, as discussed in section 4.2, because the indium-rich regions in amber QWs are no longer effective radiative recombination centres, the radiative lifetime is also increased in these longer-wavelength QWs. Secondly, the carrier capture rate of $\mathrm{In_xGa_{1-x}N}$ QWs is also governed by the internal electric field. It is well known that the internal electric field leads to a band bending of $\mathrm{In_xGa_{1-x}N}$ QWs and, hence, to unequal potential height of QBs. From a semiclassical analysis, the carrier cannot be captured when propagating through an $\mathrm{In}_x\mathrm{Ga}_{1-x}\mathrm{N}$ QW if its energy loss rate ($\Delta E/\Delta x$) is smaller than the potential drop across the $\mathrm{In}_x\mathrm{Ga}_{1-x}\mathrm{N}$ QW, which can be expressed as Equation 4.2 [30, 31]:

$$\frac{\Delta E}{\Delta x} < \frac{\Delta E_{QB}}{L_{QW}} \tag{4.2}$$

where ΔE_{QB} is the energy difference between QBs and L_{QW} is the width of QWs. As discussed, the higher indium content in QWs increases the internal electric field and, thus, the value of ΔE_{QB}. Therefore, the carrier capture is less likely to happen in amber QWs, making it is possibly for holes to traverse the amber QWs without being captured and reach the $\mathrm{In}_{0.18}\mathrm{Ga}_{0.82}\mathrm{N}$ wells to generate the blue emission. However, as operating current increases, the internal electric field in the amber QWs is gradually screened. It results in a shorter radiative recombination lifetime and a higher hole capture rate for amber QWs. Consequently, fewer holes are injected into the deeper $\mathrm{In}_{0.18}\mathrm{Ga}_{0.82}\mathrm{N}$ QWs resulting in a decreased EL intensity of the blue emission.

4.4 Summary

In this chapter, we have demonstrated colour-tunable μ-LEDs fabricated from an amber $\mathrm{In}_{0.40}\mathrm{Ga}_{0.60}\mathrm{N}$/GaN-based LED wafer. The amber QWs in this wafer were grown on top of low-indium-content blue QWs which act as an ERL and pre-strain layers. Compared with the other techniques for multi-colour displays based on III-nitride LEDs, the colour tunability of these devices is mainly due to the novel characteristics of this LED wafer and our μ-LEDs. These colour-tunable μ-LEDs supply a much simpler methodology to achieve a multi-colour display.

The optical properties of the amber LED wafer used were first studied by T-PL and CL. The amber QWs present an S-shaped peak shift with increasing temperature. Through a proper fitting process for the thermal quenching of the PL intensity, a large confinement energy (190 meV) for the carriers in different indium-content regions was obtained. Both of these results indicate that a pronounced bandgap inhomogeneity does exist in amber QWs. The further CL results support this conclusion, in that two distinct emission peaks are found thanks to the high spatial resolution of CL. In addition, for each emission peak observed in CL measurements, the influence of indium fluctuations was also discussed. It was found that the indium-rich regions are no longer effective radiative recombination centres for long-wavelength QWs.

The μ-LEDs with flip-chip configurations were fabricated. Although the relatively poor material quality leads to a degradation of electrical and optical performance of these devices, the EL spectra of μ-LEDs show a large blue-shift of the dominant emission peak and a blue emission from low-indium-content QWs. The blue-shift of the dominant emission peak directly changes the emission colour of μ-LEDs from amber to green at different operating currents. The blue emission also influences the emission colour of these devices. Through a comparison of device performance between broad-area and μ-LEDs fabricated from the same wafer, micro-scale devices show an enhanced colour tunability. This enhancement is attributed to the fact that μ-LEDs can sustain significantly high current densities due to their better thermal management. The emission colour can be adjusted by higher injection carriers more efficiently following different mechanisms. The blue-shift of the dominant emission peak can be well explained by the band-filling effect and the screening effect of internal electric field in the amber QWs. Based on the results from pulsed EL measurements, for μ-LEDs with a diameter of 40 μm, the latter effect is dominant when the operating current density is lower than 2309 A/cm^2, and the former one governs the blue-shift above this current density. The internal electric field is also believed to affect the hole distribution in these colour-tunable μ-LEDs, which leads to an efficient injection of holes into the deeper low-indium-content QWs for the generation of blue light.

References

[1] E.F. Schubert and J.K. Kim. Solid-state light sources getting smart. *Science*, 308(5726): 1274–1278, 2005.

[2] H.X. Jiang, S.X. Jin, J. Li, J. Shakya, and J.Y. Lin. III-nitride blue microdisplays. *Applied Physics Letters*, 78(9):1303–1305, 2001.

[3] H.W. Choi, C.W. Jeon, and M.D. Dawson. High-resolution 128 × 96 nitride microdisplay. *Electron Device Letters, IEEE*, 25(5):277–279, 2004.

[4] J. Day, J. Li, D.Y.C. Lie, C. Bradford, J.Y. Lin, and H.X. Jiang. III-Nitride full-scale high-resolution microdisplays. *Applied Physics Letters*, 99(3):031116, 2011.

[5] M. Koike, N. Shibata, H. Kato, and Y. Takahashi. Development of high efficiency GaN-based multiquantum-well light-emitting diodes and their applications. *Selected Topics in Quantum Electronics, IEEE Journal of*, 8(2):271–277, 2002.

[6] J.K. Sheu, S.J. Chang, C.H. Kuo, Y.K. Su, L.W. Wu, Y.C. Lin, W.C. Lai, J.M. Tsai, G.C. Chi, and R.K. Wu. White-light emission from near UV InGaN-GaN LED chip precoated with blue/green/red phosphors. *Photonics Technology Letters, IEEE*, 15(1):18–20, 2003.

[7] G. Heliotis, P.N. Stavrinou, D.D.C. Bradley, E. Gu, C. Griffin, C.W. Jeon, and M.D. Dawson. Spectral conversion of InGaN ultraviolet microarray light-emitting diodes using fluorene-based red-, green-, blue-, and white-light-emitting polymer overlayer films. *Applied Physics Letters*, 87(10):103505, 2005.

[8] M. Wu, Z. Gong, A.J. Kuehne, A.L. Kanibolotsky, Y.J. Chen, I.F. Perepichka, A.R. Mackintosh, E. Gu, P.J. Skabara, R.A. Pethrick, and M.D. Dawson. Hybrid GaN/organic microstructured light-emitting devices via ink-jet printing. *Optics Express*, 17(19):16436–16443, 2009.

[9] S.N. Lee, H.S. Paek, H. Kim, T. Jang, and Y. Park. Monolithic InGaN-based white light-emitting diodes with blue, green, and amber emissions. *Applied Physics Letters*, 92(8): 081107, 2008.

[10] C.B. Soh, W. Liu, S.J. Chua, S.S. Ang, R.J.N. Tan, and S.Y. Chow. Generation of amber III-nitride based light emitting diodes by indium rich InGaN quantum dots with InGaN wetting layer and AlN encapsulation layer. *Journal of Applied Physics*, 108(9):093501, 2010.

[11] L. Zhang, K. Cheng, M. Leys, P. Favia, H. Bender, and G. Borghs. Two-color InGaN/GaN microfacet multiple-quantum well structures grown on Si substrate. *Journal of Applied Physics*, 110(8):083518, 2011.

[12] Y.J. Hong, C.H. Lee, A. Yoon, M. Kim, H.K. Seong, H.J. Chung, C. Sone, Y.J. Park, and G.C. Yi. Visible-Color-Tunable Light-Emitting Diodes. *Advanced Materials*, 23(29): 3284–3288, 2011.

[13] X. Ni, X. Li, J. Lee, S. Liu, V. Avrutin, U. Ozgur, H. Morkoç, A. Matulionis, T. Paskova, G. Mulholland, and K.R. Evans. InGaN staircase electron injector for reduction of electron overflow in InGaN light emitting diodes. *Applied Physics Letters*, 97(3):031110, 2010.

[14] W.Y. Shiao, C.F. Huang, T.Y. Tang, J.J. Huang, Y.C. Lu, C.Y. Chen, Y.S. Chen, and C.C. Yang. X-ray diffraction study on an InGaN/GaN quantum-well structure of prestrained growth. *Journal of Applied Physics*, 101:113503, 2007.

[15] R.C. Miller, D.A. Kleinman, W.A. Nordland, and A.C. Gossard. Luminescence studies of optically pumped quantum wells in GaAs-$Al_xGa_{1-x}As$ multilayer structures. *Physical Review B*, 22:863–871, Jul 1980.

[16] Y.H. Cho, G.H. Gainer, A.J. Fischer, J.J. Song, S. Keller, U.K. Mishra, and S.P. DenBaars. S-shaped temperature-dependent emission shift and carrier dynamics in InGaN/GaN multiple quantum wells. *Applied physics letters*, 73(10):1370–1372, 1998.

[17] R. Pecharroman-Gallego, R.W. Martin, and I.M. Watson. Investigation of the unusual temperature dependence of InGaN/GaN quantum well photoluminescence over a range of emission energies. *Journal of Physics D: Applied Physics*, 37(21):2954, 2004.

[18] F.B. Naranjo, F. Calle, E. Calleja, B. Jenichen, and K.H. Ploog. Strong localization in InGaN layers with high In content grown by molecular-beam epitaxy. *Applied Physics Letters*, 80(2):231–233, 2002.

[19] Ž. Gačević, A. Das, J. Teubert, Y. Kotsar, P.K. Kandaswamy, T. Kehagias, T. Koukoula, P. Komninou, and E. Monroy. Internal quantum efficiency of III-nitride quantum dot superlattices grown by plasma-assisted molecular-beam epitaxy. *Journal of Applied Physics*, 109:103501, 2011.

[20] K. Okamoto, A. Kaneta, K. Inoue, Y. Kawakami, M. Terazima, G. Shinomiya, T. Mukai, and S. Fujita. Carrier dynamics in InGaN/GaN SQW structure probed by the transient grating method with subpicosecond pulsed laser. *Physica Status Solidi (b)*, 228(1):81–84, 2001.

[21] A. David, M.J. Grundmann, J.F. Kaeding, N.F. Gardner, T.G. Mihopoulos, and M.R. Krames. Carrier distribution in (0001) InGaN/GaN multiple quantum well light-emitting diodes. *Applied Physics Letters*, 92:053502, 2008.

[22] N. Grossman, V. Poher, M.S. Grubb, G.T. Kennedy, K. Nikolic, B. McGovern, R.B. Palmini, Z. Gong, E.M. Drakakis, M.A.A. Neil, M.D. Dawson, J. Burrone, and P. Degenaar. Multisite optical excitation using ChR2 and micro-LED array. *Journal of Neural Engineering*, 7 (1):016004, 2010.

[23] S. Süsstrunk, R. Buckley, and S. Swen. Standard RGB color spaces. In *Proc. IS&T/SIDs 7th Color Imaging Conference*, pages 127–134, 1999.

[24] S. Zhang, Z. Gong, J.J.D. McKendry, S. Watson, A. Cogman, E. Xie, P. Tian, E. Gu, Z. Chen, G. Zhang, A.E. Kelly, R.K. Henderson, and M.D. Dawson. CMOS-Controlled Color-Tunable Smart Display. *Photonics Journal, IEEE*, 4(5):1639–1646, 2012.

[25] Jonathan.J.D. McKendry. Micro-pixellated AlInGaN light-emitting diode arrays for optical communications and time-resolved fluorescence lifetime measurements. *PhD thesis, University of Strathclyde, Glasgow, U.K.*, 2012.

[26] X. Guo and E.F. Schubert. Current crowding and optical saturation effects in GaInN/GaN light-emitting diodes grown on insulating substrates. *Applied Physics Letters*, 78(21):3337–3339, 2001.

[27] H.S. Chen, D.M. Yeh, C.F. Lu, C.F. Huang, Y.C. Lu, C.Y. Chen, J.J. Huang, and C.C. Yang. Mesa-size-dependent color contrast in flip-chip blue/green two-color InGaN/GaN multi-quantum-well micro-light-emitting diodes. *Applied Physics Letters*, 89:093501, 2006.

[28] J.P. Liu, J.H. Ryou, R.D. Dupuis, J. Han, G.D. Shen, and H.B. Wang. Barrier effect on hole transport and carrier distribution in InGaN/GaN multiple quantum well visible light-emitting diodes. *Applied Physics Letters*, 93:021102, 2008.

[29] R. Charash, P.P. Maaskant, L. Lewis, C. McAleese, M.J. Kappers, C.J. Humphreys, and B. Corbett. Carrier distribution in InGaN/GaN tricolor multiple quantum well light emitting diodes. *Applied Physics Letters*, 95(15):151103, 2009.

[30] M.F. Schubert and E.F. Schubert. Effect of heterointerface polarization charges and well width upon capture and dwell time for electrons and holes above GaInN/GaN quantum wells. *Applied Physics Letters*, 96(13):131102, 2010.

[31] D. Zhu, A.N. Noemaun, M.F. Schubert, J. Cho, E.F. Schubert, M.H. Crawford, and D.D. Koleske. Enhanced electron capture and symmetrized carrier distribution in GaInN light-emitting diodes having tailored barrier doping. *Applied Physics Letters*, 96(12):121110, 2010.

Chapter 5

Performance enhancements of micro-light emitting diodes by Pd-based contacts to p-type GaN

The objective of the work presented in this chapter was to further improve the performance of III-nitride micro-light emitting diodes (μ-LEDs) by optimizing their metal contacts to p-type GaN. An oxidized Ni/Au contact to p-type GaN, which is highly transparent for visible light, was normally used in previous work. As summarized in section 5.1, Pd is another commonly used metal for making ohmic contact to p-type GaN. Its high reflectivity makes it a better candidate for III-nitride LEDs with flip-chip configurations. In this work, in order to achieve a high-quality Pd-based contact to p-type GaN, a systematic optimization of the fabrication process of Pd-based contacts to p-type GaN including surface cleaning and thermal annealing was carried out. Due to the fundamental problems of p-type GaN, the metal contacts to p-type GaN show a nonlinear current-voltage characteristic in a wider bias region and their specific contact resistivities vary with the injection current density. Thus, to directly calculate the current-density dependent specific contact resistivity, a generalized formula for the transmission line method was introduced and applied as shown in section 5.3. The electrical properties of the best annealed Pd and oxidized Ni/Au contacts to p-type GaN are then characterized and compared by this new methodology in section 5.4. To mimic the structure of LEDs with flip-chip configurations, a reflectivity study of these metal layers capped with an additional Ti/Au reflector was carried out, and the result is also described in section 5.4. Finally, the performance of μ-LEDs with different metal contacts to p-type GaN was characterized and compared.

5.1 Summary of ohmic contacts to p-type GaN

The formation of ohmic contacts with a low specific contact resistivity (ρ_c) to III-nitride semiconductors is technologically important for achieving high-power optoelectronic devices such as light emitting diodes (LEDs) and laser diodes (LDs). In principle, as introduced in section 1.4, to achieve a high-quality ohmic contact to semiconductor, the potential barrier between the metal and semiconductor should be eliminated or the semiconductor needs to be heavily doped to improve the tunnelling probability of carriers through the potential barrier. For GaN, which is an ionic compound [1], the height of the potential barrier directly depends on the work function (Φ_m) of the metals [2]. Thus, ohmic contact to n-type GaN with a low ρ_c is relatively easier to achieve by using low Φ_m metals, such as Ti (Φ_m=4.33 eV) and Al (Φ_m=4.28 eV).

However, due to the fundamental problems of p-type GaN as indicated in section 1.4, the creation of an ideal ohmic contact with a low ρ_c to p-type GaN is difficult. Thus, the fabrication and mechanism of ohmic contacts to p-type GaN have attracted much more attentions and been investigated in detail. In the past decades, a number of metallization schemes with high Φ_m metals, such as Ni (Φ_m=5.15 eV), Pd (Φ_m=5.17 eV), Pt (Φ_m=5.65 eV), have been tested with p-type GaN. Furthermore, different processes of surface cleaning for the p-type GaN layer and thermal annealing for metal layers have been extensively studied as well. The main results of previous research on ohmic contacts to p-type GaN are summarized in Table 5.1. Of these contacts, oxidized Ni/Au and Pd-based contacts to p-type GaN are commonly used for III-nitride devices because of their low ρ_c ($\sim 10^{-6} - 10^{-4}$ Ωcm^2). For Ni/Au-based contacts, it is found that ρ_c significantly decreases after a thermal annealing process at 500 °C in air or O_2 ambients [3] compared with annealing in a N_2 ambient [4]. Different mechanisms have been proposed to explain this improvement. Firstly, it is generally agreed that Ni is oxidized during thermal annealing in the ambient containing O_2 to form a semi-transparent p-type NiO semiconductor on top of the p-type GaN layer. Then, a high-quality ohmic contact with a low ρ_c is achieved between the p-type NiO and the top Au layer.

Secondly, interfacial reactions between Ni/Au and GaN are found during the thermal annealing process. These reactions lead to the formation of different gallides, such as Ga_4Ni_3 and $AuGa_2$ [5]. These interfacial reactions are enhanced when the sample is annealed in the ambient containing O_2, since the out-diffusion of Ga atoms is promoted by the incorporated O atoms [6]. The out-diffusion of Ga atoms creates acceptor-like Ga vacancies in the near-surface region of the p-type GaN layer. In this region, the hole concentration is increased, which leads to the ρ_c reduction. For Pd-based contacts, a high-quality contact to p-type GaN can be achieved even without thermal annealing. Surface cleaning plays an important role in the formation of Pd-based contacts to p-type GaN [7]. It is considered that the effective removal of the surface oxidation layer on top of the p-type GaN layer by surface cleaning is important for the formation of as-deposited Pd contacts to p-type GaN. Further experimental results show that the surface oxidation layer can also be eliminated during the thermal annealing process [8], which will further improve the contact properties of Pd-based contacts to p-type GaN. The formation of interfacial reaction phrases of Pd gallides, which creates the Ga vacancies underneath the contacts, is also a possible mechanism to form Pd-based ohmic contacts to p-type GaN [9].

The proper selection of metal contacts to p-type GaN is extremely important for achieving high-performance micro-LEDs (μ-LEDs) as, for these devices, the contact area of metal contacts to p-type GaN is greatly reduced. Furthermore, the nonlinear current-voltage (I-V) characteristics of metal contacts to p-type GaN are often observed in a wider bias region [20]. So the current-density dependent ρ_c of metal contacts to p-type GaN needs to be considered. This nonlinear contact behaviour becomes even more important for μ-LEDs which are operated in a wider current-density range, as introduced in subsection 1.4.1. On the other hand, the optical properties of metal contact layers also need to be investigated for improving LED optical characteristics. The high-transparency nature of the oxidized Ni/Au bilayer, which is the commonly used metal contact to p-type GaN for μ-LEDs, limits the light extraction efficiency (LEE) of devices with flip-chip configurations. Thus, in order to achieve high-performance μ-LEDs, further studies and optimization of the metal contact to p-type GaN are required. Pd is another commonly used material for the metal contact to p-type GaN and shows a high-reflectivity nature. These attractive properties here motivate a systematic study for the Pd-based contacts to p-type GaN with a consideration of the current-density dependent ρ_c. The performance of μ-LEDs with different metal contacts

Metal	p_0 (cm^{-3})	T (°C)	Gas	ρ_c (Ωcm^2)	Notes	Reference
Pd	1.93×10^{17}	N/A	N/A	4.3×10^{-4}	Removing of surface oxidation layer	[7]
Pd/Ni	3.3×10^{17}	500	air	5.7×10^{-5}	Formation of Pd gallides and Ga vacancies	[9]
Pd/Ru	3×10^{17}	500	N_2	2.4×10^{-5}		[10]
Pd/Mo	5×10^{17}	300-500	Vacuum	$(2-5) \times 10^{-4}$	Formation of Ga vacancies	[11]
Ni	1.7×10^{19}	750,950	N_2		Heavy doping	[12]
Ni/Au	2×10^{17}	500	air	4×10^{-6}	Formation of NiO	[3]
Ni/Ag/Ru/Ni/Au	3×10^{17}	500	air	5.2×10^{-5}	Formation of Ga vacancies	[13]
Pt	2×10^{17}	500	N_2	9.12×10^{-3}		[14]
Pt/Ru	3×10^{17}	600	N_2	2.2×10^{-6}		[15]
Ag	5×10^{17}	330	air	2.5×10^{-4}	A reduction of the potential barrier height	[16]
Ag/Pd	1×10^{17}	330-530	air	$(4-6) \times 10^{-5}$	A reduction of the potential barrier height	[17]
Ta/Ti	7×10^{17}	N/A	N/A	3×10^{-5}		[18]
Rh/Ni	4×10^{17}	N/A	N/A	3×10^{-5}	Removing of surface oxidation layer	[19]

TABLE 5.1: Summary of previous results of ohmic contacts to p-type GaN. The p_0 and T in the table are the hole concentration and annealing temperature, respectively.

to p-type GaN is also characterized and compared.

5.2 Optimization of Pd-based contacts to p-type GaN

In order to achieve a high-quality Pd-based contact to p-type GaN with a low ρ_c, the optimization of the fabrication process of Pd-based contacts to p-type GaN was first performed. The optimized processes include surface cleaning with different acid solutions prior to metal deposition and thermal annealing at different temperatures and in different ambients after metal deposition. The detailed processes and results are shown in this section.

5.2.1 Effect of surface cleaning

The surface of semiconductors is nearly instantly oxidized when exposed to air. This generates a surface oxidation layer on top of the semiconductor layer, which results in an additional potential barrier between the contact metal and semiconductor for carrier transport [21]. Thus, the removal of this surface oxidation layer is necessary to form a high-quality contact. To remove such a surface oxidation layer, a surface cleaning process using different acid solutions has usually been carried out before metal deposition. For p-type GaN, dilute HCl is the most commonly used acid solution [22]. It has been shown that some other acid solutions can also be used to remove the surface oxidation layer of p-type GaN effectively. For example, in the previous studies, it was demonstrated that the aqua regia (HCl 3:1 HNO_3) is a more effective solution with enhanced cleaning capability. The surface cleaning process using aqua regia can greatly reduce the ρ_c of as-deposited Pd contacts to p-type GaN [7, 23]. However, it is hard to reproduce this improvement on the contact properties resulting from surface cleaning using aqua regia. Thus, in this work, the systematic study of surface cleaning with different acid solutions was first carried out.

The samples used in this work were from a commercial blue $In_xGa_{1-x}N$/GaN-based LED wafer grown on a c-plane (0001) sapphire substrate by metal-organic chemical vapour deposition. As shown in Figure 5.1, the epitaxial structure of this wafer consisted of a 3.4 μm-thick GaN buffer layer, a 2.6 μm-thick n-doped GaN layer, eleven periods of $In_xGa_{1-x}N$ (2.8 nm)/GaN (13.5 nm) quantum wells (QWs) emitting at 450 nm, a 30 nm-thick p-type $Al_xGa_{1-x}N$ electron block layer and a 160 nm-thick p-type GaN with a Mg doping concentration around 2×10^{20} cm^{-3}. Although the LED wafer contains a multi-layer structure and a p-n junction, it has been demonstrated that the LED wafer can be used to study the contact properties of metal contacts to p-type GaN [24]. Thus, the top p-type GaN layer of this LED wafer was used to evaluate the contact properties of Pd-based contacts to p-type GaN. A circular-transmission line method (C-TLM) was used to determine the sheet resistance (R_s) of p-type GaN, transfer length (L_t) and ρ_c of Pd-based contacts to p-type GaN. The schematic diagram of C-TLM patterns used in our work is shown in Figure 5.2. The radius of inner disk-shaped electrode was 75 μm for all the patterns, and the spacing between the inner and outer electrodes varied from 10 to 45 μmm with a 5 μm step. To fabricate samples for characterization, the C-TLM photoresist patterns were defined on the p-type GaN layer by standard photolithography. Prior to metal deposition, the surface of unpatterned p-type GaN layers was cleaned by an acid solution for 5 min and rinsed by de-ionized (DI) water. Five different acid solutions were used in these experiments including HCl (40 %), aqua regia, diluted HCl with two different concentrations [HCl (40 %) 3:1 DI water or HCl (40 %)1:1 DI water] and HNO_3 1:3 DI water. Finally, a 30 nm-thick Pd metal layer was deposited on the sample by electron-beam evaporation. After metal lift-off, the I-V characteristic of each sample was measured by a HP 4155 semiconductor analyzer.

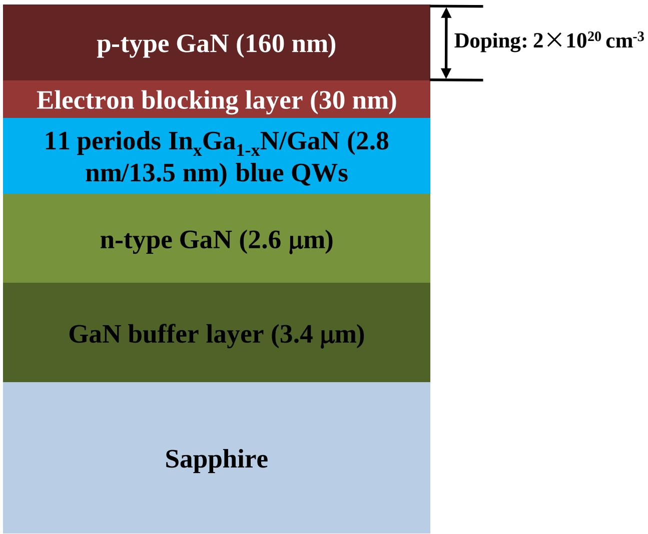

FIGURE 5.1: Epitaxial structure of a commercial blue $In_xGa_{1-x}N/GaN$-based LED wafer. The top p-type GaN layer is used to evaluate the metal contact property.

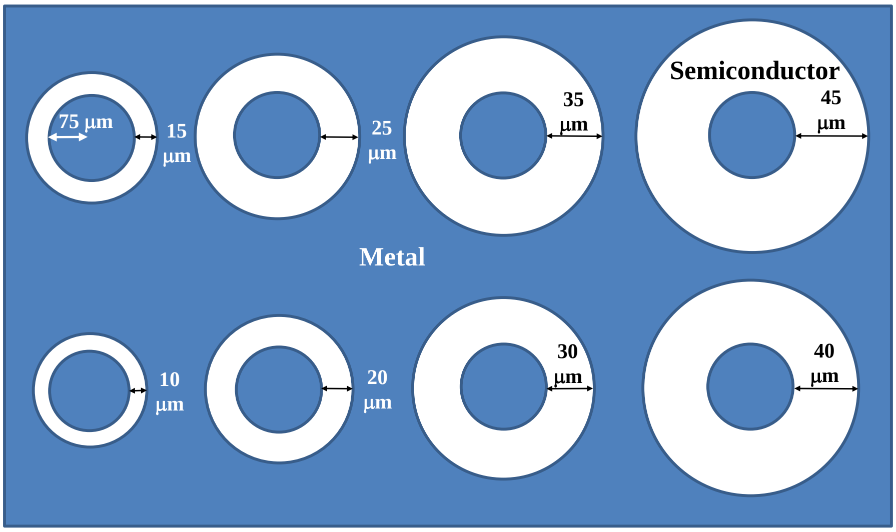

FIGURE 5.2: Schematic diagram of the C-TLM patterns used. The blue-colour region is the metal layer and the white region is the semiconductor layer.

Figure 5.3(a) shows the I-V characteristics of these as-deposited Pd contacts to p-type GaN cleaned by different acid solutions in a bias region from -0.5 to 0.5 V, measured on the contact pads with a 10 μm spacing. As shown, the sample cleaned by HCl (40 %) illustrates the best I-V characteristic. The electrical performance of this sample is even better than that of the sample cleaned by aqua regia which has been reported as an effective acid solution to achieve as-deposited Pd ohmic contacts to p-type GaN [7]. The samples cleaned by HCl (40 %) and aqua regia show a nearly linear I-V characteristic in this narrow bias region. However, as shown in Figure 5.3(b), when the bias region is extended to -2 to 2 V, all samples reveal nonlinear I-V characteristics. This is due to the non-strict ohmic behaviour of these as-deposited Pd contacts to p-type GaN.

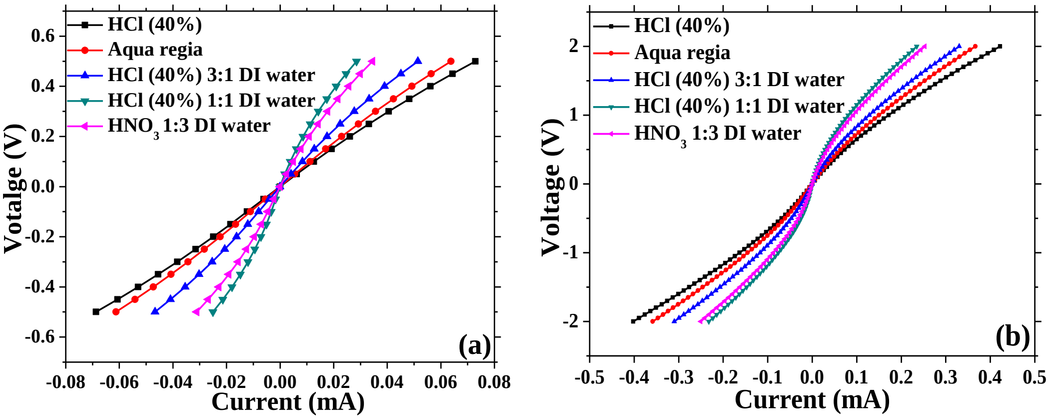

FIGURE 5.3: I-V characteristics of as-deposited Pd contacts to p-type GaN cleaned by different acid solutions in the bias regions from (a) -0.5 to 0.5 V and (b) -2 to 2 V, measured on the contact pads with a 10 μm spacing.

To quantitatively compare the contact properties of as-deposited Pd contacts to p-type GaN cleaned by different acid solutions, R_s, L_t and ρ_c of each sample were calculated through a standard C-TLM fitting process. Figure 5.4 shows a typical fitting process for the sample cleaned by HCl (40 %). Figure 5.4(a) shows the I-V characteristics of contact pads with different spacings on this sample. Based on these data, the total resistance (R) of each contact pad is calculated at a bias voltage of 2 V and plotted as black-square data points in Figure 5.4(b). For the C-TLM measurement, the R between two contact pads separated by a circular gap is given by:

$$R = \frac{R_s}{2\pi}\left[\ln\left(\frac{r_o}{r_i}\right) + L_t\left(\frac{1}{r_i} + \frac{1}{r_o}\right)\right] \tag{5.1}$$

where r_i and r_o are the inner and outer radii of C-TLM contact pads, respectively. When the spacing between inner and outer radii is much smaller than r_i, Equation 5.1 can be simplified as [3]:

$$R = \frac{R_s}{2\pi}\left[\ln\left(\frac{r_o}{r_i}\right) + \frac{2L_t}{r_i}\right] \tag{5.2}$$

Thus, the data points in Figure 5.4(b) can be linearly fitted by Equation 5.2, and the best fitting result is shown as the red line in this figure. Through Equation 5.2, the R_s and L_t can be calculated by using the slope and intercept of the fitted line by following equations:

$$R_s = slope \times 2 \times \pi = 131717\ \Omega/sq \tag{5.3}$$

$$L_t = \frac{intercept \times \pi \times r_i}{R_s} = 4.9\ \mu m \tag{5.4}$$

Finally, the ρ_c can be calculated by [3]:

$$\rho_c = L_t^2 \times R_s = 3.1 \times 10^{-2}\ \Omega cm^2 \tag{5.5}$$

Here, it is necessary to indicate that, for one sample, the calculated values of L_t and ρ_c are different at different bias voltages. This is due to the nonlinear I-V characteristics of these as-deposited Pd contacts to p-type GaN. Thus, the bias voltage for achieved L_t and ρ_c needs to be given. A new methodology will be introduced to directly calculate the changed ρ_c for the metal contact to semiconductor with a nonlinear I-V characteristic in section 5.3.

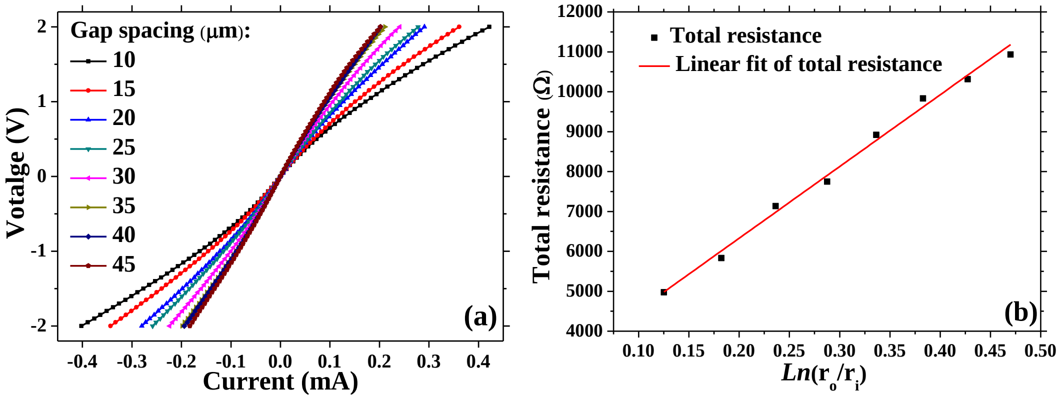

FIGURE 5.4: Typical C-TLM fitting process for an as-deposited Pd contact to p-type GaN cleaned by HCl (40 %): (a) I-V characteristics of contact pads with different spacings; (b) linear fitting process for the total resistances of contact pads with different spacings calculated at a bias voltage of 2 V.

Table 5.2 summarizes the calculated contact properties of as-deposited Pd contacts to p-type GaN cleaned by different acid solutions at a bias voltage of 2 V. These results clearly illustrate that HCl (40 %) is the most effective acid solution for surface cleaning to reduce the ρ_c of as-deposited Pd contacts to p-type GaN.

Furthermore, all samples also have a similar R_s which indicates that the possible damage to p-type GaN caused by the acid solutions can be neglected.

Metal	Acid solution	R_s (Ω/sq)	L_t (μm)	ρ_c (Ωcm^2)
Pd	HCl (40 %)	131717	4.9	3.1×10^{-2}
Pd	Aqua regia	136797	5.1	3.5×10^{-2}
Pd	HCl (40 %) 3:1 DI water	131484	7.6	7.5×10^{-2}
Pd	HCl (40 %) 1:1 DI water	157270	7.9	9.8×10^{-2}
Pd	HNO_3 1:3 DI water	137997	8.9	1.1×10^{-1}

TABLE 5.2: Contact properties of as-deposited Pd contacts to p-type GaN cleaned by different acid solutions at a bias voltage of 2 V.

5.2.2 Effect of thermal annealing

As demonstrated in the last subsection, the ρ_c of as-deposited Pd contacts to p-type GaN can be reduced after a proper surface cleaning process. However, compared with the oxidized Ni/Au contact to p-type GaN which was normally used in my work, the achieved ρ_c ($\sim 10^{-2}$ Ωcm^2) is still higher. In order to further reduce the ρ_c of Pd-based contacts to p-type GaN, experiments of thermal annealing at different temperatures were carried out in different gas ambients.

The sample structure and characterization technology used in the thermal annealing experiments were the same as those used for surface cleaning as described in subsection 5.2.1. The C-TLM patterns were defined on ten samples at first. Prior to metal deposition, the surface of unpatterned p-type GaN layers was cleaned by HCl (40 %) for 5 min. Then a 30 nm-thick Pd metal layer was deposited on the sample surface by electron-beam evaporation. After metal lift-off, nine samples were annealed at different conditions, i.e. 300 °C, 400 °C and 500 °C in N_2, air and vacuum ambients for 3 min, respectively. One sample without thermal annealing was used as a reference. The I-V characteristic of each sample was measured in a bias region from -2 to 2 V. To further understand the effect of thermal annealing, top-view scanning electron microscope (SEM) images were also taken for each sample by an FEI Sirion 200 ultrahigh-resolution Schottky field-emission SEM machine (Department of Physics).

Figure 5.5 shows the I-V characteristics of Pd-based contacts to p-type GaN annealed at different temperatures in (a) N_2, (b) air and (c) vacuum ambients, measured on the contact pads with a 10 μm spacing. As show in these figures, it can be found that the linearity of I-V characteristics is enhanced as annealing temperature increases in all gas ambients. Meanwhile, in each gas ambient, the sample annealed at 300 °C generally shows the highest current at each voltage compared with the others. With further increase of annealing temperature, the electrical properties of the Pd-based contact to p-type GaN keeps degrading and becomes even worse than that of the as-deposited Pd contact to p-type GaN. This observation is in agreement with the results shown in Ref. [17] and will be discussed later in detail. By the standard C-TLM fitting at 2 V, the contact properties (R_s, L_t and ρ_c) of each sample are calculated and summarized in Table 5.3.

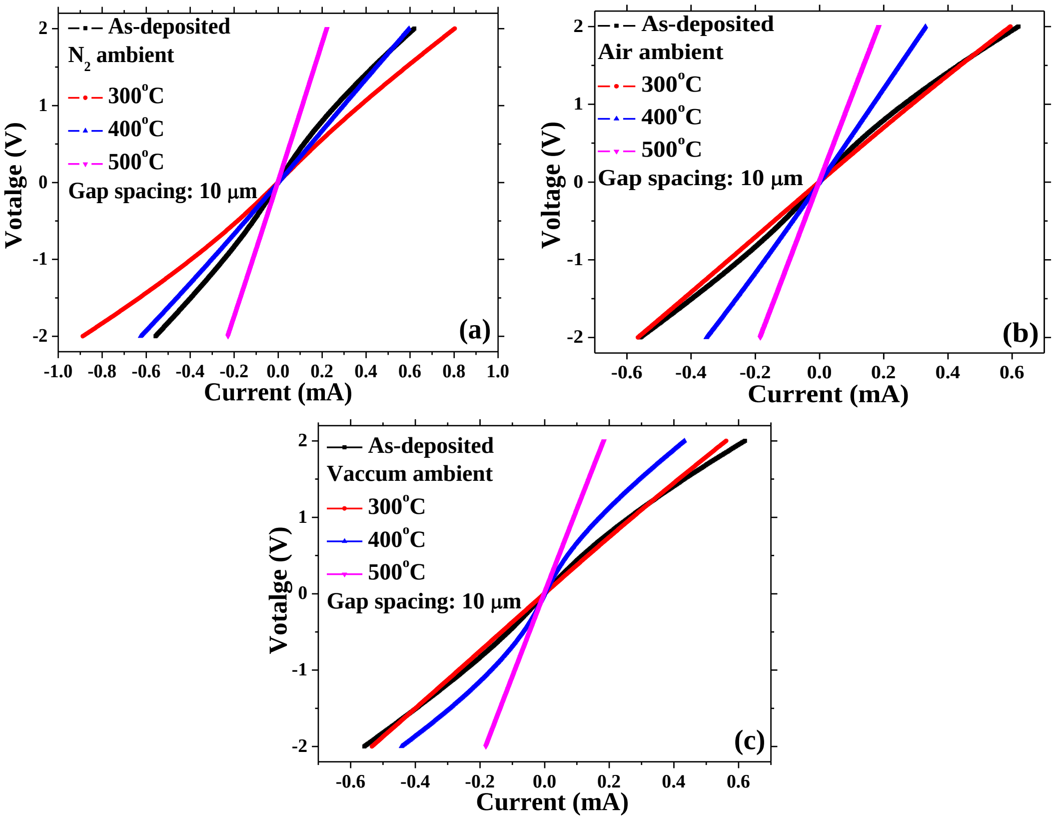

FIGURE 5.5: I-V characteristics of Pd-based contacts to p-type GaN annealed at different temperatures in (a) N_2, (b) air and (c) vacuum ambients, measured on the contact pads with a 10 μm spacing.

Acid solution	Gas	T (°C)	R_s (Ω/sq)	L_t (μm)	ρ_c (Ωcm^2)
HCl (40 %)	As-deposited	N/A	75329	6.8	3.5×10^{-2}
HCl (40 %)	N_2	300	82224	2.1	3.4×10^{-3}
HCl (40 %)	N_2	400	103093	2.8	7.8×10^{-3}
HCl (40 %)	N_2	500	188400	5.7	6.1×10^{-2}
HCl (40 %)	Air	300	105340	3.2	1.1×10^{-2}
HCl (40 %)	Air	400	127089	7.4	6.8×10^{-2}
HCl (40 %)	Air	500	227669	8.8	1.8×10^{-1}
HCl (40 %)	Vacuum	300	97020	5.1	2.5×10^{-2}
HCl (40 %)	Vacuum	400	109611	6.4	4.4×10^{-2}
HCl (40 %)	Vacuum	500	190805	8.0	1.2×10^{-1}

Table 5.3: Contact properties of Pd-based contacts to p-type GaN annealed at different temperatures and in different gas ambients at a bias voltage of 2 V. The T in the table is the annealing temperature.

The calculated ρ_c at a bias voltage of 2 V is plotted in Figure 5.6 as a function of annealing temperature. As shown, for different gas ambients, the Pd-based contacts to p-type GaN annealed at 300 °C always show the lowest ρ_c compared with those annealed at other temperatures. Thus, it is necessary to give an explanation for this phenomenon. Compared with the as-deposited Pd contact to p-type GaN, the lower ρ_c of the Pd-based contacts to p-type GaN annealed at 300 °C can be explained by two possible reasons. Firstly, it has been demonstrated that the thermal annealing process can further remove the residual surface oxidation layer on top of the p-type GaN layer. This leads to a more intimate contact between Pd and the p-type GaN surface and, hence, a reduction of the ρ_c [8]. Secondly, Pd can react with mobile excess Ga on the GaN surface to form a variety of Pd gallides during thermal annealing [25]. This reaction generates the acceptor-like Ga vacancies leading to a higher hole concentration in the near-surface region of the p-type GaN layer, which can also reduce the ρ_c. However, when the annealing temperature is higher than 300 °C, a degradation of the ρ_c is observed.

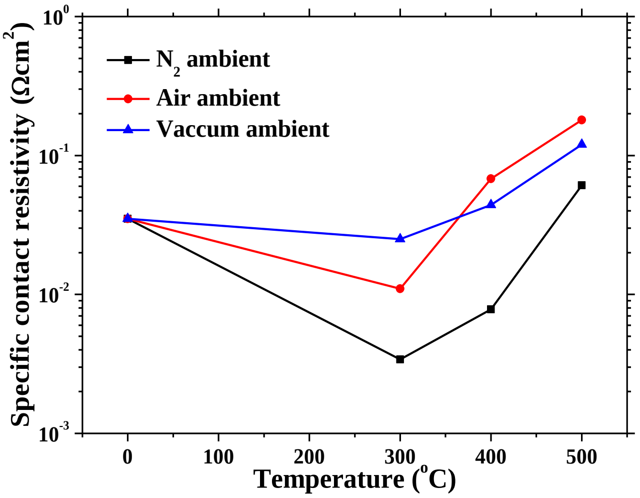

FIGURE 5.6: Calculated ρ_c of Pd-based contacts to p-type GaN annealed in different gas ambients as a function of annealing temperature. All the data are calculated at a bias voltage of 2 V.

To get a further understanding of this degradation, the surfaces of these Pd-based contacts to p-type GaN were inspected by SEM. Figure 5.7(b)-(d) show the typical SEM images of the surface of the Pd-based contact to p-type GaN annealed at 300 °C, 400 °C and 500 °C in the N_2 ambient, respectively. A reference of the as-deposited Pd contact to p-type GaN is also shown as Figure 5.7(a). As mentioned, Pd can react with Ga to form Pd gallides. As highlighted by black curves in Figure 5.7(b), the clusters observed in the SEM image of the sample annealed at 300 °C may be the formed Pd gallides. However, when the annealing temperature increases to 400 °C, as shown in Figure 5.7(c), these clusters reduce the size and become less dominant on top of the contact surface. Meanwhile, some grain boundary regions are also observed as highlighted by the white curves. These damage regions are more dominant for the sample annealed at 500 °C. As shown in Figure 5.7(d), these damage regions connect with each other generating cracks on the top surface. The large lattice mismatch (16 %) between Pd (111) and GaN (0001) at the interface is considered to result in these damage regions [26]. These damage regions reduce the effective contact area between Pd and the p-type GaN layer, which leads to the higher ρ_c of samples annealed at higher temperatures.

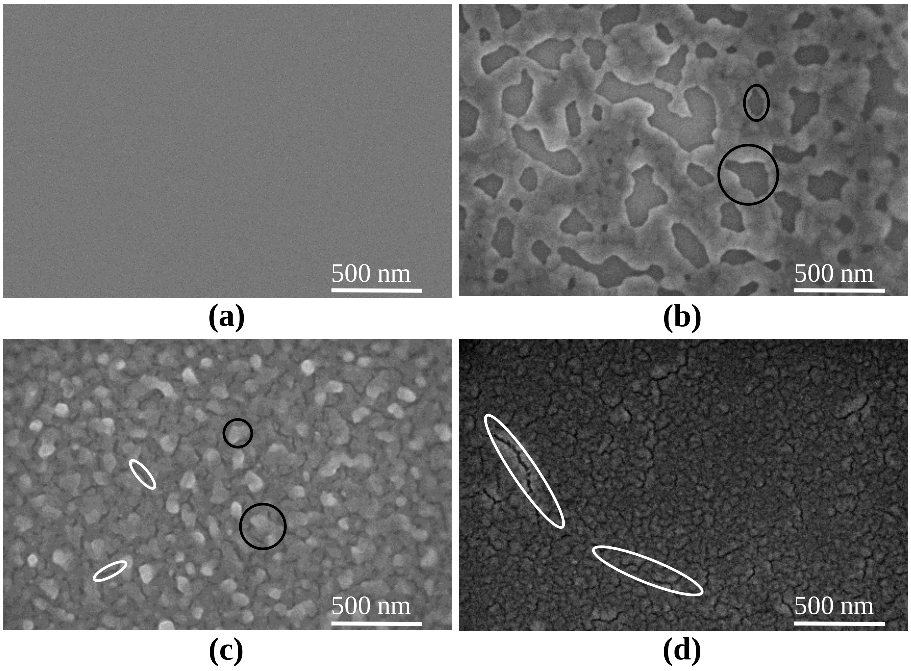

Figure 5.7: SEM images of Pd-based contacts to p-type GaN with different thermal annealing processes: (a) without thermal annealing; (b) at 300 °C in a N_2 ambient; (c) at 400 °C in a N_2 ambient; (d) at 500 °C in a N_2 ambient. Examples of Pd gallides and damage regions are labelled by the black and white curves, respectively.

From Figure 5.6, it is also found that the samples annealed in the N_2 ambient have the lowest ρ_c at each temperature compared with the samples annealed in other ambients. The exact reason of this phenomenon is still under investigation although the reduction of N vacancies is one possible explanation. As introduced in section 1.3, the N vacancy is a donor-like defect which reduces the effective hole concentration of p-type GaN. Compared with the annealing process in other ambients, the annealing process in a N_2 ambient may reduce the N vacancies, resulting in a relatively higher hole concentration of p-type GaN. Thus, a Pd-based contact to p-type GaN annealed in the N_2 ambient has a lower ρ_c compared with those annealed in other ambients.

5.3 Generalization of transmission line method for nonlinear metal-semiconductor contacts

As demonstrated in the last section, the ρ_c of Pd-based contacts to p-type GaN can be reduced by proper surface cleaning and thermal annealing. However, an ideal ohmic contact in a wider bias region is still barely achieved. This nonlinear characteristic is inherent for the metal contact to wider-bandgap semiconductors such as p-type GaN [27]. This issue has been emphasized in previous work where the ρ_c of metal contacts to p-type GaN is strongly dependent on the injection current density [20, 28]. The standard TLM method assumes that the contact is strictly ohmic and, thus, that ρ_c is identical at any injection current density. Consequently, this standard method is not suitable to calculate the current-density dependent ρ_c of a nonlinear contact to p-type GaN. Since the III-nitride μ-LEDs can be operated at a much higher current density as introduced in subsection 1.4.1, the influence of this current-density dependent ρ_c is more pronounced for them. In this section, in order to directly calculate the ρ_c as a function of injection current density, a generalized TLM method is introduced. Based on the data of an as-deposited Pd contact to p-type GaN measured from rectangle-TLM (R-TLM) patterns, the application of this generalized TLM method is also demonstrated.

Figure 5.8(a) shows the schematic diagram of a rectangular contact pad used in the R-TLM method. To calculate the ρ_c of a contact at the interface between metal and semiconductor, the basic transmission line equations consist of two differential equations. These two differential equations are used to describe the relationships between the current flowing under the contact pad and the voltage dropped across the contact interface. The model and parameters used for these two equations are schematically illustrated in Figure 5.8(b). As shown, the resistance elements contributed from the semiconductor layer and the contact between metal and semiconductor are described as $\frac{R_s \mathrm{d}x}{W}$ and $\frac{\rho_c}{\mathrm{d}x W}$, respectively, where W is the width of the rectangular contact pad shown in Figure 5.8(a) and $\mathrm{d}x$ is the length of a contact element. Based on these parameters, the basic transmission line equations are expressed as:

$$\frac{\mathrm{d}V}{\mathrm{d}x} = -\frac{R_s}{W} I(x) \tag{5.6}$$

and

$$\frac{\mathrm{d}I}{\mathrm{d}x} = -\frac{V(x)W}{\rho_c} \tag{5.7}$$

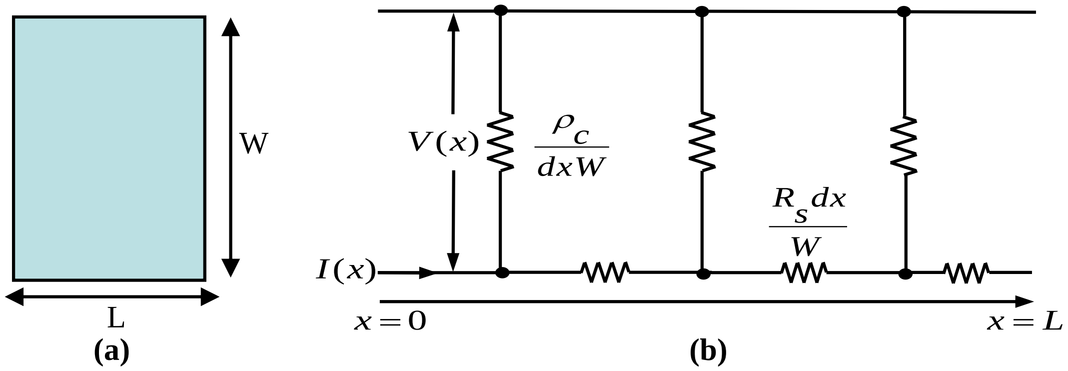

FIGURE 5.8: (a) Schematic diagram of a rectangular contact pad used in the R-TLM method; (b) transmission line model and parameters for a rectangular contact pad.

where $I(x)$ and $V(x)$ are the current flowing under the contact pad at x and the voltage dropped across the contact interface at x, respectively.

In the standard TLM method, ρ_c is assumed as a constant parameter. However, in a general case, it should be dependent on $V(x)$. Thus, Equation 5.7 can be rewritten as:

$$\frac{\mathrm{d}I}{\mathrm{d}x} = -\frac{V(x)W}{\rho_c(V(x))} \Rightarrow \frac{\mathrm{d}I}{\mathrm{d}x} = -j_c\left(V(x)\right)W \Rightarrow j_c\left(V(x)\right) = -\frac{1}{W}\frac{\mathrm{d}I}{\mathrm{d}x} \tag{5.8}$$

where $\rho_c(V(x))$ is the voltage dependent specific contact resistivity and $j_c(V(x))$ is the current density as a function of voltage. Both of these are generally nonlinear. Then, Equation 5.6 and Equation 5.8 are multiplied by each side and integrated over the length of the contact pad which varies from $x = 0$ to $x = L$, where L is the length of rectangular contact pads shown in Figure 5.8(a). At $x = 0$, the injected current and applied voltage correspond to the total current (I_c) and contact voltage (V_c) across the metal and semiconductor layers, respectively. Furthermore, by assuming L is sufficiently long, the current and voltage at $x = L$ are equal to 0. This process leads to the relation:

$${I_c}^2 = -\frac{2W^2}{R_s}\int_{V=V_c}^{V=0} j_c(V)\mathrm{d}V \tag{5.9}$$

Then after a differentiation of Equation 5.9 respected to V_c, we obtain:

$$j_c(V = V_c) = \frac{R_s}{W^2} I_c(V_c)\frac{\mathrm{d}I_c}{\mathrm{d}V_c} \tag{5.10}$$

In term of resistances, the final presentation of the formula for a generalized TLM method should be:

$$\rho_c(V_c) = \frac{W^2}{R_s}\frac{V_c}{I_c}\frac{\mathrm{d}V_c}{\mathrm{d}I_c} = \frac{W^2}{R_s}R_cR_c^* \tag{5.11}$$

where $R_c{=}\frac{V_c}{I_c}$ and $R_c^*{=}\frac{\mathrm{d}V_c}{\mathrm{d}I_c}$ are, respectively, the common and differential resistances of a single rectangular contact pad in the R-TLM method. In this generalized TLM method, since the ρ_c is dependent on the V_c, the relationship between the current density and ρ_c can be further obtained by $j_c = V_c/\rho_c$. For an ideal ohmic contact, the ρ_c is independent on the $V(x)$, where $R_c = R_c^*$. So, the formula for this generalized TLM method becomes the common one used for the standard R-TLM method:

$$\rho_c = \frac{W^2}{R_s}R_c^2 \tag{5.12}$$

A practical application of this generalized TLM method is demonstrated in the following. An as-deposited Pd contact to p-type GaN is used for demonstration because of its pronounced nonlinear characteristic. Since the generalized TLM method is developed based on R-TLM method, the R-TLM patterns were prepared on the top p-type GaN layer of the LED wafer. The schematic diagram of these patterns is shown in Figure 5.9. A large mesa was etched by $\mathrm{Cl_2}$-based inductively coupled plasma first to eliminate the unwanted current flow at the edge of contact pads. After surface cleaning by HCl (40 %) for 5 min, a 30 nm-thick Pd layer was deposited on the sample. After metal lift-off, nine Pd contact pads were formed on the mesa. Each Pd contact pad had the shape of a rectangle with a W of 500 μm and an L of 250 μm. The spacing between two adjacent contact pads varied from 5 to 40 μm with a 5 μm step. The I-V characteristics of these contact pads were measured in a bias region from -5 to 5 V.

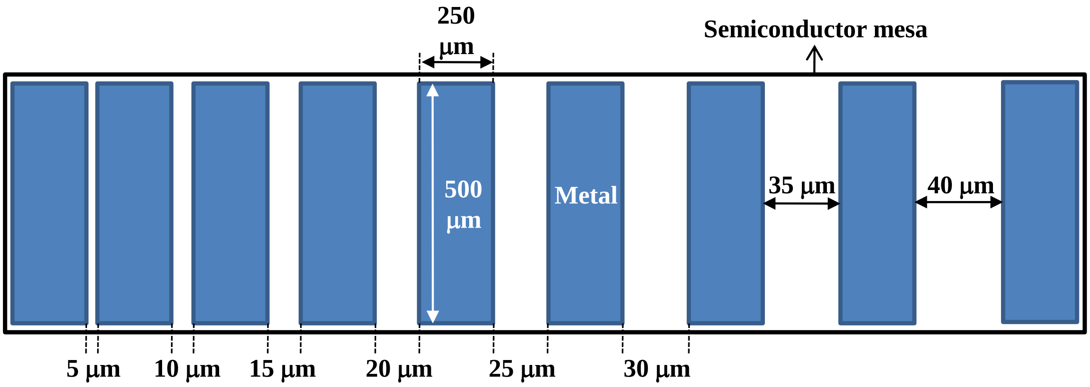

FIGURE 5.9: Schematic diagram of the R-TLM patterns used. The blue-colour region is the metal layer and the white region is the semiconductor layer.

Figure 5.10(a) shows the I-V characteristics of adjacent contact pads with different spacings for the as-deposited Pd contact to p-type GaN. The nonlinear I-V characteristics can be clearly observed from this figure. To extract the R_c, R_c^* and R_s for the generalized TLM method (Equation 5.11), the total resistance (R) of the adjacent contact pads was first calculated by $R = V/I$ at each current. The calculated R consists of the common contact resistance of two adjacent contact pads (R_{2c}) and the resistance of the p-type GaN layer between these two pads ($R_{p,gap}$). Clearly, the latter is proportional to the spacing between the adjacent contact pads. The calculated results are plotted in Figure 5.10(b). As shown, the unequal characterization of R is a result of the nonlinear properties of this as-deposited Pd contact to p-type GaN. The vertical-shift at $I = 0$ mA between each curve in Figure 5.10(b) represents the difference of $R_{p,gap}$ arising from the p-type GaN layer and, thus, can be used to calculate the R_s of the p-type GaN layer. For this sample, this difference is found to be 1381 $\Omega/5\ \mu$m giving a value of 138100 Ω/sq for the R_s of the p-type GaN layer. Then the R_{2c} and its differential counterpart (R_{2c}^*) of any two adjacent contact pads can be obtained by:

$$R_{2c} = \frac{V}{I} - R_{p,gap} = R - R_{p,gap} \tag{5.13}$$

and

$$R_{2c}^* = \frac{\mathrm{d}V}{\mathrm{d}I} - R_{p,gap} \tag{5.14}$$

As show in Figure 5.10, with a maximum bias voltage of 5 V, the two adjacent contact pads with a 5 μm spacing have the widest operation-current region. Thus, it is beneficial to use these two contact pads to investigate the current-density

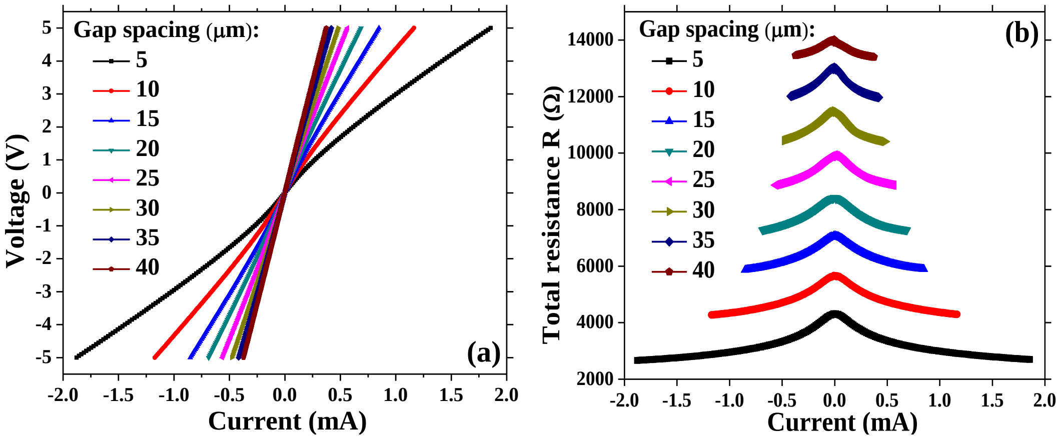

FIGURE 5.10: (a) I-V characteristics of adjacent contact pads with different spacings for an as-deposited Pd contact to p-type GaN; (b) calculated total resistances of adjacent contact pads with different spacings as a function of injected current, the vertical-shift of each curve at $I = 0$ mA can be used to determine the R_s of p-type GaN.

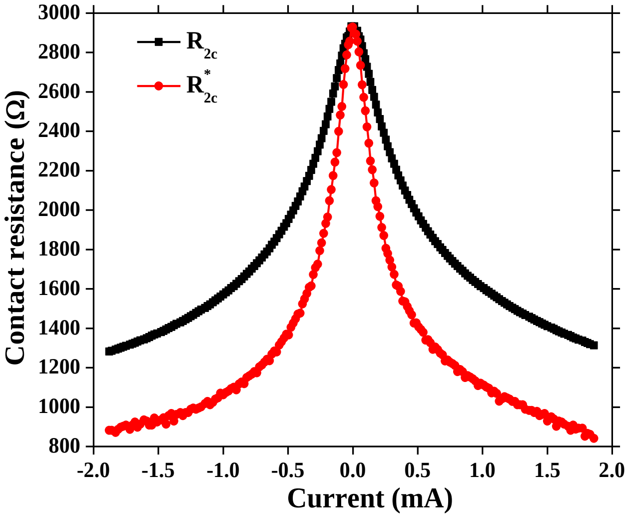

FIGURE 5.11: R_{2c} and R^*_{2c} of two adjacent pads with a 5 μm spacing.

dependent ρ_c for the as-deposited Pd contact to p-type GaN. The R_{2c} and R^*_{2c} of these two pads are calculated and shown in Figure 5.11 as a function of injection current. As illustrated in Equation 5.11, the experimental results plotted here need to be further transferred for a single contact pad as R_c and R^*_c. Unlike the ideal ohmic contact where $R_c = R^*_c = R_{2c}/2$, in this nonlinear contact case, one of the contacts is a forward-biased Schottky contact and another is a reverse-biased Schottky contact. Since the contribution from the forward-biased contact is small, it is reasonable to directly take $R_c = R_{2c}$ and $R^*_c = R^*_{2c}$ [28].

By using the R_{2c} and R^*_{2c} shown in Figure 5.11 and Equation 5.11, the ρ_c of this as-deposited Pd contact to p-type GaN was calculated at each injected current. To built the relationship between the ρ_c and current density, the V_c corresponding to the calculated ρ_c is first obtained by $V_c = R_{2c}I$. Then, the corresponding current density is further obtained by taking $j_c = V_c/\rho_c$. Figures 5.12(a) and (b) show the ρ_c of this as-deposited Pd contact to p-type GaN as a function of contact voltage and current density, respectively. Both results demonstrate that ρ_c is strongly dependent on the current voltage and/or injection current density due to the nonlinear properties of this as-deposited Pd contact to p-type GaN. As shown in Figure 5.12(b), on increasing the injection current density close to 100 A/cm^2, ρ_c becomes much smaller compared with the value at a low injection current density. This result shows clearly nonlinear characteristics of the metal contact to p-type GaN which cannot be neglected for III-nitride devices, especially when they are operated at a high current density such as μ-LEDs and LDs.

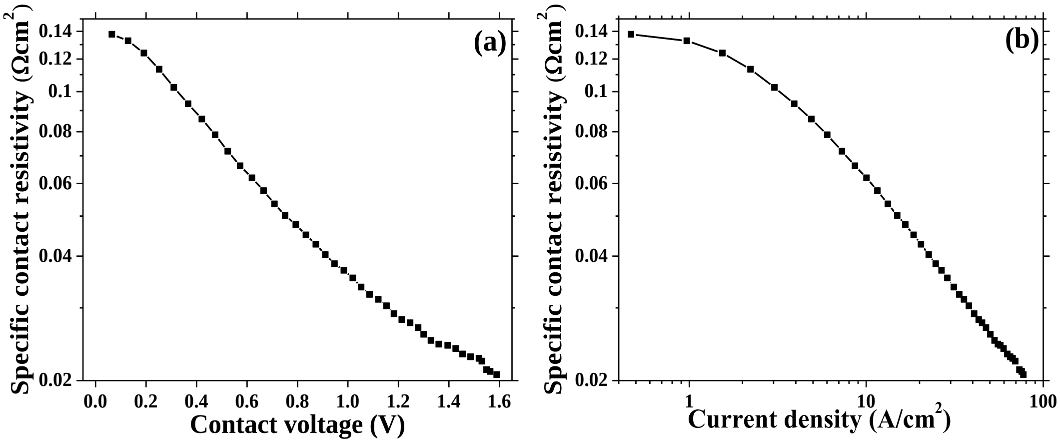

FIGURE 5.12: Calculated ρ_c of an as-deposited Pd contact to p-type GaN as a function of (a) contact voltage and (b) injection current density through the generalized TLM method.

5.4 Comparison of nonlinear metal contacts to p-type GaN

Using the generalized TLM method described in section 5.3, the ρ_c of the best annealed Pd contact to p-type GaN, which is achieved by HCl (40 %) surface cleaning and thermal annealing at 300 °C in a N_2 ambient, was characterized and is compared in this section with that of the oxidized Ni/Au contact as a function of injection current density. The structure and fabrication process of the R-TLM patterns used were the same as those described in the last section. After the mesa etching and surface cleaning, the metal layers (either 30 nm-thick Pd or 10 nm/20 nm-thick Ni/Au) were evaporated on two samples. Then the metal contact pads on the p-type GaN layer were fabricated by using the lift-off technique. The sample with Pd metal pads was annealed at the optimized temperature of 300 °C in a N_2 ambient for 3 min. The one with Ni/Au metal pads was annealed at 500 °C in an air ambient for 3 min, which is the conventional thermal annealing process for the oxidized Ni/Au contact to p-type GaN as introduced in subsection 2.1.3.

Figure 5.13(a) shows the typical I-V characteristics of annealed Pd and oxidized Ni/Au contacts to p-type GaN, measured on the adjacent pads with a 5 μm spacing from -5 to 5 V. As shown, nonlinear behaviour is observed in this wider bias region for both samples. Compared with the annealed Pd contact to p-type GaN, the oxidized Ni/Au one shows a more linear I-V characteristic. Furthermore, the electrical properties of the oxidized Ni/Au contact to p-type GaN are better than the annealed Pd one in the bias region from -2 to 2 V. However, due to the nonlinear behaviour, the annealed Pd contact to p-type GaN shows higher currents than the oxidized Ni/Au one at higher bias voltages. In order to take into account this nonlinear behaviour, the specific contact resistivities of both contacts to p-type GaN are compared as a function of injection current density through the generalized TLM method, as introduced in the last section. The calculated results for both contacts are shown in Figure 5.13(b). It can be seen that the variation trends of the current-density dependent ρ_c for these two contacts to p-type GaN are similar. Both contacts to p-type GaN show a slight decrease of the ρ_c in the low injection current-density region followed by an abrupt, exponential-like droop with increasing injection current density. In the low injection current-density region, the oxidized Ni/Au contact to p-type GaN has a lower ρ_c until the injection current density reaches 20 A/cm^2. Then, the ρ_c of the annealed Pd contact to p-type GaN becomes lower in the higher injection current-density region.

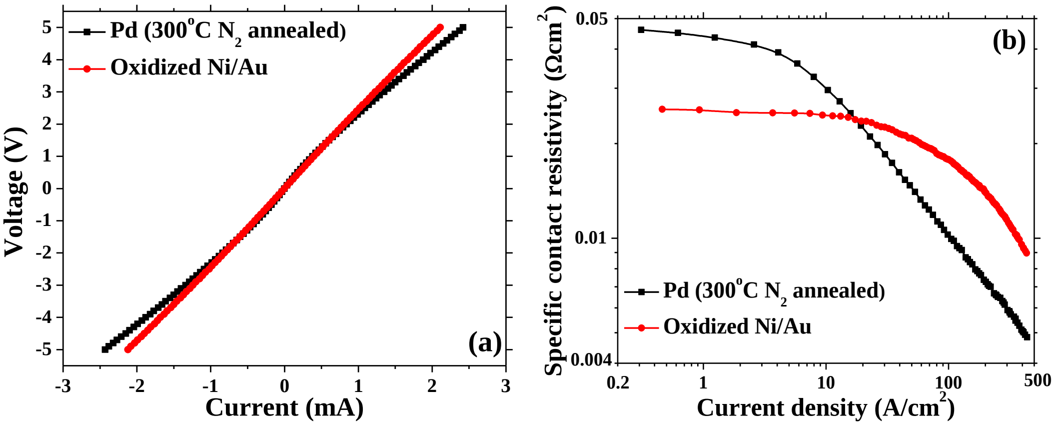

FIGURE 5.13: (a) I-V characteristics of annealed Pd and oxidized Ni/Au contacts to p-type GaN, measured on the adjacent R-TLM pads with a 5 μm spacing; (b) current-density dependent resistivities of annealed Pd and oxidized Ni/Au contacts to p-type GaN.

In order to investigate the exact influence of this current-density dependent ρ_c on III-nitride LEDs, two broad-area LEDs with either annealed Pd or oxidized Ni/Au contact to p-type GaN were fabricated by using a commercial blue $In_xGa_{1-x}N$/GaN-based LED wafer. The epitaxial structure of this wafer has been described in subsection 5.2.1. These two devices had a 300×300 μm^2 emission area. The LED fabrication process was the same as the one described in chapter 4 except that the annealed Pd and oxidized Ni/Au contacts to p-type GaN were used for each device respectively. For III-nitride LEDs, the ρ_c of the metal contact to p-type GaN is believed to have a great influence on their operating voltage and differential resistance (dV/dI) [29]. As the ρ_c increases, a larger voltage-drop across the contact is expected which leads to a higher threshold voltage and, thus, higher operating voltages at each current and/or current density. Furthermore, when the device is operated at high forward currents, it is reasonable to assume the change of dV/dI is dominated by the change from the ρ_c at different operating current densities.

The current density-voltage (j_c-V) characteristics of both broad-area LEDs are measured and shown in Figure 5.14(a). The calculated differential resistances above an operating current of 5 mA, corresponding to a current density of 6 A/cm^2, are plotted in Figure 5.14(b) for these two devices. As shown, the operating voltage of the broad-area LED with oxidized Ni/Au contact to p-type GaN is lower at each current density due to the lower ρ_c of the oxidized Ni/Au contact to p-type GaN in the low operation current-density region. However, the dV/dI of this device becomes larger than that of the broad-area LED with annealed Pd contact to p-type GaN when the operating current density is higher than 20 A/cm^2. These results agree well with the results of the current-density dependent ρ_c shown in Figure 5.13(b) and, thus, endorse the generalized TLM method. Furthermore, since the μ-LEDs can be operated at a much higher current density as introduced in subsection 1.4.1, it is expected that the μ-LEDs with annealed Pd contacts to p-type GaN should have better electrical performance compared with those with the oxidized Ni/Au contacts.

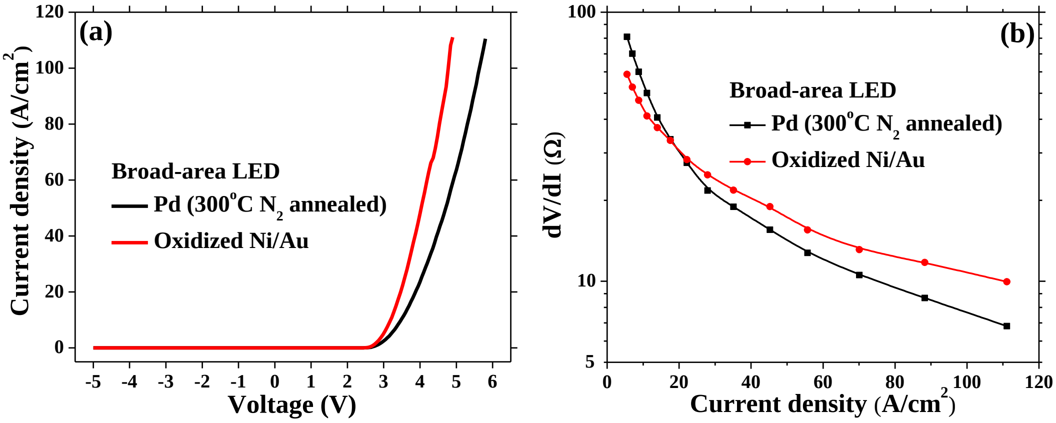

FIGURE 5.14: (a) j_c-V characteristics and (b) calculated differential resistances of broad-area LEDs with annealed Pd and oxidized Ni/Au contacts to p-type GaN.

Besides the electrical properties, the optical properties of the metal contacts to p-type GaN are also important for III-nitride LEDs, since they strongly affect the LEE of LEDs with different configurations. The high-transparency nature of the oxidized Ni/Au bilayer and high-reflectivity nature of the Pd layer lead them to be suitable for devices with top-emission and flip-chip configurations, respectively. Nevertheless, in order to mimic the structure of devices with flip-chip configurations, it is still valuable to compare the reflectivity of oxidized Ni/Au and annealed Pd layers capped with an additional Ti/Au reflector. Thus, two samples were prepared for reflectivity measurements. Figure 5.15 shows a schematic diagram of the sample structure and the measurement conditions for reflectivity measurements. The metal layers with 30 nm-thick Pd and 10 nm/20 nm-thick Ni/Au were deposited on two sapphire substrates and thermally annealed. The conditions of the thermal annealing process for Pd and Ni/Au layers were the same as those used for metal contacts to p-type GaN as described above. Then, a thick Ti/Au

(50 nm/200 nm) reflector was further capped on annealed Pd and oxidized Ni/Au layers. The reflectivity of each sample was measured by a UV/Vis spectrophotometer (Perkin Elmer Lambda 2). The incident light was passed through the surface of the sapphire substrate without metal layers. The angle of incidence was nearly 0 °.

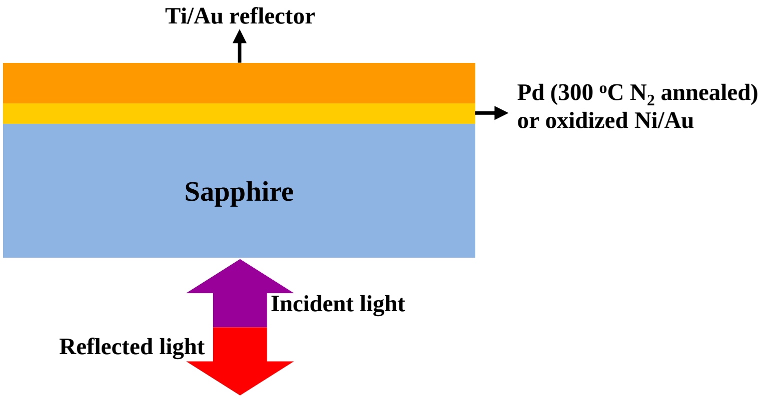

FIGURE 5.15: Schematic diagram of the sample structure and measurement condition for reflectivity measurements.

Figure 5.16 shows the reflectivity of each sample at different wavelengths. It can be found that, from the ultraviolet to green wavelengths, the reflectivity of the annealed Pd layer capped with the Ti/Au reflector is higher than that of oxidized Ni/Au bilayer capped with the Ti/Au reflector. Furthermore, due to the high transparency of the oxidized Ni/Au bilayer, the reflectivity of the sample with oxidized Ni/Au bilayer is mainly provided by the Ti/Au reflector. Thus, the sample with oxidized Ni/Au bilayer is preferred when the emission wavelength is longer than 530 nm. These results provide important information for the selection of metal contacts to p-type GaN in order to achieve the higher LEE for III-nitride LEDs with flip-chip configurations emitting at different wavelengths.

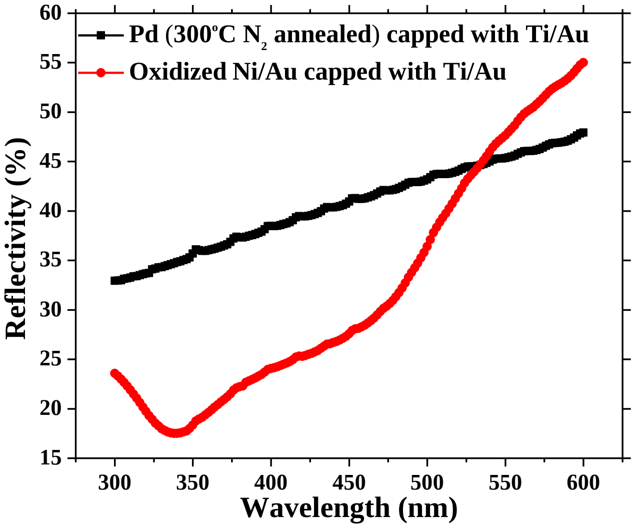

FIGURE 5.16: Reflectivities of annealed Pd and oxidized Ni/Au layers capped with a thick Ti/Au reflector though sapphire substrates.

5.5 Performance of micro-light emitting diodes with different metal contacts to p-type GaN

As presented in section 5.4, compared with the oxidized Ni/Au contact to p-type GaN, the annealed Pd one has been proven to have the lower ρ_c at injection current densities above 20 A/cm^2. Thus, the annealed Pd contact to p-type GaN is a better contact candidate for μ-LEDs which are operated at higher current densities. Furthermore, the annealed Pd contact to p-type GaN also offers a potential enhancement of the LEE from UV to green wavelengths for III-nitride LEDs with flip-chip configurations. To confirm and compare the electrical and optical performance, μ-LEDs with annealed Pd and oxidized Ni/Au contacts to p-type GaN were fabricated and characterized. These 450 nm μ-LEDs were with flip-chip configurations and an additional Ti/Au bilayer served as a reflector. These disc-shaped μ-LEDs had a diameter of 44 μm. The epitaxial structure of the blue $In_xGa_{1-x}N$/GaN-based LED wafer used and the device fabrication process were the same as those for the broad-area LEDs presented in section 5.4. In addition to the electrical property, light output power of these μ-LEDs under direct-current (DC) conditions were measured using a Si detector placed in close proximity through the transparent sapphire substrate. By using a high-resolution photomultiplier tube, the relative external quantum efficiency (EQE) of the μ-LEDs was also measured.

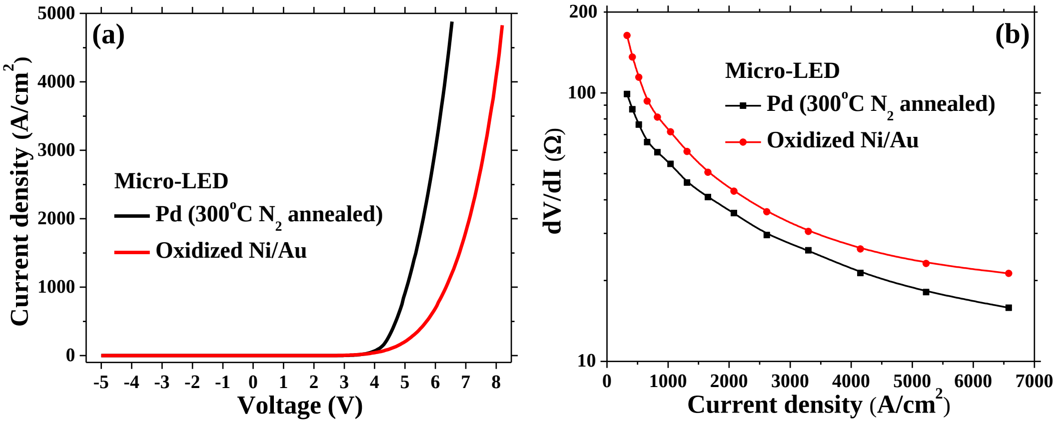

FIGURE 5.17: (a) j_c-V characteristics and (b) calculated differential resistances of μ-LEDs with annealed Pd and oxidized Ni/Au contacts to p-type GaN.

To limit the self-heating effect, the μ-LEDs were operated under 100 μs current pulses at 0.5 % duty cycle during the EQE measurements.

Figure 5.17(a) shows the j_c-V characteristics of μ-LEDs with different contacts to p-type GaN. The differential resistances of these devices above an operating current of 5 mA, corresponding to an operating current density of 330 A/cm^2, were also calculated and are shown in Figure 5.17(b). As introduced in subsection 1.4.1, the μ-LEDs can sustain a much higher operating current density compared with conventional broad-area LEDs. Although the calculated current-density dependent specific contact resistivities shown in Figure 5.13(b) do not cover such a wide current-density region, the trends illustrate that the ρ_c of the annealed Pd contact to p-type GaN should be always lower than the one of the oxidized Ni/Au contact to p-type GaN at current densities above 20 A/cm^2. Thus, it is expected that the μ-LED with an annealed Pd contact to p-type GaN should have superior electrical characteristics. As shown in Figure 5.17, the μ-LED with annealed Pd contact to p-type GaN presents not only the lower operating voltage at each current density but also a reduced dV/dI compared with the device with oxidized Ni/Au contact to p-type GaN. Based on the electrical performance of μ-LEDs and previous broad-area LEDs, it can be concluded that consideration of the current-density dependent ρ_c of metal contacts to p-type GaN is necessary for III-nitride LEDs, especially when they are operated in different current-density regions.

Figure 5.18 shows the optical power of these two μ-LEDs with flip-chip configurations measured under DC conditions. Compared with the μ-LED with an oxidized Ni/Au contact to p-type GaN, it is found that the μ-LED with the annealed Pd

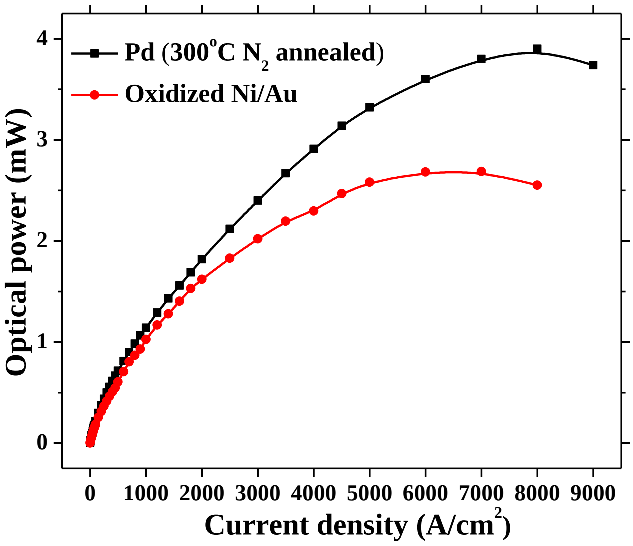

FIGURE 5.18: Optical power of μ-LEDs with annealed Pd and oxidized Ni/Au contacts to p-type GaN measured under DC conditions.

contact shows a pronounced enhancement in optical power at any operating current density. At 7000 A/cm^2, which is the roll-over current density of the μ-LED with the oxidized Ni/Au contact to p-type GaN, the device with the annealed Pd contact shows around 40 % increase in the optical power. This increase is similar to the reflectivity enhancement measured at around 450 nm as shown in Figure 5.16. Thus, the enhanced optical power of the μ-LED with the annealed Pd contact to p-type GaN is mainly attributed to the higher reflectivity of the annealed Pd layer capped with a Ti/Au reflector. Furthermore, due to the lower ρ_c of the annealed Pd contact to p-type GaN in this high current-density region, the self-heating effect for the μ-LED with the annealed Pd contact to p-type GaN is much less. Thus, this μ-LED can be operated at a higher current density to achieve the maximum output power. As shown, the roll-over current density of the μ-LED with the annealed Pd contact to p-type GaN is increased from 7000 to 8000 A/cm^2 compared with the μ-LED with an oxidized Ni/Au contact.

Another characteristic needing to be considered for these two μ-LEDs is the efficiency droop, as introduced in section 1.4. The possible difference of efficiency droop between these two devices comes from different annealing temperatures for annealed Pd and oxidized Ni/Au contacts to p-type GaN. It is well known that plasma etching induces damage on the etched GaN pillar sidewall [30]. This plasma damage is more pronounced for μ-LEDs, as they have an increased surface-to-volume ratio. The shallow and/or deep defect levels resulting from the plasma damage supply the carrier transportation paths [31, 32]. The carriers tunnelling through these defect levels generate the forward leakage current and, thus, reduce the effective current for radiative carrier recombination. This phenomenon is considered as a possible mechanism of the efficiency droop of III-nitride LEDs [33]. Thermal annealing has been demonstrated as an effective way to recover the plasma damage for III-nitride LEDs and, thus, reduce the forward leakage current. It has been shown that the efficiency of damage recovery can be enhanced by increasing of the annealing temperature [34]. Considering different temperatures used to anneal the Pd (300 °C) and oxidized Ni/Au (500 °C) contacts to p-type GaN, these two μ-LEDs may show different efficiency-droop behaviours. Thus, the relative EQE of each μ-LED was measured and is plotted in Figure 5.19. Each curve in this figure is normalized to its peak value to exclude the differences of the LEE between these two devices and the collection efficiency during the measurements. It can be seen that the efficiency droop of the μ-LED with the annealed Pd contact to p-type GaN is comparable to the droop of the μ-LED with the oxidized Ni/Au contact. A slight difference can be found when the operating current density is higher than 2000 A/cm^2. It may be due to the difference of annealing temperature or the measurement error. Based on this result, it can be concluded that the forward leakage current is not the dominant mechanism of the efficiency droop for these two devices. Other mechanisms, as discussed in section 1.4, need to be considered.

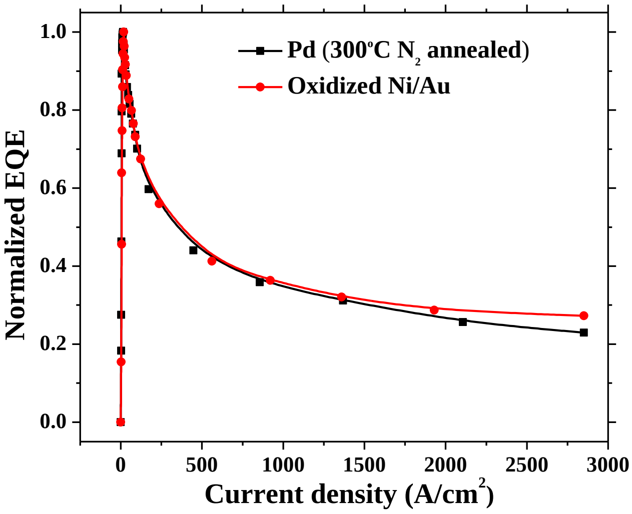

FIGURE 5.19: Normalized EQE curves of μ-LEDs with annealed Pd and oxidized Ni/Au contacts to p-type GaN.

5.6 Summary

In this chapter, as a choice of ohmic contact to p-type GaN, Pd is used to further enhance the performance of III-nitride μ-LEDs. To achieve a Pd-based contact to p-type GaN with a low ρ_c, the systematic optimization of the fabrication process were performed including surface cleaning and thermal annealing. Surface cleaning by HCl (40 %) and thermal annealing at 300 °C in a N_2 ambient proved to be the most effective way to reduce the ρ_c of Pd-based contacts to p-type GaN.

However, the fundamental problems of p-type GaN result in difficulty to achieve ideal ohmic contacts to p-type GaN. The nonlinear I-V characteristics of metal contacts to p-type GaN in a wider bias region demonstrate that the ρ_c of these contacts is a function of injection current density. So, a generalized TLM method was introduced to directly calculate the current-density dependent ρ_c. Its application was also demonstrated based on the data of an as-deposited Pd contact to p-type GaN. Then, the specific contact resistivities of the best annealed Pd and conventional oxidized Ni/Au contacts to p-type GaN were compared as a function of injection current density. The result illustrates that the ρ_c of the annealed Pd contact to p-type GaN is lower than that of the oxidized Ni/Au contact when the injection current density is higher than 20 A/cm^2. This finding was validated by comparing the electrical performance of III-nitride broad-area LEDs. Furthermore, to mimic the structure of III-nitride LEDs with flip-chip configurations, the reflectivities of annealed Pd and oxidized Ni/Au layers capped with a Ti/Au reflector were compared. The former shows higher reflectivity from the ultraviolet to green wavelengths and the latter is preferred when the emission wavelength is longer than 530 nm.

Finally, the performance of μ-LEDs with annealed Pd and oxidized Ni/Au contacts to p-type GaN was compared. These 44 μm-diameter devices had flip-chip configurations and a 450 nm emission wavelength. Since the operating current density of these μ-LEDs is higher, the ρ_c of the annealed Pd contact to p-type GaN is lower than that of the oxidized Ni/Au contact to p-type GaN. Thus, better electrical properties are observed for the device with annealed Pd contact to p-type GaN. Meanwhile, the higher reflectivity of the annealed Pd layer capped with the Ti/Au reflector leads to a clear enhancement of the optical power for the μ-LED with annealed Pd contact to p-type GaN. Furthermore, the efficiency droop is similar for these two devices with different metal contacts to p-type GaN.

Thus, the performance of III-nitride blue μ-LEDs with flip-chip configurations can be greatly improved by using the annealed Pd contact to p-type GaN developed in this chapter.

References

[1] S. Kurtin, T.C. McGill, and C.A. Mead. Fundamental transition in the electronic nature of solids. *Physical Review Letters*, 22(26):1433–1436, 1969.

[2] Y. Koide, H. Ishikawa, S. Kobayashi, S. Yamasaki, S. Nagai, J. Umezaki, M. Koike, and M. Murakami. Dependence of electrical properties on work functions of metals contacting to p-type GaN. *Applied Surface Science*, 117:373–379, 1997.

[3] J.K. Ho, C.S. Jong, C.C. Chiu, C.N. Huang, K.K. Shih, L.C. Chen, F.R. Chen, and J.J. Kai. Low-resistance ohmic contacts to p-type GaN achieved by the oxidation of Ni/Au films. *Journal of Applied Physics*, 86:4491, 1999.

[4] H. Ishikawa, S. Kobayashi, Y. Koide, S. Yamasaki, S. Nagai, J. Umezaki, M. Koike, and M. Murakami. Effects of surface treatments and metal work functions on electrical properties at p-GaN/metal interfaces. *Journal of Applied Physics*, 81(3):1315–1322, 1997.

[5] J.K. Sheu, Y.K. Su, G.C. Chi, W.C. Chen, C.Y. Chen, C.N. Huang, J.M. Hong, Y.C. Yu, C.W. Wang, and E.K. Lin. The effect of thermal annealing on the Ni/Au contact of p-type GaN. *Journal of Applied Physics*, 83(6):3172–3175, 1998.

[6] H.W. Jang, S.Y. Kim, and J.L. Lee. Mechanism for Ohmic contact formation of oxidized Ni/Au on p-type GaN. *Journal of Applied Physics*, 94(3):1748–1752, 2003.

[7] J.L. Lee, M. Weber, J.K. Kim, J.W. Lee, Y.J. Park, T. Kim, and K. Lynn. Ohmic contact formation mechanism of nonalloyed Pd contacts to p-type GaN observed by positron annihilation spectroscopy. *Applied Physics Letters*, 74:2289, 1999.

[8] C. Kim, J. Jang, J. Shin, J.W. Choi, J.H. Seo, W. Kim, J. Park, J.O. Seo, S.J. Leem, B.H. Seung, K.B. Lee, and Y.J. Park. Temperature-driven crystalline ordering and Ohmic contact formation of PdAu layers on p-type GaN. *Physical Review B*, 64(11):113302, 2001.

[9] H.W. Jang, K.H. Kim, J.K. Kim, S.W. Hwang, J.J. Yang, K.J. Lee, S.J. Son, and J.L. Lee. Low-resistance and thermally stable ohmic contact on p-type GaN using Pd/Ni metallization. *Applied Physics Letters*, 79:1822, 2001.

[10] J.S. Jang, C.W. Lee, S.J. Park, T.Y. Seong, and I.T. Ferguson. Low-resistance and thermally stable Pd/Ru ohmic contacts to p-type GaN. *Journal of Electronic Materials*, 31(9):903–906, 2002.

[11] E. Kurimoto, M. Hangyo, H. Harima, K. Takatani, M. Ishida, M. Taneya, and K. Kisoda. Ohmic contact formation on p-type GaN using Pd/Mo electrode without alloying process. *Japanese Journal of Applied Physics*, 43:6988, 2004.

[12] L.S. Yu, L. Jia, D. Qiao, S.S. Lau, J. Li, J.Y. Lin, and H.X. Jiang. The origins of leaky characteristics of Schottky diodes on p-GaN. *Electron Devices, IEEE Transactions on*, 50 (2):292–296, 2003.

[13] H.W. Jang and J.L. Lee. Low-resistance and high-reflectance Ni/Ag/Ru/Ni/Au ohmic contact on p-type GaN. *Applied Physics Letters*, 85:4421, 2004.

[14] C. Huh, H.S. Kim, S.W. Kim, J.M. Lee, D.J. Kim, I.H. Lee, and S.J. Park. InGaN/GaN multiple quantum well light-emitting diodes with highly transparent Pt thin film contact on p-GaN. *Journal of Applied Physics*, 87:4464, 2000.

[15] J.S. Jang, S.J. Park, and T.Y. Seong. Metallization scheme for highly low-resistance, transparent, and thermally stable Ohmic contacts to p-GaN. *Applied Physics Letters*, 76:2898, 2000.

[16] J.O. Song, J.S. Kwak, Y. Park, and T.Y. Seong. Ohmic and degradation mechanisms of Ag contacts on p-type GaN. *Applied Physics Letters*, 86:062104, 2005.

[17] J.O. Song, J.S. Kwak, and T.Y. Seong. Improvement of the ohmic characteristics of Pd contacts to p-type GaN using an Ag interlayer. *Semiconductor Science and Technology*, 21: L7, 2006.

[18] M. Suzuki, T. Arai, T. Kawakami, S. Kobayashi, S. Fujita, Y. Koide, Y. Taga, and M. Murakami. Formation and deterioration mechanisms of low-resistance TaTi ohmic contacts for p-GaN. *Journal of Applied Physics*, 86(9):5079–5084, 1999.

[19] J.O. Song, D.S. Leem, J.S. Kwak, O.H. Nam, Y. Park, and T.Y. Seong. High-quality nonalloyed rhodium-based ohmic contacts to p-type GaN. *Applied Physics Letters*, 83(12): 2372–2374, 2003.

[20] M. Onomura, S. Saito, L. Sugiura, M. Nakasuji, K. Sasanuma, J. Nishio, J. Rennie, S. Nunoue, and K. Itaya. The analysis of contact resistivity between a p-type GaN layer and electrode in InGaN MQW laser diodes. *Materials Science and Engineering B*, 59(1-3): 366–369, 1999.

[21] J.O. Song, J.S. Ha, and T.Y. Seong. Ohmic-contact technology for GaN-based light-emitting diodes: Role of p-type contact. *Electron Devices, IEEE Transactions on*, 57(1):42–59, 2010.

[22] J.K. Sheu, Y.K. Su, G.C. Chi, P.L. Koh, M.J. Jou, C.M. Chang, C.C. Liu, and W.C. Hung. High-transparency Ni/Au ohmic contact to p-type GaN. *Applied Physics Letters*, 74(16): 2340–2342, 1999.

[23] J.K. Kim, J.L. Lee, J.W. Lee, H.E. Shin, Y.J. Park, and T. Kim. Low resistance Pd/Au ohmic contacts to p-type GaN using surface treatment. *Applied Physics Letters*, 73(20): 2953–2955, 1998.

[24] A. Weimar, A. Lell, G. Brüderl, S. Bader, and V. Härle. Investigation of low-resistance metal contacts on p-type GaN using the linear and circular transmission line method. *Physica Status Solidi (a): Applied Research*, 183(1):169–175, 2001.

[25] T.B. Massalski, H. Okamoto, P.R. Subramanian, and L. Kacprzak. Binary alloy phase diagrams. *ASM International, 1990,*, 1990.

[26] C. Nörenberg and M.R. Castell. Atomic-scale studies on the growth of palladium and titanium on GaN (0 0 0 1). *Surface Science*, 601(18):4438–4443, 2007.

[27] V. Adivarahan, A. Lunev, M.A. Khan, J. Yang, G. Simin, M.S. Shur, and R. Gaska. Very-low-specific-resistance Pd/Ag/Au/Ti/Au alloyed ohmic contact to p GaN for high-current devices. *Applied Physics Letters*, 78:2781, 2001.

[28] R. Piotrzkowski, E. Litwin-Staszewska, and S. Grzanka. Towards proper characterization of nonlinear metal-semiconductor contacts. Generalization of the transmission line method. *Applied Physics Letters*, 99(5):052101, 2011.

[29] E.F. Schubert. *Light emitting diodes.* Cambridge University Press, 2^{nd} edition, 2006.

[30] X.A. Cao, H. Cho, S.J. Pearton, G.T. Dang, A.P. Zhang, F. Ren, R.J. Shul, L. Zhang, R. Hickman, and J.M. Van Hove. Depth and thermal stability of dry etch damage in GaN Schottky diodes. *Applied Physics Letters*, 75(2):232–234, 1999.

[31] H. Kim, J. Cho, Y. Park, and T.Y. Seong. Leakage current origins and passivation effect of GaN-based light emitting diodes fabricated with Ag p-contacts. *Applied Physics Letters*, 92:092115, 2008.

[32] J.M. Hwang, K.F. Lee, and H.L. Hwang. Optical and electrical properties of GaN micron-scale light-emitting diode. *Journal of Physics and Chemistry of Solids*, 69(2):752–758, 2008.

[33] N.I. Bochkareva, V.V. Voronenkov, R.I. Gorbunov, A.S. Zubrilov, Y.S. Lelikov, P.E. Latyshev, Y.T. Rebane, A.I. Tsyuk, and Y.G. Shreter. Defect-related tunneling mechanism of efficiency droop in III-nitride light-emitting diodes. *Applied Physics Letters*, 96:133502, 2010.

[34] Y. Yang and X.A. Cao. Complete suppression of surface leakage currents in microperforated blue light-emitting diodes. *Applied Physics Letters*, 95:011109, 2009.

Chapter 6

Development and application of novel microstructured-image light emitting diodes

In this chapter, the development and application of novel III-nitride microstructured-image light emitting diodes (LEDs) are introduced. Compared with normal III-nitride LEDs, a complex emission image with micro-scale feature size, which is produced by combining a CHF_3 plasma treatment and photoresist (PR) patterning, can be achieved for a single microstructured-image LED. In section 6.1, different applications of plasma technology used for III-nitride device fabrication are summarized, and the F-based plasma treatments are considered as a novel process to modify the electrical properties of p-type GaN. The development of III-nitride microstructured-image LEDs is described in section 6.2. The CHF_3 plasma treatment is proven the most effective process to modify the electrical properties of p-type GaN. The possible physical mechanisms of this modification are explored and discussed. Further experimental results indicate that with PR masks, well-defined localized current injection paths can be created in p-type GaN by the CHF_3 plasma treatment. Furthermore, this plasma treatment does not cause damage to the metal layer deposited on top of the p-type GaN layer. By introducing the CHF_3 plasma treatment as an additional step, complex emission images can be created in single LEDs. III-nitride LEDs containing different microstructured emission images are fabricated for demonstration, and the spatial resolution of the CHF_3 plasma treatment is also investigated. Finally, an application of these microstructured-image LEDs, i.e. maskless image writing, is further demonstrated in section 6.3. By using this technique, written patterns with nano-scale feature size can be achieved.

6.1 Applications of plasma technology for III-nitride devices

Nowadays, plasma technology plays an important role in the fabrication of III-nitride optoelectronic and electronic devices. Due to the difficulty of wet etching III-nitride materials, the main application of plasma technology in III-nitride device fabrication is plasma etching. It has been found that GaN can only be etched with a low etching rate by KOH or NaOH at temperatures above 250 °C. The application of wet etching is also not compatible with photoresist (PR) patterning. So the mesa structures of III-nitride light emitting diodes (LEDs) and laser diodes are normally formed by plasma etching. Because the bond strengths of III-nitride materials are much higher than those of the other III-V compound semiconductors [1, 2], the plasma etching process for III-nitride materials is complicated and the etching rate is normally much lower. For III-nitride device fabrication, an anisotropic plasma etching process with high etching rates and smooth etch sidewalls is required. To meet this requirement, different plasma etching techniques and processes have been developed. For example, III-nitride mesa structures have been fabricated by reactive ion etching (RIE) [3] and inductive couple plasma (ICP) etching [4]. Furthermore, the effects of plasma chemistry, including reactive gases (Cl_2 and BCl_3) and additional secondary gases (Ar, O_2, H_2 and N_2), were also investigated in detail. However, the plasma damage on mesa surfaces is an unavoidable problem for plasma etching. This damage leads to the unintentional degradation of the devices' electrical and optical properties. This degradation is more pronounced when the mesa size is reduced down to the micron and nano scale [5–7].

The plasma technology is also an attractive approach to modify the electrical properties of semiconductors. In the case of p-type GaN doped with Mg, high-energy (above several keV) plasma irradiation, such as N_2 [8] and Cl_2 [9] plasmas, has been found to compensate the p-type doping leading to a higher resistance of p-type GaN. In Ref. [9], the high-resistance regions in p-type GaN were selectively created by combining Cl_2 plasma irradiation and PR patterning. This work was performed in an ICP system to implant the Cl ions with high energy. It was proven that high-density N vacancies were created in the regions exposed to high-energy Cl ions. As introduced in section 1.3, these donor-like defects lead to a low hole concentration and, thus, to a high resistance of p-type GaN. Although the localized current injection paths in p-type GaN can be created by combining this Cl_2 plasma irradiation and PR patterning, the resulting high-density N vacancies generate more leakage currents and increase nonradiative recombination centres. These effects lead to the degradation of quantum efficiency and device reliability. Furthermore, in the Cl_2 plasma irradiation, the p-type GaN layer should be etched by the Cl_2 plasma because of the high reactivity between Cl ions and GaN. Thus, Cl_2 plasma irradiation is less suitable for the fabrication of III-nitride optoelectronic and electronic devices. On the other hand, much less N vacancies would be generated if the ion energy was greatly reduced, i.e. using a low-energy plasma treatment. The passivation of p-type GaN by a H_2 plasma treatment is one of the common processes used for III-nitride device fabrication [10]. As mentioned in section 1.3, H and Mg ions can easily form Mg-H complexes, which results in the deactivation of p-type doping and high resistance of p-type GaN. However, this treatment is not compatible with PR patterning, since it is barely effective until the processing temperature is above 300 °C. In addition, N_2 and N_2O plasma treatments have proven to be effective ways to cure the plasma damage on GaN surfaces [11, 12], as the N vacancies in GaN can be recovered by N-based plasma treatments. These treatments can reduce the device leakage current and improve surface morphology, photoluminescence intensity and contact properties. However, the N-based plasma treatments cannot be used to selectively passivate p-type GaN, because the electrical conductivity of p-type GaN cannot be modified by low-energy N ions.

Recently, F-based plasma treatments attracted great interest for $Al_xGa_{1-x}N$/GaN high electron mobility transistor (HEMT) fabrication [13–15]. It was found that after F-based plasma treatment for an $Al_xGa_{1-x}N$ layer, the threshold voltage of an $Al_xGa_{1-x}N$/GaN HEMT was shifted toward positive bias and the gate-leakage current was also reduced [13]. The detailed study has demonstrated that the negatively charged F ions, which induce acceptor-like deep levels in the $Al_xGa_{1-x}N$ [14], are mainly concentrated on the near-surface region of the $Al_xGa_{1-x}N$ layer. A large number of F ions can lead to an upward band bending and, thus, increase the surface barrier height of $Al_xGa_{1-x}N$ [15]. It is believed that this modification of the surface barrier height does not depend on the doping type of III-nitride materials. So a test of the effect of F-based plasma treatments on p-type GaN is valuable, which offers a potential to further develop a new process for III-nitride LED fabrication.

6.2 Novel microstructured-image light emitting diodes

6.2.1 Effect of different plasma treatments on p-type GaN

In order to investigate the effect of F-based plasma treatments on the electrical properties of p-type GaN, a series of plasma treatments for p-type GaN using different plasma sources was carried out. All the experiments were performed on the top p-type GaN layer of a commercial blue $In_xGa_{1-x}N$/GaN-based LED wafer emitting at 450 nm. The detailed wafer structure has been described in chapter 5. A co-planar Ti/Au metal electrode, which comprised a circular pad with a concentric outer electrode separated by a 10 μm spacing gap, was used to evaluate the effect of different plasma treatments on p-type GaN. The schematic diagram and fabrication process of this metal electrode are shown in Figure 6.1. As shown, the PR pattern of this electrode was formed on the surface of four samples by standard photolithography. Then, three samples underwent different plasma treatments in an RIE system at room temperature and one was kept as a reference. For the three plasma treated samples, CHF_3, CF_4 and H_2 were used as the main plasma source for each treatment, respectively. The flow rates of these main plasma sources were all set at 15 sccm. To stabilize the plasma density, a small amount of Ar (5 sccm) was introduced in each test. The RIE power and chamber pressure were set at 200 W and 30 mTorr, and the total treatment time was 240 s. Finally, a Ti/Au (40 nm/150 nm) metal bilayer was deposited on the plasma treated areas of each sample by sputtering. The thick Au layer was deposited to minimize the probe resistance during the measurements. After metal lift-off, the current-voltage (I-V) characteristic of each sample was measured by a semiconductor analyzer (HP 4155).

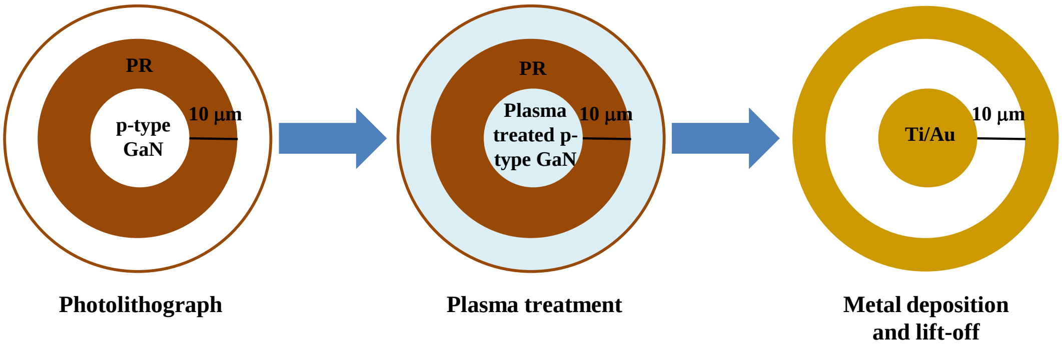

Figure 6.1: Schematic diagram and fabrication process of co-planar Ti/Au metal electrodes deposited on the p-type GaN layers with different plasma treatments.

Figure 6.2 shows a comparison of the I-V characteristics of the samples with different plasma treatments to the sample without plasma treatment. Compared with the untreated sample, a dramatic reduction of current by a factor exceeding 10^6 (at the voltages larger than 10 V) is observed for the sample treated by the CHF_3 plasma. The samples treated by the CF_4 and H_2 plasmas also show great current reductions. These results indicate that the electrical properties of the p-type GaN layers of these samples have been modified by plasma treatment. Based on these results, the greatest modification of the electrical properties of the p-type GaN layer treated by the CHF_3 plasma can be qualitatively explained as follows. As described in the last section, both F and H ions can modify the electrical properties of p-type GaN. For this CHF_3 plasma treatment, it is considered that both F and H ions play dominant roles. As the negatively charged F ions are implanted into the near-surface region of p-type GaN, the surface barrier height of p-type GaN is increased due to band bending [15]. This results in a higher contact resistivity of the metal contact to p-type GaN. Meanwhile, H ions can deactivate the Mg dopants in p-type GaN which results in a decrease of the hole concentration leading to a higher resistivity of p-type GaN. Furthermore, the hole mobility in p-type GaN may be decreased due to the reduced hole concentration and the increased impurity scattering [16]. All of these lead to the substantial current reduction observed for the sample treated by the CHF_3 plasma in Figure 6.2. Through this initial comparison study, the CHF_3 plasma treatment is considered as a new and efficient process to create the current blocking layer in p-type GaN.

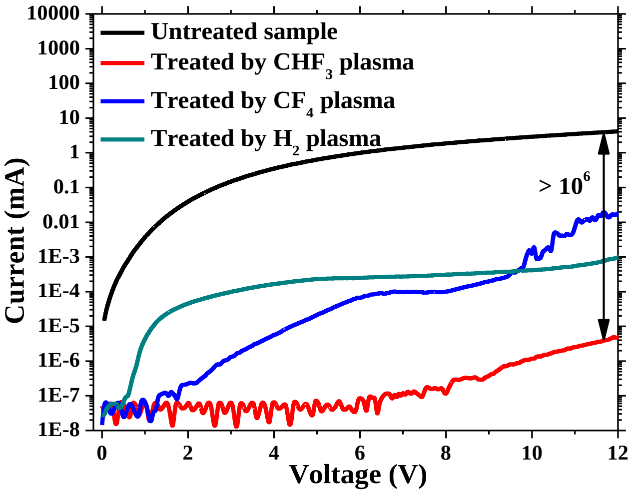

FIGURE 6.2: I-V characteristics of co-planar Ti /Au metal electrodes deposited on the p-type GaN layers with different plasma treatments.

6.2.2 Application of CHF$_3$ plasma treatment on light emitting diode fabrication

As demonstrated in the last subsection, the electrical properties of p-type GaN can be greatly modified by a CHF$_3$ plasma treatment. In order to selectively create high-resistance regions in p-type GaN, the applicability of this CHF$_3$ plasma treatment with PR patterning used in the LED fabrication process needs to be investigated. Furthermore, the reactions between the plasma treatment and the metal layer deposited on top of the p-type GaN layer also need to be considered, since the possible damage to metal layer may lead to a great degradation of LED performance. With these purposes in mind, this plasma treatment was introduced into the conventional LED fabrication process. The epitaxial structure of the LED wafer used for device fabrication was the same as the one described in the last subsection. The detailed device fabrication process is schematically shown in Figure 6.3. For this experiment, a broad-area LED array was fabricated. Each LED element had a mesa size of 250×250 μm^2, but the whole fabrication process could be applied to other mesa sizes and shapes. The mesa structures were initially formed by ICP etching. After surface cleaning by a dilute HCl solution, a Ni/Au (10 nm/20 nm) metal bilayer was deposited on top of the p-type GaN layer and thermally annealed at 500 °C for 3 min in an air ambient. As introduced in section 1.4, the formed oxidized Ni/Au bilayer serves as the metal contact to the p-type GaN and current spreading layer. Then, some mesas were covered by a

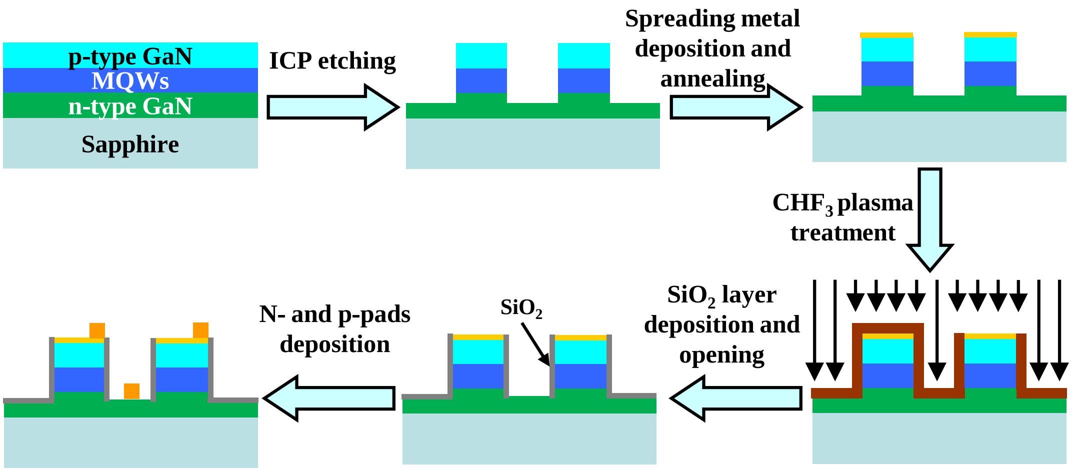

FIGURE 6.3: Process flow for the fabrication of LEDs with an additional CHF_3 plasma treatment.

thin 500 nm-thick PR layer and the others were left uncovered. Subsequently, the whole LED array underwent the CHF_3 plasma treatment with the same recipe and duration as described in the last subsection. Finally, after a 300 nm-thick SiO_2 isolation layer deposition and selective opening, n- and p-pads consisting of a Ti/Au (50 nm/200 nm) bilayer were deposited by sputtering. As shown, the additional CHF_3 plasma treatment was introduced after the formation of the oxidized Ni/Au contact to p-type GaN. This process sequence not only avoids the thermal reactivation of Mg dopants which are deactivated by H ions during the CHF_3 plasma treatment, but also provides an opportunity to study the direct reactions between the CHF_3 plasma and the oxidized Ni/Au metal bilayer. To characterize these fabricated LEDs, their I-V and optical output power-current (L-I) characteristics were measured.

Figures 6.4(a) and (b) show the I-V and L-I characteristics of the plasma untreated and plasma treated LEDs, respectively. In these figures, the LED which was protected by the thin PR layer during the CHF_3 plasma treatment is labelled as the ‘plasma untreated LED’, and the one without the PR protection is labelled as the ‘plasma treated LED’. As shown in Figure 6.4(a), compared with the plasma untreated LED, the electrical performance of the plasma treated LED is greatly modified. For untreated and treated LEDs, the operating currents at 6 V are 67 and 3 mA, respectively. Thus, there is nearly no light emitted from the device treated by the CHF_3 plasma which shows a maximum power of 0.4 mW at 10 mA as illustrated in Figure 6.4(b). These results confirm that, after the CHF_3 plasma treatment, the current cannot be injected efficiently into the LED active region for

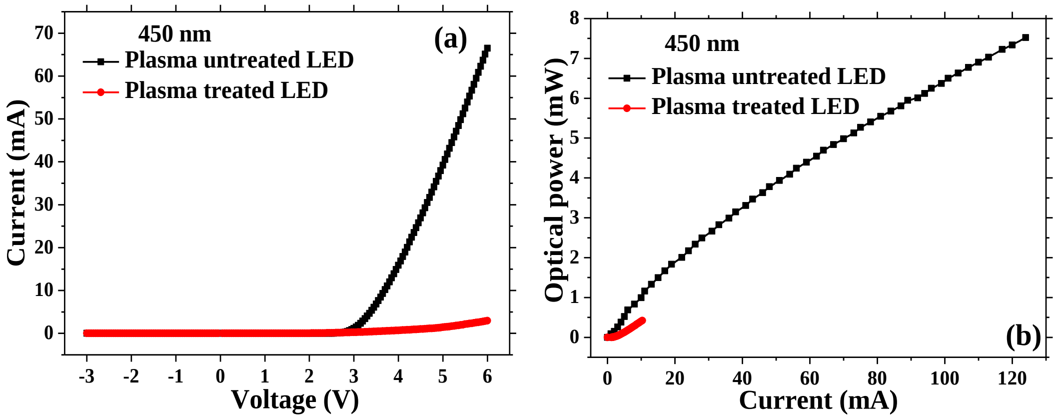

FIGURE 6.4: (a) I-V and (b) L-I characteristics of LEDs without and with a CHF_3 plasma treatment.

light generation. Since there is no measurable damage and etching for the oxidized Ni/Au metal bilayer after the CHF_3 plasma treatment which will be discussed later in detail, these results also demonstrate that all applied voltages are dropped at the oxidized Ni/Au contact to p-type GaN and the p-type GaN layer.

The emission images of LEDs without and with the CHF_3 plasma treatment are shown in Figure 6.5(a) and (b), respectively. Both images are taken at an operating current of 5 mA. It is necessary to point out again that both devices are from the same LED array and the LED without plasma treatment is protected by a thin PR layer. As shown in Figure 6.5(a), the LED without the CHF_3 plasma treatment emits light uniformly. On the other hand, nearly no light can be found for the LED treated by the CHF_3 plasma as shown in Figure 6.5(b). These results indicate that a PR layer can act as an effective mask to protect the LED from the CHF_3 plasma treatment. Consequently, this plasma treatment is fully applicable with PR patterning used in the LED fabrication process. This applicability enables us to create micro-current injection paths in p-type GaN by the selective CHF_3 plasma treatment. In this way, microstructured-image LEDs can be achieved, which will be described in the next subsection.

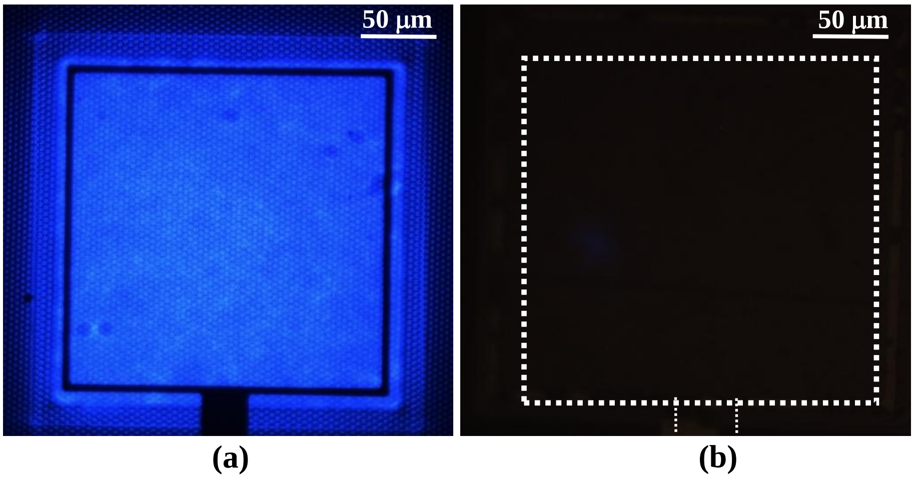

FIGURE 6.5: Emission images of LEDs (a) without and (b) with a CHF_3 plasma treatment at an operating current of 5 mA.

For the plasma treated LED, we have also directly performed an electrical measurement on the oxidized Ni/Au metal bilayer before and after the CHF_3 plasma treatment. No apparent change of the metal bilayer's conductivity was observed. Furthermore, no measurable etching of the metal bilayer was detected after a 10 min CHF_3 plasma treatment. These results confirm that the changes of the electrical properties of the plasma treated LED are not caused by the plasma damage to the oxidized Ni/Au metal bilayer, but are dominated by direct reactions between the CHF_3 plasma and the p-type GaN layer underneath. It has been reported the oxidized Ni/Au metal bilayer is porous, which may result from a reconstruction of the initially continual metal layers during the thermal annealing in an air ambient [17]. The porosity of the oxidized Ni/Au metal bilayer may make it possible for plasma species (F and H ions) to diffuse through this metal bilayer and directly react with the p-type GaN layer.

6.2.3 Fabrication and characterization of novel microstructured-image light emitting diodes

Based on above systematic studies, III-nitride LEDs containing the complex microstructured emission images were developed. The fabrication process of these microstructured-image LEDs is similar to that described in the last subsection. To produce different microstructured images on single LEDs, these images were first transferred from a photomask to the thin PR layer covering the oxidized Ni/Au metal bilayer on top of the p-type GaN layer by standard photolithography. Then, the CHF_3 plasma treatment was applied for these LEDs with different PR images. As described above, the resistance of the areas on the p-type GaN layer exposed to the plasma is greatly increased after the CHF_3 plasma treatment. This results in the formation of conductivity images, which are protected by the PR images during the plasma treatment, on the p-type GaN layer. When applying a voltage to the LEDs with such patterned p-type GaN layers, the current is only injected into these PR protected images and, thus, the LEDs can emit the light images. Furthermore, because this CHF_3 plasma treatment only shows a pronounced effect on p-type GaN, the microstructured-image LEDs can be fabricated on the commercial $In_xGa_{1-x}N$/GaN-based LED wafers with different emission wavelengths. Thus, by combining the CHF_3 plasma treatment and PR patterning, we have successfully fabricated microstructured-image LEDs with different emission wavelengths at 370 nm, 405 nm, 450 nm and 520 nm for demonstrations. The complete and uniform emission images with different wavelengths from these devices are shown in Figure 6.6. These high-quality emission images also confirm that, after the plasma treatment, the oxidized Ni/Au metal bilayer still functions efficiently as a current spreading layer. This metal bilayer enables the electrical connections between the regions without the plasma treatment. If the metal bilayer is damaged during the process, the spreading of the current would be dramatically degraded leading to a strong nonuniformity of light emission or even no light generation.

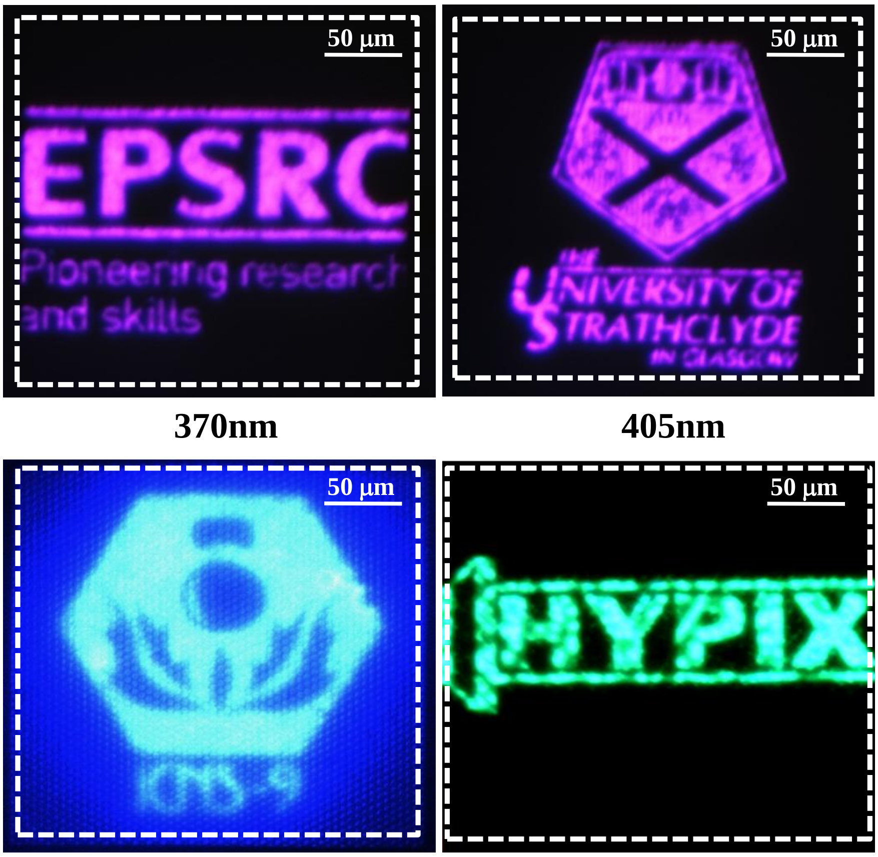

370nm **405nm**

450nm **520nm**

Figure 6.6: Novel III-nitride microstructured-image LEDs with different emission images and emission wavelengths.

As shown in Figure 6.6, a micro-scale feature size can be achieved for the emission images of these novel LEDs indicating that the CHF_3 plasma treatment has high spatial resolution. In order to further investigate the spatial resolution of this plasma treatment, an array of disc-shaped emitters with decreasing diameters down to 2 μm (limited by the resolution of the standard photolithography used) was produced on a single LED by the CHF_3 plasma treatment. The emission image of this disc-emitter array is shown as the insert of Figure 6.7. The intensity profile of the smallest micro-disc emitter with a diameter of 2 μm is plotted along a diameter as shown in Figure 6.7. From this profile, the full width at half maximum of the emission intensity of this micro-disc emitter is 2.5 μm, demonstrating the CHF_3 plasma treatment can be used to produce very small emission images for III-nitride LEDs. The size of emitters on these microstructured-image LEDs is dependent on the current injection area and the diffusion length of holes in GaN. As discussed in subsection 6.2.1, because of the high surface barrier and resistivity

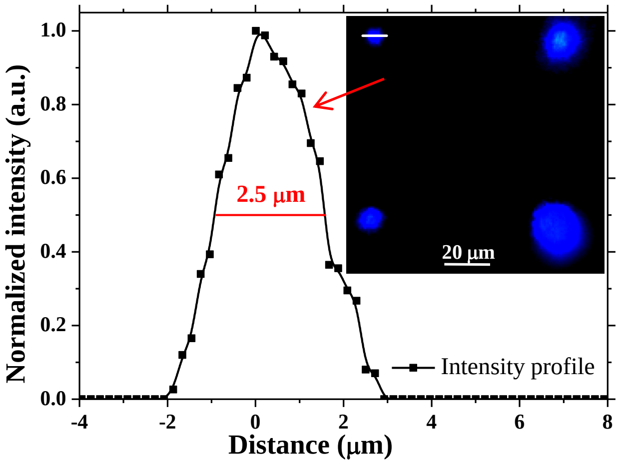

FIGURE 6.7: Intensity profile of a micro-disc emitter with a diameter of 2 μm. This profile is along the diameter labelled as a white line in the insert. The insert shows the emission image of the used device.

of p-type GaN treated by the CHF_3 plasma, the current injection areas of LEDs are defined by the PR masks. Furthermore, due to the intrinsic poor mobility of holes in GaN, the diffusion length of holes is less than a few hundred nanometers in GaN [18]. After the CHF_3 plasma treatment, the hole mobility can be further decreased by the reduced hole concentration and the increased impurity scattering. Thus, for these microstructured-image LEDs, light is only emitted from the areas covered by the PR masks during the CHF_3 plasma treatment. We believed that emitters with a sub-micron feature size can be fabricated by combining the CHF_3 plasma treatment with a higher resolution patterning technique, such as deep-ultraviolet or nanoimprint lithography.

6.3 Maskless image writing by microstructured-image light emitting diodes

As demonstrated in subsection 6.2.3, through a CHF_3 plasma treatment it is possible to produce complex microstructured emission images on single LEDs. Thus, these novel microstructured-image LEDs lead to simple fabrication and operation processes to display customized images with micro-scale feature size. Furthermore, due to the flat surface of these microstructured emission images, the integration of micro-elements on these images for further applications is much simpler. In addition, these devices also offer the potential application of image direct writing, with

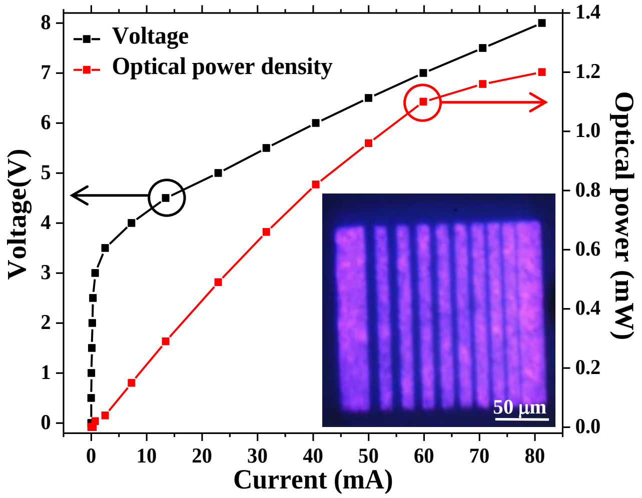

FIGURE 6.8: I-V and L-I characteristics of a 405 nm microstructured-image LED used in image writing. The insert is the emission image of this device containing bar-shaped emitters produced by a CHF_3 plasma treatment.

complex images [19]. In this section, this application is introduced and demonstrated. A microstructured-image LED with an emission wavelength of 405 nm was used as a light source for the image writing with different demagnification factors. The emission image of this device should contain 11 bar-shaped emitters separated by gaps varied from 10 to 1 μm. However, limited by the resolution of used standard photolithography, only 10 bar-shaped emitters with varied gaps from 10 to 2 μm can be clearly distinguished in the emission image, shown as the insert of Figure 6.8. Figure 6.8 shows the I-V and L-I characteristics of this device. These results are used to determine the operating current of this device for image writing. It can be found that the optical power of this device begins to saturate due to the self-heating effect when the operating current is higher than 60 mA. So in the following experiments, the device was operated at 60 mA to obtain high contrast for the image writing and to protect it. Through our home-built maskless image writing setup which has been described in subsection 2.1.1 in detail, the emission image was transferred to a thin PR layer coated on a SiO_2 layer, which was placed at the focal plane underneath the projection objective. The SiO_2 layer with 1.4 μm thickness was deposited by plasma-enhanced chemical vapour deposition on a Si substrate.

1-to-1 image writing

The 1-to-1 image writing was initially carried out by using two 4× microscope objectives in our maskless image writing setup to collect and project the light emitted from the LED. At the focal plane underneath the projection objective of the 1-to-1 maskless image writing setup, the LED operated at 60 mA provided an average optical power of 11 μW, corresponding to an optical power density of 60 mW/cm^2. To determine the exposure times used for different PRs, the exposure doses were calculated as a function of exposure time (60 mW/cm^2 × exposure time) and are shown in Figure 6.9. The required exposure doses for positive PR (S1805) and negative PR (N1405) with the same thickness (500 nm) are also labelled in this figure according to the parameter provided by the manufacturers. The positive PR with a short exposure time is considered as suitable for 1-to-1 image writing, because the much longer exposure time for the negative PR in 1-to-1 image writing may degrade the device performance and PR quality. The positive PR was spin-coated on the test samples and then exposed with different times from 0.5 to 2 s. After that, all the samples were soaked in a suitable developer (Micro DEV) for 40 s. The areas of the PR layer exposed to the light emitted from the bar-shaped emitters were removed after development due to the positive nature of the PR used. The written patterns were further checked by an optical microscopy and the thickness of the PR patterns was measured by a Dektak 3 profilometer.

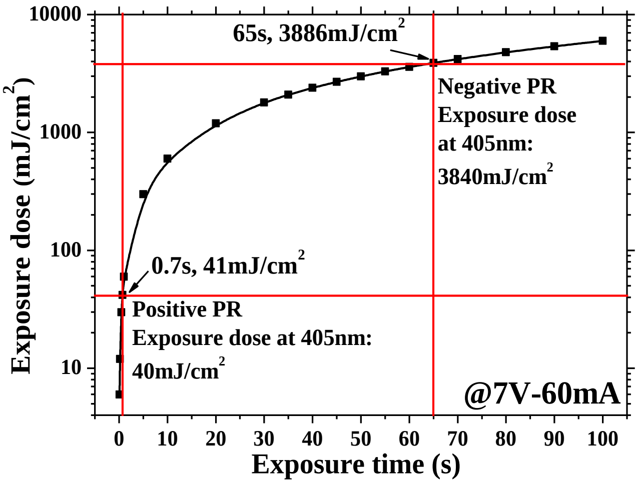

FIGURE 6.9: Calculated exposure doses as a function of exposure time for 1-to-1 image writing when the LED is operated at 60 mA (7 V). The exposure times of two PRs are also labelled.

Figure 6.10 shows the optical images of 1-to-1 written patterns with different exposure times. It can be seen that the LED emission image has been successfully transferred to the PR layer, while no PR patterns can be found on the samples when the exposure time is shorter than 0.8 s. As observed, with a shorter exposure time such as 1 s, the PR bars down to 4 μm, which correspond to the gaps of the LED emission image, can be clearly distinguished in the written pattern. However, the quality of the pattern with 1 s exposure time is quite low. Some defects can be seen in each gap which corresponds to the bar-shaped emitter of the used LED. These defects are probably caused by the nonuniformity of light intensity emitted from the single bar-shaped emitter. As shown as the insert of Figure 6.8, some bright emission dots are clearly observed on each bar-shaped emitter. These dots may be caused by the clusters formed on the oxidized Ni/Au metal bilayer during the thermal annealing in air. During the image writing, these bright dots lead to the relatively higher exposure doses. With a short exposure time, the PR layer irradiated by these bright dots would be fully exposed first, which results in the defects and the low-quality patterns. As the exposure time increases, the whole PR layer can be fully exposed and the quality of the written patterns is improved. However, if the exposure time is too long, for instance, 2 s, the narrow PR bars in the written patterns (right part of the optical images) disappear. This observation indicates that with the increasing exposure time, the PR layer corresponding to the gaps of the LED emission image is fully exposed and then developed. This is mainly due to the unexpected light in the gaps of the LED emission image, which will be discussed later in detail. The 1-to-1 written pattern with a exposure time of 1.5 s is considered as the best one achieved in these experiments. High-quality PR patterns including 6 PR bars with reducing widths down to 5 μm are achieved.

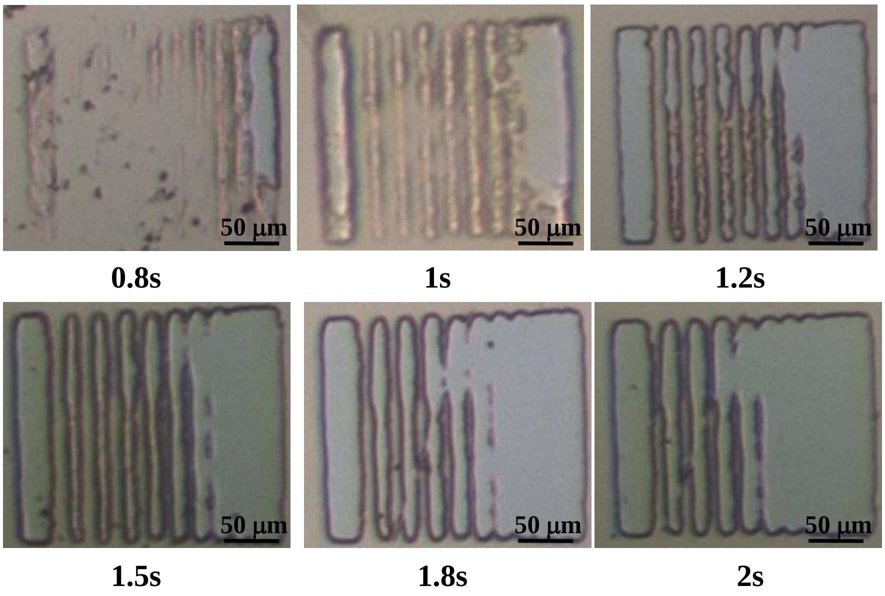

Figure 6.10: Optical images of 1-to-1 written patterns with different exposure times.

The 1-to-1 written patterns were also investigated by a Dektak 3 profilometer to further understand their structural properties. The height profiles of three 1-to-1 written patterns with exposure times of 1 s,1.5 s and 2 s, respectively, are shown in Figure 6.11(a), (b) and (c). These profiles are obtained through a scan along a line across the whole written pattern. The scan line position is labelled as a white line in the insert of each figure. Two important phenomena can be found from these figures. Firstly, the 'depth' of the gaps is not the same in each written pattern, especially when the exposure time is short. Since the gaps in each written pattern correspond to the bar-shaped emitters of the LED used, these results indicate that the light intensity of each bar-shaped emitter is not the same. Secondly, the narrow PR bars in the written patterns (right part of each figure) disappear with increasing exposure time, which is the same as was observed in Figure 6.10. As mentioned above, this is attributed to the unexpected light in the gaps of the LED emission image. To confirm these explanations, an emission image of the LED used was taken at the focal plane underneath the projection objective of the maskless writing setup and is shown as the insert of Figure 6.11(d). The intensity profile along a typical line across this image is shown in Figure 6.11(d). Clearly, the maximum intensity of each bar-shaped emitter is not the same, which provides direct evidence for the nonuniformity of the height profile of the 1-to-1 written patterns. The unequal intensities of the bar-shaped emitters are probably due to the nonuniform current distribution induced by the current crowding effect of III-nitride LEDs [20]. On the other hand, light intensity is also observed in the gaps of the LED emission image, which increases with the decreasing gap width. The difference of intensities between the bar-shaped emitters and the gaps is barely distinguished when the gap width is smaller than 3 μm. This unexpected light in the gaps is probably caused by the lambertian angular distribution of the emission light from LEDs and the light scattering at the edge of the bar-shape emitters. The observation of this unexpected light in the gaps supports the previous explanation as to the disappearance of the narrow PR bars.

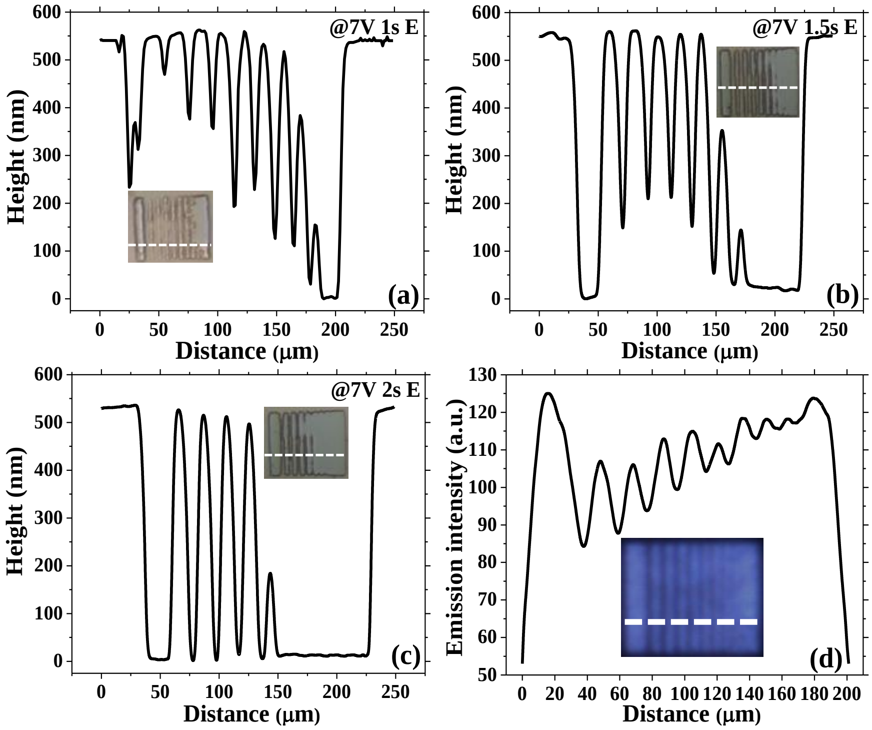

Figure 6.11: Height profiles of three 1-to-1 written patterns with exposure times of (a) 1 s, (b) 1.5 s and (c) 2 s, the insert of (a)-(c) highlights the scanned line across each written patten by a white line; (d) intensity profile of the used LED along a typical line across the device image shown as the insert.

10-to-1 image writing

We have also carried out image writing through a 10-to-1 demagnification approach to investigate the resolution limitation of this maskless writing technology. The 10-to-1 demagnification factor can be easily achieved by using a 4× collection objective and a 40× projection objective in the maskless image writing setup. The same microstructured-image LED as before was used in these experiments. The optical power of this device was first measured at the focal plane underneath the projection objective of the 10-to-1 maskless image writing setup. Compared with the results through the 1-to-1 maskless image writing setup, although the measured optical power at 10-to-1 is decreased from 11 to 2.5 μW at an operating current of 60 mA, the optical power density is much higher ($\sim$1.3 W/cm^2 at 60 mA) due to the reduction of dimensions of the projected emission image. This high optical power density leads to the much shorter exposure time required for both PRs as shown in Figure 6.12. For positive PR (S1805), the required exposure time is 0.03 s, which is too short to be well controlled in image writing. So, the negative PR (N1405) with an exposure time of 3 s was used in 10-to-1 image

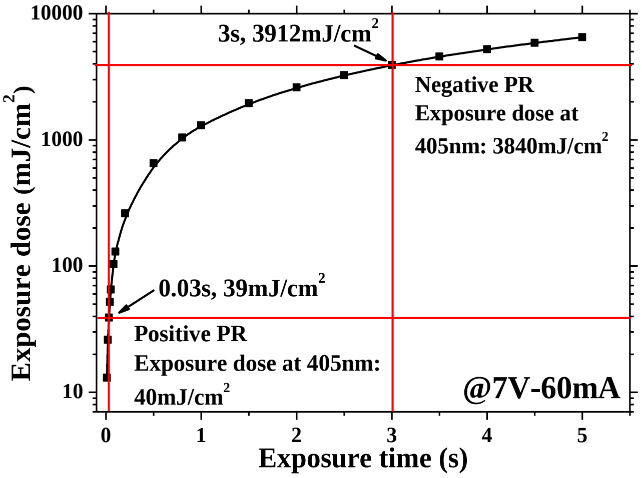

FIGURE 6.12: Calculated exposure doses as a function of exposure time for 10-to-1 image writing when the LED is operated at 60 mA (7 V). The exposure times of two PRs are also labelled.

writing. After exposure, the samples were soaked in the developer (ma-D 331S) for 30 s to form the patterns. For negative PR, the areas of the PR layer exposed by the light remain after development. Because the 10-to-1 written patterns are too small to be observed by a conventional optical microscope, an atomic force microscope (AFM) was used.

Figure 6.13(a) shows the three-dimentional (3D) AFM image of the best 10-to-1 written pattern with an exposure time of 2.8 s. As shown, at least 7 PR bars, which correspond to the bar-shaped emitters of the LED used, can be clearly distinguished in this AFM image. Furthermore, as shown in Figure 6.13(b), the average height profile of this 10-to-1 written pattern shows that 10 PR bars have been achieved. This result is even better than the one achieved in 1-to-1 image writing, which may be due to the negative PR used for 10-to-1 image writing. It can be also found that the 4 largest gaps have been fully developed. The well-developed gaps have a minimum width less than 800 nm indicating the nano-scale feature size can be achieved by combining the novel microstructured-image LED and our home-built maskless image writing setup. However, the thickness of the PR bars is also not uniform in this 10-to-1 written pattern. The variation of light intensities from different bar-shaped emitters [as shown in Figure 6.11(d)] is considered to be the dominant reason for this height nonuniformity. The optical diffraction effect of maskless image writing setup may also affect 10-to-1 written patterns. As introduced in subsection 2.1.1, the resolution and depth of focus

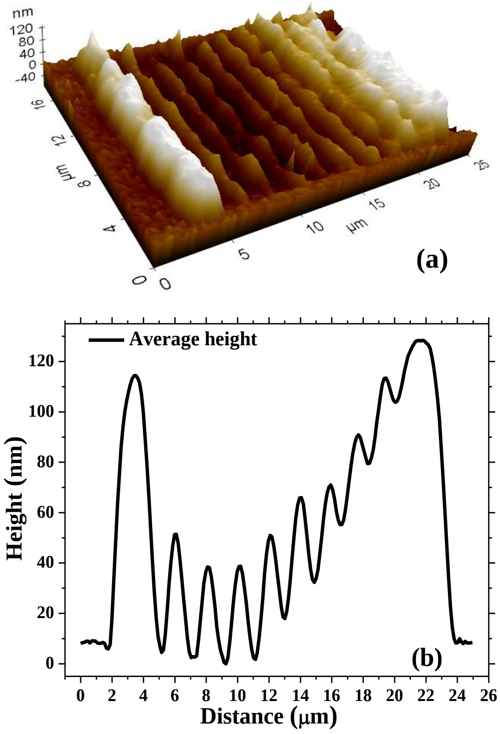

FIGURE 6.13: (a) 3D AFM image of the best 10-to-1 written pattern with an exposure time of 2.8 s; (b) average height profile of this whole AFM image.

of an optical system always work against each other. To achieve a small feature size in 10-to-1 image writing, the depth of focus of our 10-to-1 maskless image writing setup is reduced. Thus, the surface flatness plays a more important role in the 10-to-1 image writing compared with the 1-to-1 image writing. The image quality is more sensitive to the thickness fluctuation coming from the PR layer and substrate material.

Although both 1-to-1 and 10-to-1 written patterns still need to be further optimized, the achieved PR micro- and nano-patterns demonstrated the principle of image writing using the novel microstructured-image LEDs. These PR patterns can also serve as a mask for further transferring the emission images to other substrates by plasma etching. It is believed that better written patterns can be obtained by improving the uniformity of the LED emission. Furthermore, as introduced in subsection 2.1.1, a microstructured-image LED emitting at a shorter wavelength can also improve the writing resolution.

6.4 Summary

In this chapter, novel III-nitride microstructured-image LEDs have been developed and characterized. The emission region of conventional III-nitride LEDs is normally spatially defined by the mesa structure which is formed by plasma etching. This etching process induces some drawbacks to the LED performance. In this work, a complex emission image in a single mesa structure was produced by combining a CHF_3 plasma treatment and PR patterning. The CHF_3 plasma treatment leads to a large change in the electrical properties of p-type GaN. This modification mainly results from the increased surface barrier height and the lower hole concentration of p-type GaN, which are caused by F and H ions respectively. Thus, the resistivity of the metal contact and p-type GaN can be greatly increased by the CHF_3 plasma treatment. Further experimental results indicate that the PR layer is an effective mask to protect p-type GaN from the CHF_3 plasma treatment. Furthermore, there is no measurable damage to the plasma treated metal layer, which indicates the metal layer can spread current efficiently even after the CHF_3 plasma treatment. Based on these results, different complex microstructured images were created in single LEDs. These microstructured-image LEDs demonstrate that the CHF_3 plasma treatment shows high spatial resolution. The highest spatial resolution obtained here is a few microns, which is limited by the standard photolithography used. It is believed sub-micron resolution can be achievable because of the low diffusion length of holes in p-type GaN.

These microstructured-image LEDs were further used for maskless image writing through our home-built setup. These novel devices offer a simple process to write a complex image. The emission images have been successfully transferred to a PR layer through both 1-to-1 and 10-to-1 maskless image writing setups. Nano-scale (< 800 nm) structures were obtained in the 10-to-1 written pattern. The written patterns achieved can act as the mask for further processes.

References

[1] I. Adesida, A. Mahajan, E. Andideh, M.A. Khan, D.T. Olsen, and J.N. Kuznia. Reactive ion etching of gallium nitride in silicon tetrachloride plasmas$^{a)}$. *Applied Physics Letters*, 63 (20):2777–2779, 1993.

[2] W.A. Harrison. *Elementary electronic structure.* World Scientific Publishing Company Incorporated, 1999.

[3] M.E. Lin, Z.F. Fan, Z. Ma, L.H. Allen, and H. Morkoc. Reactive ion etching of GaN using BCl_3. *Applied Physics Letters*, 64(7):887–888, 1994.

[4] R.J. Shul, G.B. McClellan, S.A. Casalnuovo, D.J. Rieger, S.J. Pearton, C. Constantine, C. Barratt, R.F. Karlicek, C. Tran, and M. Schurman. Inductively coupled plasma etching of GaN. *Applied Physics Letters*, 69(8):1119–1121, 1996.

[5] R.J. Shul, L. Zhang, A.G. Baca, C.G. Willison, J. Han, S.J. Pearton, F. Ren, J.C. Zolper, and L.F. Lester. High-density plasma-induced etch damage of GaN. In *MRS Proceedings*, volume 573. Cambridge Univ Press, 1999.

[6] X.A. Cao, S.J. Pearton, A.P. Zhang, G.T. Dang, F. Ren, R.J. Shul, L. Zhang, R. Hickman, and J.M. Van Hove. Electrical effects of plasma damage in p-GaN. *Applied Physics Letters*, 75(17):2569–2571, 1999.

[7] R.J. Shul, L. Zhang, A.G. Baca, C.G. Willison, J. Han, S.J. Pearton, and F. Ren. Inductively coupled plasma-induced etch damage of GaN p-n junctions. *Journal of Vacuum Science & Technology A: Vacuum, Surfaces, and Films*, 18(4):1139–1143, 2000.

[8] S.J. Pearton, C.B. Vartuli, J.C. Zolper, C. Yuan, and R.A. Stall. Ion implantation doping and isolation of GaN. *Applied Physics Letters*, 67(10):1435–1437, 1995.

[9] T.W. Kuo, S.X. Lin, P.K. Hung, K.K. Chong, C.I. Hung, and M.P. Houng. Formation of Selective High Barrier Region by Inductively Coupled Plasma Treatment on GaN-Based Light-Emitting Diodes. *Japanese Journal of Applied Physics*, 49(11):6504, 2010.

[10] A.Y. Polyakov, N.B. Smirnov, A.V. Govorkov, K.H. Baik, S.J. Pearton, B. Luo, F. Ren, and J.M. Zavada. Hydrogen plasma passivation effects on properties of p-GaN. *Journal of Applied Physics*, 94(6):3960–3965, 2003.

[11] J.M. Lee, K.M. Chang, S.W. Kim, C. Huh, I.H. Lee, and S.J. Park. Dry etch damage in n-type GaN and its recovery by treatment with an N_2 plasma. *Journal of Applied Physics*, 87(11):7667–7670, 2000.

[12] H.M. Kim, C. Huh, S.W. Kim, N.M. Park, and S.J. Park. Suppression of Leakage Current in InGaN/GaN Multiple-Quantum Well LEDs by N_2O Plasma Treatment. *Electrochemical and Solid-State Letters*, 7(11):G241–G243, 2004.

[13] R. Chu, C.S. Suh, M.H. Wong, N. Fichtenbaum, D. Brown, L. McCarthy, S. Keller, F. Wu, J.S. Speck, and U.K. Mishra. Impact of CF_4 Plasma Treatment on GaN. *Electron Device Letters, IEEE*, 28(9):781–783, 2007.

[14] Y. Cai, Y. Zhou, K.M. Lau, and K.J. Chen. Control of threshold voltage of AlGaN/GaN HEMTs by fluoride-based plasma treatment: From depletion mode to enhancement mode. *Electron Devices, IEEE Transactions on*, 53(9):2207–2215, 2006.

[15] B.K. Li, M.J. Wang, K.J. Chen, and J.N. Wang. Enhanced electroluminescence from the fluorine-plasma implanted Ni/Au-AlGaN/GaN Schottky diode. *Applied Physics Letters*, 99 (6):062101, 2011.

[16] B.K. Li, W.K. Ge, J.N. Wang, and K.J. Chen. Persistent photoconductivity and carrier transport in AlGaN/ GaN heterostructures treated by fluorine plasma. *Applied Physics Letters*, 92:082105, 2008.

[17] J. Liday, I. Hotovỳ, H. Sitter, K. Schmidegg, P. Vogrinčič, A. Bonnani, J. Breza, G. Ecke, and I. Vávra. Auger electron spectroscopy of Au/NiO_x contacts on p-GaN annealed in N_2 and O_2+ N_2 ambients. *Applied Surface Science*, 253(6):3174–3180, 2007.

[18] R. Hickman, J.M. Van Hove, P.P. Chow, J.J. Klaassen, A.M. Wowchak, C.J. Polley, D.J. King, F. Ren, C.R. Abernathy, S.J. Pearton, K.B. Jung, H. Cho, and J.R. La Roche. GaN PN junction issues and developments. *Solid-State Electronics*, 44(2):377–381, 2000.

[19] D. Elfström, B. Guilhabert, J. McKendry, S. Poland, Z. Gong, D. Massoubre, E. Richardson, B.R. Rae, G. Valentine, G. Blanco-Gomez, E. Gu, J.M. Cooper, R.K. Henderson, and M.D. Dawson. Mask-less ultraviolet photolithography based on CMOS-driven micro-pixel light emitting diodes. *Optics Express*, 17(26):23522–23529, 2009.

[20] X. Guo and E.F. Schubert. Current crowding and optical saturation effects in GaInN/GaN light-emitting diodes grown on insulating substrates. *Applied Physics Letters*, 78(21):3337–3339, 2001.

Chapter 7

Conclusion and perspectives

7.1 Conclusion

The work presented in this thesis has concentrated on the mechanisms and development of III-nitride microstructured light emitting diodes (LEDs) including micro-LEDs (μ-LEDs) and microstructured-image LEDs. The III-nitride μ-LEDs are an attractive format of LEDs, because they show potential enhancements in device performance and many novel applications. The results achieved in this thesis are not only helpful to understand in more depth the mechanisms of μ-LEDs, but are also valuable to further extend the fields of application for these devices. The microstructured-image LEDs are novel devices developed in this work. These devices contain highly complex emission patterns on single III-nitride LEDs. The development and application of these novel microstructured-image LEDs was introduced.

Chapter 1 provided a general introduction to LEDs, and more specifically to the LEDs based on III-nitride materials. The motivations for the work presented in this thesis were given in this chapter as well. Great success has been achieved in the development of LEDs. At present, high-performance commercial LEDs covering a wide spectral range are used for various applications in our daily life. The operating principles of LEDs were also described in this chapter including the carrier recombination processes in semiconductors and related special designs to achieve high-performance LEDs. The main contents of this chapter focused on III-nitride materials and related LEDs. III-nitride materials offer exciting properties for the development of LEDs, due to their bandgap energy, they can in principle cover a broad emission wavelength range from deep-ultraviolet to infrared including the whole visible-light region. The growth processes of III-nitride materials were then presented. The structure of III-nitride LED wafer and common configurations of III-nitride LEDs were also introduced. Although there are still some problems to be addressed, high-performance III-nitride LEDs with blue and green emissions are already a commercial success. The outstanding performance of III-nitride blue LEDs promotes the development of white-light LEDs as well. Two particular formats of III-nitride microstructured LEDs were introduced. The III-nitride μ-LEDs are the main devices discussed in this thesis. An overview of III-nitride μ-LEDs was given including their development, main advantages and novel applications. The other type of III-nitride microstructured LEDs is the microstructured-image LEDs developed in this work. These devices offer a simple way to achieve the complex emission images for display.

In order to develop and investigate the III-nitride microstructured LEDs, a range of experimental techniques were used for microstructured LED fabrication and characterization. Chapter 2 focused on introducing these techniques. Fully operational microstructured LEDs were fabricated by a process consisting of three main steps which are pattern definition, pattern transfer and formation of metal contacts. For pattern definition, conventional photolithography and our home-built maskless image writing were introduced and commented on. Two basic techniques for pattern transfer, being wet etching and dry (plasma) etching were then introduced. The latter is the dominant technique used for microstructured LED fabrication. The mechanisms of dry (plasma) etching and related facilities were described, and recipes used for the dry (plasma) etching of different materials were also illustrated. Metal deposition and thermal annealing are main operations for formation of metal contacts. The working principles of each operation were summarized. Then, the introduction of two techniques used for microstructured LED characterization, namely cathodoluminescence (CL) and temperature-dependent photoluminescence (T-PL), was given. The working principles, advantages and disadvantages of both techniques were discussed. Since these two techniques were performed on the home-built facilities, the designs of these facilities were described as well.

From chapter 3 onwards, the results achieved in this work were presented. The compressive strain resulting from the lattice mismatch between $In_xGa_{1-x}N$ and GaN leads to an internal electric field in the quantum wells (QWs) and, thus, a red-shift of the emission wavelength. Micro-pillars can partly relax the strain because of their free sidewalls resulting in a blue-shift of the emission wavelength. The size-dependent strain relaxation and its effect on the optical properties of $In_xGa_{1-x}N$/GaN-based micro-pillars was investigated in chapter 3. High-quality micro-pillars with diameters ranging from 2 to 150 μm were fabricated from a yellow-green $In_{0.25}Ga_{0.75}N$/GaN-based LED wafer. The CL technique was used to record emission wavelength maps of the micro-pillars to investigate the strain relaxation process. The localized shifts of emission wavelength in micro-pillars have been observed through CL maps with high spatial resolution. It was found that the strain relaxation at the pillar centre and edge are dramatically different. A broad ring-shaped strain relaxation region at the pillar edge was also observed in the CL maps. The strain relaxation in micro-pillars was further simulated by a finite element method. The simulation results agree well with the experimental ones when the strain within the QWs and whole wafer bending are considered in the model. The experimental and simulation results of micro-pillars with different diameters were then summarized to explore the size effect on strain relaxation. Pronounced strain relaxation can be observed for micro-pillars with diameters below 30 μm. Thus, it is reasonable to conclude that the efficiency of μ-LEDs with diameters less than 30 μm can be significantly improved.

A blue-shift of the emission wavelength can also be observed for III-nitride LEDs under electrical operation. The injected carriers can screen the internal electric field and lead to the blue-shift of the emission wavelength for III-nitride LEDs at different operating currents. In chapter 4, colour-tunable μ-LEDs were demonstrated. The colour tunability of these devices is mainly dependent on this screening effect. These colour-tunable μ-LEDs were fabricated from an amber $In_{0.40}Ga_{0.60}N$/GaN-based LED wafer. In this case, the dominant amber QWs were grown on top of low-indium-content blue QWs. The optical properties of this LED wafer were first studied by T-PL and CL. Through these measurements, the luminescence efficiency at room temperature was found to be around 1 % for this LED wafer. A pronounced bandgap inhomogeneity was also found for the amber QWs. The μ-LEDs fabricated from this wafer show a great blue-shift of the dominant emission peak and a blue emission from the low-indium-content QWs. This effectively means that these devices have a tunable emission colour, which changes from amber to green depending on the operating current. Therefore, these colour-tunable μ-LEDs offer a simple method to achieve III-nitride multi-colour displays based on a single epitaxial structure. Furthermore, compared with broad-area

LEDs fabricated from the same wafer, it is found the colour tunability is enhanced for μ-LEDs. This is mainly due to the fact that μ-LEDs can sustain significantly higher current densities than broad-area LEDs. The mechanisms of this colour tunability were also discussed. A larger internal electric field in the amber QWs is believed to be the dominant reason.

Driven by the prospect for further improvement of III-nitride μ-LED performance, chapter 5 presented our work on the development of Pd-based contacts to p-type GaN. The fabrication process of Pd-based contacts to p-type GaN was first optimized. Surface cleaning by HCl (40 %) and thermal annealing at 300 °C in a N_2 ambient proved to be the most effective way to reduce the specific contact resistivity (ρ_c) of Pd-based contacts to p-type GaN. However, it was typically observed that the current-voltage characteristics of metal contacts to p-type GaN are non-linear. This indicates that the ρ_c of metal contacts to p-type GaN is a function of injection current density. Thus, a generalized transmission line method (TLM) was introduced to calculate the current-density dependent ρ_c. Then, the ρ_c of the Pd contact to p-type GaN annealed under optimal conditions was compared with that of a normal oxidized Ni/Au contact by this methodology. The results demonstrate that the annealed Pd contact to p-type GaN shows a lower ρ_c at high injection current densities above 20 A/cm^2. The performance of μ-LEDs with annealed Pd and oxidized Ni/Au contacts to p-type GaN were further compared. These 44 μm-diameter devices emitting at 450 nm had flip-chip configurations. Since the annealed Pd contact to p-type GaN has a lower ρ_c at high injection current densities and higher optical reflectivity in blue emission region, μ-LEDs with this contact to p-type GaN show better electrical properties and 40 % higher optical power compared to devices with oxidized Ni/Au contact. These improvements are important for the applications of μ-LEDs in which high optical power is required.

Chapter 6 described the development and application of novel III-nitride micro-structured-image LEDs. CHF_3 plasma treatment plays an important role in the fabrication process of these devices. For the CHF_3 plasma, the F and H ions can increase the surface barrier height and reduce the hole concentration of p-type GaN. This leads to a great modification of the electrical properties of p-type GaN after the CHF_3 plasma treatment. Further experimental results indicate that the CHF_3 plasma treatment is not only compatible with photoresist patterning but also does less damage to the metal layer on top of the p-type GaN layer. Thus, a complex microstructured emission image can be easily created in a single III-nitride LED by combining the CHF_3 plasma treatment and photoresist patterning. Through these microstructured-image LEDs, the spatial resolution of the CHF_3 plasma treatment was proven to be a few micrometres. Furthermore, compared with the other lithographic methods, the microstructured-image LEDs offer a much simpler process for the direct writing of complex images. The direct image writing with different magnification factors was demonstrated using these novel devices and our home-built image writing setup.

7.2 Further work

7.2.1 Individually-addressable nano-light emitting diodes

As demonstrated in chapters 3 and 4, μ-LEDs relax the strain and efficiently relieve the polarization effects in III-nitride LEDs. It is expected that reducing the size of devices, for example, to the nano-scale, can further enhance the performance and create new applications for III-nitride LEDs. Although some work on III-nitride nano-LEDs has been published [1, 2], it is still a major challenge to achieve individually-addressable nano-LEDs. Further work will concentrate on developing and characterizing the individually-addressable nano-LEDs. In our approach, unlike the photolithographic and imprint techniques used for nano-patterning, the scanning probe lithography methods, such as dip-pen nanolithography [3], are employed to deposit materials with nano-scale features as the mask for further etching. Besides the novel fabrication process, these individually-addressable nano-LEDs will also be used to investigate the mechanism of the efficiency droop of III-nitride LEDs.

7.2.2 Ultra-parallel visible light communications by micro-light emitting diode array

As introduced in subsection 1.4.1, the compact μ-LED array is a good candidate for micro-displays. Meanwhile, it has been found that the μ-LEDs also have the potential for visible light communications due to their high-frequency modulation bandwidth [4]. Thus, combined with displays, each element in the μ-LED array can provide individual communication channels through a complementary metal-oxide-semiconductor driver. However, the absolute optical power of μ-LEDs is still relatively low compared to the requirement for long-distance data transmission. Further optimization of the metal contact to p-type GaN is thus necessary for improving the power output of μ-LEDs. Since the generalized TLM method supplies a new methodology to compare the ρ_c of different metal contacts to p-type GaN, more work will be carried out to identify suitable metal contact to p-type GaN for μ-LEDs with different configurations. Ag is a promising candidate because it offers an even higher optical reflectivity and, thus, higher optical power for μ-LEDs with flip-chip configurations [5].

7.2.3 Further development of microstructured-image light emitting diodes

To achieve high-quality microstructured-image LEDs and high-resolution written patterns by using these novel devices, more work on the optimization of the processes of device fabrication and direct image writing is necessary. The physical mechanisms of the electrical property modification of p-type GaN by the CHF_3 plasma treatment have also not been fully understood yet and further investigation is being carried out at the time of writing of thesis. The as-deposited Pd contact to p-type GaN developed in chapter 5 is now used to evaluate the influence of different plasma treatments on p-type GaN. The modulation bandwidth of these microstructured-image LEDs is also valuable to be measured for demonstrating their possible application for visible light communications.

References

[1] J. Bai, Q. Wang, and T. Wang. Characterization of InGaN-based nanorod light emitting diodes with different indium compositions. *Journal of Applied Physics*, 111(11):113103, 2012.

[2] C.H. Chang, L.Y. Chen, L.C. Huang, Y.T. Wang, T.C. Lu, and J.J. Huang. Effects of Strains and Defects on the Internal Quantum Efficiency of InGaN/GaN Nanorod Light Emitting Diodes. *Quantum Electronics, IEEE Journal of*, 48(4):551–556, 2012.

[3] A. Hernandez-Santana, A.R. Mackintosh, B. Guilhabert, A.L. Kanibolotsky, M.D. Dawson, P.J. Skabara, and D. Graham. Dip-pen nanolithography of nanostructured oligofluorene truxenes in a photo-curable host matrix. *Journal of Materials Chemistry*, 21(37):14209–14212, 2011.

[4] J.J.D. McKendry, R.P. Green, A.E. Kelly, Z. Gong, B. Guilhabert, D. Massoubre, E. Gu, and M.D. Dawson. High-speed visible light communications using individual pixels in a micro light-emitting diode array. *Photonics Technology Letters, IEEE*, 22(18):1346–1348, 2010.

[5] J.O. Song, J.S. Kwak, Y. Park, and T.Y. Seong. Ohmic and degradation mechanisms of Ag contacts on p-type GaN. *Applied Physics Letters*, 86(6):062104, 2005.

List of Publications

Papers

Drafted/Submitted

[1] E.Y. Xie, D. Massoubre, B. Guilhabert, E. Gu, I.M. Watson, and M.D. Dawson. Microstructured light emission from planar InGaN light-emitting diodes. *In preparation.*

[2] E.Y. Xie, D. Massoubre, P.R. Edwards, Z. Gong, I.M. Waston, E. Gu, R.W. Martin, M.D. Dawson. Effect of nonlinear p-type metal contacts on GaN-based optoelectronic devices with different operation current densities. *In preparation.*

[3] E. Richardson, A.J.C. Kuehne, Z. Gong, B. Guilhabert, E.Y. Xie, A.R. Mackintosh, E. Gu and M.D. Dawson. Hybrid organic-inorganic micro-LED arrays of inkjet printed novel red, green and blue light emitting polymers. *In preparation.*

Accepted/Published

[4] E.Y. Xie, Z.Z. Chen, P.R. Edwards, Z. Gong, N.Y. Liu, Y.B. Tao, Y.F. Zhang, Y.J. Chen, I.M. Watson, E. Gu, R.W. Martin, G.Y. Zhang and M.D. Dawson. Strain relaxation in InGaN/GaN micro-pillars evidenced by high resolution cathodoluminescence spectral imaging. *Journal of Applied Physics*, **112**(1):013107, 2012.

[5] D. Massoubre, P.R. Edwards, E.Y. Xie, E. Richardson, I.M. Watson, E.Gu, R.W. Martin and M.D. Dawson. Individually-addressed planar nanoscale InGaN-based light emitters. *in Proceedings of IEEE Photonics 2012 Conference*, 754, 2012.

[6] Y.B. Tao, S.Y. Wang, Z.Z. Chen, Z. Gong, E.Y. Xie, Y.J. Chen, Y.F. Zhang, J. McKendry, D. Massoubre, E.D. Gu, B.R. Rae, R.K. Henderson and G.Y. Zhang. Size effect on efficiency droop of blue light emitting diode. *Physica Status Solidi (c)*, **9**(3-4):616, 2012.

[7] Z. Gong, N.Y. Liu, Y.B. Tao, D. Massoubre, E.Y. Xie, X.D. Hu, Z.Z. Chen, G.Y. Zhang, E. Gu and M.D. Dawson. Electrical, spectral and optical performance of yellowgreen and amber micro-pixelated InGaN light-emitting diodes. *Semiconductor Science and Technology*, **27**(1):015003, 2012.

[8] S. Zhang, Z. Gong, J. McKendry, S. Watson, A. Cogman, E.Y. Xie, P. Tian, E. Gu, Z.Z. Chen, G.Y. Zhang, A.E. Kelly, R.K. Henderson and M.D. Dawson. CMOS-Controlled Color-Tunable Smart Display. *Photonics journal, IEEE*, **4**(5):1639, 2012.

[9] P. Tian, E.Y. Xie, Z. Gong, Z. Chen, T. Yu, Y. Sun, S. Qi, Y. Chen, Y. Zhang, S. Calvez, E. Gu, G. Zhang, and M.D. Dawson. Flexible vertical structure GaN-based light emitting diodes on an AuSn substrate. *in Proceedings of IEEE Photonics 2011 Conference*, 551, 2011.

Conferences

(Presenter highlighted by bold letters)

[10] **D. Massoubre**, P.R. Edwards, E.Y. Xie, E. Richardson, I.M. Watson, E. Gu, R.W. Martin and M.D. Dawson. Individually-addressed planar nanoscale InGaN-based light emitters. *IEEE Photonics 2012* (Arlington, Virginia, USA, October 2012), Oral presentation.

[11] **E.Y. Xie**, Z.Z. Chen, P.R. Edwards, Z. Gong, Y.F. Zhang, Y.J. Chen, I.M. Watson, E. Gu, R.W. Martin, G.Y. Zhang, and M.D. Dawson. Strain relaxation in InGaN/GaN micro-pillars evidenced by high resolution cathodoluminescence spectral mapping. *The 9th International Conference on Nitride Semiconductors* (Glasgow, UK, July 2011), Oral presentation.

[12] Y. Tao, **Z.Z. Chen**, Z. Gong, E.Y. Xie, Y. Chen, Y. Zhang, J. McKendry, D. Massoubre, E. Gu, and G. Zhang. Size effect on efficiency droop of blue light emitting diode. *The 9th International Conference on Nitride Semiconductors* (Glasgow, UK, July 2011), Poster presentation.

[13] **D. Massoubre**, B. Guilhabert, E.Y. Xie, Z. Gong, E. Gu, I.M. Watson, M.D. Dawson. Image-containing InGaN LED. *The 9th International Conference on Nitride Semiconductors* (Glasgow, UK, July 2011), Oral presentation.

[14] P. Tian, E.Y. Xie, Z. Gong, Z. Chen, T. Yu, Y. Sun, S. Qi, Y. Chen, Y. Zhang, S. Calvez, E. Gu, G. Zhang, and **M. D. Dawson**. Flexible vertical structure GaN-based light emitting diodes on an AuSn substrate. *IEEE Photonics 2011* (Arlington, Virginia, USA, October 2011), Oral presentation.

[15] Z. Gong, D. Massoubre, E.Y. Xie, J. McKendry, E. Gu, **M.D. Dawson**, N.Y. Liu, Y.B. Tao, Z.Z. Chen and G.Y. Zhang. Yellow-green and amber InGaN micro-pixellated light-emitting diode arrays. *IEEE Photonics 2010* (Denver, USA, November 2010), Oral presentation.